Particle Dark Matter in the Solar System

Annika H. G. Peter

A Dissertation
Presented to the Faculty
of Princeton University
in Candidacy for the Degree
of Doctor of Philosophy

Recommended for Acceptance
by the Department of
Physics

June, 2008

UMI Number: 3305294

ProQuest Information and Learning Company
300 North Zeeb Road
P.O. Box 1346
Ann Arbor, MI 48106-1346

Abstract

Particle dark matter in the Galactic halo may be bound to the solar system either by elastic scattering through weak interactions with nucleons in the Sun (weak scattering) or by gravitational interactions with the planets, mainly Jupiter (gravitational capture). In this thesis, I simulate weak scattering, gravitational capture, and the subsequent evolution of the bound orbits to determine the distribution of bound dark matter at the position of the Earth. Previous work on this subject suggested that the event rate in dark matter detection experiments due to bound particles could be of order the event rate of halo particles in direct detection experiments, and several orders of magnitude higher for neutrinos arising from dark matter annihilation in the Earth. I use direct integration of orbits in a simplified solar system consisting of the Sun and Jupiter. I follow bound orbits until the particles are either rescattered in the Sun onto orbits that no longer intersect the Earth, ejected from the solar system, or reach the lifetime of the solar system $t_{SS} = 4.5$ Gyr. Since many aspects of the particle orbits pose severe problems for traditional orbit integration methods, I develop a novel integration scheme for this problem, which has only small and oscillatory energy errors even for highly eccentric orbits over very long times. Using the bound dark matter distribution functions I generate from the simulations, I show that bound dark matter has a small effect on direct detection event rates, and that it will be almost impossible to detect neutrinos from dark matter annihilation in the Earth with the new generation of km^3-scale neutrino telescopes. I also show how the distribution functions and resulting direct detection and neutrino telescope event rates can be scaled to other particle masses and elastic scattering cross sections.

Acknowledgements

There are many people who have guided my interests and academic path through life, and many other who have kept me sane during graduate school. I'd like to thank a few of those people here.

First and foremost, I would like to thank my parents, Lyle and Beate Peter, for providing an example and a home life that encouraged learning and discovery. Thanks to their support, my siblings and I are each following our passions and we know that we can do anything we want as long as we put our noses to the grindstone. I would also like to thank my parents for their advice and cheerleading ("it's too late to quit now", "Augen zu und durch") when I was discouraged and tired of working on this thesis, as well as celebrating the many milestones along the way. I have also benefited from the guidance and love of my grandparents, Bernie and Eleanor Peter, and Dr. Hans and Else Vossloh, as well as our dear great-aunts, Anni Vossloh and Reinhild Vossloh. Each has lived a remarkable life, and each is an inspiration to me. In particular, I would like to recognize Tante Reinhild for leading by example and by encouraging my studies by sending books on women in science.

The Shoreline School District has many excellent teachers, but has been especially successful in staffing its Highly Capable Program. I would like to thank the district and all my teachers for their dedication to and belief in their students.

I am grateful to the Early Entrance Program at the University of Washington for giving me (and many others) with a solid foundation for college, providing a safe and nurturing place on campus, and allowing nerds from all over Puget Sound to become lifelong friends. I would like to thank the Ronald Geballe, Maren Halvorsen, Bill Horder, Kate Noble, Ellen

Mosolf, Nancy Robinson, Nancy Sisko, and Kay Soberg for their support during my years as a TSer and EEPer.

There are many people in the Physics-Astronomy Building at the University of Washington who have put me on the path to graduate school. The SNO group provided me with my first glimpse of how physics works outside of the classroom. The Astronomy Department was especially good at fostering a community that was inclusive of undergraduates. In particular, Julianne Dalcanton, Chris Stubbs, and Paula Szkody were instrumental in inspiring undergrads, and encouraging us to consider a careers in astrophysics.

I am grateful to George Fuller and UC San Diego and Andreas Zezas at the CfA for mentoring me during my NSF REU summers.

In graduate school, I have found homes in Gravity Group and the Department of Astrophysical Sciences, not just my home department. I would like to thank Paul Steinhardt and Suzanne Staggs for advising me on projects during my first years, and for bringing me into the Gravity Group fold. My advisor, Scott Tremaine, is a model of prudence, patience, and productivity. I have learned a lot about how to do science from him. I am indebted to Alice Shapley for cheerleading and guiding me through both an observational project and post-doc applications.

My thesis work was heavily computational, and I could not have completed the work without the facilities at Princeton or the people who maintain the computers. I'd like to that Steve Huston, Leigh Koven, and Bill Wichser in the Department of Astrophysical Sciences, Neelesh Arora and Vinod Gupta in the Physics Department, and the dedicated staff at the Computer Science and Engineering Support Group (CSES) for keeping the computers (Hydra, Feynman, Della, Orangena) up and running.

And now, on to the question of sanity. Graduate school turned out to be much harder and quite different than I imagined as an undergraduate. My friends from Seattle have been a source of strength and valued outside observers through the past five years. My siblings (Lukas, Elias, and Cara) keep me laughing with jokes of questionable taste and photos and videos of Milo engaging in ridiculous feline antics. I have made a lot of treasured friends

at Princeton. I would especially like to thank Eric Dahl for getting people to socialize. I would like to thank Janice and Khali Hester and Amin Nasr for putting up with my dismal apartment-cleaning skills for two years. My officemates, Amol Upadhye and Beth Reid, and my across-the-wall neighbors Kevin Huffenberger and Nikhil Padmanabhan, always guaranteed a good time in the office. The (astro)physics women are a fantastic bunch. In a department that is $> 90\%$ male, it is wonderful to have such a cool group of women surrounding me. I have acquired a husband, Chris Hirata, and another family (the Hiratas and Lefevres), thanks to my association with the Physics Department at Princeton.

Even though I have been known to complain, on occasion, about the state of New Jersey, there are institutions here that sustained me and which I miss now that I have moved. Crown of India has fed me well (no other chicken tikka masala compares!), and the Wawa has satisfied every junk food craving (especially for Haribo Goldbären). Chris and I have spent a lot of time drinking coffee and reading books at Market Fair, and whiling away happy evenings with friends in the dbar.

Finally, I would like to thank my husband Chris for emotional support, being an invaluable sounding board, and the many trips to the Wawa and Starbucks on my behalf.

Contents

Abstract **iii**

Acknowledgements **iv**

Contents **vii**

List of Figures **x**

List of Tables **xxii**

1 Introduction **1**

1.1 Evidence for Dark Matter 1

1.1.1 Astrophysical Evidence 2

1.1.2 Tantalizing Hints from Particle Physics 20

1.2 Various Probes of Dark Matter Properties 23

1.2.1 (Extra)Galactic Methods 23

1.2.2 Solar System Methods 28

1.3 The Local Dark Matter Distribution Function 46

1.3.1 The Halo Dark Matter Distribution Function at the Solar Circle . . 47

1.3.2 Motion of the Earth in the Halo 57

1.4 Corrections to the Distribution Function: Effects Within the Solar System . 62

1.4.1 Weak Scattering 63

1.4.2 Gravitational Scattering 69

1.5 This Approach 71

2 Initial Conditions **74**

2.1 Particle and Astrophysics Input 74

2.1.1 The Dark Matter Candidate 74

2.1.2 The Halo Distribution Function 80

2.1.3 The Sun 82

2.1.4 The Solar System 82

2.2 Weak Scattering in the Sun 83

2.3 Gravitational Scattering 88

2.4 Simulation Specifics 94

3 Numerical Methods **96**

3.1 The Integrator 96

3.1.1 The Adaptive Time Step Symplectic Integrator 97

3.1.2 Errors Along the Orbital Path 101

3.1.3 Special Cases: Strong Perturbations to the Keplerian Potential . . . 109

3.1.4 Coordinate Choice 117

3.2 Subsequent Scattering in the Sun 119

3.3 Simulation Specifics 122

3.3.1 Weak Scattering Simulations 122

3.3.2 Gravitational Scattering Simulations 128

3.3.3 Computing 131

4 From Simulations to Distribution Functions **132**

4.1 Distribution Function Estimators 132

4.2 Estimating Distribution Functions in Practice 137

4.3 The Distribution Function in the Earth 138

5 Results **141**

5.1 Distribution Functions 142

5.1.1 Weak Scatter Simulations 142

5.1.2 Gravitational Capture Simulations 187

5.1.3 Summary of the Gravitationally Captured WIMPs 199

5.2 Impact on Direct Detection Experiments 200

5.3 Impact on Neutrino Telescope Event Rates 211

5.3.1 An Aside on Neutrinos from the Sun 225

6 Conclusion **229**

6.1 Summary 229

6.2 Future Directions 231

6.2.1 Possible Speed-Ups 231

6.2.2 The Full Solar System Simulation 234

6.2.3 Other Applications of the Integration Code 245

A The 1-d Velocity Dispersion of Galactic WIMPs in the Solar Neighborhood **250**

B WIMP Elastic Scattering **253**

B.1 Spin-Independent Scattering 253

B.2 Spin-Dependent Scattering 255

References **258**

List of Figures

1.1 *Left:* The spiral galaxy NGC 6503. Image from Frei et al. (1996). *Right:* The rotation curve of NGC 6503. The curves labeled "gas," "disk," and "halo" represent the contributions from the mass in gas, stars, and a dark halo. This plot of the rotation curve is from Bertone et al. (2005b) using data from Begeman et al. (1991). 4

1.2 Observations of the bullet cluster at a variety of wavelengths. Green lines indicated the lensing reconstruction of the mass distribution in the cluster. *(a)*: Contours lie on top of an BVR composite optical image to indicate the distribution of galaxies relative to the mass of the cluster. *(b)*: An X-ray image of the hot gas in the cluster. Both figures come from Clowe et al. (2006a). 11

1.3 An equatorial slice from the Sloan Digital Sky Survey. Figure from Gott et al. (2005). 13

1.4 Simulations of structure formation for *(a)* cold dark matter and *(b)* hot dark matter universes. Each image is $300h^{-1}$ Mpc on a side. Images are from Martin White's primer on cosmological models: http://astro.berkeley.edu/∼mwhite/modelcmp.html 15

1.5 Structure formation as a function of time for $\Omega = \Omega_m = 1$ (labeled τ in the figure) and ΛCDM ($\Omega_\Lambda = 0.7, \Omega_m = 0.3$) universes using the Virgo Consortium Hubble Volume simulations. The points mark the location of clusters in redshift space. This figure is from Evrard et al. (2002). 16

1.6 Relationship between the number density of relic dark matter particles and the annihilation cross section. The solid line represents the equilibrium number density of cold dark matter particles. The dashed lines represent the number density at freeze out for a variety of annihilation cross sections. Figure originally from Dodelson (2003). 18

1.7 Limits on the spin-independent WIMP-nucleon cross section from recent experiments. The CDMS and XENON experiments are discussed in the text. EDELWEISS is a germanium experiment like CDMS, and ZEPLIN-II is another xenon-based experiment. The plot is made using the interface available at
http://dendera.berkeley.edu/plotter/entryform.html. 31

1.8 Limits on the spin-dependent WIMP-proton cross section from recent experiments. The plot is made using the interface available at
http://dendera.berkeley.edu/plotter/entryform.html. 32

1.9 Limits on the spin-dependent WIMP-neutron cross section from recent experiments. The plot is made using the interface available at
http://dendera.berkeley.edu/plotter/entryform.html. 33

1.10 Predicted spin-independent event rates per unit detector mass for a WIMP of mass $m_{\mathrm{WIMP}} = 470$ GeV and interaction cross section $\sigma_P^{SI} = 10^{-43}$ cm^2. The dashed green line indicates scatters with xenon ($A = 131$), the blue dotted line indicates a target mass of germanium ($A = 73$), and the red solid line denotes interactions with argon ($A = 40$). 34

1.11 The ratio of the muon event rate above an energy threshold E_μ^{th} to the event rate with an energy threshold of 1 GeV in a km^3-scale experiment assuming that the muons result from WIMP annihilation in the Earth. These ratios were computed using only muons created outside of the experimental volume, not muons created within the detector volume. This figure is from Bergström et al. (1998a). 41

1.12 Limits on the flux of muons resulting from WIMP annihilations in the Earth. The upper (lower) AMANDA line corresponds to the limit for a soft (hard) annihilation spectrum. The dots mark individual MSSM models. Models in the hatched region are above the Bernabei et al. (1996) spin-independent cross section limit, which is grossly out-of-date. This figure is taken from Ahrens et al. (2002). 42

1.13 Artistic rendering of a muon passing through the IceCube array. From http://www.icecube.wisc.edu/index.php 44

1.14 Cutoff speed in the frame of the Earth as a function of WIMP mass (*solid line*). WIMPs with speeds to the left of the solid line may be captured by the Earth via weak interactions. The minimum possible speed of halo particles in the absence of scattering processes $v_{\rm min} = (\sqrt{2}-1)v_{\oplus}$ is marked with the dashed line. 47

1.15 The ratio of the differential event rate $\mathrm{d}F(v_{\odot})/\mathrm{d}Q$ for several choices of WIMP mass (in units of the proton mass), and for $v_{\odot} = 0$ (*black line*), $v_{\odot} = 100$ km s^{-1} (*red dots*), $v_{\odot} = 180$ km s^{-1} (*blue dash*), $v_{\odot} = 220$ km s^{-1} (*green long dash*), and $v_{\odot} = 260$ km s^{-1} (*cyan dot-dash*). The target mass is assumed to be ^{73}Ge. 60

1.16 The estimated geocentric distribution function for Kozai-cycling dark matter particles. The case of $\lambda = 1$ corresponds to absolute conservation of H. In the case of $\lambda = 2$, Bergström et al. (1999) allow small variations in H. This figure is originally from Bergström et al. (2001). The version of this plot resulting from my simulations is shown in Figure 5.2. 67

2.1 Points in the $\sigma_p^{SI} - m_{\chi}$ parameter space used for the weak scattering simulations, plotted along with exclusion curves from recent experiments. This plot was generated with the help of an interface available at: http://dendera.berkeley.edu/plotter/entryform.html 78

3.1 Jacobi constant errors as a function of distance from the primary for a trajectory with $a = 1.73$ AU, followed for 2×10^4 Kepler periods. This trajectory was integrated with 500 steps/orbit. Errors are calculated at perihelion and aphelion. The gap in the plot is due to the fact that the minimum eccentricity of this trajectory is $e_{min} = 0.38$. Points to the left of the vertical line lie within the volume of the Sun; however, I used a point-mass Sun for this integration. 103

3.2 Errors in the Jacobi constant as a function of eccentricity and semi-major axis. Each point shows the maximum error for 10 trajectories initialized with the same eccentricity but with random initial orientation, and followed for 2×10^4 Kepler orbits. Since the size and frequency of the eccentricity oscillations depend on the initial orientation, I use only the maximum Jacobi errors for each orbit in the trajectory whose eccentricity matches the initial eccentricity to calculate the averaged maximum error. Open points denote those trajectories for which the semi-major axis $a = a_J/3 = 1.73$ AU; closed points refer to trajectories with $a = a_J/6 = 0.87$ AU. Circles mark trajectories with initial eccentricity $e_i = 0.9999$, squares denote those with $e_i = 0.999$, diamonds indicate those with $e_i = 0.99$, and triangles those with $e_i = 0.9$. 105

3.3 Energy errors using the maximum value of $|\Delta E/E|$ for a given a at $r = 2$ $R_\odot$ using 50 steps/orbit (*black solid line*), 100 steps/orbit (*red dashed line*), and 500 steps/orbit (*blue long dashes*). There is a sharp peak at $r = a_J/2$ where the initial position of the particle lies exactly within Jupiter. The energy error asymptotes at large values of a. 110

3.4 Error in the Jacobi constant as a function of time for several particles. The Jacobi constant is recorded at aphelion at 10^5 year intervals. *Top left:* A particle with $a = 1.54$ AU. This particle repeatedly goes through the Sun (about 10^7 times), but never goes through the bubble around Jupiter. It is integrated with $h = 6 \times 10^{-5} R_\odot^{-1}$ year, which corresponds to ≈ 100 steps/orbit. *Top right:* A particle that gets stuck near a Sun-skimming 2:1 resonance with Jupiter. This particle repeatedly goes through the Jupiter bubble. It is integrated with $h = 2 \times 10^{-5} R_\odot^{-1}$ year, which corresponds to ≈ 350 steps/orbit. *Bottom left:* A particle gets stuck near a 3:2 resonance with Jupiter. This orbit was integrated with $h = 1.5 \times 10^{-5} R_\odot^{-1}$ year, which corresponds to ≈ 650 steps/orbit. *Bottom right:* This particle repeatedly crosses r_c, the transition radius between barycentric and heliocentric coordinates (dashed green line marks $r_c/2$, the crossing semi-major axis for an orbit with $e \sim 1$) and has its last aphelion before ejection from the solar system at $t = 1.6 \times 10^6$ years. It is integrated with $h = 2 \times 10^{-6} R_\odot^{-1}$ year, which corresponded initially to 9×10^3 steps/orbit. 114

3.5 Flowchart for the simulation algorithm for the weak scattering experiments. 124

3.6 Flowchart for the simulation algorithm for the gravitational capture experiments. 129

5.1 Distribution functions divided by n_χ in the $v - \cos\theta$ plane (integrated over ϕ) for both (a) heliocentric and (b) geocentric frames. These distribution functions come from the CDMS simulation, and the units are $(\text{km s}^{-1})^{-3}$. 143

5.2 Geocentric distribution functions from the simulations. (a) Results from all simulations. (b) The CDMS distribution function relative to theoretical distribution functions for unbound WIMPs. 144

5.3 Locations of various types of orbits in the (a) $\phi = 0$ and (b) $\phi = \pi/2$ slices of heliocentric velocity space, and (c) $\phi = 0$ and (d) $\phi = \pi/2$ slices of geocentric velocity space. 145

5.4 Particle lifetime distributions for the DAMA (*solid black*), CDMS (*red dot-dashes*), Medium Mass (*short green dashes*), and Large Mass (*long blue dashes*) simulations. 152

5.5 Lifetime distributions as a function of initial semi-major axis for the DAMA (*upper left*), CDMS (*upper right*), Medium Mass (*lower left*) and Large Mass (*lower right*) simulations. The solid black line represents particles with 0.5 AU $\leq a_i <$ 1.0 AU, red dots those with 1.0 AU $\leq a_i <$ 1.5 AU, short green dashes those with 1.5 AU $\leq a_i <$ 2 AU, long cyan dashes those with 2 AU $\leq a_i <$ 2.6 AU, and the blue dash-dotted line indicates those with $a_i \geq$ 2.6 AU $= a_J/2$. 156

5.6 Growth of the distribution functions as a function of time for the (a) DAMA and (b) CDMS simulations. 159

5.7 Geocentric distribution functions for $a_i > a_J/2$. 160

5.8 Contributions to the number density of bound particles at the Earth as a function of both the initial semi-major axis and initial perihelion in the Sun for the (a) DAMA and (b) CDMS simulations. 162

5.9 Initial semi-major axis distribution of particles with lifetimes $t_{\rm surv} > 1$ Gyr. The top panel is for the Large Mass run, middle for the Medium Mass run, and the bottom panel shows the results from the CDMS run. The light yellow histogram shows the distribution of semi-major axes for $a < 3$ AU. The red line indicates the subset of particles which had initial perihelia ($r < 0.5 R_\odot$), i.e., the particles that initially scattered deep within the Sun. The solid vertical lines indicate the major resonances, and the small thick lines indicate all minor resonances between the 8:1 and 3:1 resonances up to $m : n$ with $m = 15$. 163

5.10 Contributions to the number density of bound particles at the Earth as a function of both the initial semi-major axis and initial perihelion in the Sun for the (a) Medium Mass and (b) Large Mass simulations. 166

5.11 Percentages of particles in each (a) initial semi-major axis bin or (b) initial perihelion bin. The semi-major axis bins were designed such that, if $\mathrm{d}\dot{N}_\oplus/\mathrm{d}a \propto a^{-1}$, each bin would have the same percentage of particles (apart from Poisson errors). 168

5.12 In each plot, the red solid line denotes all species in the Sun, and the dotted blue line represents hydrogen. (*a*): The capture rate $\dot{N}$ of WIMPs by the Sun for $\sigma_p^{SI} = 10^{-43}$ cm^2, divided by the halo number density of WIMPs. The short solid black line gives the slope $\dot{N}/n_\chi \propto m_\chi^{-1}$, the limiting slope for $m_\chi \gg m_A$ for a nuclear species A. (*b*): The capture rate $\dot{N}_\oplus$ to Earth-crossing orbits divided by the halo WIMP number density. (*c*): $\dot{N}/\dot{N}_\oplus$. . . 170

5.13 Distribution functions for the three simulations with $\sigma_p^{SI} = 10^{-43}$ cm^2 scaled by $\dot{N}_\oplus$. 171

5.14 *(a):* Limits on the spin-dependent WIMP-proton cross section from the NAIAD (*dashed*) and KIMS (*solid*) experiments. These are the most stringent current limits. *(b):* Spin-dependent vs. spin-independent neutralino-proton cross sections for a selection of supersymmetric models with $0.05 < \Omega_\chi h^2 < 0.135$. Only models with $\sigma_p^{SI} > 8 \times 10^{-44}$ cm^2 are shown. 179

5.15 Predicted geocentric distribution function if $\sigma_p^{SD} = 10^{-36}$ cm^2, assuming $f(v) \propto \sigma_p^{SI,SD}$ for Jupiter-crossing orbits. This prediction is based on the output of the DAMA simulation, without contributions from long-lived near-resonant particles. 181

5.16 Estimated geocentric distribution functions for $\sigma_p^{SD} = 1.3 \times 10^{-39}$, 10^{-38}, 10^{-37}, and 10^{-36} cm^2. The estimated distribution function for $\sigma_p^{SD} = 1.3 \times 10^{-39}$ cm^2 is based on the DAMA simulation result, since the optical depth of the Sun for $\sigma_p^{SI} = 10^{-41}$ cm^2 is approximately the same as $\sigma_p^{SD} = 1.3 \times 10^{-39}$ cm^2. 184

5.17 The Jupiter-crossing part of the estimated geocentric distribution functions with various WIMP-proton spin-dependent cross sections. *(a)*: Distribution functions on a linear scale. *(b)*: Distribution functions plotted on a logarithmic scale to highlight dependence on the cross section. 186

5.18 Distribution function from the gravitational capture experiments. The distribution function is normalized such that $\int_0^{v_{\max}} f(v)v^2 \mathrm{d}v = n_\chi^{sim}(v < v_{\max})$, where n_χ^{sim} is the number density of particles in the simulation with $v < v_{\max}$. The error bars are estimated using bootstrap resampling of the original particle distribution. 188

5.19 The distribution function from the High Energy run compared with that which is analytically derived using Liouville's theorem. 189

5.20 The total distribution function from the gravitational capture simulations (using the theoretical High Energy curve) compared against several theoretical distribution functions. 190

5.21 (a) Particle lifetime distribution for the Regular run (*solid black*) and the High Perihelion run (*red dots*). (b) Distribution of times at which particles cross the Earth's orbit. 192

5.22 Comparison of the geocentric bound distribution functions for $m_\chi = 500$ AMU. The dashed black line indicates the phase space density of unbound orbits. The blue line shows the results from the gravitational capture simulations, the red line is the Large Mass distribution function ($\sigma_p^{SI} = 10^{-43}$ cm^2 and $\sigma_p^{SD} = 0$, and the green dashed line indicates the estimated distribution function for the maximal value of $\sigma_p^{SD} = 10^{-36}$ cm^2. 194

5.23 The distribution of total optical depth per particle of those particles that enter the Sun. The solid red line indicates the distribution for the Regular simulation, while the dashed black line indicates that of the High Perihelion run. 196

5.24 The distribution function of bound particles from the gravitational capture simulations. The solid red line indicates the raw distribution function from the simulations minus the unbound halo distribution function. The long-dashed green line with data points indicates the distribution function of particles before they are lost to the solar system by Galactic tides. The short-dashed blue line and data points indicate the distribution function of particles that never enter the Sun. 197

5.25 Direct detection event rates as a function of the energy transfer Q for a WIMP of mass 500 AMUs and interaction cross section $\sigma_p^{SI} = 10^{-43}$ cm^2 with argon (*solid red line*), germanium (*blue dots*), and xenon (*green dashed*) as targets. The upper curves indicate the event rate for the full halo distribution function under the gravitational influence of the Sun. The lower curves indicate the contribution to the total event rate from only the unbound orbits in the halo distribution function with $v < (\sqrt{2}+1)v_\oplus$ in the frame of the Earth, the range of speeds accessible to bound particles. 201

5.26 Differential direct detection rates for each weak scattering simulation. As in Figure 5.25, solid red lines indicate detection rates for a target of argon, dotted blue lines assume germanium as a target, and dashed green lines indicate rates for xenon. 205

5.27 Contribution of the estimated distribution functions for significant spin-dependent cross sections to the event rate for a target composed of xenon and for a WIMP of mass $m_\chi = 500$ AMUs. The spin-independent cross section, used to estimate the scattering rate on xenon, is $\sigma_p^{SI} = 10^{-43}$ cm^2. Shown are the contribution from all unbound orbits (*green solid line*), unbound orbits with $v < (\sqrt{2}+1)v_\oplus$ (*red dots*), bound orbits for a distribution function estimated for $\sigma_p^{SD} = 1.3 \times 10^{-39}$ cm^2 (*black dot-dashes*) and for $\sigma_p^{SD} = 10^{-36}$ cm^2 (*magenta long dashes*), and for direct result from the Large Mass simulation (*cyan short dashes*). *(a)*: Log scale. *(b)*: Linear scale. In this case, the contribution from unbound orbits alone with $v < (\sqrt{2}+1)v_\oplus$ is shown with a red solid line, and the results from the weak simulation have the contribution from the unbound orbits with $v < (\sqrt{2}+1)v_\oplus$ added in. 207

5.28 Direct detection rates from the gravitational capture simulations with $m_\chi =$ 500 AMU. The two red lines represent differential event rates for a target of argon for the purely unbound orbits with $v < (\sqrt{2}+1)v_\oplus$ (*dot-dashed*) and the sum of the simulations (*with data points*), the middle two blue lines represent scattering on germanium (*dashes, unbound; solid with data points, simulation*), and the top green lines denote scattering on xenon (*solid, unbound; dotted with data points, simulation*). Error bars are of the same size as the points marking the data. 208

5.29 The maximum contribution to the differential direct detection rate for $m_\chi =$ 500 AMU and $\sigma_p^{SI} = 10^{-43}$ cm^2. The solid green line shows the contribution to the total differential event rate for unbound orbits with $v < (\sqrt{2}+1)v_\oplus$, while the dotted line shows the sum of the gravitational capture experiment and the estimated rate for the bound orbits from weak scattering in the Sun with $\sigma_p^{SD} = 10^{-36}$ cm^2. 210

5.30 Capture rate of WIMPs in the Earth as a function of WIMP mass for $\sigma_p^{SI} = 10^{-43}$ cm^2. The lines correspond to distribution functions for: the halo in the absence of the gravitational field of the Sun (*black solid line*), the result from the gravitational simulation along with the Liouville traced distribution function of unbound orbits above $v = (\sqrt{2}+1)v_\oplus$ (*blue medium dashes*), the estimate for $\sigma_p^{SD} = 10^{-36}$ cm^2 with $\sigma_P^{SI} = 10^{-43}$ cm^2 (*magenta long dash dotted line*), the estimate for $\sigma_p^{SD} = 1.3 \times 10^{-39}$ cm^2 and $\sigma_p^{SI} = 10^{-43}$ cm^2 (*cyan short dash dotted line*), the result of the simulations for $\sigma_p^{SI} = 10^{-43}$ cm^2 (*green long dashed*), and for only unbound orbits (*thick red line*). . . . 214

5.31 Muon event rates with an optimistic energy threshold of 1 GeV for a sample of SUSY models. The dark matter distribution function is the halo distribution function in the absence of the solar system. The SUSY models marked with red open circles have spin-independent cross sections above the Edelweiss limit (see Figure 1.7 and Sanglard et al., 2005), those marked with open green triangles have σ_p^{SI} lying between the Edelweiss and Zeplin-II limits (Alner et al., 2007), cyan triangles denote those with the cross section between the Zeplin-II and CDMS limits (Akerib et al., 2006b), blue dots mark models with spin-independent cross sections between the CDMS (Akerib et al., 2006b) and XENON10 limits, and magenta-outlined boxes denote models with σ_P^{SI} lower than the XENON10 limit (Angle et al., 2007). 218

5.32 Muon event rates from halo WIMPs unbound to the solar system. The symbols have the same meanings as those in Figure 5.31. 219

5.33 Muon event rates using the results of the weak scattering simulation and including the contribution particles unbound to the solar system. The distribution function is based on the average of the three simulations with $\sigma_P^{SI} = 10^{-43}$ cm^2. The symbols have the same meaning as those in Figure 5.31. 220

5.34 Muon event rates using the estimated distribution function for $\sigma_p^{SD} = 10^{-36}$ cm^2. Symbols mark the same models as in Figure 5.31. 222

5.35 Muon event rates using the result from the gravitational capture simulations. Symbols mark the same models as in Figure 5.31. 223

5.36 Muon event rates using the estimated distribution function for $\sigma_p^{SD} = 10^{-36}$ cm^2 and the results from the gravitational capture simulation. This is the maximum total event rate in Jupiter is the only planet in the solar system. Symbols mark the same models as in Figure 5.31. 224

5.37 Limits on the proton-WIMP cross section from the Super-Kamiokande (Desai et al., 2004), ELEGANT V (Yoshida et al., 2000b) and UKDMC (NAIAD) (Alner et al., 2005) experiments. This figure is from Desai et al. (2004). . . 226

List of Tables

2.1 Weak Scattering Simulations 95
2.2 Gravitational Scattering Simulations 95

3.1 The fictitious time step h as a function of semi-major axis for the DAMA run. 125
3.2 The fictitious time step h as a function of semi-major axis for the CDMS, Medium Mass, and Large Mass runs. 126
3.3 The initial integration conditions for the gravitational capture simulation as a function of initial speed v and Kepler perihelion r_p. The values of h are in units of $R_{\odot}^{-1}$ yr. 128
3.4 Choices for the fictitious time step h as a function of semi-major axis for the gravitational capture simulations. The semi-major axis refers to bound particles unless otherwise indicated. 130

5.1 Ranges of Parameters for the Restricted DarkSUSY MSSM Inputs at the Weak Scale 215

Chapter 1

Introduction

1.1 Evidence for Dark Matter

One of the most fundamental questions pertaining to the cosmos is: *What is the universe made of?* In the twentieth century, there have been several paradigm shifts (quantum mechanics, quantum electrodynamics, quantum chromodynamics, electroweak unification) in our understanding of ordinary matter (nucleons, electrons, etc.; generally referred to by astronomers as "baryons"). When this knowledge is combined with the twentieth century concept of general relativistic cosmology, with observations of the abundances of light elements such as deuterium and helium, and observations that show that the universe is homogeneous and isotropic and emerged from an initial singularity, it is even possible to calculate just how much ordinary matter exists in the universe.

However, in the latter half of the last century, it became clear that although ordinary matter was a "known known",[1] it is only a small component of the total energy density ρ_{tot} of the universe. A suite of observations (described below) indicate that the concordance model, as proposed by Ostriker & Steinhardt (1995), provides a good description of the universe. In this model, which I now describe, the universe is flat ($\Omega \equiv \rho_{tot}/\rho_{crit} = 1$, which defines the critical density ρ_{crit}). A mechanism such as inflation (Guth, 1981; Albrecht

[1] former Secretary of Defense Donald Rumsfeld '54, Feb. 12, 2002.

et al., 1982; Linde, 1982, 2007) or cyclic models (Khoury et al., 2001, 2002a,b) smooths and isotropizes the universe on scales of at least the current horizon size, and provides the initial tiny quantum density fluctuations that lead to structure formation once matter and not radiation governs the expansion of the universe. In this model, baryons make up only $\sim 4\%$ of the total mass-energy density of the universe. Recent observations (e.g., Spergel et al., 2007) show that non-baryonic gravitationally *attractive* material ("dark matter") contributes 23% to the energy density, and a substantial 72% of the total energy density is made of gravitationally *repulsive* material ("dark energy"). Therefore, an overwhelming $\sim 95\%$ of the universe is made up of "known unknowns,"[2] assuming that general relativity is an accurate description of gravity on large scales.

Dark energy has only recently been established to exist, and its nature will be difficult to ascertain (see Kamionkowski, 2007, and references therein). However, it is thought that the nature of dark matter may be possible to determine in the next decade. There is already a large body of astrophysical evidence, from a wide range of physical scales, on the existence and distribution of dark matter, and hints from both astrophysics and particle physics as to its properties. This evidence is guiding future experimental and observational efforts to determine the nature of dark matter. The following is a description of some of the observations, simulations, and theoretical arguments that lead to the current consensus on dark matter.

1.1.1 Astrophysical Evidence

Galactic Rotation Curves

The classic evidence for the existence for dark matter comes from the rotation curves of spiral galaxies. Spiral galaxies are dynamically cold systems, so stars and gas move on almost circular orbits. The circular velocity $v_c(R)$ for stars in the plane of an axisymmetric disk ($z = 0$ in cylindrical coordinates) at a distance R from the galactic center is

$$v_c^2(R) = -R\frac{\partial \Phi_d}{\partial R}\Big|_{z=0}, \tag{1.1}$$

[2] Ibid.

where $\Phi_d(\mathbf{r})$ is the gravitational potential of the disk. For a thin, axisymmetric disk with a surface mass density $\Sigma(R)$ (Eq. 2-139 in Binney & Tremaine, 1987),

$$\Phi_d(\mathbf{r}) = -G_N \int_0^\infty \Sigma(R')R'\mathrm{d}R' \int_0^{2\pi} \frac{\mathrm{d}\phi'}{|\mathbf{r}-\mathbf{r}'|}, \tag{1.2}$$

where G_N is Newton's constant and ϕ is the azimuth in cylindrical coordinates. Disk galaxies typically have light curves for stars and gas that fall rapidly at large radii. If the mass-to-light ratio $\Upsilon = (M/M_\odot)/(L/L_\odot)$ is constant throughout the disk, where M is the mass of an element of the disk and L is its luminosity, then the surface mass density has the same shape as the surface brightness. Therefore, $\Sigma(R)$ should fall rapidly with R at large radii, and Φ_d and v_c should asymptotically behave as $\Phi_d \propto R^{-1}$ and $v_c \propto R^{-1/2}$. This is illustrated for the SA(s)cd galaxy NGC 6503 in Figure 1.1. The left side of this Figure shows a *gri* composite image from Frei et al. (1996), and the curve marked "disk" in the right half of the Figure shows the circular velocity due to stars in the disk if the surface brightness is scaled by a fitted Υ and inserted into Eqs. (1.1) and (1.2) (Begeman et al., 1991). The circular velocity due to the stellar component is falling rapidly as a function of galactocentric distance for $R > 2$ kpc. If stars were the main source of matter in NGC 6503, then the velocity profile of any cold tracer should mimic this circular velocity curve. The contribution to the circular velocity curve from the mass in gas is even smaller, as shown by the lowest curve in Figure 1.1. This is generically true of other spiral galaxies, too.

Observations have been made of atomic gas clouds (using the 21 cm hyperfine transition of hydrogen) in circular orbits both inside and beyond the stellar disk of many galaxies (i.e., out to radii of $25 - 100$ kpc; Rubin et al., 1978, 1980; Bosma, 1981). If galaxies were made mostly of stars, than the rotation curve of the atomic gas should follow a curve akin to the "disk" curve in Figure 1.1. However, these observations show that instead, the circular speed is constant or rising as far out as measurements are made. This is true, for example, for NGC 6503, for which the points with error bars mark the observed circular velocity. The observed circular velocity curve can be fit by adding to the baryonic components (stars and gas) a spherical distribution of dark matter, which contributes $v_c^{dm}(r) = \sqrt{GM(r)/r}$, where $M(r)$ is the total dark mass within r. The flatness or rise in the circular velocity

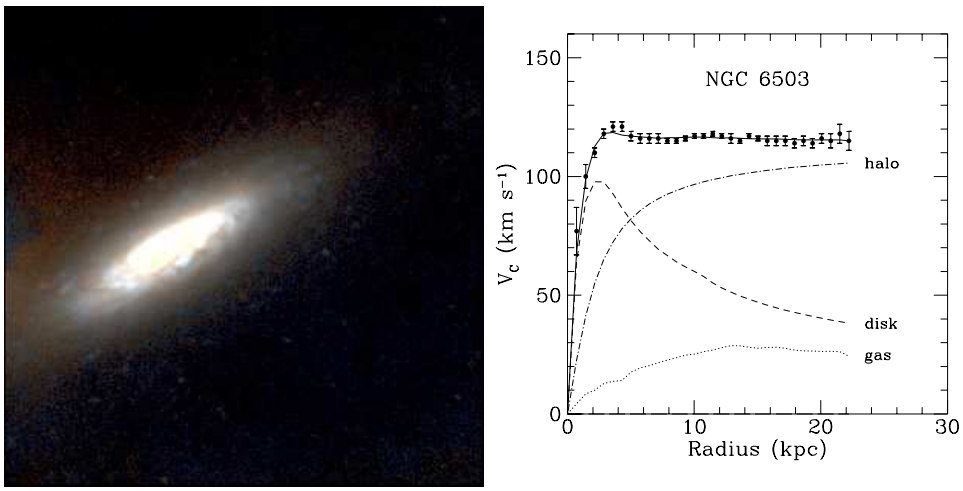

Figure 1.1: *Left:* The spiral galaxy NGC 6503. Image from Frei et al. (1996). *Right:* The rotation curve of NGC 6503. The curves labeled "gas," "disk," and "halo" represent the contributions from the mass in gas, stars, and a dark halo. This plot of the rotation curve is from Bertone et al. (2005b) using data from Begeman et al. (1991).

imply that the interior dark mass rises like $M(r) \propto r^{\alpha}$ with $\alpha \gtrsim 1$ at large radii. This contribution is labeled "halo" in Figure 1.1.

There have been several attempts to model these data without resorting to non-baryonic dark matter. Persic & Salucci (1992) and others argued that the luminous matter density in spiral galaxies implied $\Omega_b = \rho_b/\rho_{crit} = 0.0007$, while the total stellar density (derived from both elliptical and spiral galaxies) implied $\Omega_* = \rho_*/\rho_{crit} = 0.002$, both of which are far below the Big Bang nucleosynthesis value of $\Omega_b h^2 = 0.023$, where h is the Hubble parameter such that the Hubble constant $H_0 = 100h$km s^{-1}Mpc^{-1} (the best current estimate is $h = 0.7$; see Komatsu et al., 2008). More recent estimates of the total mass of stars and stellar remnants are somewhat higher, with Fukugita & Peebles (2004) suggesting $\Omega_* = 0.0024$ and Cole et al. (2001) estimating $\Omega_* = 0.0029$, but still far below the baryonic density implied by nucleosynthesis. Therefore, some have suggested that perhaps so-called "dark baryons" could flatten the rotation curves. However, Zaritsky et al. (1993) used the orbits of satellite galaxies about spiral galaxies similar to the Milky Way to demonstrate that the circular velocity remains high and constant out to $r \gtrsim 200$ kpc, and this result

is consistent with weak lensing estimates of the mass distribution. The dark halos likely extend even beyond this radius. Given that the mass within a radius r of the galactic center rises like r^{α} for a significant part of the halo, there could simply not be enough dark baryons to completely fill the dark matter halo without violating the nucleosynthesis limit. In addition, in the Milky Way, it appears that about 40% of the baryons predicted to be in a Milky Way-sized halo if $\Omega_m/\Omega_b \simeq 6$ are in stars (Xue et al., 2008). Given the estimated mass of the Milky Way halo, there are not nearly enough baryons, both dark and luminous, to build up the entire mass of our halo.

Another attempt to explain the rotation curves involves altering gravity. Milgrom (1983a,b) postulated that the acceleration of gravity deviates from its Newtonian behavior for small accelerations. While this simple model can successfully reproduce the flat rotation curves of many galaxies, relativistic formulations of this idea (TeVeS, or tensor-vector-scalar theory; Bekenstein, 2004; Bekenstein & Sanders, 2006) face increasing pressure from recent gravitational lensing observations of clusters (Clowe et al., 2006b), which seem to require at least *some* dark matter (see below for more detail).

While the rotation curves of spiral galaxies imply that a significant amount of dark matter exists in the universe, the rotation curves of low surface brightness (LSB) galaxies may provide important clues to the nature of dark matter. LSB galaxies provide a unique insight into dark matter halos because of their very low baryon content. The baryonic contribution to galactic rotation curves must be modeled in order to extract information about the non-baryonic content, but disentangling the baryonic and non-baryonic contributions to the mass is difficult. Galaxies with a small total baryon contribution therefore provide the most direct probes of the dark matter distribution. Observations of LSB galaxies have been made using long slit and integral field spectroscopy of the Hα line (McGaugh & de Blok, 1998; de Blok et al., 2001; de Blok & Bosma, 2002; Kuzio de Naray et al., 2006). The velocity fields are fit with baryonic disks and spherically symmetric dark matter halos. These fits indicate that the dark matter density near the center of the galaxy is flat, $\rho(r) \approx$ const for small r, a "core" rather than "cusp" structure.

This finding may indicate that there is a problem with standard assumptions about dark matter. Typically, non-baryonic dark matter is modeled as "cold" (non-relativistic) and collisionless (for large scale structure reasons, as discussed below). Cosmological simulations using cold, collisionless dark matter (CDM) indicate that the density of dark matter halos is cuspy at the center (Navarro et al., 1997, 2004; Hayashi et al., 2004). The presence of baryons at the center of dark matter halos is thought to steepen the cusp. This is very much in contrast to the observed flatness of the inner dark matter halos. Other than invoking modified gravity, several lines of thought exist to explain the discrepancy between LSB galaxy observations and simulations. Spergel & Steinhardt (2000) suggest that particle dark matter may have a strong, short-range ($\sim$ nuclear scale) self-interaction. This is only valid if dark matter consists of non-Standard Model particles and not, for example, primordial black holes (PBH, though there are limits on Ω_{PBH}; see Mack et al., 2006, and references therein). If dark matter were self-interacting, the inner part of dark matter halos would heat, leading to a flatter density profile at the center of the halo. Another line of argument seeks to resolve the discrepancy within the framework of CDM. In CDM-only simulations, halos have significant triaxiality. It has been suggested that the LSB data can be fit well using realistically triaxial halos with cuspy profiles (Hayashi et al., 2004; Hayashi & Navarro, 2006; Hayashi et al., 2007).

Therefore, from galactic rotation curves, we find that non-baryonic dark matter must exist unless Newtonian gravity is not valid at large distances.

Galaxy Cluster Dynamics

There are several different types of observation of galaxy clusters that argue for the existence of dark matter and hint at its properties. Cluster- and larger-scale observations are preferred over galaxy-scale ones for estimating the total matter density in the universe ρ_m because they sample a larger percentage of the observed universe, and should be less susceptible to local fluctuations in the baryon-to-matter ratio.

The first indication that any type of dark matter might exist came from measurements of

the velocity dispersion of galaxies in the Coma cluster (Zwicky, 1933). To see how velocity dispersion measurements can translate into a statement about cluster mass, I make the following simplified argument. For virialized, spherical equilibrium systems with isotropic velocity dispersion, the Jeans equation relates the rms radial velocity σ of galaxies at a particular radius r to the mass interior to that radius in the form

$$M(r) = \frac{r\sigma^2}{G}\left(\frac{\mathrm{d}\ \ln\rho}{\mathrm{d}\ \ln r} + \frac{\mathrm{d}\ \ln\sigma^2}{\mathrm{d}\ \ln r}\right), \tag{1.3}$$

where $\rho(r)$ is the mass density of galaxies. If the mass density traces the luminosity density, then

$$\rho(r) = \Upsilon j(r), \tag{1.4}$$

where Υ is the ratio of *all* mass (luminous and dark) to the luminosity, and $j(r)$ is the luminosity density of galaxies. Therefore,

$$M(r) = \int_0^r \rho(r')r'^2\mathrm{d}r' \tag{1.5}$$

$$= \Upsilon\int_0^r j(r')r'^2\mathrm{d}r', \tag{1.6}$$

and so one can rearrange Eq. (1.3) in the form

$$\sigma^2 = \Upsilon\frac{G\int_0^r j(r')r'^2\mathrm{d}r'}{r\left(\frac{\mathrm{d}\ \ln j}{\mathrm{d}r} + \frac{\mathrm{d}\ \ln\sigma^2}{\mathrm{d}r}\right)}. \tag{1.7}$$

Both the luminosity density $j(r)$ and the RMS velocity profile $\sigma(r)$ can be estimated by deconvolving the observed line-of-sight integrals of these functions. Therefore, one must fit Υ in order to satisfy Eq. (1.7). Since Zwicky's time, many more clusters have been observed with much greater precision to demonstrate that $\Upsilon \approx 360 - 600$, which is several orders of magnitude higher than Υ inferred from galactic scale measurements (Kent & Gunn, 1982; Merritt, 1987; Ostriker et al., 1988; van der Marel et al., 2000). This translates to a *total matter* component $\Omega_m = \rho_m/\rho_{crit} \sim 0.3$, where ρ_m is the density of both baryons and non-baryonic dark matter, as measured using clusters, since

$$\Omega_m = \frac{\rho_m}{\rho_{crit}} = \frac{\Upsilon j_{tot}}{\rho_{crit}}. \tag{1.8}$$

The total luminosity density j_{tot} can be estimated from galaxy counts and the galaxy luminosity function.

Clusters can also constrain any possible self-interaction between dark matter particles in several ways. For example, (i) cluster halos are observed to be triaxial in N-body simulations (Thomas et al., 1998; Jing & Suto, 2002), and there are hints of triaxiality in gravitational lensing observations of clusters (Corless & King, 2007). However, numerical simulations of cluster-sized dark matter halos indicate that self-interaction tends to makes halos more spherical unless the cross section for interaction is smaller than what is necessary to flatten LSB halo cores (Yoshida et al., 2000a; Miralda-Escudé, 2002). (ii) Gnedin & Ostriker (2001) argue that a large self-interaction cross section would cause the evaporation of galaxy halos, thus strongly affecting galaxy evolution in clusters. (iii) Further constraints on the self-interaction cross section come from interpretations of cluster lensing data, which will be discussed next.

Therefore, from probes of clusters that do not involve gravitational lensing, one can estimate the total mass density of the universe $\Omega_m \sim 0.3$ and place more stringent limits on the self-interaction cross section than one could with only galactic-scale data.

Gravitational Lensing

Gravitational lensing is a consequence of general relativity. The trajectory of light must bend as it encounters massive objects, since light travels on geodesics. There are three general regimes of gravitational lensing: microlensing, in which a small object transits the line of sight to a background object, causing the background object to temporarily brighten; weak lensing, in which the images of background objects (usually galaxies) are slightly distorted by foreground galaxies or clusters; and strong lensing, in which case multiple images of the background object are created, each of which can be strongly distorted and (de)magnified (see Narayan & Bartelmann, 1996, for a review). Both strong and weak lensing can be used to constrain the shapes and density profiles of galactic and cluster halos (Keeton, 2001; Mandelbaum et al., 2006a) since the path of light from background galaxies is altered by

all the matter within the foreground galaxy or cluster, not just the luminous component.

Strong lensing probes the inner regions of galaxies ($r \lesssim 1$ kpc) and clusters ($r \lesssim 100$ kpc). It is important to emphasize several key points about strong lensing. First, strong lensing probes the innermost part of the galaxy or cluster. In galaxy-galaxy strong lensing, baryons dominate the gravitational potential (Treu & Koopmans, 2004). In clusters, dark matter usually dominates the potential. However, most clusters have a large galaxy sitting at the bottom of the potential well, and there are usually many galaxies interior to the lensing arcs. In addition, strong lensing is sensitive to halo triaxiality and substructure (Meneghetti et al., 2007). Therefore, careful modeling of both the baryons and dark matter halo is necessary to extract useful information about the dark component.

Initial examination of strong lensing data from the 1990's implied that halo profiles predicted by numerical simulations were too steep to be consistent with strong lensing, although these data were modeled with only a halo and without a baryonic component. Even when stellar components were added to models, there was still a significant discrepancy with simulations (Keeton, 2001). It was suggested that self-interacting dark matter might alleviate this discrepancy by smoothing the centers of galaxy and cluster halos (Keeton, 2001; Wyithe et al., 2001). However, galaxy and cluster modeling has become significantly more sophisticated in the past decade; most analyses of strong lensing now include detailed modeling of galaxies (including kinematics), and include ellipticity and substructure in the host dark matter halo. Recent analyses of strongly lensed galaxies and clusters suggest that the dark matter halos inferred from observation are consistent with those found in cosmological simulations (Treu & Koopmans, 2004; Comerford et al., 2006; Limousin et al., 2008).

Weak lensing probes the outer parts of galaxies and clusters, and is thus less sensitive to the distribution of baryons than strong lensing. It is possible to reconstruct the mass distribution of a galaxy cluster using weak lensing alone, or using a combination of weak and strong lensing (Bradač et al., 2007; Kubo et al., 2007). However, for galaxy-galaxy weak lensing, it is necessary to stack data from many ($> 10^4$) lenses to constrain the matter

distribution. This is due to the fact that galaxies that are weakly lensed only experience a tiny amount of shearing, and so the lensing signal has to be extracted statistically. Careful analysis of weak lensing data from the Sloan Digital Sky Survey (SDSS; York et al., 2000) demonstrates that the halos of groups and clusters are consistent with those predicted by cosmological simulations using the CDM concordance model (Kubo et al., 2007; Mandelbaum et al., 2006a; Navarro et al., 1997, 2004). Mandelbaum et al. (2006a) use weak lensing data from $\sim 43,000$ luminous red galaxies on scales $r > 40$ kpc from the cluster or group center to perform their fits, while Kubo et al. (2007) use $\sim 270,000$ galaxies from the SDSS Data Release 5 to model the mass distribution of the Coma cluster.

The observation of a rare merging cluster (commonly called the "bullet cluster") provides yet another way to constrain modified gravity theories and the self-interaction cross section (Clowe et al., 2006b; Randall et al., 2007). Observations of gravitational lensing have historically been a strong challenge to theories of modified gravity. The vector field in TeVeS exists solely to mimic gravitational lensing. However, observations of the bullet cluster strain modified gravity even more. As in most clusters, most of the baryonic mass is in the form of hot (~ 10 keV, depending on the mass of the cluster) gas. This constitutes $5 - 15\%$ of the total mass in the cluster, while stars make up only about 1% of the total mass, assuming Einstein gravity (Kochanek et al., 2003; Mahdavi et al., 2007).

Unlike most clusters, though, the bullet cluster consists of a smaller cluster that has just undergone a head-on collision with a larger cluster. This is not readily apparent from the optical image of the cluster, Figure 1.2a, which does not show the gas component. However, as one can see in Figure 1.2b, the smaller concentration of hot gas (on the right) has experienced significant ram pressure as it passed through the gas of the larger initial cluster (Markevitch et al., 2002). The ram pressure slows the bulk motion of the gas relative to the galaxies, which are collisionless. If the two original clusters consisted only of baryons, then the mass should be concentrated in the hot gas.

Using optical data from the Hubble Space Telescope Advanced Camera for Surveys (*HST*/ACS) and the Magellan Telescope, the gravitational potential of the cluster was re-

(a) (b)

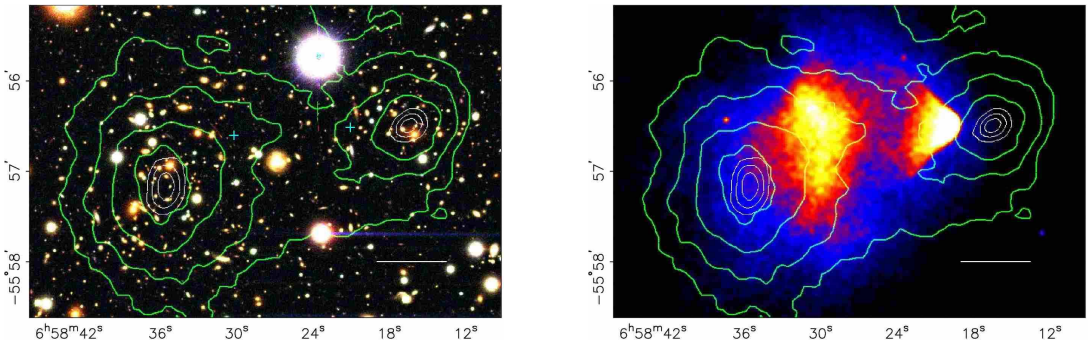

Figure 1.2: Observations of the bullet cluster at a variety of wavelengths. Green lines indicated the lensing reconstruction of the mass distribution in the cluster. *(a)*: Contours lie on top of an BVR composite optical image to indicate the distribution of galaxies relative to the mass of the cluster. *(b)*: An X-ray image of the hot gas in the cluster. Both figures come from Clowe et al. (2006a).

constructed with weak lensing (Clowe et al., 2006a). The mass contours are denoted by green lines in Figure 1.2. It is claimed that the centroids of the masses of the two original clusters are offset from the gas mass by 8σ (Figure 1.2; the centers of the gas masses are marked with + marks in the optical image), while the mass distribution is coincident with the distribution of galaxies in the cluster. The offset between the bulk of the baryons and the mass distribution appears to be extremely difficult to resolve with modified gravity theories without invoking at least some dark matter (Angus et al. 2007; Feix et al. 2007; although see Brownstein & Moffat 2007).

The bullet cluster can also be used to constrain the dark matter self-interaction cross section. There are two main ways to constrain the cross section. First, self-interactions tend to slow down the bulk flow of dark matter, just as ram pressure slows the gas. Therefore, there ought to be a cross section-dependent offset between the center of the mass distribution from the lensing maps and the center of the galaxy distribution. The data demonstrate that the centroids of the galaxy and mass distributions are within 1σ error bars of each other. Secondly, self-interactions can scatter dark matter particles out of the centers of the original clusters, thereby reducing the mass-to-light ratio. Randall et al. (2007) perform

a suite of N-body simulations with various velocity-independent self-interaction cross sections, impact parameters, and initial halo mass profiles. They find that the lack of centroid offset constrains the cross section to $\sigma/m < 1.25$ cm^{2}g^{-1}, while the mass-to-light ratio forces $\sigma/m < 0.7$ cm^{2}g^{-1}. These limits rule out most of the cross section range that would flatten the inner profiles of LSB galaxies.

Therefore, from lensing of galaxies and clusters, we find that modified gravity is increasingly untenable as an alternate explanation to dark matter of the types of observations listed above, that dark matter profiles from weak lensing surveys are in agreement with CDM simulations of galaxy and cluster halos, and that self-interacting dark matter does not need to be invoked to resolve apparent discrepancies between CDM simulations and data.

Large Scale Structure

Comparisons of dark matter N-body simulations with observations of large scale structure provide strong evidence that dark matter is cold and collisionless at large scales, and provide further evidence that the universe has both dark matter ($\Omega_m \sim 0.3$) and dark energy ($\Omega_\Lambda \sim 0.7$). While a variety of statistical tests (e.g., the galaxy correlation function or power spectrum) exist to relate observations to theoretical predictions for specific values of Ω_m and Ω_Λ, conclusions about dark matter can be reached simply by looking at maps of the positions of galaxies (dark matter halos) obtained from observations (simulations).

The last decade has seen an explosion in the types and sizes of surveys available to map structures in the distribution of galaxies and their evolution from $z \sim 1$. The SDSS main galaxy sample contains $\sim 500,000$ galaxies brighter than $r = 17.77$ and extends to $z \sim 0.2$. Once the SDSS main survey is complete, it will cover $\sim 10^4$ deg^2 of sky. In addition, a sample of large red galaxies (LRGs) extends the galaxy redshift survey to $z \sim 0.5$ (Percival et al., 2007). A slice of this survey is shown in Figure 1.3. One can see in this slice both the homogeneity on very large scales, which is consistent with predictions from inflation and observations of the cosmic microwave background (CMB; Hinshaw et al.,

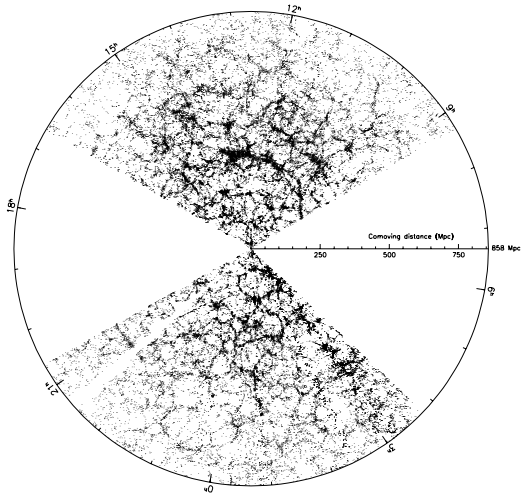

Figure 1.3: An equatorial slice from the Sloan Digital Sky Survey. Figure from Gott et al. (2005).

2007; Spergel et al., 2007), but also the exquisite filaments and voids on scales < 100 Mpc. Additionally, there are many surveys existing or planned to count galaxy clusters as a function of redshift. These data are important because the formation of clusters, which are the largest equilibrium structures in the universe, is highly sensitive to the recent expansion history of the universe (see Dodelson, 2003, and references therein). Signatures of clusters include X-ray emission from hot gas (XCS, Miller et al., 2006), Sunyaev-Zel'dovich foregrounds in small-scale CMB experiments (ACT, SPT, APEX; see Sehgal et al., 2005, for a review), and statistical overdensities of photometric redshifts from infrared galaxy surveys (Brodwin et al., 2006).

The structure on small scales ($\lesssim 100$ Mpc) alone indicates that most of the dark matter in the universe must have been non-relativistic well before the matter-radiation equality epoch $z_{eq} \approx 3500$. The simple explanation for this fact comes from the Jeans instability. During the era of radiation domination, the Jeans length is approximately the size of the horizon, which means that density perturbations cannot grow in size. If collisionless dark

matter is relativistic in this era, then it can stream out of the density perturbations, hence completely washing out density perturbations on scales smaller than the free-streaming scale, which is set by the coordinate distance a particle travels before matter-radiation equality (Kolb & Turner, 1990). Matter which is relativistic near the time of matter-radiation equality is called "hot," while matter which becomes non-relativistic well before this epoch is called "cold."

One of the original candidates for dark matter was the neutrino. The advantage of this candidate is that neutrinos are known to exist, unlike almost all other candidates. However, the severe disadvantage of neutrinos as dark matter, other than the fact that current experimental limits on the mass are too low for them to contribute significantly to Ω_m, is that neutrinos remain relativistic up to nearly matter-radiation equality. The free-streaming length scales as $\lambda_{FS} = 20\,(m_\nu/30\text{ eV})^{-1}$ Mpc, which is much larger than even superclusters for realistic ($\lesssim 1$ eV) neutrino masses (Kolb & Turner, 1990; Kraus et al., 2005). When hot dark matter was considered in the 1980's, the much looser constraints on the neutrino mass (compared to today) suggested that the smallest structures that could form if dark matter were hot were superclusters, although these could potentially fragment to form galaxies. However, it was evident even then that simulations of hot dark matter structure formation (see Figure 1.4) indicated that the clustering of galaxies differed significantly from that of the contemporary observations of samples of $\sim 10^4$ galaxies (Huchra et al., 1983). Furthermore, in the hot dark matter paradigm, superclusters (and hence, galaxies) could only have virialized relatively recently. This is in sharp contrast to observations, which indicate that stars and galaxies must have started forming within $\sim 10 - 100$ Myr after recombination (Bouwens et al., 2006). Currently, constraints on neutrino masses are tight enough that the minimum free-streaming length, $\lambda_{FS} \sim 600$ Mpc, is far larger than a supercluster, so the present limits on the neutrino mass rule it out as the dominant dark matter component in the universe. In general, observations of structure formation and evolution place extremely stringent constraints on hot dark matter. The data resemble what one would expect if dark matter were cold.

(a) (b)

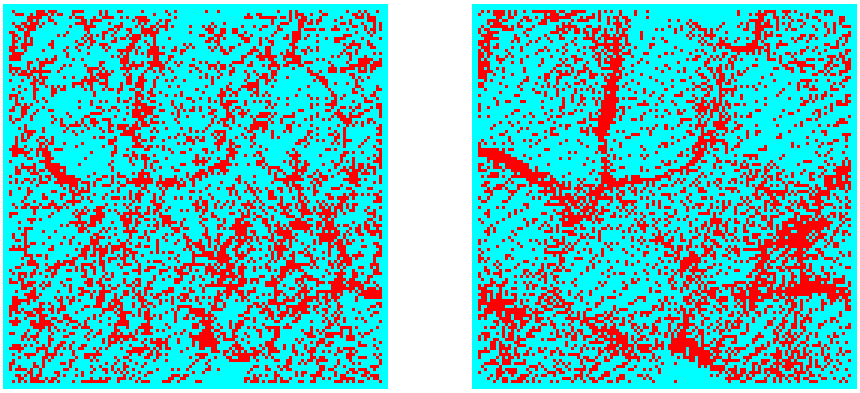

Figure 1.4: Simulations of structure formation for *(a)* cold dark matter and *(b)* hot dark matter universes. Each image is $300h^{-1}$ Mpc on a side. Images are from Martin White's primer on cosmological models:
http://astro.berkeley.edu/∼mwhite/modelcmp.html

Observations and simulations of structure formation in a ΛCDM universe also agree with the value of $\Omega_m \sim 0.3$ derived from cluster mass estimates, and indicate that the universe must have a significant dark energy contribution. There are two major indicators from large scale structure that the value of Ω_m is small ($\Omega_m < 1$). The first indicator comes from small scale structure. Recall that density perturbations can only grow if the scale of the perturbation exceeds the Jeans length and lies within the horizon. During radiation-domination, the Jeans length is approximately the same size as the horizon, but during matter-domination, the Jeans length becomes vanishingly small. Perturbations that enter the horizon before matter-radiation equality have their growth retarded relative to scales that enter during matter-domination. Matter-radiation equality happens earlier for larger Ω_m, so that small scale power increases as a function of Ω_m.

Secondly, structure growth depends on the expansion history of the universe. Growth is much slower at late times for a dark energy dominated universe relative to a universe with $\Omega_m = 1$, since the expansion rate is accelerating in the universe with significant dark energy but not in the case where $\Omega_m = 1$. The matter correlation functions and cluster counts ought to be more or less in place by $z \sim 1$ for a dark energy-dominated universe,

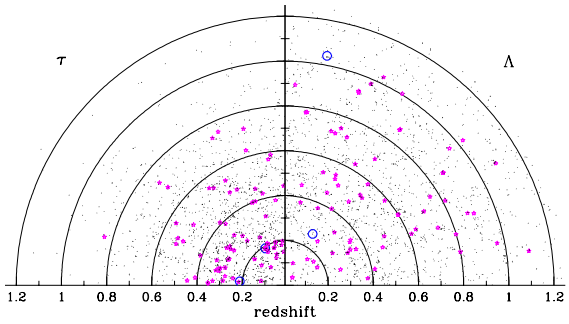

Figure 1.5: Structure formation as a function of time for $\Omega = \Omega_m = 1$ (labeled τ in the figure) and ΛCDM ($\Omega_\Lambda = 0.7, \Omega_m = 0.3$) universes using the Virgo Consortium Hubble Volume simulations. The points mark the location of clusters in redshift space. This figure is from Evrard et al. (2002).

but be rapidly evolving from $z = 1$ to $z = 0$ in a universe that is matter-dominated to the present. This is readily apparent in simulations, as indicated in Figure 1.5. In this Figure, the redshift slice marked τ is the result of a simulation with $\Omega_m = 1$, while the slice marked Λ results from a canonical ΛCDM simulation. The number of clusters and distribution of galaxies as a function of redshift in the ΛCDM simulation is consistent with observations, while the τ-simulation is not.

Therefore, from observations and simulations of large scale structure, we find that dark matter must be cold, and have an abundance $\Omega_{dm} = \Omega_m - \Omega_b \sim 0.25$.

Relic Abundance

From the dark matter fraction $\Omega_{dm} \approx 0.25$, it is possible to infer the dark matter annihilation cross section directly if the dark matter is a thermal relic particle. In the early universe, if the dark matter annihilation rate Γ is much greater than the Hubble expansion H, then dark matter particles remain in thermal equilibrium. The equilibrium number density is determined by the temperature of the universe, which is also related to the Hubble expansion. Since the universe cools as it expands, the equilibrium number density of dark matter particles drops with time. However, once the annihilation rate drops below the rate of expansion of the universe, the dark matter particles drop out of equilibrium, and the number density of particles "freezes out."

A simplified version of the relationship between the annihilation cross section and the current dark matter density goes as follows. The time (equivalently, temperature or scale factor of the universe) at which dark matter decouples from the other thermal particle species can be determined by $\Gamma \sim H$, where $\Gamma \approx \langle \sigma_A v \rangle n_{eq}$, $\langle \sigma_A v \rangle$ is the thermally averaged annihilation cross section, and n_{eq} is the equilibrium dark matter density. Since both H and n_{eq} are temperature-dependent, the temperature of freeze-out T_f can be determined approximately by

$$\frac{H(T_f)}{n_{eq}(T_f)} = \langle \sigma_A v \rangle. \tag{1.9}$$

Therefore, the temperature of freeze-out is uniquely related to the thermally averaged an-

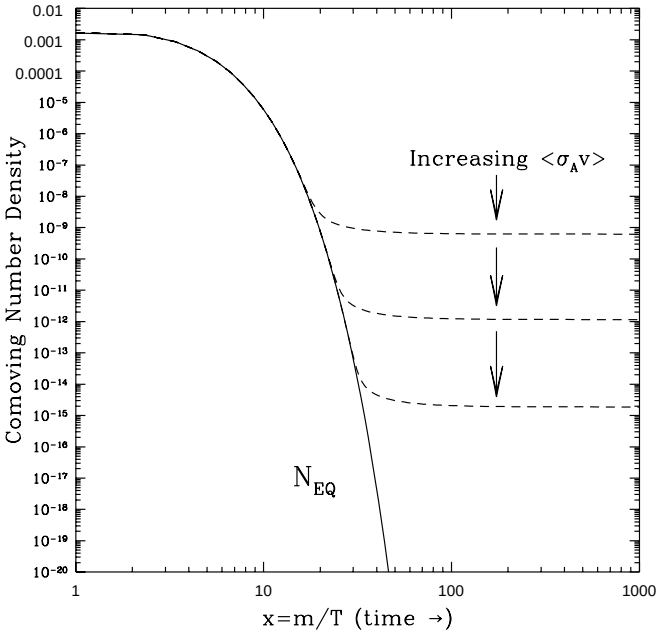

Figure 1.6: Relationship between the number density of relic dark matter particles and the annihilation cross section. The solid line represents the equilibrium number density of cold dark matter particles. The dashed lines represent the number density at freeze out for a variety of annihilation cross sections. Figure originally from Dodelson (2003).

nihilation cross section, and the thermally averaged cross section is inversely proportional to equilibrium number density at freeze out.

Since the universe is radiation-dominated at the time of freeze out, the Hubble expansion is related to the scale factor a by (cf. Kolb & Turner, 1990)

$$H \propto a^{-2}. \tag{1.10}$$

By convention, the current value of the scale factor is set to $a_0 = 1$. During radiation domination, the scale factor depends on the temperature as

$$a \propto T^{-1}, \tag{1.11}$$

such that the Hubble expansion is

$$H \propto T^{-2}. \tag{1.12}$$

To relate Eq. (1.9) to the dark matter fraction today, I use the fact that

$$\rho_{dm,f} = \rho_{dm,0} a_f^{-3}, \tag{1.13}$$

where a_f is the scale factor of the universe at the time of freeze-out, and $\rho_{dm,f}$ is the dark matter density at freeze-out. The current dark matter density $\rho_{dm,0}$ can be related to Ω_{dm} using the relation

$$\rho_{dm,0} = \Omega_{dm} \rho_{crit}. \tag{1.14}$$

For simplicity, I set $n_{eq}(T_f) = \rho_{dm,f}/m$, where m is the dark matter particle mass, although in the full relic calculation, there is equality only within a factor of order unity between the equilibrium number density $n_{eq}(T_f)$ and the freeze-out number density (Kolb & Turner, 1990; Jungman et al., 1996). The value of n_{eq} sets the freeze-out time through Eq. (1.9). Therefore combining Eqs. (1.9), (1.13), and (1.14), one can estimate the velocity-averaged annihilation cross section as a function of today's dark matter fraction

$$\langle \sigma_A v \rangle \propto \frac{m H(T_f) a_f^3}{\rho_{crit} \Omega_{dm}} \tag{1.15}$$

$$\propto \left(\frac{m}{T_f} \right) \frac{1}{\rho_{crit} \Omega_{dm}}. \tag{1.16}$$

Jungman et al. (1996) find that the quantity m/T_f is a fairly weak function of particle mass and cross section (they say the dependence is logarithmic), so that $\langle \sigma_A v \rangle \propto \Omega_{dm}^{-1}$. This is also demonstrated in Figure 1.6, which shows the equilibrium number density (*solid line*) as a function of m/T. The spin-averaged cross section (or equilibrium number density) may change by orders of magnitude even if m/T only changes by a few percent.

The relationship between Ω_{dm} and the cross section can be simply understood using Figure 1.6. For a fixed particle mass, if the annihilation cross section is low, then dark matter falls out of equilibrium early and at a high temperature. Therefore, the equilibrium number density is high, and so is the density of dark matter today. However, if the annihilation cross section is high, the dark matter falls out of equilibrium much later, and so the relic number density is low. For the measured value of $\Omega_{dm} \approx 0.25$, the annihilation cross section is $\langle \sigma_A v \rangle \approx 3 \times 10^{-26}$ cm^{3}s^{-1}.

There are several caveats to the simple scaling between Ω_{dm} and the annihilation cross section, which are described at length in Kolb & Turner (1990) and Jungman et al. (1996). I will briefly discuss two examples. If the velocity-averaged cross section is energy-dependent, then the calculation is much more complicated. Also, if there is a particle only slightly more massive than the dark matter particle, and if it has a lifetime comparable to the age of the universe at freeze-out or if the annihilation cross section is a bit higher than that of the dark matter particle, abundances depend sensitively on the nature of the slightly higher mass particle.

1.1.2 Tantalizing Hints from Particle Physics

There are several well-motivated cold dark matter candidates from extensions to the Standard Model. The Standard Model, which unifies the weak and electromagnetic forces in one framework, is most likely an effective theory of a much higher energy theory. The reasons for this are that the Higgs mechanism, which exists to impart mass to particles, is put into the Standard Model by hand; and that it is desirable to unify all forces of nature at the Planck scale. However, the Planck scale is some ~ 17 orders of magnitude higher than the

electroweak unification scale, so radiative corrections to the Higgs mass from any high energy unification theory drive the Higgs mass to that high energy scale unless there is severe fine-tuning. This problem is often called the "hierarchy problem." Two methods have been generally employed to address this issue. First, there are methods to cancel the radiative corrections to stabilize the Higgs mass. The other approach is to significantly lower the scale of unification. Both approaches yield natural dark matter candidates.

The most prominent framework to eliminate radiative corrections for high energy theories is supersymmetry (SUSY). In the simplest form of this theory, the minimal supersymmetric model (MSSM), each Standard Model particle has a supersymmetric counterpart ("sparticle") with spin differing by a half integer. The bosonic and fermionic loops for corrections to the Higgs mass cancel. The supersymmetry must be broken so that particles and sparticles have mass, but the mechanism for symmetry breaking is not understood. In many formulations of supersymmetry, including the MSSM, there exists a symmetry called R-parity which makes the least massive supersymmetric particle (LSP) stable against decays to Standard Model particles. Therefore, the LSP is a natural dark matter candidate. Another intriguing aspect of the LSP is that it can be produced thermally in the early universe. For a broad swath of MSSM parameter space, the density of LSPs matches that required by astrophysics. In most cases the LSP is the neutralino, a Majorana particle that is the lowest-mass eigenstate of the supersymmetric partners of gauge and Higgs bosons. For reviews of SUSY phenomenology, see Jungman et al. (1996) and Chung et al. (2005).

Alternatively, one can lower the unification scale to lower radiative corrections. In order to accomplish this, extra dimensions are usually invoked (Arkani-Hamed et al., 1998, 1999; Randall & Sundrum, 1999a; Appelquist et al., 2001). In these extra-dimension theories, gravity propagates in $4+n$ dimensions. The Planck mass in the bulk dimensions of theory is of order TeV scale, but particles on the $3+1$-dimensional branes perceive the Planck mass as being $\sim 10^{19}$ GeV. The $(4+n)-$dimensional Planck scale is related to the 4-dimensional Planck scale by factors of either the volume of the compact space (Arkani-Hamed et al., 1998, 1999) or the curvature of warped extra dimensions (Randall & Sundrum, 1999a).

Of particular interest are theories in which Standard Model particles can propagate in compact extra dimensions. Such theories are called "universal extra-dimension theories" (UED; Appelquist et al., 2001; Hooper & Profumo, 2007). In such theories, the particle momenta must be quantized in the extra dimension. However, on our 3+1-dimensional slice of the space-time, the momentum appears as mass. Therefore, for each Standard Model particle, there is a tower of particles with identical quantum numbers but with higher mass

$$m_{i,q}^2 = m_{i,0}^2 + \frac{q^2}{R^2}, \tag{1.17}$$

where $m_{i,q}$ is the mass of the q^{th} excitation of the i^{th} particle species, $m_{i,0}$ is the Standard Model mass of particle i, and R is the compactification scale. There are some subtleties due to radiative corrections (Hooper & Profumo, 2007) which impact the mass hierarchy of the particles. The particles are called "Kaluza-Klein" particles, since the first formulation of extra dimension theories came from Kaluza and Klein in the early part of the 20^{th} century, albeit in a completely different context. These UED theories are of interest because, as in supersymmetry with R-parity, there exists a lightest Kaluza-Klein particle (LKP) which is stable against decay to ordinary Standard Model particles. This comes about from "Kaluza-Klein parity," which states that the q^{th} excitation can only decay in such a way that the total q for the interaction must remain even for even initial q or odd for odd initial q. Therefore, even-q particles can decay to Standard Model particles, but odd-q particles can only decay to the first-excitation modes. Therefore, the lightest particle in the first excitation is stable. For much of KK parameter space, the LKP is the $B^{(1)}$, the first excitation of the weak hypercharge gauge boson (sometimes called the "KK photon").

Candidates for particle dark matter quite naturally arise from the most prominent beyond-Standard Model theories. In these models, dark matter particles have weak interactions with matter; they are therefore generically referred to as WIMPs, Weakly Interacting Massive Particles. It should be cautioned that there could, in fact, be more than one species of dark matter.

1.2 Various Probes of Dark Matter Properties

While the observations described in Section 1.1.1 provide strong evidence for the existence of dark matter, and give some insight into its abundance and properties, the fact remains that dark matter has not been observed. In order to confirm the existence of dark matter, it is necessary to observe dark matter directly (by its interactions with baryons) or indirectly (by its annihilation spectrum). The properties of WIMPs that have been inferred by probes described in the previous section do not seriously constrain particle theories of dark matter, with the exception that structure formation requires that the bulk of dark matter must be non-relativistic well before matter-radiation equality. Direct or indirect detection of dark matter would also yield valuable information about its mass, interaction cross sections with baryons, and branching ratios for annihilation. These data can be used to constrain and distinguish between particle theories of dark matter.

In this section, I will describe astrophysical observations to probe WIMPs and their properties. I will divide my discussion into Galactic-scale and solar system-scale tests of dark matter. There is a large body of work on interpretations of collider signatures, as well as constraints on theory space using a combination of astrophysical and collider experiments, which I will not address (but see, e.g., Arkani-Hamed et al., 2006b,a; Canepa, 2006; Carena et al., 2007; Hooper & Profumo, 2007; Hooper & Taylor, 2007).

1.2.1 (Extra)Galactic Methods

Galactic and extra-galactic methods for observing WIMPs focus on the annihilation products. The energy spectrum of annihilation products is a rich source of information on the dark matter particle and its underlying theory. Of special interest are the spectra of γ-rays and synchrotron emission from ultra high energy e^+e^- resulting from dark matter annihilation. Annihilation to neutrinos will be important for solar system methods, and so will be discussed in that section. There are also experiments underway to examine the local positron, anti-proton, and anti-deuteron abundances, each of which could harbor a signal of WIMP annihilation (for a review, see Bertone et al., 2005b). However, in this section,

the focus is restricted to photon signatures of dark matter.

Dark matter annihilation can produce a continuum of γ-rays in showers from the initial annihilation products (e.g., W^+W^-, $b\bar{b}, \tau^+\tau^-$), since WIMPs cannot decay directly to photons. This continuum spectrum depends on the dark matter particle mass as well as the annihilation branching fractions. In particular, annihilation to $\tau^+\tau^-$ leads to a much harder γ-ray spectrum since these particles can decay directly to neutral pions, which in turn decay by $\pi^0 \rightarrow \gamma\gamma$. It is perhaps possible to distinguish between supersymmetric and UED dark matter on the basis of the γ-ray spectrum since UED dark matter generically has a much higher branching fraction to $\tau^+\tau^-$, although the branching fractions span a large range in the case of supersymmetric WIMPs (Hooper & Zaharijas, 2007).

It may also be possible to determine the WIMP mass exactly. Even though dark matter cannot annihilate directly to photons at tree level (or else it would not truly be dark), it can annihilate to two photons through loops (Bertone et al., 2005b). Dark matter can also annihilate to a photon and a Z-boson through loops. Therefore, line emission, though suppressed relative to continuum emission, would if detected precisely nail the WIMP mass.

There are two main methods for detecting astrophysical γ-rays. Hard ($\gtrsim 10^2$ GeV) γ-rays can be observed with terrestrial air Čerenkov telescopes (ACTs). These telescopes generally have large fields of view and angular resolution of order arcminutes or tens of arcminutes. Telescopes include CANGAROO (Kubo et al., 2004), VERITAS (Holder et al., 2006), and H.E.S.S. (The H. E. S. S. Collaboration, 2006). Space telescopes can probe a much broader spectrum than ACTs, generally $E_\gamma \sim$ MeV$-$TeV. These telescopes have a much larger field of view than ACTs, but lower sensitivity at high energies. The EGRET instrument aboard the Compton Gamma Ray Observatory provided the first glimpse into the soft γ-ray universe (e.g., Esposito et al., 1999; Hartman et al., 1999), while the upcoming GLAST telescope, scheduled to launch in 2008, is eagerly anticipated (Wai et al., 2007).

Since the annihilation rate scales as $\Gamma \propto n^2$, where n is the dark matter number density, any regions with large dark matter concentrations are potentially observable. Therefore, much effort has been expended into predicting and observing signals from the Galactic cen-

ter, substructure within the Milky Way, and Milky Way satellite galaxies. I will highlight the prospects for and complications associated with each astrophysical site.

The Galactic Center

There are many serious uncertainties associated with assessing the prospects of observing dark matter annihilation products at the Galactic center. The issues can be categorized into:

- Dark matter modeling uncertainty: There are several layers of uncertainties in modeling the density of dark matter, all due to the fact that annihilation is most effective at scales $\ll 1$ kpc. A major uncertainty in the density profile is that the inner density profile of dark matter halos is poorly constrained from simulations. The first large-scale dark matter-only simulations implied that the dark matter density profile could be well modeled by

$$\rho(r) = \frac{\rho_s}{(r/r_s)^{\alpha}\,[1+(\,r/r_s\,)^{\gamma}]^{(\beta-\alpha)/\gamma}}, \tag{1.18}$$

  where ρ_s is $2^{-(\beta-\alpha)/\gamma}$ times the density at the turnover radius r_s, and $(\alpha, \beta, \gamma) = (1, 3, 1)$ for the Navarro-Frenk-While simulations (NFW; Navarro et al., 1997) and $(1.5, 3, 1.5)$ for the Moore simulations (Moore et al., 1999). For small r/r_s, $\rho \propto r^{-1}$ for the NFW profile and $\rho \propto r^{-1.5}$ for the Moore profile. However, these fits were made for radii $\gtrsim$ tens of kpc from the halo centers for Milky Way-sized halos, well outside of our region of interest. More recent, higher resolution simulations indicate that the density profile never converges to a power law at small radii (Navarro et al., 2004). The uncertainty in the dark matter profile estimated from simulations leads to a factor of ~ 100 uncertainty in the γ-ray flux from annihilations, with steeper dark matter profiles having a much stronger signal. The uncertainty is exacerbated by the fact that gravitational potential at $r < 1$ kpc is heavily dominated by baryons, and is dominated by the central supermassive black hole (SMBH) at scales $r < 2$ pc. It was proposed that the adiabatic growth of the SMBH could yield a high density, highly

cuspy "spike" of dark matter for $r < 2$ pc (Gondolo & Silk, 1999), in which case the flux of photons from the Galactic center ought to be significantly boosted. However, this scenario is quite dependent on the merger history of the black hole, and is only effective if the black hole sits at the very center of the Galactic potential well (Ullio et al., 2001a). Mergers of black holes can actually reduce the dark matter density near the center ("core scouring"). More generally, the density profile of dark matter depends on the accretion and merger history of the galaxy and the central black hole, as well as on long-term interactions with stars and the SMBH (Merritt et al., 2002; Bertone & Merritt, 2005). It is possible that two-body scattering off stars could yield a density cusp $\rho \propto r^{-1.5}$ within the SMBH's sphere of influence if the last major merger happened long before the present (Merritt et al., 2007). Therefore, it is still unclear how the dark matter density profile evolves for $r < 1$ kpc.

- Surprise backgrounds: Initial results from CANGAROO (Tsuchiya et al., 2004) and H.E.S.S. (Aharonian et al., 2006) indicate a significant TeV-scale excess at the Galactic center that is likely due to a previously unknown astrophysical source, given that the power-law spectrum of these γ-rays is inconsistent with predictions of WIMP annihilation (Aharonian et al., 2006). This source may be related to the SMBH (Aharonian & Neronov, 2005). In any case, this signal will make it extremely difficult to observe line emission from WIMP annihilations (Zaharijas & Hooper, 2006), although it should still be possible to observe continuum emission for some subset of parameters for dark matter models (Hooper & Zaharijas, 2007; Hooper et al., 2007a). An excess of radiation was also observed at $\sim$ GeV energies with EGRET (Mayer-Hasselwander et al., 1998). The interpretation of this source is unclear, as it may be offset from the Galactic center (Hooper & Dingus, 2002) and may be variable (Nolan et al., 2003). Nevertheless, it will also be a significant background for GLAST, although GLAST has sufficient spatial resolution ($\sim$ arcminutes) that it could distinguish the offset source from the Galactic center.

- Propagation of e^+e^-: Upon careful examination and modeling of the Galactic mi-

crowave emission observed by *WMAP* (Bennett et al., 2003), Finkbeiner (2004a) found a spherically symmetric excess of emission located at the Galactic center, which he has interpreted as synchrotron emission from e^+e^- resulting from dark matter annihilation (Finkbeiner, 2004b). It is necessary to model the e^+e^- diffusion and energy loss as these particles travel out from the Galactic center. While Hooper et al. (2007a) demonstrate that synchrotron spectra do not vary significantly for several choices of boundary conditions for solving the diffusion equation PDE, it is still possible that astrophysical details for the diffusion constant and energy loss, such as the geometry of the Galactic magnetic field, can have a large impact on the predicted synchrotron spectrum for a given dark matter model (Finkbeiner, 2004b). Hooper et al. (2007a) indicate that a dark matter profile with $\rho \propto r^{-1.2}$ can provide a good fit to the observed synchrotron excess. If this is the case, it may be possible for GLAST to observe continuum γ-rays from the Galactic center. The prospects dim for shallower dark matter profiles.

Therefore, while the Galactic center appears at first glance to be a likely place to observe photons resulting from WIMP annihilation, the prospects for observing γ-rays, and confirming the dark matter interpretation of excess synchrotron emission, are far from certain.

Substructure

Cosmological simulations of structure formation indicate that Milky Way-sized galaxy halos ought to have a significant amount of substructure (e.g., Tasitsiomi & Olinto, 2002; Diemand et al., 2007). It is expected that the substructures will contribute significantly to the total annihilation signal of the halo. Some of these substructures are likely to be seen as point sources, but unresolved substructures can contribute to the global diffuse emission of the halo. The smallest substructures that can be resolved in simulations are of order $\sim 10^6 M_\odot$ (Kuhlen et al., 2007). If dark matter is clumpy on even smaller scales, it will enhance the dark matter annihilation signal since $\Gamma \propto n^2$. This will increase the global diffuse γ-ray emission.

The number and brightness of point sources due to substructures may be increased if these substructures contain intermediate mass black holes (IMBH) of masses $\sim 10^2 - 10^6\ M_\odot$ (Zhao & Silk, 2005; Bertone et al., 2005a). These IMBH can arise naturally in hierarchical structure formation models if Population III stars leave massive ($\sim 10^2\ M_\odot$) remnants and then merge as the host halos merge (Islam et al., 2004; Volonteri & Perna, 2005), or may form directly if gas collapses to large black holes in the early universe (Bromm & Loeb, 2003). These IMBH could cause dark matter to settle into steady state density spikes about them, as was suggested for the SMBH at the Galactic center (Gondolo & Silk, 1999; Bertone & Merritt, 2005). It is thought that these spikes could survive to the present (Bertone et al., 2005a). If this is the case, then it is quite likely that GLAST will be able to see annihilation from these spikes, and likely that statistics will be high enough to distinguish between dark matter models (Bertone et al., 2006). One caveat to this scenario is that there is little evidence that IMBH actually exist (see van der Marel, 2004, and references therein).

Satellite Galaxies

The Milky Way is surrounded by a number of satellite galaxies. These galaxies could potentially be observed as point sources by GLAST (Tasitsiomi et al., 2004; Hooper & Zaharijas, 2007). As with the Milky Way halo, there is significant uncertainty in the galaxy dark matter density profiles. The prospects for detection are therefore quite uncertain (Wood et al., 2008).

1.2.2 Solar System Methods

Since the interpretation of Galactic probes of the annihilation spectrum is fraught with serious uncertainties, it is worthwhile to search for dark matter in cleaner systems, or at least systems for which there are fewer large uncertainties. In this section, I will describe methods of detecting dark matter in the solar system; in the next sections, I will describe the main uncertainties associated with these strategies, other than, of course, the WIMP mass and WIMP-nucleon cross section, namely uncertainties in the dark matter distribution

function.

Direct Detection

If WIMPs are produced thermally in the early universe, they must have a non-negligible interaction with matter. Since the solar system sits in a bath of dark matter particles, it is possible to design experiments to detect WIMP interactions with a baryonic target. WIMPs can scatter either *elastically* or *inelastically* off target baryons. Since elastic scattering rates are predicted to be substantially higher than inelastic rates (Ellis et al., 1988; Engel & Vogel, 2000), the vast majority of direct detection experiments are focused on detecting the small energy transfers from WIMPs to baryons during their rare elastic interactions (exceptions being the DAMA LXe (Bernabei et al., 2000a) and PICO-LON (Fushimi et al., 2006) experiments). From the event rates in these experiments, limits on the dark matter particle mass and cross section can be inferred using astrophysical assumptions about the dark matter distribution at the Earth's surface.

To get a sense of how model assumptions affect how the event rate and energy spectrum of interactions are translated to constraints on particle physics models, it is useful to examine the formula for predicted event rates. In general, the WIMP-nucleus scattering rate per kg of detector mass per unit energy transfer can be expressed as (cf. Jungman et al., 1996)

$$\frac{\mathrm{d}R}{\mathrm{d}Q} = \left(\frac{m_A}{\mathrm{kg}}\right)^{-1} \int_{v_{cut}}^{\infty} \mathrm{d}^3\mathbf{v} \frac{\mathrm{d}\sigma_A}{\mathrm{d}Q} g_A f(\mathrm{x}, \mathrm{v}), \tag{1.19}$$

where $\mathrm{d}\sigma_A/\mathrm{d}Q$ is the differential interaction cross section between a WIMP and a nucleus of mass m_A and atomic number A, $\mathbf{v}$ is the velocity of the dark matter particle with respect to the experiment, v_{cut} is the minimum WIMP speed that can yield an energy transfer Q, and g_A is the relative speed between the WIMP and the target nucleus. Since any target atoms have small speeds relative to the speeds of dark matter particles, to a good approximation $g_A = v$. The dark matter distribution function at the Earth is $f(\mathbf{x}, \mathbf{v})$. Since favored particle physics candidates for dark matter (LSP in the MSSM, LKP in UED models) may have both *spin-independent* (SI) and *spin-dependent* (SD) interactions with matter, it is customary to place separate limits on the SI and SD cross sections. Only nuclei with an

odd number of protons or neutrons (or both) will have spin-dependent interactions with WIMPs (Appendix B). Therefore, it is also customary to separate the limits on the spin-dependent cross sections of protons and neutrons. In Figure 1.7, I show the current limits on the WIMP mass and WIMP-nucleon spin-independent cross section σ_p^{SI}. Figure 1.8 shows limits on the spin-dependent WIMP-proton cross section σ_p^{SD} as a function of WIMP mass, and Figure 1.9 shows upper bounds on the WIMP-neutron spin dependent cross section σ_n^{SD}. It should be obvious from Figures 1.7, 1.8, and 1.9 that the spin-independent cross section is much more tightly constrained than the spin-dependent cross sections. This is due to the fact (see Appendix B) that the total interaction cross section $\sigma_A^{SI} \approx A^4 \sigma_p^{SI}$ for $m_{\mathrm{WIMP}} \gg m_A$, while the spin-dependent cross section grows only as A^2, and also has a complicated relationship with the nuclear spin content. Currently, there exist only upper bounds on the WIMP-nucleon event rates $\mathrm{d}R/\mathrm{d}Q$ (with the exception of the DAMA annual modulation result, the red patch in Figure 1.7, which will be discussed later). For a heavy target, an upper bound on the event rate translates to a much lower upper limit for the spin-independent WIMP-proton cross section than the spin-dependent cross section since $\sigma_p^{SI,upper} \propto A^{-4}\mathrm{d}R/\mathrm{d}Q$ while $\sigma_{p,n}^{SD,upper} \propto A^{-2}\mathrm{d}R/\mathrm{d}Q$.

For a given WIMP-proton (or WIMP-neutron) cross section, the integrated event rate $R = \int_0^\infty \mathrm{d}R/\mathrm{d}Q\mathrm{d}Q$ is higher for a target of higher A. Many experiments use very heavy atoms as targets in order to maximize the interaction probability. However, the event rate $\mathrm{d}R/\mathrm{d}Q$ falls off dramatically with Q, which is apparent in Figure 1.10. This fall-off results from increasing incoherence in WIMP-nucleon scattering as a function of energy transfer Q, with the slope of the fall-off in Figure 1.10 set by the coherence energy Q_A (see Appendix B). In this Figure, I have shown differential event rates for three common target materials: ^{40}Ar, ^{73}Ge, and ^{131}Xe. The steepness of the slope of the differential event rate is clearly an increasing function of target mass. Therefore, in order to make use of the dramatically higher interaction spin-independent cross section for heavy atoms, it is necessary to have a low experimental energy threshold.

The event rate is proportional to the integral of the WIMP speed over the dark matter

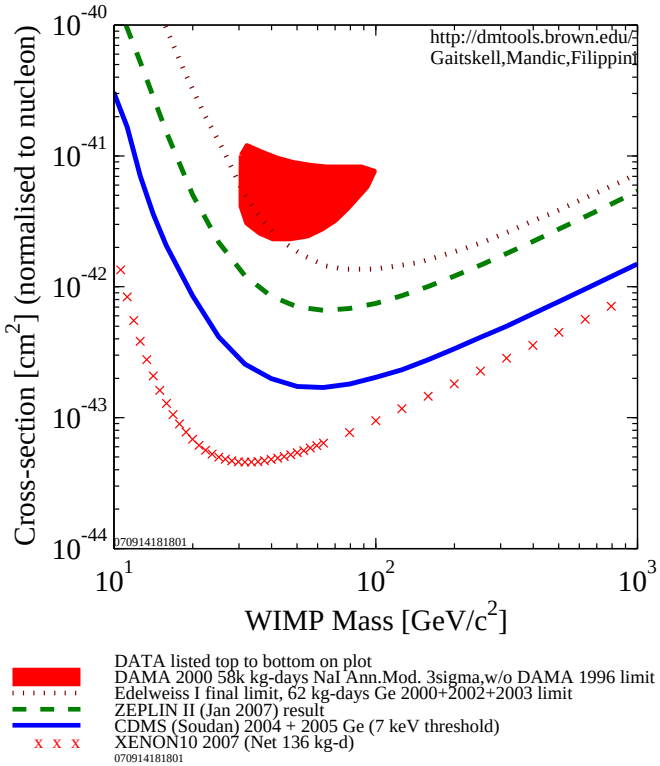

Figure 1.7: Limits on the spin-independent WIMP-nucleon cross section from recent experiments. The CDMS and XENON experiments are discussed in the text. EDELWEISS is a germanium experiment like CDMS, and ZEPLIN-II is another xenon-based experiment. The plot is made using the interface available at http://dendera.berkeley.edu/plotter/entryform.html.

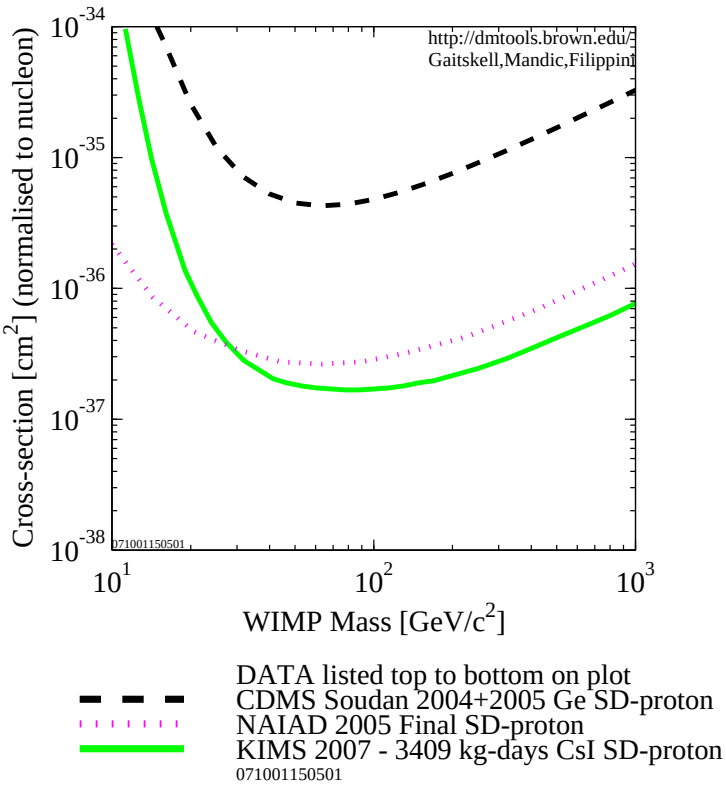

Figure 1.8: Limits on the spin-dependent WIMP-proton cross section from recent experiments. The plot is made using the interface available at http://dendera.berkeley.edu/plotter/entryform.html.

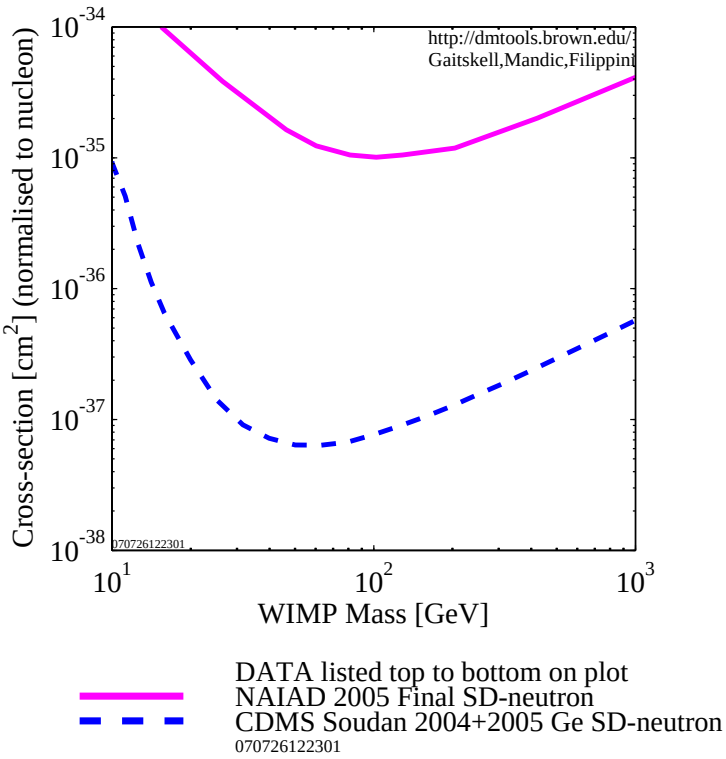

Figure 1.9: Limits on the spin-dependent WIMP-neutron cross section from recent experiments. The plot is made using the interface available at http://dendera.berkeley.edu/plotter/entryform.html.

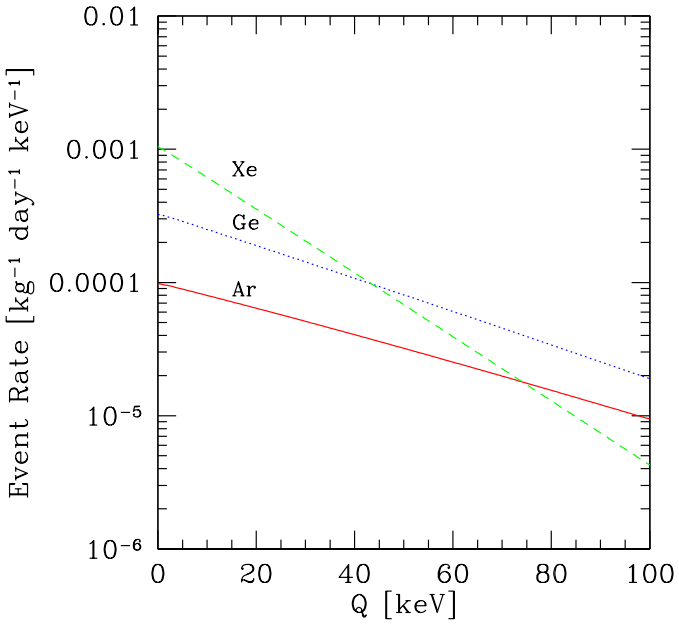

Figure 1.10: Predicted spin-independent event rates per unit detector mass for a WIMP of mass $m_{\mathrm{WIMP}} = 470$ GeV and interaction cross section $\sigma_P^{SI} = 10^{-43}$ cm^2. The dashed green line indicates scatters with xenon ($A = 131$), the blue dotted line indicates a target mass of germanium ($A = 73$), and the red solid line denotes interactions with argon ($A = 40$).

distribution function. Therefore, good knowledge of the distribution function is required to accurately translate event rates to constraints on particle physics models of dark matter. Estimating the distribution function requires assumptions about the distribution function of the dark matter halo, the motion of the Earth through the Galaxy, and effects within the solar system. These various assumptions will be discussed in greater detail in Sections 1.3 and 1.4, but here I will describe the types of assumptions that are usually made in the analysis of direct detection experiments. Exclusion plots in $\sigma - m_{\rm WIMP}$ space are usually made by modeling the Galactic distribution function as locally Maxwellian with a mass density $\rho_{\rm WIMP} = 0.3$ GeV cm$^{-3} = 8 \times 10^{-3}$ M$_\odot$ pc^{-3}. The dark matter density is assumed to be smooth on scales much larger than the solar system. In translating the halo distribution function to the dark matter distribution function at the Earth, one must take into account the solar system's nearly circular motion about the Galactic center, and the Earth's motion about the Sun. In particular, the Earth's motion leads to an annual modulation of the direct detection signal with a peak around June 2 every year, although this peak is somewhat model dependent (Freese et al., 1988; Green, 2003). Some experiments (e.g., DAMA) are designed to investigate such modulations. Lastly, it is important to consider the effects of the solar system on the dark matter distribution function. Most analyses are performed using only the effect of the Sun's gravitational potential on the distribution function. In practice, this means applying Liouville's theorem to the distribution function (see Eq. 2.9), so that phase space density is conserved. However, the dark matter distribution function can be influenced both by the gravitational potentials of the planets and by elastic scattering off baryons in the Sun and Earth. These effects are the focus of this thesis.

Using the fiducial set of assumptions, existing limits on event rates have been translated into constraints on the $m_{\rm WIMP} - \sigma_p^{SI}$ (Figure 1.7), $m_{\rm WIMP} - \sigma_p^{SD}$ (Figure 1.8), and $m_{\rm WIMP} - \sigma_n^{SD}$ (Figure 1.9) parameter spaces. The DAMA collaboration claims to have discovered an annual modulation signature in their data (Belli et al., 2000; Bernabei et al., 2000b). However, this finding is virtually impossible to reconcile with the results of all other experiments (Ullio et al., 2001b; Savage et al., 2004; Gondolo & Gelmini, 2005). Until

recently, the best experimental constraints on the spin-independent cross section came from the CDMS experiment (Akerib et al., 2006b). This experiment, which is ongoing, consists of towers of cryogenically cooled silicon and germanium, located in the Soudan Mine in Minnesota. Events are identified by their thermal and ionization signatures. The exclusion curve in Figure 1.7 is based on 34 kg $\cdot$ day of data from germanium and 12 kg $\cdot$ day of silicon. Recently, the XENON collaboration presented its first results on the spin-independent cross section from the XENON10 experiment (Angle et al., 2007). The exclusion limit is based on ≈ 60 days of data on their 10 kg xenon target located in the Gran Sasso National Laboratory. The threshold for this experiment is 4.5 keV, but it may be possible to push the threshold lower since event discrimination improves in xenon for smaller recoil energies (Shutt et al., 2007). Event discrimination is crucial due to the high background of these experiments and the fact that expected event rates from WIMPs are $R \ll 1$ event kg^{-1} day^{-1}.

The best direct detection limit on the σ_p^{SD} cross section comes from the NAIAD experiment, a NaI(Tl) crystal-based experiment that was located in the Boulby Underground Laboratory (Alner et al., 2005), and the KIMS experiment, a CsI(Tl) experiment in the Yangyang Underground Laboratory. The NAIAD experiment is primarily sensitive to the proton cross section because both the sodium (^{23}Na) and iodine (^{127}I) in the target crystal have an unpaired proton. NAIAD's limit on the WIMP-proton cross section is based on an analysis on 44.9 kg·day of data. The KIMS limit is based on 3409 kg·day of data, and both the iodine and ^{133}Cs in the crystals have unpaired protons. The CDMS experiment currently boasts the tightest constraint on the WIMP-neutron cross section (Akerib et al., 2006a). Both the ^{29}Si and ^{73}Ge that comprise the detector target mass have odd numbers of neutrons.

Current limits are based on experiments with target masses $\lesssim 10$ kg. These experiments are just now able to probe regions of $\sigma^{SI} - m_{\rm WIMP}$ parameter space for plausible MSSM models, but limits on spin-independent cross sections are still several orders of magnitude above the cross sections predicted by the simplest UED model. Limits on the spin-

dependent cross sections are also somewhat above those predicted in the simplest MSSM and UED models. The next generation of direct detection experiments is slated to have masses approaching 1000 kg (e.g., DEAP/CLEAN (Hime, 2007), LUX (Gaitskell, 2007), SuperCDMS (Brink et al., 2005; SuperCDMS Collaboration, 2005; Akerib et al., 2006c), WARP (Brunetti et al., 2005), XENON1T (Aprile et al., 2002), XMASS (The Xmass Collaboration, 2005)) and to be sensitive to event rates $\lesssim 10^{-4}$ events kg^{-1} day^{-1}. These experiments should be able to place significant constraints on particle physics models of dark matter, either by actually observing statistically significant WIMP-nucleon events or by placing even more stringent upper bounds on the interaction cross section. However, it should be strongly emphasized that knowledge of the dark matter distribution function is required for a proper translation between detector event rates and particle physics models for dark matter. The interested reader should consult the Dark Matter Plotter webpage (http://dendera.berkeley.edu/plotter) for a relatively complete listing of previous experimental results and predictions for forthcoming experiments and Gaitskell (2007) for a summary of detector technologies with an emphasis on noble liquid targets.

Neutrinos from the Earth

WIMPs may accumulate and annihilate within the Sun and the planets. WIMP annihilation in the solar system will not be observable in photons or charged particles, since none of these would escape from any solar system body. Instead, the signature of WIMP annihilation in the solar system will be GeV to TeV neutrinos. The various neutrino observatories around the planet are sensitive to the muon neutrinos, more specifically, to the Čerenkov radiation from muons from charged-current interactions of muon neutrinos in and around the experiment target mass. In general, the expected signals are likely to be strongest for neutrinos from the Earth and the Sun. In this section, I focus on neutrinos from the Earth. I will address neutrinos from the Sun in Section 5.3.1. I will outline the calculation of and the experimental constraints on the neutrino-induced muon event rate, and highlight important astrophysical uncertainties in predicting and interpreting the muon signal.

The number of WIMPs N captured in the gravitational potential of a celestial body can be described by

$$\dot{N} = C - 2\Gamma, \tag{1.20}$$

where the capture rate of WIMPs in the body by elastic scattering is defined as

$$C = \int \mathrm{d}^3\mathbf{x} \int_{v_{final}<v_{esc}(\mathbf{x})} \mathrm{d}^3\mathbf{v}\mathrm{d}\Omega \sum_A \frac{\mathrm{d}\sigma_A}{\mathrm{d}\Omega} n_A(\mathbf{x}) g_A f(\mathbf{x}, \mathbf{v}, t). \tag{1.21}$$

As in Eq. (1.19), $\mathrm{d}\sigma_A/\mathrm{d}\Omega$ is the WIMP-nucleus elastic scattering cross section for nuclear species A and g_A is the relative speed between the WIMP and a nucleus. The number density of species A is described by $n_A(\mathbf{x})$. The cutoff in the velocity integral reflects the fact that the WIMP's speed after scattering must be less than the local escape velocity $v_{esc}(\mathbf{x})$. The second term in Eq. (1.20) is twice the annihilation rate

$$\Gamma = \frac{1}{2} C_{ann} N^2. \tag{1.22}$$

The factor of two in Eq. (1.20) refers to the fact that the most popular WIMP candidates (the neutralino or $B^{(1)}$) are self-annihilating. The coefficient C_{ann} is proportional to the WIMP annihilation cross section. As demonstrated in Section 1.1.1, the annihilation cross section can be estimated from the dark matter density of the universe, assuming that dark matter consists only of one species of WIMP. Therefore, the annihilation rate is relatively well-known, mostly independent of specific particle physics models for WIMPs and the WIMP mass.

If the capture rate C is time independent (i.e., the distribution function is time independent), then the number of particles inside a celestial body, and hence, the annihilation rate, can be determined analytically:

$$\Gamma = \frac{1}{2} C \tanh^2(t/\tau_{eq}), \tag{1.23}$$

where

$$\tau_{eq} = (C C_{ann})^{-1/2} \tag{1.24}$$

is the equilibrium timescale. In the limit that the equilibrium timescale is small or large relative to the age of the solar system $t_{SS} \approx 4.5$ Gyr,

$$\Gamma = \begin{cases} \frac{1}{2}C & \text{if } t_{SS}/\tau_{eq} \gg 1 \\ \frac{1}{2}C^2 C_{ann} t_{SS}^2 & \text{if } t_{SS}/\tau_{eq} \ll 1. \end{cases} \tag{1.25}$$

I would like to emphasize several points concerning the annihilation rate. The annihilation rate depends most strongly on the capture rate of particles in the celestial body, and the annihilation cross section. The annihilation cross section can be estimated from the relic density of dark matter. The capture rate is determined by three things: the WIMP-nucleon elastic cross section, the structure and composition of the body, and the dark matter distribution function. The structure and composition of the Sun (Bahcall et al., 2005) and the Earth (see, e.g., Anderson, 2005) are well known. The dark matter distribution function is an astrophysical quantity. Therefore, the only dependence of the annihilation rate on the particle physics model comes from the WIMP-nucleon elastic scattering cross section.

However, the muon flux through a detector is dependent on several aspects of the underlying particle physics model for both WIMPs and neutrinos. The flux of neutrinos at the surface of the Earth is (cf. Jungman et al., 1996)

$$\frac{\mathrm{d}\Phi_{\nu_\mu}}{\mathrm{d}E} = \frac{\Gamma}{4\pi R_\oplus^2} \sum_F B_F \frac{\mathrm{d}N_i^F}{\mathrm{d}E} \mathbf{f}_{i\nu_\mu}(E), \tag{1.26}$$

where $\mathrm{d}N_i^F/\mathrm{d}E$ is the differential energy spectrum of neutrino species $i \in \{\nu_e, \nu_\mu, \nu_\tau\}$ resulting from annihilations into channel F, and B_F is the branching ratio. The factor $\mathbf{f}_{ij}(E)$ $(i, j \in \{\nu_e, \nu_\mu, \nu_\tau\})$ describes neutrino oscillations between the center and surface of the Earth. Neutrino oscillations can be ignored for neutrinos with energy $E \gtrsim 50$ GeV, but oscillations will be important for lower energy neutrinos. Not only will the precise effect of neutrino oscillation depend on the particle WIMP model, but the uncertainties in the neutrino mixing parameters are still large enough for there to be a wide margin of possible effects on the neutrino flux at the surface of the Earth (Cirelli et al., 2005; Barger et al., 2007a; Blennow et al., 2007; Lehnert & Weiler, 2007). The neutrino flux results in a muon event rate for a given neutrino experiment that is approximately (cf. Halzen & Hooper,

2006)

$$\dot{N}_\mu \approx \int \mathrm{d}y \int_{E>E_{th}} \mathrm{d}E \frac{\mathrm{d}\Phi_\nu}{\mathrm{d}E} \frac{\mathrm{d}\sigma_\nu}{\mathrm{d}y}(E,y) n_A R[(1-y)E] A_{\mathrm{eff}}. \tag{1.27}$$

In this equation, σ_ν is the muon neutrino-nucleon charged-current cross section to create a muon, n_A is the number density of nuclear species A in and about the experimental volume, $(1-y)$ is the fraction of the neutrino's energy that gets transfered to the muon, $R[(1-y)E]$ is the distance the muon travels before its energy drops below the detector threshold, and A_{eff} is the (energy-dependent) effective area of the experiment. The actual calculation of $\dot{N}_\mu$ requires detailed information about the experimental configuration. It is standard in neutrino telescope literature to express detection limits in terms of muon flux

$$\Phi_\mu \approx \dot{N}_\mu / A_{\mathrm{eff}} \tag{1.28}$$

in order to compare results of experiments that may have very different configurations.

There are several things to note in the expressions for the neutrino flux at the Earth, Eq. (1.26), and the muon event rate, Eq. (1.27). The first point is that the characteristic energy of the muons will likely be far less than the mass of the WIMP. WIMPs do not annihilate directly to neutrinos in the MSSM, and so neutrinos are the byproducts of decays and hadron showers (Jungman et al., 1996). Kaluza-Klein particles can annihilate directly to neutrinos, but the branching fraction is expected to be small (e.g. Hooper & Kribs, 2003). In addition, the characteristic muon energy will be less than the characteristic neutrino energy. A typical muon will have an energy only about 1/4 or so of the WIMP mass. Therefore, it is highly desirable for neutrino experiments to have low energy thresholds. The importance of low thresholds is illustrated in Figure 1.11, which shows the ratio of flux at several energy thresholds to the flux above $E_\mu^{th} = 1$ GeV for a variety of supersymmetric models. A km^3 experiment with a threshold of $E_\mu^{th} = 10$ GeV may be sensitive to only $\sim 50\%$ of muon flux relative to an experiment with a threshold $E_\mu^{th} = 1$ GeV for a 100 GeV neutralino. For a threshold of $E_\mu^{th} = 25$ GeV, the signal drops to $\sim 10\%$ or less of the signal at $E_\mu^{th} = 1$ GeV (Bergström et al., 1998a). Another consequence of the relatively low energy of the neutrinos and muons relative to the WIMP mass is that neutrino oscillations may become

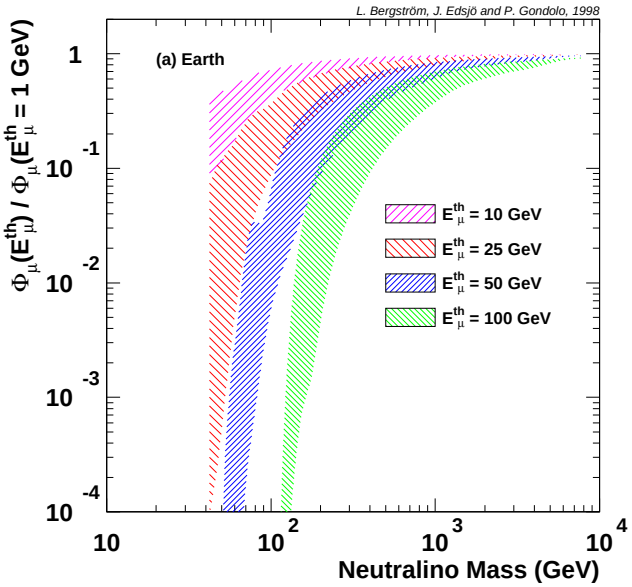

Figure 1.11: The ratio of the muon event rate above an energy threshold $E_\mu^{\rm th}$ to the event rate with an energy threshold of 1 GeV in a km^3-scale experiment assuming that the muons result from WIMP annihilation in the Earth. These ratios were computed using only muons created outside of the experimental volume, not muons created within the detector volume. This figure is from Bergström et al. (1998a).

important in predicting event rates for massive WIMPs.

No neutrino-induced muons have as yet been identified as having an origin in the center of the Earth. Current constraints on the muon flux come from two classes of neutrino telescope. The first consists of the traditional configuration of a tank filled with liquid scintillator, surrounded by photomultiplier tubes (PMTs). These telescopes are usually deep underground so as to reduce the incidence of cosmic ray muons. Such experiments have typical target masses of $\sim 1 - 10$ kton, and can have low muon energy thresholds $E_\mu^{th} \lesssim 1$ GeV. Upper limits from BAKSAN (Boliev et al., 1996), MACRO (Ambrosio et al., 1999), and Super-Kamiokande (Habig et al., 2001) for the muon flux from WIMP annihilations in the Earth are typically a few times 1000 km^{-2} yr^{-1} (Figure 1.12).

Much better sensitivity to neutrino-induced muons will come from a new class of neutrino

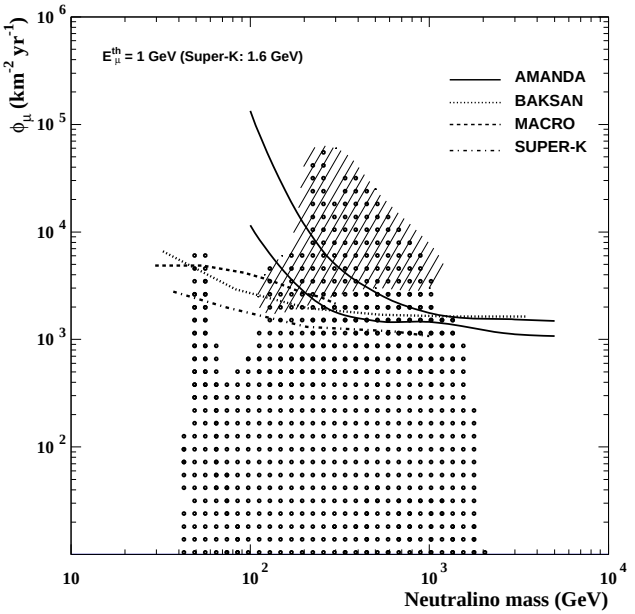

Figure 1.12: Limits on the flux of muons resulting from WIMP annihilations in the Earth. The upper (lower) AMANDA line corresponds to the limit for a soft (hard) annihilation spectrum. The dots mark individual MSSM models. Models in the hatched region are above the Bernabei et al. (1996) spin-independent cross section limit, which is grossly out-of-date. This figure is taken from Ahrens et al. (2002).

telescope. Instead of using an enclosed volume of liquid scintillator, these new experiments place strings of PMTs inside natural scintillators, namely ocean water and the icecap of Antarctica. Neutrino-induced muon tracks and energies are identified by the timing and energy deposited in individual PMTs (Figure 1.13). The advantage of this approach is that the target volume is drastically increased. The actual sensitivity of these observatories to neutrinos from WIMP annihilation in the Earth depends on the spacing of PMTs within the volume of water or ice, and the spacing is driven by the primary goals for the observatories, which were designed to be sensitive to neutrinos from astrophysical engines (gamma-ray bursts, supernovae, active galactic nuclei) and to determine the sources of cosmic rays. The latter is especially interesting since neutrinos will point directly to the source of cosmic rays, while charged particles produced by the same source will have their directions scrambled by the Galactic magnetic field. Since the neutrino energies for the astrophysical engines are thought to be high (TeV-PeV, see Halzen & Hooper (2002) for a discussion), PMTs can be widely spaced since higher energy muons will have longer tracks. Therefore, for a fixed number of PMTs, one can increase the effective area (at high energies) of the telescope with a larger spacing of PMTs. However, this wide spacing means that the telescope has a high energy threshold.

Even if the overall energy threshold for the observatory is high, the threshold for neutrino-induced muons from the Earth can be designed to be much lower without sacrificing much effective area. The reason for this is that PMTs are connected to each other vertically on strings, and the PMT spacing on a string is much denser than the spacing of strings within the volume of the experiment. Since the center of the Earth is a point source of neutrinos for high mass WIMPs, the muon tracks ought to be parallel (or nearly so) to the PMT strings. Since the PMTs are more densely spaced in this direction, the muon threshold is much lower. For example, the initial design of the IceCube experiment implied an overall muon energy threshold of $\sim$ 400 GeV and an effective area of 1 km^2. However, the threshold muon energy along a string could be 10 GeV or lower (The IceCube Collaboration, 2001).

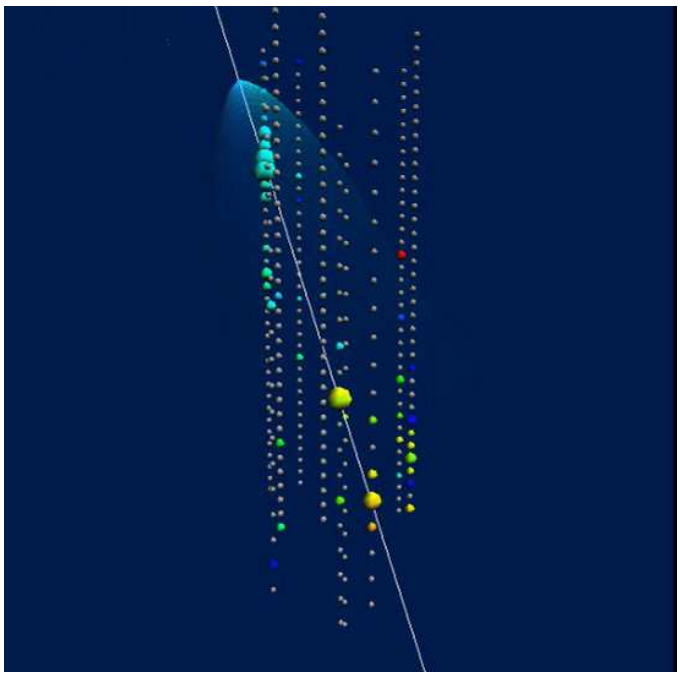

Figure 1.13: Artistic rendering of a muon passing through the IceCube array. From http://www.icecube.wisc.edu/index.php

The first generation of experiments of this ilk are the BAIKAL-NT200 experiment using the waters of Lake Baikal in Russia (Aynutdinov et al., 2006) and the AMANDA experiment (The IceCube Collaboration, 2001; Achterberg et al., 2006; Hill et al., 2006), which takes advantage of the Antarctic icecap. The Baikal experiment has 192 PMTs on 8 strings spread out over a surface area of $\approx 2 \times 10^3$ m^2. The AMANDA experiment was deployed incrementally, with a final count of 677 PMTs on 19 strings over a surface area of ~ 0.03 km^2. Both have energy thresholds of $E_\mu^{th} \lesssim 10$ GeV. As demonstrated by Figure 1.12, the limits on neutrinos from the center of the Earth are comparable to those derived from more traditional neutrino observatories. However, the next generation of experiments ought to be sensitive to muon fluxes two or more orders of magnitude below the sensitivities of the first generation of water- and ice-based experiments. The IceCube observatory will eventually deploy 4800 PMTs on 80 strings (the goal is completion in 2011) over a geometric surface area of 1 km^2, with an effective volume of 1 km^3 (Hill et al., 2006). It will overlap

the AMANDA experiment, and is projected to be sensitive to muon event rates of a few tens per square kilometer per year with three years of data. As previously discussed, while its fiducial energy threshold will be high ($E_\mu^{th} \approx 400$ GeV), the muon energy threshold is much lower if the muon track is parallel to the PMT strings. Several ~ 0.1 km^2 experiments (ANTARES, NEMO, NESTOR) are under construction deep in the Mediterranean Sea. Because the absorption length of light in this medium is short (≈ 60 m), the PMTs will need to be more closely spaced than in IceCube. However, this means that the muon threshold will be lower, too. The NEMO site is a potential location for a km^3-volume experiment, KM3Net (Katz, 2006), which is currently in the design stage. For astrophysical reasons, it is desirable to have a northern hemisphere counterpart to IceCube.

The main uncertainty in predicting and interpreting neutrino and neutrino-induced muon event rates, given a specific particle physics model for dark matter, is the capture rate of WIMPs in the Earth. Not only are there the usual uncertainties in the local dark matter density and velocity distribution (see the next section for a discussion), but for even modest WIMP masses, the capture rate depends on the part of the dark matter distribution function that is not accessible to halo dark matter particles in the absence of scattering processes. Halo particles are not bound to the solar system unless there are processes that scatter halo particles onto bound orbits. The escape velocity from the solar system at the Earth's orbit is $v_{esc}^{\odot} = \sqrt{2} v_\oplus \approx 42$ km s^{-1}, where $v_\oplus$ is the speed of the Earth about the Sun. Making a Galilean transformation to a frame corotating with the Earth, the minimum speed for a particle just escaping the solar system is $v_{min} = v_{esc}^{\odot} - v_\oplus \approx 12.3$ km s^{-1}. Therefore, all halo particles must have speeds $v \geq 12.3$ km s^{-1} with respect to the Earth. By definition, though, in order for these particles to be captured to the Earth, the speed of the WIMP after interacting with an atom in the Earth must be below the small escape speed for the Earth ($v_{esc}^{\oplus}(R_\oplus) \approx 11$ km s^{-1} at the surface of the Earth, $v_{esc}^{\oplus}(0) \approx 15$ km s^{-1} at the center). The maximum initial speed a WIMP can have with respect to the Earth and still be captured is set by the maximum energy transfer from the WIMP to an atom

with atomic mass A in the Earth. If

$$E_i = \frac{1}{2} m_{\rm WIMP} v^2 \tag{1.29}$$

is the initial energy of a WIMP of speed v in the frame of the Earth but *outside the Earth's sphere of influence*, then the maximum value v can take is set by

$$E_f = E_i - Q_{max} = 0, \tag{1.30}$$

where Q_{max} is determined by setting $\cos\theta = -1$ in Eq. (B.5). This implies that

$$v \leq 2 \frac{\sqrt{m_A m_{\rm WIMP}}}{m_{\rm WIMP} - m_A} v_{esc}^{\oplus}, \tag{1.31}$$

for an atom with mass m_A in the Earth. This relation is shown in Figure 1.14. In this Figure, $v_{esc}^{\oplus}$ is set to its value at the center of the Earth, and the scattering atom used is iron, which dominates the mass of the core of the Earth. Particles with speeds to the left of the solid line may be captured by the Earth for a given WIMP mass; particles with speeds to the right cannot be captured in the Earth. One can see that the minimum halo speed corresponds to a mass $m_{\rm WIMP} = 410$ GeV. Therefore, for WIMP masses above 410 GeV, the capture rate in the Earth is completely dominated by any WIMPs that become captured to the solar system. Since the capture and annihilation rates of particles will likely not yet have come to equilibrium (Lundberg & Edsjö, 2004), the event rate in neutrino detectors will scale as $\Phi_\mu \propto C^2$ (see Eq. 1.25), and so any uncertainties in the distribution function of WIMPs bound to the solar system will be magnified in predicted event rates for neutrino observatories.

1.3 The Local Dark Matter Distribution Function

As demonstrated in the previous section, both the direct (Eq. 1.19) and the indirect (Eqs. 1.23 and 1.27) event rates depend on powers of integrals over the dark matter distribution function at the Earth. Both the direct detection event rate and the rate of WIMP capture in the Earth are proportional to the velocity integral of the distribution function times the

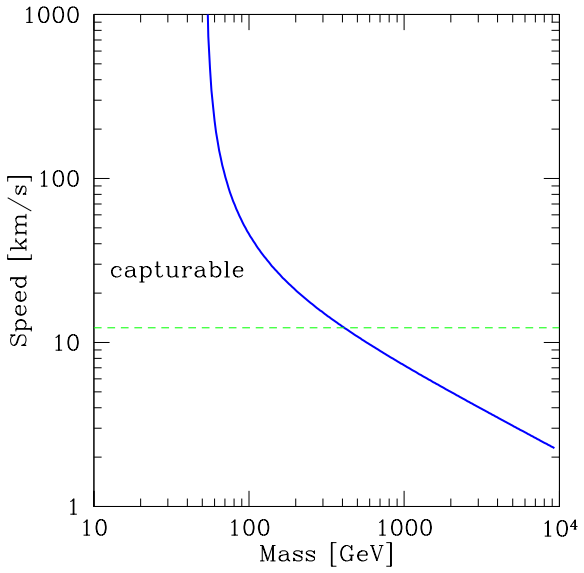

Figure 1.14: Cutoff speed in the frame of the Earth as a function of WIMP mass (*solid line*). WIMPs with speeds to the left of the solid line may be captured by the Earth via weak interactions. The minimum possible speed of halo particles in the absence of scattering processes $v_{\rm min} = (\sqrt{2}-1)v_{\oplus}$ is marked with the dashed line.

WIMP speed. In order to predict realistic event rates, it is necessary to understand the dark matter phase space distribution function at the detectors. I will break up the discussion of the distribution function into several sections. In Section 1.3.1, I discuss the current state of knowledge about the halo dark matter distribution function. In Section 1.3.2, I will show how the motion of the Earth through the dark matter halo translates the halo distribution function to the distribution function at the Earth. In Section 1.4, I summarize previous attempts to quantify the effects of scattering within the solar system on the distribution function at the Earth. These sections will lay the groundwork for the rest of this thesis.

1.3.1 The Halo Dark Matter Distribution Function at the Solar Circle

For the purposes of calculating direct and indirect detection rates, it is not necessary to know the global structure of the dark matter distribution function in the Galaxy. It is only necessary to know the distribution function in the vicinity of the Sun. Therefore, even though equilibrium distribution functions $f(\mathbf{x}, \mathbf{v})$ are generally not separable in the form

$f_x(\mathbf{x})f_v(\mathbf{v})$ on scales much smaller than the scale of variation of the number density, the distribution function can be described by the local mass or number density of WIMPs and their velocity probability distribution. In order to understand the distribution function of dark matter in a small region along the Sun's orbit through the halo, I divide the discussion of what is known or inferred about the distribution function into a section on the dark matter density and a section on the velocity distribution of halo WIMPs. I will also address the question of substructure in the Milky Way.

The WIMP mass density $\rho_{\rm WIMP}$

What methods can be used to infer the existence of a dark component in the Milky Way? Since dark matter is obviously not visible, it is necessary to use the kinematics of observable objects to map the gravitational potential of the Galaxy. If the potential of the Galaxy is roughly axisymmetric, and we are concerned with the potential in and near the plane of the Milky Way disk, then the gravitational potential $\Phi(\mathbf{x})$ can be approximated by $\Phi(\mathrm{x}) = \Phi_R(R) + \Phi_z(z)$. Here, R is the cylindrical radial coordinate ($R = 0$ is the Galactic center) and z is the height above the plane of the disk. Estimates of Φ_R (or the force $F_R = -\mathrm{d}\Phi_R/\mathrm{d}R$) throughout the disk and Φ_z at the position R_0 of the Sun (relative to the Galactic center) are combined to yield estimates of the local dark matter density $\rho_{\rm WIMP}$. I will discuss some results from the literature on each component of the potential in turn.

As described in Section 1.1.1, early evidence for the existence of dark matter came from the rotation curves of spiral galaxies. Rotation curves probe the quantity

$$v_c(R) = \left[R\frac{\partial\Phi}{\partial R}\right]^{1/2} \tag{1.32}$$

$$= \left[R\,|F_R|\right]^{1/2}. \tag{1.33}$$

The total rotation curve has contributions from both the disk (d) and the halo (h),

$$v_c(R) = \left[v_d^2(R) + v_h^2(R)\right]^{1/2}. \tag{1.34}$$

It is important to note that the "disk" component is not necessarily synonymous with "baryonic matter". For a time in the 1980's, it appeared that there might be a dark matter

component to the disk, although this is now highly disfavored (Kuijken & Gilmore, 1991; Holmberg & Flynn, 2000, 2004). It is also clear that the relative contributions to the rotation curve from the disk and halo cannot be determined by the rotation curve alone, thus other data are needed to determine the halo contribution.

The rotation curve of the Galaxy is fairly well determined, at least within the solar circle. The shape of the rotation curve has been established by observations of atomic and molecular gas interior to the solar circle, and by tracers such as planetary nebulae in the outskirts of the visible disk (see Section 9.2 of Binney & Merrifield, 1998, for a more in-depth discussion). The absolute calibration of the rotation curve is determined using estimates of the circular speed at the radius R_0, called the velocity of the Local Standard of Rest $v_{\rm LSR}$. There are several methods to determine this quantity. A review of International Astronomical Union (IAU) standard values for Galactic quantities lists many techniques to determine $v_{\rm LSR}$, two of which involve either measuring Oort's constants or measuring the 21-cm emission of atomic gas clouds in the outer reaches of the Galaxy (Kerr & Lynden-Bell, 1986).

The method of determining the local circular velocity with Oort's constants makes use of the epicycle approximation of orbits in an axisymmetric potential (see Section 3.2.3 of Binney & Tremaine, 1987, and Section 10.3.3 of Binney & Merrifield, 1998, for longer discussions). Oort's constants, called A and B, quantify the velocity shear (A) and vorticity (B) of stars on nearly circular orbits about the Galactic center. Estimates of these constants are derived from both line-of-sight velocities and proper motions of stars near the Sun. The velocity of the Local Standard of Rest is then given by $v_{\rm LSR} = R_0(A - B)$.

The velocity of the Local Standard of Rest can also be estimated using observations of H I clouds in the outskirts of the Milky Way (Knapp et al., 1978; Gunn et al., 1979). The line-of-sight speed of an object in the Galaxy is

$$v_{\rm los} = \left[v_c(R)\frac{R_0}{R} - v_{\rm LSR} \right] \sin l, \tag{1.35}$$

where l is the galactic longitude. The first term in Eq. (1.35) vanishes for large radii $R \gg R_0$, and so

$$v_{\rm los} \approx -v_{\rm LSR} \sin l. \tag{1.36}$$

Therefore, 21-cm emission displaced by $-v_{\rm LSR} \sin l$ from the rest frame is the superposition of emission from all distant atomic gas clouds along the line of sight, thus making even faint emission observable. Knapp et al. (1978) modeled the 21-cm emission, and found it to be most compatible with a local circular velocity of $v_{\rm LSR} \approx 220$ km s^{-1}.

The second piece of dynamical data is an estimate of $\Phi_z(z)$ (or, rather, the force $F_z = -{\rm d}\Phi_z/{\rm d}z$) in and near the plane of the Galaxy. The premise is to map out the potential using a sample of a steady-state tracer population, usually F or K stars. Properties of the tracer population and the gravitational potential (or force) are linked via the Jeans equation expressed in cylindrical coordinates

$$\frac{1}{R}\frac{\partial(\nu\overline{v_R v_z}R)}{\partial R} + \frac{\partial(\nu\overline{v_z^2})}{\partial z} = -\nu\frac{{\rm d}\Phi_z}{{\rm d}z} \tag{1.37}$$

$$= \nu F_z, \tag{1.38}$$

where $\nu(z)$ is the number density of the tracer population, $\overline{v_z^2}$ is the mean-square speed in the z-direction, and $\overline{v_R v_z}$ is the velocity-averaged $R-z$ moment of the velocity distribution. Different groups have used different estimators to derive F_z from their datasets (Bahcall, 1984a,b; Kuijken & Gilmore, 1989a,b,c, 1991; Gould, 1990; Holmberg & Flynn, 2000, 2004). It should be noted that, while $\nu(z)$ and $\overline{v_z^2}$ can be reasonably well determined from the tracer datasets, $\overline{v_R v_z}$ is poorly constrained outside of the $z = 0$ midplane (Kuijken & Gilmore, 1991). Therefore, F_z is often estimated using only the second term of Eq. (1.37), although some groups estimate corrections to F_z using estimates of the velocity ellipsoid outside of the plane. Once F_z has been estimated, the mass surface or volume density can be estimated

using Poisson's equation and the observed circular velocity curve:

$$\frac{1}{R}\frac{\mathrm{d}}{\mathrm{d}R}\left(R\frac{\mathrm{d}\Phi_R}{\mathrm{d}R}\right)+\frac{\mathrm{d}^2\Phi_z}{\mathrm{d}z^2} = 4\pi G\rho \tag{1.39}$$

$$-\left[\frac{1}{R}\frac{\mathrm{d}(RF_R)}{\mathrm{d}R}+\frac{\mathrm{d}F_z}{\mathrm{d}z}\right] = 4\pi G\rho \tag{1.40}$$

$$-\left[-\frac{1}{R}\frac{\mathrm{d}v_c^2}{\mathrm{d}R}+\frac{\mathrm{d}F_z}{\mathrm{d}z}\right] = 4\pi G\rho, \tag{1.41}$$

such that the *total* volume density (including baryonic and dark matter) in the plane of the Galaxy is

$$\rho(R_0,0) = -\frac{1}{4\pi G}\left[\frac{\mathrm{d}F_z(0)}{\mathrm{d}z}-\frac{1}{R_0}\frac{\mathrm{d}v_c^2(R_0)}{\mathrm{d}R}\right] \tag{1.42}$$

and the surface density at a height z above the plane is (e.g., Binney & Merrifield, 1998)

$$\Sigma(R_0,z) = 2\int_0^z \mathrm{d}z'\rho(R_0,z') \tag{1.43}$$

$$= -\frac{1}{2\pi G}\left[F_z-\frac{z}{R}\frac{\mathrm{d}v_c^2(R_0)}{\mathrm{d}R}\right]. \tag{1.44}$$

It is common for densities to be expressed in terms of the surface density because it involves one less derivative of the data. However, the volume density of dark matter is what is needed for WIMP experiments.

This method can yield estimates for the total surface density of the Galaxy below some height. In order to separate the contributions from disk and halo matter, it is necessary to fit disk and halo models not only to the tracer data, but to the Galactic rotation curve. One can then ask: Is the density in the disk consistent with star and gas counts in the Galactic disk? What halo models are consistent with both types of data, and what do these imply for the local WIMP volume density ρ_{WIMP}? Holmberg & Flynn (2000, 2004) demonstrate that the dynamical estimate for Σ_{disk} is consistent with star counts and gas content in the solar neighborhood. This indicates that it is unlikely that there is much (if any) dark matter confined to a disk in the Milky Way. Bergström et al. (1998b) fit a variety of N-body inspired spherical halo models to the Galactic rotation curve, using a variety of disk models constrained by dynamical estimates of the disk surface density, to determine plausible ranges for ρ_{WIMP}. They find that WIMP mass densities $\rho_{\mathrm{WIMP}} = 0.2 - 0.8$

GeV cm^{-3} are consistent with the dynamical data. The value $\rho_{\rm WIMP} = 0.3$ GeV cm^{-3} is considered the canonical value but there is at least a factor of several uncertainty in this parameter. It is very unlikely that $\rho_{\rm WIMP} = 0$ (Kamionkowski & Koushiappas, 2008).

The uncertainty in the direct and indirect detection rates is simple to compute. A factor of 4 separates the lower and upper bounds of the local dark matter density. Therefore, since the direct detection rate is proportional to the density, there is a factor of 4 uncertainty in the direct detection rate for a given WIMP mass and cross section. Since the indirect detection rate goes as the density squared if the capture and annihilation rates are not in equilibrium in the Earth, the uncertainty in the dark matter density yields a factor of 16 uncertainty in the indirect detection rate.

Dark Matter Velocity Distribution

It is impossible to glean information about the velocity distribution of WIMPs directly from observations. Instead, one must deduce the velocity distribution from self-consistent equilibrium models of the halo distribution function. Unfortunately, quite different distribution functions can yield similar spatial distributions of matter (see Chapter 4 in Binney & Tremaine, 1987). It is necessary to examine cosmological N-body simulations of the formation of Milky Way-sized halos, and hope that these simulated halos are close enough to the actual Milky Way halo for results to be transferable, and that the poorly understood effects of baryonic infall do not grossly change the dark matter distribution.

In order to understand the effects of mergers on the velocity distributions within a halo, Helmi et al. (2002) perform a dark matter-only N-body simulation of a cluster-sized halo. To make the comparison with a Milky Way-mass halo, they simply scale the whole simulation down. They find that the velocity distribution of dark matter particles is the result of hundreds of thousands of overlapping tidal streams. At the solar circle, this velocity distribution is well described by a multivariate Gaussian except at the highest speeds. The simulations of Moore et al. (2001) of a Local Group-type halo also indicate that dark matter at the solar circle can be approximately described as having a Gaussian velocity distribu-

tion. Both groups suggest that the velocity ellipsoid at the solar circle is approximately isotropic. The effects of velocity anisotropy on direct detection rates have been examined, e.g., by Green (2002). In general, the effect of anisotropy on exclusion limits is fairly small. However, the biggest differences in the differential event rate $\mathrm{d}R/\mathrm{d}Q$ among the models occur for small Q. Therefore, Green (2002) has suggested that low threshold experiments will be more sensitive to, or the analysis complicated by, velocity anisotropy.

Substructure

There are two types of dark matter substructure that potentially have a significant impact on WIMP detection rates and their interpretation. The relatively more concretely established type of substructure consists of hierarchically grown subhalos which have been accreted by the Milky Way. Several groups have simulated Milky Way-mass (or clusters scaled to match the Milky Way mass) halos at high resolution in order to track the accretion and evolution of very small subhalos within the Galaxy. In order to understand the results of the simulations, it is necessary to introduce several scales. Our Galaxy is thought to reside in a halo of mass $M_{\mathrm{dm}} \approx 2 \times 10^{12}$ $\mathrm{M}_{\odot}$ with a virial radius $r_{\mathrm{vir}} \approx 200 - 400$ kpc. The Sun is located a distance $R_{\odot} \simeq 8$ kpc from the Galactic center (see Section 7.4.1 in Binney & Merrifield, 1998, and references therein). Therefore, substructures that may be observable by either direct or indirect detection lie within the inner 5% of the virial radius. Of the various simulations to be discussed below, Diemand et al. (2007) can resolve subhalos of $M_{\mathrm{sub}} = 4 \times 10^{6}$ $\mathrm{M}_{\odot}$ $(= 2 \times 10^{-6} M_{\mathrm{dm}})$ and Moore et al. (2001) can identify $M_{\mathrm{sub}} = 10^{8}$ $\mathrm{M}_{\odot}$. Helmi et al. (2002), who simulate a cluster and rescale results to the Milky Way, can identify parent halos down to $M_{\mathrm{sub}} = 10^{5.5}$ $\mathrm{M}_{\odot}$.

None of the simulations above show much evidence of substructure within the solar circle. Diemand et al. (2007) find five subhalos with maximum circular velocities (a proxy for the pre-accretion mass of the subhalo, since a substantial fraction of the original mass is tidally stripped, but the maximum circular velocity remains relatively unchanged) of > 10 km s^{-1} inside $r < 0.1 r_{\mathrm{vir}}$. However, this group suggests that the true number of subhalos within

$0.1r_{\rm vir}$ could be significantly higher due to the finite resolution and large force softening length, which wash out substructures in dense environments (Moore et al., 1996; Taylor & Babul, 2005). This phenomenon of "overmerging" is also cited as contributing to the lack of substructures in the innermost parts of the Moore et al. (2001) and Helmi et al. (2002) simulated galaxy halos. It should also be noted that the number of halos with mass above the subhalo resolution threshold goes as $N(M_{\rm sub} > M_{\rm thresh}) \propto M_{\rm sub}^{-1}$, in which case both the number of subhalos and the mass in subhalos diverge as $M_{\rm sub} \to 0$ (Diemand et al., 2007). Thus, it is possible that there is significant substructure within the solar circle, but it has yet to be properly simulated.

Substructures are relevant for direct and indirect detection in the following ways.[3] First, one can think of dark matter in the solar circle as having *smooth* and *lumpy* components. If the smooth fraction is large relative to the lumpy fraction, then the signal in both types of experiments is dominated by the smooth component. Any signal from the lumpy component depends on the number density, mass, and size of such structures along the Sun's orbit, and whether the solar system happens to be inside a lump, or not. As the smooth fraction decreases, the density of dark matter in the solar system will become increasingly stochastic. The direct detection rate is sensitive to the real-time density of dark matter at the Earth, averaged at most over several years. Therefore, if dark matter is extremely clumpy, chances are that direct detection experiments will see nothing, with a small probability that there will be a huge signal. The case of indirect detection is more complicated. The capture rate will be a function of time, thereby changing the solution of the annihilation rate from its constant C form, Eq. (1.23). However, the neutrino-induced muon rate is governed by the capture and annihilation rates on timescales of the age of the solar system. Therefore, naively one would expect that the indirect detection rate should be largely insensitive to the presence of lumps, although Kamionkowski & Koushiappas (2008) suggest that the signal may be boosted since the subhalos will be far denser than the local smooth dark matter

[3]This discussion refers only to unbound halo WIMPs. Substructure has almost no effect on the distribution of bound WIMPs to be discussed below in Section 1.4 since the long lifetime of bound WIMPs means that the distribution is sensitive only to the time-averaged properties of the halo WIMP population.

density.

An interesting source of dark matter substructure has its origins near the Big Bang itself. Recall from Section 1.1.1 that the smallest dark matter structures to form in the universe are of order the free-streaming scale at the time of matter-radiation equality. This is due to the fact that dark matter density perturbations cannot grow until the universe becomes matter-dominated and that density perturbations on scales below the free-streaming length get washed out. One can therefore ask, what is the smallest dark matter halo that can form assuming a SUSY or Kaluza-Klein WIMP? Using linear perturbation theory, several authors calculated the dark matter power spectrum at scales near the free-streaming scale assuming SUSY physics (plus a standard spectrum of primordial fluctuations), and determined that the power spectrum sharply cuts off at mass scales of approximately the Earth mass $M_\oplus$ (Hofmann et al., 2001; Berezinsky et al., 2003; Green et al., 2004, 2005). This implies that the first non-linear objects (i.e., the smallest and first dark matter halos) should also have masses of order $M_\oplus$. Loeb & Zaldarriaga (2005) found that the acoustic oscillations in the photon-baryon fluid also suppress the dark matter power spectrum on small scales, effectively increasing the minimum possible halo mass by a factor of a few. Another unique feature of these "microhalos" is that they form almost monolithically, not hierarchically, over several orders of magnitude in mass. This is because the condition for a perturbation to collapse is related to $\sigma(M)$, the rms density fluctuation in linear theory, which usually is larger at smaller M. However, near the low-mass cutoff of the dark matter power spectrum, $\sigma(M)$ is nearly independent of M.

The formation of the first halos has also been studied with N-body simulations (Diemand et al., 2005, 2006). One simulation focused on "average" parts of the universe, simulated from $z = 350$ to $z = 26$ (Diemand et al., 2005). The authors of this simulation found that about 5% of the dark matter was contained in Earth-mass microhalos by $z = 26$, in good agreement with analytic work. They also consider how many subhalos exist in the Milky Way halo by extrapolating the $z = 0$ subhalo mass function down to masses $M_{\rm sub} = 10^{-6}$ M$_\odot$, the mass of the smallest microhalos, neglecting any tidal disruption of

the smallest halos. Using this extrapolation, they find a whopping 10^{15} subhalos in the Milky Way at a density of $n_{sub} = 500$ pc^{-3}, with approximately half of the dark matter residing in subhalos. It is expected that Earth hits a microhalo approximately every 10^4 yr, and spends about 50 yr passing through the halo. Therefore, the Earth is in a microhalo about 0.5% of the time, and during this period the WIMP number density is increased by a factor of ≈ 100 (assuming that the virial density of a microhalo forming at $z = 60$ is 200 times the critical density at that time, and assuming that $H_0 = 70$ km s^{-1} Mpc^{-1}).

The critical issue for direct detection experiments, which are sensitive to fluctuations of dark matter flux on scales $\lesssim 1$ yr, is how many of these microhalos survive at the solar circle. There are several means of disrupting microhalos. Microhalos may be disrupted in the era of the nearly simultaneous (monolithic) halo formation across mass scales. Diemand et al. (2006) identify an unusually overdense fluctuation at high redshift (with initial conditions set by the power spectrum of Green et al., 2004), which they simulate at high resolution to $z = 75$. At the end of the simulation, the halo has a mass $M_{\rm halo} = 0.01$ M$_\odot$, several orders of magnitude larger than the smallest halos. Because this halo grew so rapidly, instead of the more leisurely accretion of later times, $20 - 40\%$ of the subhalos have disintegrated by $z = 75$. Various authors have examined microhalo mass loss at later times (Zhao & Silk, 2005; Berezinsky et al., 2006; Angus et al., 2007; Goerdt et al., 2007; Green & Goodwin, 2007), focusing on mass loss or disruption by stars and dark matter substructure. Since it is impossible to run a full N-body simulation across the $\sim 10^{18}$ orders of magnitude between the microhalo and Milky Way masses, these authors instead focus on trial orbits through the Galactic potential, and use the impulse approximation to treat microhalo-stellar encounters. There are some discrepancies among the treatments, but it is generally found that most of the mass is stripped from microhalos. The very centers of the microhalos, being extremely dense, may survive at the solar circle to the present. However, it is not clear how much additional stripping occurs in the process of hierarchical structure formation, and it is not clear how realistic or accurate the predictions from analytic models of stripping are.

There are several major consequences of the work on microhalo disruption. Assuming

that the authors are correct that most of the microhalo mass is stripped at the solar circle, the lumpy fraction of dark matter is not large. Therefore, the direct detection signal is largely immune from any large fluctuations in signal due to microhalo lumpiness. However, when microhalos lose mass or become completely disrupted, they leave tidal streams. These streams can retain their filamentary morphology for > 4 Gyr (the maximum time that Angus & Zhao, 2007, follow microhalos in the Milky Way), and are quite dynamically cold. It is not clear how much these streams will be heated on timescales of order the age of the universe, given the crudeness of microhalo simulations (Angus & Zhao, 2007; Zhao et al., 2007). If the streams survive on long timescales, their filling fraction is thought to be $\gtrsim 5\%$ (Zhao et al., 2007). Therefore, it is possible that a large percentage of the dark matter at the solar circle consists of overlapping streams of dark matter. The small scale (sub-parsec) structure of the microhalo tidal stream could make it difficult to interpret dark matter properties, such as the WIMP mass, from the next generation of direct detection experiments (Green, 2007). This is due both to the uncertainty in the density enhancement as well as the unknown velocity of the streams in the halo.

1.3.2 Motion of the Earth in the Halo

The unbound dark matter distribution function at the Earth $f_\oplus$ can be written as a function of the halo distribution function f_{halo},

$$f_\oplus(\mathbf{x}, \mathbf{v}) = f_{halo}(\mathbf{v} + \mathbf{v}_\odot + \mathbf{v}_\oplus), \tag{1.45}$$

where $\mathbf{v}$ is a geocentric velocity, $\mathbf{v}_\odot$ is the Sun's velocity with respect to the Galactic center, and $\mathbf{v}_\oplus$ is the velocity of the Earth relative to the Sun. In this Section, I will outline estimates for the both the Sun's and Earth's motion, what the uncertainties are, and interesting implications of the Earth's motion.

The Sun's Motion About the Galactic Center

The Sun's motion about the Galactic center can be broken into two components: the circular motion of the LSR, and the peculiar velocity relative to the LSR (often simply

called "solar motion"). Methods for determining the motion of the LSR were summarized in the discussion on $\rho_{\rm WIMP}$. The best estimate for the local circular speed, adopted by the IAU, is $v_{\rm LSR} = 220 \pm 20$ km s^{-1} (Kerr & Lynden-Bell, 1986). The solar motion relative to the LSR can be estimated by measuring either the line of sight velocities or proper motions of stars in the solar neighborhood, since the mean velocity of a given population near the Sun should be zero relative to the LSR. Briefly, in the case of line of sight measurements (see Binney & Merrifield, 1998, for a more thorough discussion), the speed of a star in a given direction $\hat{\mathbf{x}}$ is

$$v_{\rm los} = (\mathbf{v} - \mathbf{v}_{\odot,{\rm pec}}) \cdot \hat{\mathbf{x}}, \tag{1.46}$$

so that the average line of sight speed for a population of stars is

$$\langle v_{\rm los} \rangle = -\mathbf{v}_{\odot,{\rm pec}} \cdot \hat{\mathbf{x}}. \tag{1.47}$$

Using data gathered with the *Hipparcos* space astrometry mission, a telescope specifically designed for precision astrometry, Dehnen & Binney (1998) estimated that the solar motion is

$$\mathbf{v}_{\odot,{\rm pec}} = (U, V, W) = (10.0 \pm 0.36, 5.2 \pm 0.62, 7.17 \pm 0.38) \text{ km s}^{-1}, \tag{1.48}$$

where U points radially inward toward the Galactic center, V is in the direction of Galactic rotation, and W points in the same direction as the north Galactic pole. How do the uncertainties in the solar velocity with respect to the Galactic center affect the interpretation of direct and indirect detection signals? In this discussion, I will focus on the direct detection rate, although since the calculation of the capture rate in the Earth has the same form as the integral over the differential direct detection rate, many of the results will be similar.

The effects of the uncertainty in the Sun's motion on the interpretation of direct detection experiments has been examined in detail by Green (2007). To illustrate her findings, it is useful to examine the form of ${\rm d}R/{\rm d}Q$ (Eq. 1.19) for a simple distribution function. As an example, one can use a Maxwellian distribution function

$$f_{halo}(\mathbf{x}, \mathbf{u}) = \frac{1}{(2\pi\sigma^2)^{3/2}} \frac{\rho_{\rm WIMP}}{m_{\rm WIMP}} e^{-\mathbf{u}^2/2\sigma^2}, \tag{1.49}$$

for the halo, with σ described by Appendix A (for the distribution function called f in Eq. A.4), and $\mathbf{u}$ the velocity in the Galactocentric frame. In heliocentric coordinates, the distribution function is

$$f_s(\mathbf{x}, \mathbf{v}) = \frac{1}{(2\pi\sigma^2)^{3/2}} \frac{\rho_{\mathrm{WIMP}}}{m_{\mathrm{WIMP}}} e^{-(\mathbf{v}+\mathbf{v}_\odot)^2/2\sigma^2}. \tag{1.50}$$

For illustrative purposes, I calculate $\mathrm{d}R/\mathrm{d}Q$ using this heliocentric expression well outside the gravitational well of the Sun, and without accounting for the Earth's orbital motion. The results should generalize to a more careful treatment of the distribution function. In Figure 1.15, I plot the ratio

$$\frac{\mathrm{d}F(v_\odot)}{\mathrm{d}Q} = \frac{\mathrm{d}R(v_\odot)/\mathrm{d}Q}{\mathrm{d}R(v_\odot = 0)/\mathrm{d}Q}, \tag{1.51}$$

the ratio of the differential event rate for a given value of the Sun's speed relative to the rate if the Sun were motionless with respect to the dark matter halo, for a variety of WIMP masses. One can see that the event rate is suppressed for small energy transfers, pushing signal into the higher energy bins. The slope of the event rate ratio increases with increasing $\mathbf{v}_\odot$. This is simply due to the fact that there are more high speed particles in the heliocentric frame, which can generate larger energy transfers. There is an approximate degeneracy between $v_\odot$ and m_{WIMP}. As demonstrated in Figure 1.15, the differential event curve for $m_{\mathrm{WIMP}} = 200 m_p$ and $v_\odot = 180$ km s^{-1} is similar to that of $m_{\mathrm{WIMP}} = 500 m_p$ and $v_\odot = 260$ km s^{-1}.

Therefore, if the true speed of the Sun about the Galactic center were 180 km s^{-1}, but the differential event rate data were analyzed using $v_\odot = 220$ km s^{-1} as a prior, one would systematically underpredict the WIMP mass. Green (2007) finds that the shift in WIMP mass relative to the Sun's speed can be described by

$$\frac{\Delta v_\odot}{v_\odot} = -\frac{\Delta m_{\mathrm{WIMP}}}{m_{\mathrm{WIMP}}\,(1 + m_{\mathrm{WIMP}}/m_A)}. \tag{1.52}$$

The effect of uncertainties in the Sun's speed for indirect detection is less clear, in large part because there is such a spread in possible branching fractions for WIMP annihilation modes at a given WIMP mass. It may not be possible to disentangle small errors in $v_\odot$ from

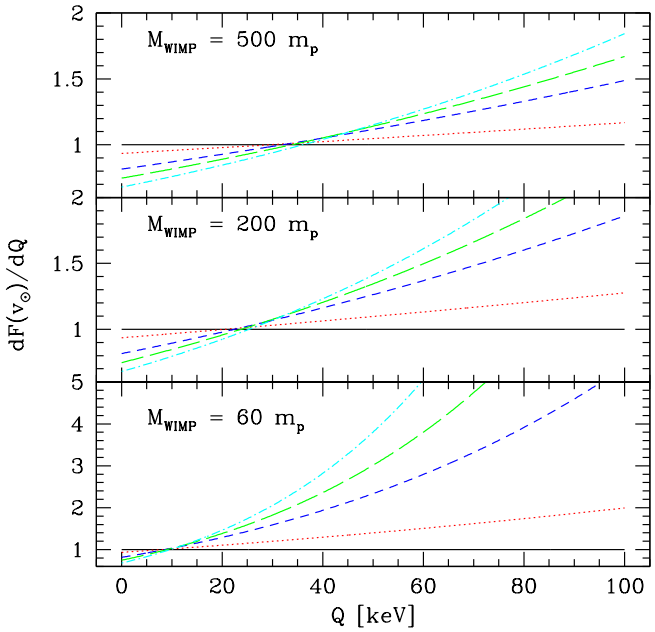

Figure 1.15: The ratio of the differential event rate $\mathrm{d}F(v_\odot)/\mathrm{d}Q$ for several choices of WIMP mass (in units of the proton mass), and for $v_\odot = 0$ (*black line*), $v_\odot = 100$ km s^{-1} (*red dots*), $v_\odot = 180$ km s^{-1} (*blue dash*), $v_\odot = 220$ km s^{-1} (*green long dash*), and $v_\odot = 260$ km s^{-1} (*cyan dot-dash*). The target mass is assumed to be ^{73}Ge.

$m_{\rm WIMP}$ unless the WIMP mass is near a value where an annihilation begins to be allowed, or unless there exists another method to determine $m_{\rm WIMP}$.

Because of the motion of the Sun, even an isotropic halo distribution function is anisotropic in the heliocentric frame. This means that extra care must be taken in transforming the distribution function into the geocentric frame. However, for calculations of the indirect detection rate, it is often sufficient to consider the angle-average of Eq. (1.50), since the indirect detection rate is sensitive to the integral of the capture rate over the lifetime of the solar system, while the period of the Sun's orbit about the Galactic center is ≈ 200 Myr. As will be discussed in Chapter 2, the angle-averaged distribution function is not quite equivalent to the time-averaged distribution function, but it is close.

The Earth's Orbit

While it is necessary to include the Earth's orbital motion when computing indirect and direct detection rates, it does not introduce much uncertainty in the distribution function, especially relative to the other complexities inherent in estimating the halo distribution. However, the short-period nature of the Earth's orbit leads to an annual modulation of the direct detection signal. As we saw in the discussion of the Sun's motion, changes in the magnitude of the Sun's speed lead to changes in the shape of the differential event rate. As the Earth moves about the Sun, its velocity vector changes its orientation with respect to the Sun's motion. When the two vectors are most closely aligned, the Earth has its maximum motion with respect to the dark matter halo; when the Earth's motion is roughly anti-aligned with the Sun's velocity, the Earth has its slowest speed relative to the Galactic center. Therefore, the expected differential direct detection rate is a function of the location of the Earth along its orbit. Freese et al. (1988) suggested that the annual modulation in the spectrum of event rates would be easier to detect than the absolute spectrum since the annual modulation could be detected in experiments that did not have good background discrimination.

Authors have investigated the effects of velocity dispersion anisotropy (e.g., Ullio &

Kamionkowski, 2001), uncertainty in the Sun's motion, and approximations of the Earth's orbit (Green, 2003) on the amplitude and phase of the annual modulation rate. This became a popular subject in the literature when the DAMA collaboration announced a detection of annual modulation (Belli et al., 2000; Bernabei et al., 2000b), which appeared to be in conflict with the exclusion limits of all other experiments running at the time. However, while all the effects listed above could significantly alter the phase and amplitude of the annual modulation signal, it has been impossible to reconcile the DAMA results with the other experiments unless $m_{\rm WIMP} \approx 10$ GeV (Ullio et al., 2001b; Savage et al., 2004; Gondolo & Gelmini, 2005). Since DAMA, the focus of direct detection experiments has been on event discrimination, an effort to determine the absolute differential event rate in analysis windows predicted to have little or no backgrounds.

1.4 Corrections to the Distribution Function: Effects Within the Solar System

Without scattering mechanisms, all dark matter particles are unbound to the solar system. There are, however, two types of scatters that may occur. Since WIMPs have a non-zero interaction with baryons, WIMPs can scatter elastically in the Sun, planets, or other baryonic matter such as dust. I call this "weak scattering." Since the Sun is by far the most massive reservoir of baryons, and has the deepest potential well, it will also scatter the most dark matter. Secondly, particles can be gravitationally captured into the solar system. Even though two-body gravitational interactions conserve energy, the energy of a particle will not generally be conserved as it traverses N-body systems with $N > 1$. If the newly bound particles have a long lifetime before being ejected or thermalized in the Sun, then they can provide a significant contribution to the low velocity phase space distribution function. Since, in particular, the indirect detection event rate is extremely sensitive to the number density of particles at low speeds, a correct calculation of these processes is vital. Up to the present, analytic approximations have been used to estimate the size of the bound

particle population. I review these approaches below.

1.4.1 Weak Scattering

If the Sun had no surrounding planets, dark matter particles that scattered elastically in the Sun would either be scattered onto orbits unbound to the Sun or would scatter onto bound orbits that quickly thermalize from repeated elastic scattering in the Sun. A WIMP detector located on the Earth's orbit would find a small signal due to particles that originally scattered onto Earth-crossing orbits, which survive for a characteristic time $t \sim P_{\rm WIMP}/\tau$, where $P_{\rm WIMP}$ is the characteristic WIMP orbital period and τ is the optical depth of the Sun. However, the Sun is not a lonely body in free space, but enjoys the company of 8 (as per the IAU) planets, as well as a number of moons, asteroids, comets, and dust. The planets influence the motion of WIMPs in the solar system by their gravity, and can significantly change the distribution function of bound WIMPs at the location of the Earth.

Damour & Krauss (1999) identified a secular mechanism for dramatically extending the lifetimes of some bound particles to the solar system. This mechanism is called "Kozai cycling." Kozai (1962) examined the Hamiltonian of a system with a central star M, an outer planet M' on a circular orbit, and an asteroid $m \ll M, M'$ with its orbit entirely interior to that of the outer planet. In order to walk through Kozai's argument, it is useful to introduce the Delaunay coordinates. In solar system dynamics, it is common to express the Hamiltonian not in the usual position and momentum coordinates $\mathbf{q}$ and $\mathbf{p}$, but in terms of the canonical Delaunay variables. The Delaunay momenta are

$$L = \sqrt{G_N M a} \tag{1.53}$$

$$G = L\sqrt{1-e^2} \tag{1.54}$$

$$H = G\cos I \tag{1.55}$$

for a particle with semi-major axis a, eccentricity e, and with an orbit inclined an angle I with respect to the reference plane, and in the limit that $M \gg M'$. Newton's constant is labeled as G_N. The momentum G is the magnitude of the particle's specific angular

momentum J/m, while H is the z-component of the specific angular momentum, with the z-direction defined as the direction orthogonal to the reference plane. The corresponding Delaunay coordinates are

$$l = n(t - t_0) \tag{1.56}$$

$$g = \omega \tag{1.57}$$

$$h = \Omega, \tag{1.58}$$

where $n = 2\pi/P$ is the mean motion of a particle with period $P = 2\pi\sqrt{a^3/G_N M}$, t_0 is the time of pericenter passage, ω is the argument of the pericenter (the angle between the pericenter and the intersection between the reference and orbital planes, the ascending node), and Ω is the longitude of the ascending node (the angle between a reference direction in the reference plane and the ascending node). A graphical description of the latter angles can be found in Figure 2.13 of Murray & Dermott (2000).

Kozai's observation was that if the Hamiltonian of this particular configuration of the three-body problem were averaged over the short period variables l of the planet and asteroid (i.e., averaged over both the mean motion of the asteroid and the planet), the Hamiltonian expanded to quadrupole order would be independent of both the l and the h coordinates if $a_{planet} \gg a$. Note that this sort of averaging can only be done if resonant or short timescale effects are unimportant. Since Hamilton's equations of motions for a Hamiltonian $\mathcal{H}$ with canonical coordinates $q_i,\ p_i$ are

$$\dot{q}_i = \frac{\partial \mathcal{H}}{\partial p_i} \tag{1.59}$$

$$\dot{p}_i = -\frac{\partial \mathcal{H}}{\partial q_i}, \tag{1.60}$$

this implies that L, also the particle energy E, is secularly conserved since the time-averaged Hamiltonian no longer depends on l. In addition, the momentum H is conserved since the time-averaged Hamiltonian is independent of h. The Hamiltonian will still depend on g, so the momentum G is not conserved. However, if the potential energy of the planet is expanded only to the quadrupole term, the asteroid Hamiltonian per unit mass has a

harmonic dependence on g, such that (cf. Fabrycky & Tremaine, 2007)

$$\begin{aligned}\mathcal{H} &= \left\{-\frac{G_N^2 M_\odot^2}{2L^2} - \frac{G_N^2 M_\odot M'}{8}\frac{L^4}{L'^3 G'^3}\left[5+3(H/L)^2\right]\right\} \\ &+\frac{3}{4}G_N^2 M_\odot M'\frac{L^2G^2}{L'^3G'^3} \\ &+\frac{15}{8}G_N^2 M_\odot M'\frac{L^4}{L'^3G'^3}\left[1-(G/L)^2-(H/G)^2+(H/L)^2\right]\sin^2 g,\end{aligned} \tag{1.61}$$

where the primed quantities refer to the planet. The first line of Eq. (1.61) contains the parts of the Hamiltonian that do not depend on G or g, the second line contains the part that depends on G but not g, and the last part of the Hamiltonian depends on both G and g. This Hamiltonian has some special features: above a critical inclination $I_{crit} \approx 39.2^o$, solutions exist for librations in g, not just circulation. There are also unstable fixed points at $e = 0$ and $g = \pm\pi/4, \pm 3\pi/4$. While G can oscillate cyclically in circulating solutions of $\mathcal{H}$, generally the large oscillations in G occur if g is librating about a fixed point. Therefore, asteroids will high eccentricity can cycle through much smaller values. Since H is conserved, the cycles in eccentricity are accompanied by oscillations in the inclination of the orbital plane.

Damour & Krauss's idea was to apply the idea of Kozai cycles to particles captured in the Sun. Any particle on a Kozai cycle survives much longer because during most of a Kozai cycle the perihelion is larger than the solar radius. In particular, they applied this idea to particles that initially scattered in the outer parts, $r > 0.5R_\odot$ of the Sun. The reasons for focusing on this region were twofold, but both follow from the fact that the mass of the Sun is very centrally concentrated ($M(r = 0.5R_\odot) = 0.9M_\odot$). This means, for one, that perihelion precession is fairly slow in the outskirts of the Sun, so it does not kill the Kozai cycles, which require a near-Keplerian potential. Secondly, because the density of solar matter is substantially lower in the outer part of the Sun, the optical depth is also much lower in the outer layer of the Sun than it is near the center. This means that the survival time is much higher for particles that only pass through the outer part.

Damour & Krauss (1999) estimate the bound dark matter distribution function in the following way. First, they focus only on particles on Kozai cycles with initial scatters at

$r > 0.55R_\odot$ up to semi-major axis $a < 2.6$ AU. This upper bound is set by the orbit of Jupiter, which is on an approximately circular orbit of $a_J = 5.2$ AU. Since $e \approx 1$ for Earth-crossing orbits which originate in the Sun, any captured particle with $a(1+e) \simeq 2a > a_J$ will cross Jupiter's orbit. All Jupiter-crossing orbits are ignored because they are likely to be short-lived, as are all particles which initially scatter at $r < 0.55R_\odot$. All particles initially scattered in the outskirts of the Sun on orbits for which the perihelion never exits the Sun are also ignored. To find out how many particles can exit the Sun, Damour & Krauss add a term to the Hamiltonian, Eq. (1.61) to represent the perturbation due to the non-Keplerian nature of the Sun. This term is a function of G^2 (see their Section 3). They use this Hamiltonian to determine for an initial semi-major axis, inclination, and eccentricity (or G) if the particle remains in the Sun (i.e., G always remains below some critical value) or if G may become large enough to exit the Sun. If the particle can exit the Sun, it may either have circulating or librating g. Since the initial eccentricity is so great, even circulating solutions will have relatively large oscillations in G (see their Figure 1).

Next, they assume that all particles on Kozai cycles (circulating or librating) survive at least the lifetime of the solar system without rescattering in the Sun onto non-Earth-crossing orbits. This is assumed regardless of the strength of the WIMP-nucleon interaction. The velocity distribution of these dark matter particles in the geocentric frame is estimated by weighting the initial distribution of semi-major axes by the probability that the particle is Kozai-cycling and the time a particle with initial eccentricity e spends between r and $r + \mathrm{d}r$ centered on $r = 1$ AU.

Given these assumptions, Bergström et al. (2001) estimate the geocentric velocity distribution to have the form of Figure 1.16 with $\lambda = 1$, the case for which the z-component of angular momentum is exactly conserved (see Bergström et al., 1999, for details on λ and calculations). The upper and lower cutoffs to the distribution are fairly straight-forward to understand. The lower velocity cutoff arises from particles that just barely are Earth-

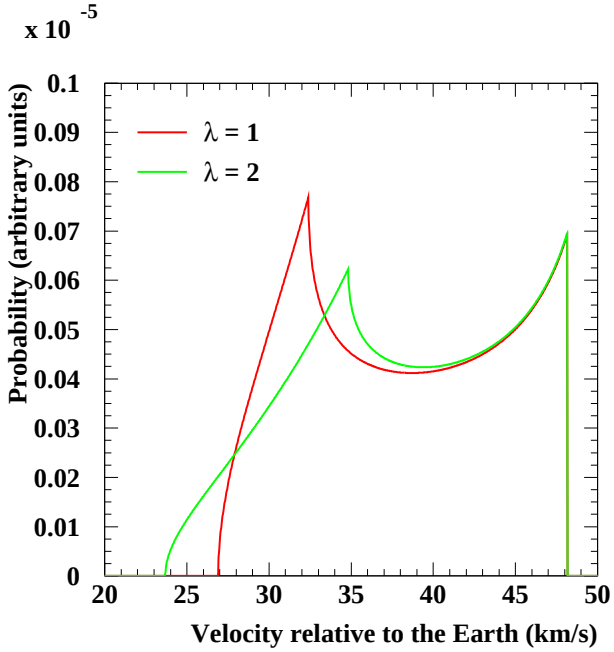

Figure 1.16: The estimated geocentric distribution function for Kozai-cycling dark matter particles. The case of $\lambda = 1$ corresponds to absolute conservation of H. In the case of $\lambda = 2$, Bergström et al. (1999) allow small variations in H. This figure is originally from Bergström et al. (2001). The version of this plot resulting from my simulations is shown in Figure 5.2.

crossing, $a = 0.5a_\oplus$. The heliocentric speed of a particle with semi-major axis a is

$$v(a) = \left[2 - \left(\frac{a}{a_\oplus}\right)^{-1}\right]^{1/2} v_\oplus. \tag{1.62}$$

This means that the heliocentric speed for a particle of $a = 0.5a_\oplus$ is $v(0.5a_\oplus) = 0$. Transforming to the geocentric frame, $v_g(0.5a_\oplus) = v_\oplus \approx 29.8$ km s^{-1}. The upper limit is set by the upper limit of the semi-major axis range, $a = 2.6a_\oplus$. The heliocentric speeds of these particles is $v(2.6a_\oplus) = 1.27v_\oplus = 37.9$ km s^{-1}. Since the orbits are initially radial, the geocentric speed is $v_g(2.6a_\oplus) = \left[v_\oplus^2 + v^2\right]^{1/2} = 48.2$ km s^{-1}.

This population of bound WIMPs makes only a modest contribution to the direct detection rate, but could dominate the indirect detection rate. Damour & Krauss (1999) state that the bound particles can double the direct detection signal for large WIMP-nucleon cross sections. However, most of the large spin-independent cross sections they considered

have been excluded since the appearance of the original Damour & Krauss paper. The consequences for indirect detection are more extreme since all the bound particles populate a fairly narrow region of phase space. Bergström et al. (1999) found that the bound population could increase the neutrino-induced muon rate by a factor of 100 for WIMP masses $m_{\rm WIMP} = 60 - 130$ GeV, with the mass range corresponding to the upper and lower limits of WIMP speed in the geocentric frame, using Fig. 1.14 to translate between mass and velocity limits for capture in the Earth.

Given these tantalizing results, it is essential to do a careful calculation of the bound WIMP distribution function at the position of the Earth. There are several reasons why the Damour & Krauss (1999) calculation is incomplete. (i) They do not consider the effects of rescattering in the Sun. This means that they likely overestimate the Kozai-cycling population. (ii) The translation between the identification of particles on Kozai cycles and the distribution function is somewhat suspect. In both Damour & Krauss (1999) and Bergström et al. (1999), the distribution function is estimated by assuming that the bound particles only cross the Earth's orbit (or rather, anywhere on the spherical shell with $r = 1$ AU) with the eccentricity from the initial scatter. However, the Kozai cycles allow the orbital plane of the particles to intersect the plane of the Earth's orbit with different I and e than their original values. Given that a is conserved in the secular approximation, the heliocentric speed of the particles does not change, but the arrival directions may. If H is exactly conserved, then the particle speed in the direction of the Earth's motion is conserved, so changes in the arrival direction will always be orthogonal to the Earth's motion. Therefore, the geocentric speed is independent of the Kozai-cycling particle arrival direction. However, Damour & Krauss (1999) and Bergström et al. (1999) weight the distribution function by the time a particle spends between r and $r + {\rm d}r$. The time a particle spends in that annulus depends on the particle direction with respect to the radial. If a particle's eccentricity is modulated by the Kozai cycles, then the orbit of the particle may be significantly non-radial when it intersects the Earth's orbit, which increases the time the particle spends in the annulus between r and $r + {\rm d}r$. Another consequence of the change in arrival direction is relevant

for those particles with $a \rightarrow 2.6a_{\oplus}$. For particles with relatively large semi-major axis, the approximation that H is conserved is no longer very good. Therefore, the geocentric speed distribution will be smeared. If the speeds get smeared to lower values, then the indirect detection rate will increase for more massive particles.

There are a few more questions about bound particles. First, how will the presence of resonances affect the Kozai cycles? In addition, how important are Jupiter-crossing particles? Particles that approach Jupiter can experience large changes to their orbital elements, and can reach parts of the geocentric phase space that are simply not accessible by particles with small semi-major axis. Thirdly, how important are the bound particles that have small semi-major axes but are not on Kozai cycles? This is important because far more particles scatter in the volume $r < 0.5R_{\odot}$ than outside that radius. One would also like to examine how the resulting distribution function depends on the particle physics model for dark matter. In particular, it is important to determine if the bound dark matter distribution function depends on the mass, strength or type of the WIMP-nucleon cross section.

The only way to really understand this problem is to simulate large numbers of orbits in the solar system. The Damour & Krauss (1999) and Bergström et al. (1999) results are intriguing, enough so that a more thorough examination of WIMPs bound to the solar system by weak scattering in the Sun is necessary.

1.4.2 Gravitational Scattering

The original work on gravitational capture in the solar system was done by Gould (1991). In this paper, Gould observed that, when a particle undergoes a close gravitational scatter with a planet, its speed relative to the planet does not change as a result of its interaction, but its angle with respect to the direction of motion of the planet does. Transforming back to the heliocentric frame, this means that the particle's speed does change. The interaction with the planet can bind or unbind the particle with respect to the Sun. Gould estimated that Jupiter could rapidly "diffuse" unbound particle orbits to bound orbits, reaching equilibrium after only a few million years by altering the planet-centric directions of the particles.

He then stated that the other planets in the solar system, but Venus and Earth in particular, could then "diffuse" those bound orbits into other regions of the velocity phase space. He concluded that the resulting geocentric velocity distribution of dark matter particles would not be noticeably different from the velocity distribution in free space. In other words, if $f_s(\mathbf{v}_\infty)$ is the distribution function of particles with velocity $\mathbf{v}_\infty$ with respect to the Sun but outside its sphere of influence, and $\mathbf{v}$ is the speed of a particle with respect to the Earth and at the position of the Earth within the Sun's gravitational potential, then the distribution function at the Earth $f_\oplus(\mathbf{v}) = f_s(\mathbf{v})$.

However, Gould's argument was based on rough estimations of timescales and ignored any type of scattering in the Sun. Lundberg & Edsjö (2004) attempted to do a more careful calculation of the geocentric phase space density of dark matter particles. Instead of simulating particle orbits, they solved differential equations for the number density of particles in velocity space. They used estimates of the scattering probability with planets based on Gould (1988) and Gould (1991). In order to take into account scattering in the Sun, they solved the differential equations for the dark matter distribution function two different ways. In the first approach, they treated the Sun as a point mass and ignored all WIMP-nucleon scatters. In the second approach, they ran simulations of 2000 orbits in the solar system, and estimated the survival time of the particles as a function of geocentric velocity. However, an integration was stopped if the particle entered the Sun; this is the approximation that the Sun has infinite optical depth for WIMPs. In solving the differential equations for the density of particles at the Earth, orbits were removed with a frequency $\nu(\mathbf{u}) = 1/t_{surv}(\mathbf{u})$, where $\mathbf{u}$ is the geocentric velocity. In both the cases of the point-mass Sun and the infinite optical depth Sun, the only planets included in the differential equation solutions are Jupiter, Earth, and Venus. These planets are assumed to be on circular orbits about the Sun.

Lundberg & Edsjö (2004) state that they have confirmed Gould's claim that the geocentric velocity distribution looks like the free space distribution function if the Sun is a point mass, and that the distribution function reaches equilibrium in about 500 Myr. There is

actually a very low velocity cutoff in the distribution function at $u = 2.5$ km s^{-1}, which is the lowest speed to which Venus can scatter particles. If the calculation had included Mercury or the eccentricities of the planets, the cutoff speed would have been lower. Lundberg & Edsjö find that the distribution function in the optically thick Sun calculation is highly suppressed with respect to that of the point mass Sun solution (see their Figure 14). Therefore, the neutrino-induced muons from WIMP annihilation in the Earth will not be observable by the next generation of km^3-scale experiments. This conclusion from the infinite optical depth Sun calculation is widely cited in particle astrophysics literature.

There are several shortcomings with this approach and the interpretation of implications for neutrino telescopes. (i) The calculations ignore any and all mean motion resonances or secular effects that may occur in the solar system. (ii) Since Lundberg & Edsjö (2004) assume that perihelion precession is much faster than, for example, the rate of change of the inclination of the orbit, Kozai cycles cannot be modeled. As noted in the discussion of WIMPs captured in the Sun through weak interactions, particles on Kozai cycles can have a potentially large effect on the dark matter distribution function. (iii) Lundberg & Edsjö (2004) model the Sun as either having an optical depth of zero or an infinite optical depth. In reality, the optical depth of the Sun to WIMPs will depend on the strength and type of the WIMP-nucleon cross section. In fact, it may even be possible to distinguish among particle physics models based on the low-velocity distribution function. Therefore, it would be quite nice to be able to predict the distribution function as a function of WIMP mass and cross section.

As in the case of WIMPs captured in the Sun, in order to make robust predictions of the bound WIMP velocity distribution, it is necessary to simulate orbits in the solar system with an appropriate treatment of scattering in the Sun.

1.5 This Approach

The approach of this thesis is to estimate the bound dark matter distribution function resulting from both gravitational and weak scattering by numerically tracing particle orbits

in the solar system, including a proper treatment of scattering in the Sun. Only by tracing the orbits of a statistically significant number of particles can one evaluate all the effects that may determine the bound WIMP population. The major reason why such a numerical approach has not yet been attempted is because the large samples of orbits need to be integrated for very long times to get an accurate statistical description of the distribution function. Moreover, typical orbits of bound WIMPs are challenging to follow numerically. For example, WIMPs scattered in the Sun initially have eccentricities $e > 0.995$. However, most integrators start to fail unless one goes to tiny time steps for $e > 0.9$. Also, it is necessary to integrate particle orbits through strongly non-Keplerian potentials. Finally, the numerical integrations must have no numerical dissipation over the lifetime of the solar system. A large percentage of the work in this thesis was devoted to developing fast methods to integrate particle orbits.

I focus on estimates of the bound dark matter population in a solar system that includes only the Sun and Jupiter (which is placed on a circular orbit). This simplification speeds up the calculations and makes them easier to interpret. Moreover, one advantage of this circular three-body problem is that there is a constant of motion, the Jacobi constant. This allows for an easy check on the code stability. For the simulations in this thesis, I also neglect weak scatters in Jupiter and treat it as having constant mass density.

Using this simplified model of the solar system, I estimate the bound dark matter distribution function, running separate simulations to evaluate the weak and gravitational components. In Chapter 2, I outline the particle physics model used for the simulations, as well as the WIMP masses and cross sections used. Fiducial models for the halo distribution function and other astrophysical quantities will be presented. I also discuss the choice for the initial conditions for the simulations, including arguments for the choice of those conditions. In Chapter 3, I will describe the integrator used for the orbit simulations. Even though the simulations are performed with only one planet, the integrator can be applied to multi-planet systems. Chapter 4 outlines how I turn the output of the simulations into distribution functions. Chapter 5 is the heart of the paper. In that chapter, I discuss the

results and the interpretation of the distribution functions. I also calculate the impact of bound dark matter particles on direct and indirect detection rates. Finally, in Chapter 6, I summarize the results of this thesis and conclude with some thoughts on future work.

Chapter 2

Initial Conditions

In this chapter, I will discuss the initial conditions for the simulations. First, I will discuss the choices of dark matter properties, as well as choices for astrophysical parameters. Secondly, I will describe how I select starting positions and velocities for the dark matter particles for both the weak and gravitational capture simulations.

2.1 Particle and Astrophysics Input

2.1.1 The Dark Matter Candidate

In order to perform the orbit simulations, it is necessary to specify some dark matter properties. The particle mass and elastic scattering cross sections completely determine scattering properties in the Sun, and hence, these are the only WIMP-dependent parameters necessary to run the simulations and find the WIMP distribution function at the Earth. Since different particle physics models can yield the same masses and elastic scattering cross sections, and different parts of parameter space within each particle physics model map to the same WIMP masses and elastic scattering cross sections, the particle physics model and parameter space within each model do not need to be specified for the simulations. In contrast, a specific particle physics model *is* needed to determine the neutrino-induced muon signal from capture and annihilation of WIMPs in the Earth, since the decay modes

and branching ratios are model-dependent. The masses and cross sections used in the simulations below are typical of supersymmetric models, but not UED models, since the latter models give much smaller event rates.

The goals of my simulations are to predict the direct and indirect detection signals from particles bound to the solar system (relative to the signal from unbound particles), to determine how such signals depend on WIMP mass and cross section, and to find the maximum signals consistent with current experimental constraints on WIMP properties. These goals constrain my choices for both the WIMP mass and the absolute and relative strengths of the elastic spin-independent and spin-dependent cross sections. I would like to consider WIMPs that have $m_{\rm WIMP} \lesssim 1$ TeV such that it is kinematically possible to scatter significant numbers of halo WIMPs onto bound Earth-crossing orbits via elastic scattering in the Sun. If the WIMP mass is much higher than 1 TeV, scattering onto bound orbits is significantly suppressed because of momentum and energy conservation (this will be demonstrated in the discussion about Eq. 2.33 in Section 2.2).

The relative strengths of the spin-dependent and spin-independent elastic scattering cross sections are important in the context of scattering in both the Sun and the Earth. For simplicity in interpreting the simulations, I would like to use either a spin-independent *or* spin-dependent cross section, but not a mixture of the two. I choose to focus on the spin-independent cross section for the simulations for the following reasons. First, for nuclei with even numbers of protons and neutrons, the spin of the nucleus is zero, and so the spin-dependent interactions are identically zero. Of the most common elements in the Sun, only hydrogen and nitrogen have non-zero spin, so only those elements can have a spin-dependent interaction. However, scattering on hydrogen is kinematically suppressed for even modest WIMP masses ($m_{\rm WIMP} \gtrsim 100$ GeV). In addition, if the spin-independent and -dependent WIMP-proton cross sections are equal, the spin-independent cross section will yield a much larger opacity in the Sun since the Sun contains heavy elements and the spin-independent cross section is a steeply increasing function of atomic number (see Appendix B). Therefore, unless the spin-dependent elastic scattering cross section is far larger (by a factor of $\gtrsim 100$

for hydrogen, although this depends on the WIMP mass) than the spin-dependent cross section, spin-independent interactions will dominate the scattering of WIMPs from the halo onto orbits bound to the Sun.

Secondly, in the case of capture in the Earth, spin-independent interactions will dominate unless the spin-dependent cross section is many, many orders of magnitude larger than the spin-independent interactions. This is due to the fact that the Earth largely consists of iron, which has even numbers of both neutrons and protons. There are only trace amounts of elements with unpaired protons or neutrons in the Earth. Therefore, in the simulations in this thesis, I focus exclusively on spin-independent interactions between WIMPs and nuclei, effectively setting $\sigma_p^{SD} = 0$.

However, with current constraints on the elastic scattering cross sections, it is possible that the spin-dependent interactions would dominate in the Sun. In the MSSM, there are regions of parameter space for which $\sigma_p^{SI} \ll \sigma_p^{SD}$, as well as regions for which $\sigma_p^{SI} \gg \sigma_p^{SD}$. Rather than carrying out a separate set of simulations for spin-dependent interactions, in Chapter 5 I scale the results from the spin-independent simulations to estimate the approximate distribution functions for the case of high spin-dependent cross sections.

At the time I started the simulations, the most recent constraints on the spin-independent cross section came from the CDMS collaboration (Akerib et al., 2006b), and so these constraints guided my choice of $m_{\rm WIMP}$ and σ_p^{SI} for the simulations. In the case of weak capture by the Sun, I wanted to explore the dependence of the bound distribution function on both mass and cross section. While the interest in the cross section is fairly obvious, the mass dependence is also important for at least three reasons: (i) Particles of different masses will have slightly different distributions following their first scatter in the Sun, with heavier particles tending to scatter onto more loosely bound orbits. (ii) The opacity in the Sun is a (weak) function of particle mass. (iii) Heavier particles will tend to require more scatters by the Sun before their orbits decay into the Sun, thereby extending the lifetime of Earth-crossing orbits of heavy WIMPs.

I chose to run four simulations with different choices of $m_{\rm WIMP}$ and σ_p^{SI}. The first

simulation, called "DAMA", used $m_{\rm WIMP} = 60$ atomic mass units (AMUs) and $\sigma_p^{SI} = 10^{-41}$ cm^2. These parameters lie in the DAMA annual modulation region (Belli et al., 2000; Bernabei et al., 2000b). A second simulation, called "CDMS", used the same WIMP mass as in the DAMA simulation but a cross section two orders of magnitude lower, $\sigma_p^{SI} = 10^{-43}$ cm^2, below the minimum of the CDMS exclusion curve (see Figure 2.1). Two more simulations were chosen to have $\sigma_p^{SI} = 10^{-43}$ cm^2 but with larger WIMP masses. The "Medium Mass" simulation uses $m_{\rm WIMP} = 150$ AMU, and the "Large Mass" simulation uses $m_{\rm WIMP} = 500$ AMU. The mass for the Medium Mass simulation was chosen so that its corresponding maximum speed for capture in the Earth lies just at the upper edge of the Kozai-cycle distribution function of Bergström et al. (1999, 2001, see also Figure 1.16). The Large Mass WIMP mass was selected to explore the dependence of the simulations on WIMP mass. The choices for $m_{\rm WIMP}$ and σ_p^{SI} are plotted in Figure 2.1 in addition to some recent direct detection results. The details on the initial conditions of the simulations are summarized in Table 2.1.

For the gravitational capture simulations, I used only one point in the $m_{\rm WIMP} - \sigma_p^{SI}$ plane, $m_{\rm WIMP} = 500$ AMU and $\sigma_p^{SI} = 10^{-43}$ cm^2, the same as in the Large Mass simulation. I only chose one point because for most plausible masses and cross sections, the distribution function of gravitationally captured particles is dominated by particles that either never entered the Sun or did so fairly infrequently, so the flux at the Earth would likely be almost independent of the mass and cross section. To check this assumption, I kept track of the total optical depth experienced by each particle on its trajectory and confirmed, once the simulation was over, that the WIMP-proton coupling had only a small effect on the distribution function of bound particles. The details on the initial conditions of the simulations are summarized in Table 2.2.

The spin-independent cross sections in these simulations arise naturally in large swaths of the MSSM parameter space. The spin-dependent and spin-independent cross sections in the simplest UED model are predicted to be much smaller than those I consider here, and, in particular, are too small for there to be appreciable capture in the Earth, even for dark

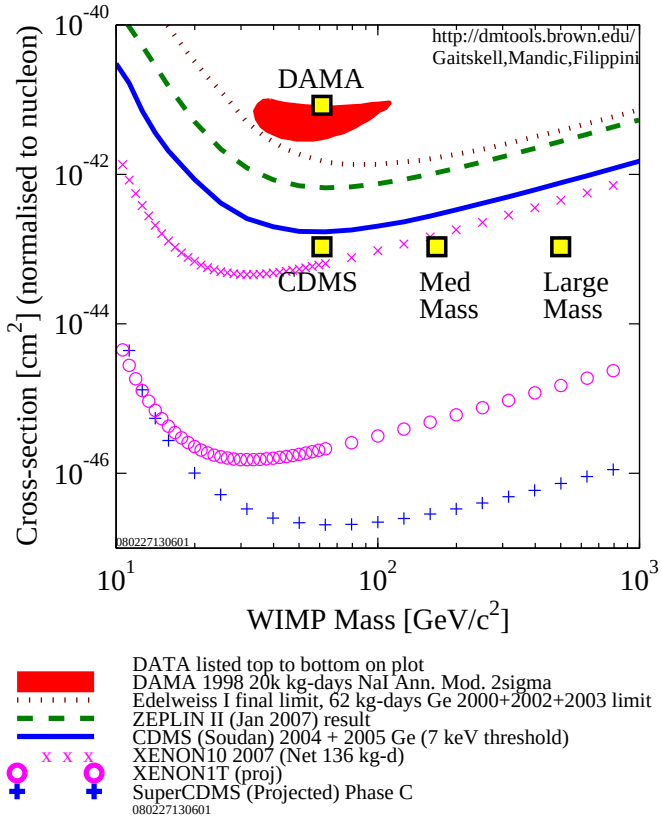

Figure 2.1: Points in the $\sigma_p^{SI} - m_\chi$ parameter space used for the weak scattering simulations, plotted along with exclusion curves from recent experiments. This plot was generated with the help of an interface available at:
http://dendera.berkeley.edu/plotter/entryform.html .

matter distribution functions as large as those predicted by Damour & Krauss (1999)–and I will demonstrate in Chapter 5 that the actual distribution functions of bound WIMPs are far smaller. Therefore, when I predict event rates in neutrino telescopes, I shall assume that the dark matter particle is the lightest supersymmetric particle (LSP) in the MSSM. For much of the MSSM parameter space, and for models that do not over-predict Ω_m, the LSP is the neutralino χ, the lowest mass eigenstate of the supersymmetric partners of the B, W_3, and Higgs bosons (see Jungman et al., 1996, and Chung et al., 2005, for reviews of the MSSM). The neutralino can take on a wide range of masses. Since the neutralino is a Majorana particle, it can have both spin-dependent (axial-vector) and spin-independent (scalar) elastic scattering interactions with baryonic matter.

For the rest of this thesis, I shall assume that the dark matter particle is a neutralino, even though, as previously stated, most of the results are independent of the nature of the dark matter particle. Thus, I will use m_χ instead of $m_{\rm WIMP}$ to denote the WIMP mass, and, in general, use χ subscripts instead of WIMP subscripts to indicate dark matter-related parameters.

To summarize, I run four sets of simulations of the evolution of dark matter particles captured from the halo by elastic scattering in the Sun, with various WIMP (neutralino) masses and spin-independent cross sections, setting the spin-dependent cross section to zero. I run one set of simulations of the evolution of dark matter particles captured by gravitational scattering by Jupiter, with the WIMP mass and cross section set to $m_\chi = 500$ AMU and $\sigma_p^{SI} = 10^{-43}$ cm^2. Even though I do not need to specify a dark matter model to run the simulations, supersymmetry provides the most natural particle physics model for which the simulations are relevant. Therefore, I employ the MSSM when predicting neutrino-induced muon event rates in neutrino telescopes. Descriptions of the forms of the elastic scattering cross sections appear in Appendix B.

2.1.2 The Halo Distribution Function

I adopt the Maxwellian distribution function

$$f_{\rm halo}(\mathbf{x},\mathbf{v}) = \frac{n_\chi}{(2\pi\sigma^2)} e^{-\mathbf{v}^2/2\sigma^2} \tag{2.1}$$

to describe the dark matter distribution function in the solar neighborhood in the frame of the halo and far outside the gravitational sphere of influence of the Sun. Here, σ is the one-dimensional dark matter velocity dispersion, set to $\sigma = v_\odot/\sqrt{2}$ (see Appendix A for explanation), and I set the speed of the Sun around the Galactic center to be $v_\odot = 220$ km/s. I do not include solar motion. The observational uncertainty in $v_\odot$ is about 10%. The WIMP number density is $n_\chi = \rho_\chi/m_\chi$. I assume that the dark matter density is smooth and time-independent in the neighborhood of the Sun, and that $\rho_\chi = 0.3$ GeV cm^{-3}. Even if the dark matter were somewhat lumpy, my results will still be valid if ρ_χ is interpreted as the average density in the solar neighborhood (Kamionkowski & Koushiappas, 2008), since I am interested in the long-term build-up of bound dark matter in the solar system.

I next translate the halo distribution function to an inertial frame moving with the Sun. Transforming to the heliocentric frame via a velocity transformation $\mathbf{v}_s = \mathbf{v} - \mathbf{v}_\odot$,

$$f_s(\mathbf{x},\mathbf{v}_s)\mathrm{d}^3\mathbf{x}\mathrm{d}^3\mathbf{v}_s = f_{halo}(\mathbf{x},\mathbf{v}_s+\mathbf{v}_\odot)\mathrm{d}^3\mathbf{x}\mathrm{d}^3\mathbf{v}_s \tag{2.2}$$

$$= \frac{n_\chi}{(2\pi\sigma^2)^{3/2}} e^{-(\mathbf{v}_s+\mathbf{v}_\odot)^2/2\sigma^2}\mathrm{d}^3\mathbf{x}\mathrm{d}^3\mathbf{v}_s. \tag{2.3}$$

This distribution is anisotropic in the frame of the Sun, and anisotropic with respect to the plane of the solar system (the ecliptic). The direction of the anisotropy with respect to the ecliptic depends on the phase of the Sun's orbit about the Galactic center. In order to avoid choosing a specific direction for the anisotropy (in other words, to avoid choosing to start our simulations at a particular *phase* of the Sun's motion about the Galactic center), I angle-average this anisotropic distribution function to obtain an isotropic distribution

function of the form

$$\bar{f}_s(x, v_s) = \frac{1}{4\pi}\int f_s(\mathbf{x}, \mathbf{v}_s) d\Omega \tag{2.4}$$

$$= \frac{1}{2}\int_{-1}^{1} \frac{n_\chi}{(2\pi\sigma^2)^{3/2}} e^{-(v_s^2+2v_s v_\odot \cos\theta + v_\odot^2)/2\sigma^2} d(\cos\theta) \tag{2.5}$$

$$= \frac{1}{2(2\pi)^{3/2}} \frac{n_\chi}{\sigma v_\odot v_s} \left[e^{-(v_s - v_\odot)^2/2\sigma^2} - e^{-(v_s+v_\odot)^2/2\sigma^2} \right]. \tag{2.6}$$

Using the angle-averaged distribution function is approximately valid for two reasons: (i) Scattering in the Sun is isotropic, so any bound WIMPs produced by elastic scattering will initially be isotropically distributed. (ii) The time-averaged distribution function (averaged over the Sun's $\approx$ 200 Myr orbit about the Galactic center) only has a small anisotropic component (Gould, 1988), a consequence of the large (60^o) inclination of the ecliptic pole with respect to the rotation axis of the Galaxy, and if the flux at the Earth is dominated by particles whose lifetime in the solar system is greater than the period of the Sun's motion about the Galactic center, the use of time-averaged distribution function is appropriate. I will discuss the lifetime distributions in depth in Chapter 5. This second argument holds whether the bound WIMPs are produced by gravitational capture or elastic scattering, but only if the WIMPs that dominate the distribution functions are long-lived ($\gtrsim 10^8$ yr).

I now determine how the Sun's gravity modifies the distribution function by using Liouville's theorem. Liouville's theorem states that in conservative systems, the phase space density does not change along a path. If I neglect the gravitational potential of the planets and the extremely rare interactions between dark matter particles, then each particle's energy E is conserved:

$$E = \frac{1}{2}v_s^2 \tag{2.7}$$

$$= \frac{1}{2}v^2 + \Phi_\odot(r), \tag{2.8}$$

where v is the speed of particle with respect to and in the gravitational sphere of influence of the Sun, and $\Phi_\odot(r)$ is the gravitational potential of the Sun ($\Phi_\odot = -GM_\odot/r$ for $r > R_\odot$, where $R_\odot$ represents the surface of the Sun). Thus, the distribution function within the

Sun's potential well is

$$f(r,v) = \bar{f}_s(r, v_s(r,v)), \tag{2.9}$$

$$v_s(r,v) = \sqrt{2\Phi_\odot(r) + v^2}. \tag{2.10}$$

An important consequence of this result is that the distribution function is identically zero for local velocities $v < \sqrt{-2\Phi_\odot(r)} = v_{esc}(r)$ below the escape velocity at that radius.

2.1.3 The Sun

The Sun is modeled as spherical and non-rotating. The gravitational potential and chemical composition are described by the BS(OP) solar model (Bahcall et al., 2005). I include the elements ^{1}H, ^{4}He, ^{12}C, ^{14}Ni, ^{16}O, ^{20}Ne, ^{24}Mg, ^{28}Si, and ^{56}Fe in computing the elastic scattering rate.

2.1.4 The Solar System

The solar system is modeled as having only one planet, Jupiter, since Jupiter has the largest mass of any planet by a factor of 3.3 and therefore dominates gravitational scattering. I place Jupiter on a circular orbit about the Sun, with a semi-major axis $a_J = 5.203$ AU, its current value, for the entire simulation, since its eccentricity is only $e \approx 0.05$ (Murray & Dermott, 2000), and the fractional variation in its semi-major axis is $\lesssim 10^{-9}$ over the lifetime of the solar system (Ito & Tanikawa, 2002). Jupiter is modeled as having constant mass density to simplify calculations of particle trajectories. This is not a realistic representation of Jupiter's actual mass density but only a small fraction of particles scattered by Jupiter actually penetrate the planet. WIMP-baryon interactions in Jupiter are neglected since the optical depth of Jupiter is small enough that the probability of even one scatter occurring in each simulation is significantly less than unity.

The orbit of Jupiter defines the reference plane for the simulation. The Earth's orbit is assumed to be coplanar with the reference plane, since the actual relative inclination of the two orbits is currently only 1.3°.

2.2 Weak Scattering in the Sun

The goal of this section is to compute the rate of elastic scattering of halo WIMPs by baryons in the Sun onto bound orbits, as a function of the energy and angular momentum of particles after the scatter. There are two natural approaches to this problem: (i) Sample the dark matter flux through a shell a distance $R < R_\odot$ from the center of the Sun, treating scatter in the Sun probabilistically, and keeping only those particles which scatter onto Earth-crossing bound orbits. (ii) Calculate the scattering probability in the Sun directly. The second approach is more efficient, and this is the one described below.

The dark matter distribution function f evolves in accordance with the Boltzmann equation, which has the form

$$\frac{\mathrm{D}f}{\mathrm{D}t} = \sum_A \Gamma[f, f_A] \tag{2.11}$$

$$= \Gamma_{tot}[f], \tag{2.12}$$

where $\mathrm{D}/\mathrm{D}t$ is the Lagrangian derivative in phase space, and $\Gamma[f, f_A]$ is the collision term for interactions involving dark matter and a nuclear species A in the Sun with a distribution function $f_A(\mathbf{x}_A, \mathbf{v}_A)$. In the case of elastic scattering of a dark matter particle on a nucleus A, the collision term has the form

$$\Gamma[f, f_A] = \int \mathrm{d}^3\mathbf{v}_A \mathrm{d}\Omega g_A \frac{\mathrm{d}\sigma_A}{\mathrm{d}\Omega} \left[f(\mathbf{x}', \mathbf{v}') f_A(\mathbf{x}_A, \mathbf{v}'_A) - f(\mathbf{x}, \mathbf{v}) f_A(\mathbf{x}_A, \mathbf{v}_A) \right], \tag{2.13}$$

where the WIMP has an initial velocity $\mathbf{v}$, the nucleus A has an initial velocity $\mathbf{v}_A$ such that the magnitude of the relative speed $g_A = |\mathbf{v} - \mathbf{v}_A|$, the final velocities of the dark matter particle and the nucleus are $\mathbf{v}'$ and $\mathbf{v}'_A$ respectively, and $\mathrm{d}\sigma_A/\mathrm{d}\Omega$ is the differential cross section, having the form of Eq. (B.7). The derivation of this collision term can be found in any statistical mechanics text (cf. Liboff, 2003), so I will focus on the meaning of the terms in Eq. (2.13) instead of its derivation. I start with the second term in Eq. (2.13), the one $\propto f(\mathbf{x}, \mathbf{v}) f_A(\mathbf{x}, \mathbf{v}_A)$. This describes the scattering of dark matter particles *out* of the phase space patch centered on $(\mathbf{x}, \mathbf{v})$, hence the minus sign in front of the term. The integral over $\mathbf{v}_A$ signifies that I consider scattering from all species A particles. The outgoing velocities

are specified by energy and momentum conservation and by the center-of-mass scattering angle Ω. The integral over Ω accounts for all possible center-of-mass scattering angles. Therefore, this term describes the scattering of dark matter particles out of the volume $(\mathbf{x}, \mathbf{v}; \mathbf{x} + \mathrm{d}\mathbf{x}, \mathbf{v} + \mathrm{d}\mathbf{v})$ by all possible interactions with particles of species A. The first term in Eq. (2.13) describes the inverse reaction, the rate of scatter of dark matter particles *into* the phase space volume centered on $(\mathbf{x}, \mathbf{v})$. I can take the integrals over $\mathbf{v}_A$ and Ω instead of $\mathbf{v}'_A$ and Ω' due to conservation of phase space volume in elastic interactions.

The kinetic energy of nuclei in the Sun is much less than the kinetic energy of dark matter particles. At the center of the Sun, the temperature is $T_c \sim 10^7$ K, so the average kinetic energy of a nucleus is of order

$$KE_A = \tfrac{3}{2} k T_c \tag{2.14}$$

$$\sim 1 \text{ keV}. \tag{2.15}$$

In the cooler outer layers of the Sun, the nuclei have even less kinetic energy. In contrast, the kinetic energy of dark matter particles in the Sun is of order

$$KE_\chi \sim m_\chi v_{esc}^2 \tag{2.16}$$

$$\sim 10^3 \left(\frac{m_\chi}{100 \text{ GeV}} \right) \text{keV}. \tag{2.17}$$

The scattering rate on hydrogen to bound orbits is unimportant in the cases where the WIMP-proton elastic scattering cross section is dominated by spin-independent interactions because of the large mass imbalance between neutralinos and hydrogen, so in this case the total scattering rate is dominated by the other, heavier species in the Sun. In Chapter 5, I will address the case in which the spin-dependent cross section dominates the total scattering rate in the Sun, in which hydrogen dominates scattering in the Sun. The rms velocity of the nuclear species A is $\langle v_A^2 \rangle^{1/2} = \sqrt{2KE_A/m_A} \approx 500 (m_A/\text{GeV})^{-1/2}$ km s^{-1}, much lower than the $\sim 10^3$ km/s speed of dark matter particles for nuclei heavier than hydrogen. Therefore, to good approximation, one can treat the baryonic species in the Sun as being at rest (i.e., having $T = 0$), so $g_A = v$ and

$$f_A(\mathbf{x}, \mathbf{v}_A) = n_A(\mathbf{x}) \delta^3(\mathbf{v}_A), \tag{2.18}$$

where $n_A(\mathbf{x})$ is the number density of species A. If I were simulating cases in which the spin-dependent cross section were much higher than the spin-independent cross section, it would be advisable to include the thermal velocity of the baryons in the Sun. Since I make the approximation that the Sun is spherical, I can further simplify Eq. (2.18) by stating that $n_A(\mathbf{x}) = n_A(r)$.

I can further simplify the collision term by restricting attention to scatters that place WIMPs on bound orbits. Particles that scatter onto hyperbolic orbits only have a small probability of intersecting the Earth as they stream through the solar system, while particles that scatter onto bound orbits can intersect the Earth's orbit many times before they are annihilated in the Sun or ejected from the solar system. The consequence of restricting our attention to bound particles is that the first term of Eq. (2.13), which describes particles scattering into the phase space volume centered on $(\mathbf{x}, \mathbf{v})$, can be ignored. The reason this term can be eliminated is that $\mathbf{v}'$ corresponds to a bound orbit, but the halo distribution function $f(\mathbf{x}', \mathbf{v}') = 0$ for bound orbits.

The constraint that the post-collision WIMP is bound can be expressed in terms of the incoming speed and the center-of-mass scattering angle. The initial energy of a dark matter particle is

$$E = \frac{1}{2} m_\chi v^2 + \Phi_\odot(r) \tag{2.19}$$

$$= \frac{1}{2} m_\chi \left[v^2 - v_{esc}^2(r) \right], \tag{2.20}$$

where I have expressed the gravitational potential in terms of the local escape velocity from the Sun. The final energy of the dark matter particle is

$$E' = E - Q \tag{2.21}$$

$$= \frac{1}{2} m_\chi \left[v'^2 - v_{esc}^2(r) \right], \tag{2.22}$$

where Q is the energy transfer between the dark matter particle and the nucleus during the collision. The energy transfer can be expressed in terms of the center-of-mass scattering angle θ as (cf. Eq. B.5)

$$Q(v, \cos\theta) = 2 \frac{\mu_A^2}{m_A} v^2 \left(\frac{1 - \cos\theta}{2} \right), \tag{2.23}$$

where

$$\mu_A = \frac{m_A m_\chi}{m_A + m_\chi} \tag{2.24}$$

is the reduced mass. The maximum energy transfer $Q_{max} = 2\mu_A^2 v^2/m_A$ occurs if the dark matter particle is back-scattered, i.e., $\theta = \pi$. Since I am interested in particles that scatter onto bound, Earth-crossing orbits,[1] the interesting range of outgoing energy is

$$-\frac{GM_\odot m_\chi}{2(0.5a_\oplus)} \leq E' \leq 0, \tag{2.25}$$

where $a_\oplus$ is the semi-major axis of the Earth's orbit, with the lower bound determined by the fact that the aphelion of a highly eccentric orbit is $2a$.

For a given incoming energy E, it may not be kinematically possible to scatter into the full range of bound, Earth-crossing orbits. In particular, if $E - Q_{max} = E'_{min} > 0$, the particle cannot scatter onto a bound orbit at all. Therefore, the lower bound on allowed outgoing energy is

$$E'_{min} = \max\left(-\frac{GM_\odot m_\chi}{2(0.5a_\oplus)}, \min(E - Q_{max}, 0)\right), \tag{2.26}$$

while the upper bound remains

$$E'_{max} = 0. \tag{2.27}$$

This restriction on outgoing energy can be translated into a restriction on the center-of-mass scattering angle for a given initial energy. Solving Eqs. (2.20), (2.21), and (2.23) for $\cos\theta$, I find

$$(\cos\theta)_{min,max} = 1 - \frac{m_A}{\mu_A}\frac{\frac{1}{2}m_\chi(v^2 - v_{esc}^2) - E'_{min,max}}{\mu_A v^2}. \tag{2.28}$$

[1] In principle, particles scattered to bound orbits with $a < a_\oplus/2$ could later evolve onto Earth-crossing orbits. However, the torque from Jupiter is never high enough to pull a particle with $a < a_\oplus/2$ onto an Earth-crossing orbit unless $((a_\oplus/2) - a)/a \lesssim 10^{-3}$. The inner planets could make a particle with an initially small energy migrate to Earth-crossing orbits if those planets were included in the simulation, but these have such small mass that their gravitational scattering is very weak. Moreover, each additional scatter in the Sun reduces the energy of the orbit in the limit of a cold Sun, so the semi-major axis may only shrink.

Using this expression and Eq. (2.13), I can express the scattering rate of particles onto bound, Earth-crossing orbits as

$$\begin{aligned}\frac{\mathrm{d}\dot{N}_{\oplus}}{\mathrm{d}r\mathrm{d}v\mathrm{d}\Omega} &= (4\pi)^2 \sum_A r^2 n_A(r) v^3 \frac{\mathrm{d}\sigma_A}{\mathrm{d}\Omega} f(r,v) \\ &\quad \times \Theta(R_\odot - r)\Theta[\cos\theta - (\cos\theta)_{min}]\Theta[(\cos\theta)_{max} - \cos\theta],\end{aligned} \tag{2.29}$$

where I have imposed spherical symmetry on the Sun, $f(x,v)$ is the distribution function in Eq. (2.9), and $\Theta(x)$ is the step function. This is the distribution I sample to obtain the energy and angular momentum distribution of the outgoing particles.

The energy distribution of scattered particles can be understood heuristically in the following way. One can change variables from the center-of-mass angle to the outgoing energy E' in two steps using Eqs. (2.21) and (2.23),

$$\mathrm{d}\Omega = 2\pi \frac{m_A}{\mu_A^2 v^2} \mathrm{d}Q \tag{2.30}$$

$$\mathrm{d}E' = \mathrm{d}Q. \tag{2.31}$$

Therefore, the outgoing energy is distributed uniformly unless there is kinematic suppression (see Eq. 2.29) in a particular energy range. The kinematic suppression is most pronounced for large WIMP masses and very negative energies because, in order for a particle to scatter onto a bound orbit,

$$v_s \leq 2\frac{\sqrt{m_\chi m_A}}{m_\chi - m_A} v_{esc}(r) \tag{2.32}$$

where v_s is the particle velocity at infinity. If $m_\chi \gg m_A$, then

$$v_s \leq 2\sqrt{\frac{m_A}{m_X}} v_{esc}(r), \tag{2.33}$$

so heavy dark matter particles can only scatter onto bound orbits if their velocities at infinity are only a small fraction of the escape velocity from the Sun a distance r from the Sun.

For energies for which the kinematic suppression is minimal, I can express the uniformity of $\mathrm{d}\dot{N}_{\oplus}/\mathrm{d}E'$ in terms of the semi-major axis. Since $E' = -GM_\odot/2a$ for particles on elliptical

orbits, $\mathrm{d}\dot{N}_\oplus/\mathrm{d}a \propto a^{-2}$, or

$$\frac{\mathrm{d}\log \dot{N}_\oplus}{\mathrm{d}\log a} = -1. \tag{2.34}$$

Therefore, most particles scatter onto relatively small orbits; only half of the particles on Earth-crossing orbits have $a > 1$ AU.

The angular momentum of each scattered particle is in the range $J \in [0, rv']$, where r is the radius from the center of the Sun at which the particle scatters. To determine the distribution of magnitudes and directions for the angular momentum, I assume that the direction of the final velocity $\mathbf{v}'$ is isotropically distributed with respect to the position vector $\mathbf{r}$. If I specify θ_v to be the colatitude of the velocity vector with respect to the position vector, and the magnitude of the angular momentum is $J = rv' \sin\theta_v$, then the distribution in angular momentum at fixed $\mathbf{r}$, $\mathbf{v}'$ has the form

$$\mathrm{d}\dot{N}_\oplus \propto \mathrm{d}\cos\theta_v = \frac{\mathrm{d}J^2}{2r^2v'^2\sqrt{1 - J^2/(r^2v'^2)}}. \tag{2.35}$$

The effect of kinematic suppression due to a large WIMP mass is that the particles that do scatter onto bound orbits can only do so close to the center of the Sun. This reduces the maximum angular momentum of the outgoing particle, and so eccentricity is an increasing function of WIMP mass.

2.3 Gravitational Scattering

The gravitational capture simulation consists of lobbing billions of dark matter particles at the solar system and observing how many stick, and for how long. In deciding how to arrange the initial conditions, it is useful to think about the flux of dark matter particles *into* a sphere of radius R centered on the Sun. The flux for our isotropic distribution function f is

$$\begin{aligned} F(R,v) &= 4\pi v^2 f(v_s(R,v)) \times \frac{1}{2} v \cos\theta \mathrm{d}\cos\theta & (2.36)\\ &= \pi v^3 f(v_s(R,v)) \mathrm{d}v \mathrm{d}(\cos^2\theta), & (2.37) \end{aligned}$$

where $\pi/2 < \theta < \pi$ is the angle between the velocity $\mathbf{v}$ and the position vector $\mathbf{R}$ for incoming particles, and v_s is the speed of the particle relative to the Sun but far outside its gravitational sphere of influence. Therefore, the total number of particles going inward through this spherical shell per unit time is

$$\dot{N}(R) = 4\pi^2 R^2 v^3 f(v_s(R,v))\mathrm{d}v\mathrm{d}(\cos^2\theta). \tag{2.38}$$

It is useful to express this rate in terms of the energy E and specific angular momentum J (i.e., angular momentum per unit mass) instead of v and $\cos^2\theta$. Given that

$$E = \frac{1}{2}v^2 + \Phi_\odot(R) \tag{2.39}$$

$$J = Rv\sin\theta, \tag{2.40}$$

I find (see also Press & Spergel, 1985)

$$\dot{N} = \pi f\left(\sqrt{2E}\right)\mathrm{d}E\mathrm{d}J^2. \tag{2.41}$$

Therefore, the number of particles going through any shell is independent of the radius of the shell for a given energy and angular momentum; this is to be expected since there is no loss mechanism between shells.

If I were to sample all particles that flow in towards the Sun, I would sample the energy according to to $f(\sqrt{2E})$ and the angular momentum to be uniform in J^2. However, by restricting the range of incoming particles that are sampled to those that could be scattered onto bound orbits, I can speed up the calculation.

To find the range of E (with respect to the Sun) for which particles might possibly be gravitationally scattered by Jupiter onto bound orbits, it is useful to think of gravitational capture in the following way. In the frame of the scattering planet, Jupiter, the particle speed does not change during the encounter, but its direction with respect to the direction of motion of Jupiter does. Therefore, if the particle has a velocity $\mathbf{v}$ with respect to the Sun before encountering Jupiter, it will have an initial speed with respect to Jupiter of $\mathbf{u} = \mathbf{v} - \mathbf{v}_J$, where $\mathbf{v}_J$ is the velocity of Jupiter with respect to the Sun. After encountering Jupiter, the particle will have a velocity $\mathbf{u}' = \mathrm{T}\mathbf{u}$, where T is a rotation matrix. Therefore,

the post-encounter velocity of the particle will be $\mathbf{v}' = \mathrm{T}\mathbf{u}' + \mathbf{v}_J$. For particles that were barely unbound to the solar system to begin with, it takes only a tiny deflection of the orbit to bind it to the solar system. However, for particles with increasingly higher energy with respect to the Sun, it takes an ever greater deflection by Jupiter to bind the particle.

In order to find an upper limit to the energy from which particles may be captured, consider the most extreme encounter possible. This is the case of a particle that has a tiny impact parameter with respect to Jupiter, and which has its initial velocity aligned with Jupiter's direction of motion. Therefore, the particle's velocity with respect to Jupiter is

$$\mathbf{u} = v - v_J, \tag{2.42}$$

where $v = |\mathbf{v}|$. The particle will be deflected through 180°, so that

$$\mathbf{u}' = -(v - v_J) \tag{2.43}$$

$$\mathbf{v}' = 2v_J - v. \tag{2.44}$$

The requirement that the particle is bound to the solar system after the scatter is equivalent to the statement

$$\left|v'\right| \leq \sqrt{2}v_J. \tag{2.45}$$

Therefore,

$$2v_J \leq v \leq (2+\sqrt{2})v_J, \tag{2.46}$$

or

$$(2-\sqrt{2})v_J \leq v \leq 2v_J, \tag{2.47}$$

and so

$$E_{max} \approx \frac{1}{2}\left(2+\sqrt{2}\right)^2 v_J^2 - \frac{GM_\odot}{a_J} \tag{2.48}$$

$$= 2\left(1+\sqrt{2}\right)v_J^2. \tag{2.49}$$

This corresponds to a speed outside the gravitational sphere of influence of the Sun of

$$v_{s,max} = 2\left(1+\sqrt{2}\right)^{1/2} v_J \tag{2.50}$$

$$= 41 \text{ km/s}. \tag{2.51}$$

In other words, no WIMP with a velocity far from the Sun that exceeds 41 km s^{-1} with respect to the Sun can be gravitationally captured.

I want to be able to check my simulation and analysis methods against something analytic. I choose to probe the energy range for which particles cannot be bound to the solar system ($E > E_{max}$) but may have geocentric speeds less than $v_{geo} < (\sqrt{2}+1)v_\oplus$, the range that overlaps the geocentric speed range of bound particles. Also, by simulating particles in that energy range, I will simulate all orbits with $v_{geo} < (\sqrt{2}+1)v_\oplus$. Even though the speeds of bound and unbound WIMPs may overlap if $v < (\sqrt{2}+1)v_\oplus$, the direction of the velocity with respect to the Earth depends on whether or not the particles are bound. In principle, if an experiment had directional sensitivity and one were most interested in the bound particles, it would not matter what the velocity distribution of halo WIMPs is. However, knowing the full distribution of particle speeds below this limit is important because most WIMP detectors (either direct or indirect) are insensitive to the direction of the WIMPs (see, e.g., Green & Morgan, 2008, for a list of the few experiments that do have directional sensitivity). The distribution function in the geocentric frame for these higher energy particles can simply be found using Liouville's theorem and appropriate Galilean transformations of the halo distribution function for the relevant energy range. The maximum speed an unbound particle can have with respect to the Sun and match v_{geo} in the frame of the Earth is $v_{max} = (\sqrt{2}+2)v_\oplus$, which occurs when the Earth's motion and the particle's motion are exactly aligned. Therefore, the maximum energy with respect to the Sun is obtained using $v = v_{max} - v_\oplus$,

$$E_{max}^{unbound} = \frac{1}{2}\left(2+\sqrt{2}\right)^2 v_\oplus^2 - v_\oplus^2, \tag{2.52}$$

since $GM_\odot/a_\oplus = v_\oplus^2$, corresponding to a maximum speed outside the gravitational sphere of influence of the Sun of

$$v_{s,max} \approx 93 \text{ km/s}. \tag{2.53}$$

In Chapter 5, I show that the distribution function of these particles derived from the simulations is a match to the analytic distribution function, a nice verification of my simulation and analysis techniques.

In addition to limiting the range of E that I sample, I can also speed up the calculation by constraining the range of J^2 sampled. This constraint is equivalent to specifying a range of orbital perihelia to probe, given that the perihelion r_p is defined by

$$E = \frac{1}{2}J^2/r_p^2 - GM_\odot/r_p \tag{2.54}$$

such that the angular momentum for a given energy E and perihelion is described by

$$J^2(E, r_p) = 2r_p\left(Er_p + GM_\odot\right). \tag{2.55}$$

The goal is to make the range of r_p (and hence, J^2) large enough to encompass all orbits that might become bound to the solar system while keeping the range small enough so as not to waste computing resources by following unnecessary orbits.

I divide the gravitational scattering simulation into three parts, each defined by a different range of energy and perihelion: the "Regular run", the "High Perihelion" run, and "High Energy run." The Regular run samples particle orbits with:

$$0 \leq E < v_\odot^2/50 = \frac{1}{2}(44 \text{ km/s})^2, \quad r_p < 10 \text{ AU}. \tag{2.56}$$

The upper end of the energy range is slightly larger than the value of E_{max} determined in Eq. (2.49), while the maximum perihelion of 10 AU was chosen to be large enough–twice the semi-major axis of Jupiter–so that this run would contain the vast majority of particles that are gravitationally captured. If the Regular run misses any bound orbits due to the limit on r_p, those orbits should be found in the High Perihelion run, defined by

$$E < v_\odot^2/50, \quad 10 < r_p < 20 \text{ AU}. \tag{2.57}$$

The High Energy run samples particles with

$$v_\odot^2/50 < E < v_\odot^2/10 = \frac{1}{2}(98 \text{ km/s})^2, \quad r_p < 10 \text{ AU}. \tag{2.58}$$

The upper end of the energy range is approximately that found in Eq. (2.52). These orbits cannot be gravitationally captured by Jupiter, but I can check my analysis methods by determining if the geocentric distribution function of these particles matches the analytic prediction. Among the three simulation runs, the distribution function of WIMPs with $v_{geo} \leq (\sqrt{2}+1)v_\odot$ at the Earth should be completely sampled. I spend about 70% of the total CPU time for the gravitational scattering simulations on the Regular run, 25% on the High Perihelion run, and the remainder on the High Energy simulations.

If I were to sample E and J^2 according to the distribution of particle energy and angular momentum squared flowing in towards the Sun, Eq. (2.41), the sampling probability would be:

$$g(E, J^2) \propto \begin{cases} f(\sqrt{2E}), & J^2(E, r_p^{min}) \leq J^2 < J^2(E, r_p^{max}) \\ 0, & J^2(E_{min}, r_p^{min}) \leq J^2 < J^2(E, r_p^{min}) \\ & \text{or } J^2(E, r_p^{max}) \leq J^2 \leq J^2(E_{max}, r_p^{max}) \end{cases} \tag{2.59}$$

in the range $E_{min} \leq E < E_{max}$ and $J^2(E_{min}, r_p^{min}) \leq J^2 < J^2(E_{max}, r_p^{max})$, where r_p^{max} and r_p^{min} are the maximum and minimum perihelia allowed in each run. These ranges describe the maximum extent of E and J^2 for any given run. This sampling probability is highest in the high energy, high angular momentum part of the range considered. However, I want to sample proportionally more low energy orbits in both the Regular and High Perihelion runs, since these are most easily capturable. There are many sampling schemes one could use, but I choose to sample

$$g(E) = f(\sqrt{2E}), \tag{2.60}$$

in the range $E_{min} \leq E < E_{max}$, and uniformly sample $J^2(E, r_p^{min}) \leq J^2 < J^2(E, r_p^{max})$.

The difference between the two schemes can also be described in a more pragmatic way. To sample the flux according to Eq. (2.59), I would use the rejection method for

sampling, described in Chapter 7 of Press et al. (1992) in a box with sides of length $(E_{max} - E_{min})$ and $(J^2(E_{max}, r_p^{max}) - J^2(E_{min}, r_p^{min})$. In this scheme, I sample $f(\sqrt{2E})$ in the designated energy range to find a trial energy coordinate, and uniformly sample J^2 in the range $J^2(E_{min}, r_p^{min}) \leq J^2 < J^2(E_{max}, r_p^{max})$. I then randomly choose a value between zero and a point slightly above the maximum value of $g(E, J^2)$ in the box. If that value lies below $g(E, J^2)$ using the trial values of E and J^2, the trial values are kept; if not, the trial values are rejected. For $E \to E_{min}$, the range of angular momentum for which $g(E, J^2)$ is non-zero is much smaller than the angular momentum range for $E \to E_{max}$.

However, in the scheme of Eq. (2.60), I use the same sampling technique for E *only*. Once E is selected, I choose J^2 in the range $J^2(E, r_p^{min}) \leq J^2 < J^2(E, r_p^{max})$. In effect, I oversample low energy orbits relative to Eq. (2.41) because there is no trial for J^2. This oversampling is a result of the fact that many low-energy trials in (2.59) are rejected due to the trials in J^2. In Section 4.1, I demonstrate how I account for the oversampling when building the distribution functions from the simulations.

Once a sample particle's orbital parameters E and J^2 are selected, its initial position is determined by randomly orienting the position vector to a point on a spherical shell with fixed radius R relative to the Sun. The initial speed vector is chosen to be oriented inward, with the angle θ relative to the position vector determined by J^2. The speed v is fixed by R and J^2 since $J = Rv \sin\theta$. The azimuth of the velocity vector relative to the position vector is also randomly chosen. Thus, the initial position and velocity of the particle are completely determined.

2.4 Simulation Specifics

Since integrating the orbits of particles in the solar system is computationally expensive, it is more important to integrate just enough orbits to determine the approximate size of the bound distribution function relative to the unbound distribution, and to get a sense of which effects matter the most, than it is to get extremely tiny error bars. This principle guides my choices in the sizes of the ensembles of particles.

Table 2.1: Weak Scattering Simulations

Name	m_χ [AMU]	$\sigma_p^{\rm SI}$ [cm^2]	N_p [$a > 0.48$ AU]
DAMA	60	10^{-41}	1078586
CDMS	60	10^{-43}	145223
Medium Mass	150	10^{-43}	144145
Large Mass	500	10^{-43}	148173

Table 2.2: Gravitational Scattering Simulations

Name	N_p
Regular	4.8212×10^9
High Perihelion	3.994×10^9
High Energy	7.998×10^9

NOTE: All simulations have $m_\chi = 500$ AMU, $\sigma_p^{SI} = 10^{-43}$ cm^2.

The number of particles simulated in each of the weak scattering simulations is given in Table 2.1. Over a million particles scattered onto orbits with initial semi-major axes $a_{init} > 0.48 a_\oplus$ are simulated in the DAMA run. I follow particles with semi-major axes slightly below the Earth-crossing threshold so that if the semi-major axis increases modestly during the simulation, the contribution to the Earth-crossing flux is included. Fewer particles were simulated in the runs with lower cross section because the lifetimes were far longer than in the DAMA run. In other words, it took fewer particles to achieve a similar level of confidence on the distribution function.

The numbers of particles simulated in each gravitational scattering run are given in Table 2.2. The Regular run was subdivided into 5000 runs of either 8×10^5 or 10^6 particles each, depending on which beowulf cluster the runs were simulated on (see Chapter 3 for details on the computers). Three of the runs needed to be discarded due to file corruption, which was an issue on one cluster at the time these experiments were performed. The High Perihelion simulation consisted of 4000 runs of 10^6 particles each. Due to file corruption, six runs were eliminated from the analysis. The High Energy simulation consisted of 8000 runs of 10^6 particles, only two of which had problems with file corruption.

Chapter 3

Numerical Methods

In this chapter, I discuss the numerical algorithms relevant to the particle orbit simulations. In Section 3.1, I describe the orbit integration algorithm. In Section 3.2, I demonstrate how I treat scattering in the Sun. Finally, in Section 3.3, I describe all simulation-specific details, including descriptions of the computers and CPU time used, stopping conditions for individual orbit integrations, and the parameters used in the simulations.

3.1 The Integrator

The problem of determining the long-term trajectories of bound dark matter particles imposes a set of difficult challenges to the integration algorithm. The algorithm must:

- be stable and accurate over 4.5 Gyr.
- accurately follow highly eccentric ($e > 0.995$) orbits with no numerical dissipation.
- accurately integrate trajectories that are influenced by perturbing forces that may be comparable to the force from the Sun for short intervals. This includes close encounters with and passages through the planets.
- be fast, since one needs to integrate a large number of orbits to obtain an adequate statistical sample.

Much progress has been made in the past fifteen years to address the first and last criteria. This progress has largely been motivated by interest in the long-term stability of planetary systems. The most significant development has been the advent of geometric integrators (symplectic and/or time-reversible integrators), which have the desirable property that errors in conserved quantities (such as the Hamiltonian) are oscillatory rather than growing. However, the most commonly used algorithms (Wisdom & Holman, 1991; Saha & Tremaine, 1994; Chambers, 1999) are not immediately applicable to the present problem, for two main reasons. First, one would like to use an adaptive time step to quickly but accurately integrate a highly eccentric orbit (using very small time steps near perihelion and larger ones otherwise), or to resolve close encounters with the planets. It is difficult to introduce an adaptive time step in a symplectic or time-reversible way since varying the time step by criteria that depend on phase-space position destroys symplecticity. Secondly, since for practical purposes the integrations of planetary or comet orbits end when two bodies collide, there has been little attention to integrating systems for which the potential can deviate significantly from the Keplerian point-mass potential, as it does in the solar interior.

In the following sections, I will describe an algorithm to efficiently carry out the long-term integration of dark matter particles in the solar system. In Section 3.1.1, I will discuss an adaptive time step symplectic integrator (simultaneously formulated by Preto & Tremaine, 1999, and Mikkola & Tanikawa, 1999) that is used for most of the orbital integrations. In Section 3.1.2, I describe the error properties of this integrator. In Section 3.1.3, I will discuss procedures to handle special cases, such as close planetary encounters. I discuss the merits of various coordinate systems in Section 3.1.4. After the discussion of rescattering in the Sun in Section 3.2, I will summarize the algorithm in Section 3.3.

3.1.1 The Adaptive Time Step Symplectic Integrator

One approach to designing a symplectic integrator with an adaptive time step is to find a Hamiltonian that is separable in a set of canonical coordinates, but which incorporates a

transformed time coordinate. I will closely follow the arguments of Mikkola & Tanikawa (1999) and Preto & Tremaine (1999) in the description of the adaptive time step symplectic integrator, which is an example of such an approach. Let me start with a separable Hamiltonian $H(\mathbf{q},\mathbf{p},t) = T(\mathbf{p}) + U(\mathbf{q},t)$, a function of the canonical position $\mathbf{q}$ and momentum $\mathbf{p}$, such that the Hamiltonian equations of motion are:

$$\dot{\mathbf{q}} = \frac{\partial H}{\partial \mathbf{p}} \tag{3.1}$$

$$\dot{\mathbf{p}} = -\frac{\partial H}{\partial \mathbf{q}}. \tag{3.2}$$

Typically, T is the kinetic energy and U is the potential energy. I would like to transform from t to a new time coordinate s using the rule

$$\mathrm{d}t = g(\mathbf{q},\mathbf{p},t)\mathrm{d}s. \tag{3.3}$$

In order to construct a new, separable Hamiltonian (called Γ in both papers) for the system, which incorporates the new time coordinate s, it is necessary to extend the phase space, assigning $q_0 = t$ and $p_0 = -E$, where E is the total energy, and defining a new set of canonical variables $\mathbf{Q} = (q_0, \mathbf{q})$ and $\mathbf{P} = (p_0, \mathbf{p})$. This new Hamiltonian is written as:

$$\Gamma(\mathbf{Q},\mathbf{P}) = g(\mathbf{Q},\mathbf{P})\left[H(\mathbf{q},\mathbf{p},t) - p_0\right], \tag{3.4}$$

which one can see is the appropriate Hamiltonian for the time-transformation of Eq. (3.3) by examining the time-transformed equations for the system:

$$\frac{\mathrm{d}q_0}{\mathrm{d}s} = \frac{\partial \Gamma}{\partial p_0} = g(\mathbf{q},\mathbf{p},t) \tag{3.5}$$

$$\frac{\mathrm{d}\mathbf{q}}{\mathrm{d}s} = \frac{\partial \Gamma}{\partial \mathbf{p}} = g(\mathbf{q},\mathbf{p},t)\frac{\partial H}{\partial \mathbf{p}} + \frac{\partial g(\mathbf{q},\mathbf{p},q_0)}{\partial \mathbf{p}}\left[H(\mathbf{q},\mathbf{p},q_0) + p_0\right] \tag{3.6}$$

$$= g(\mathbf{q},\mathbf{p},t)\frac{\partial H}{\partial \mathbf{p}}$$

$$\frac{\mathrm{d}p_0}{\mathrm{d}s} = -\frac{\partial \Gamma}{\partial q_0} = -g(\mathbf{q},\mathbf{p},t)\frac{\partial H(\mathbf{q},\mathbf{p},t)}{\partial q_0} - \frac{\partial g(\mathbf{q},\mathbf{p},q_0)}{\partial \mathbf{q_0}}\left[H(\mathbf{q},\mathbf{p},q_0) + p_0\right] \tag{3.7}$$

$$= -g(\mathbf{q},\mathbf{p},t)\frac{\partial H(\mathbf{q},\mathbf{p},t)}{\partial q_0} \tag{3.8}$$

$$\frac{\mathrm{d}\mathbf{p}}{\mathrm{d}s} = -\frac{\partial \Gamma}{\partial \mathbf{q}} = -g(\mathbf{q},\mathbf{p},t)\frac{\partial H}{\partial \mathbf{q}} - \frac{\partial g(\mathbf{q},\mathbf{p},q_0)}{\partial \mathbf{q}}\left[H(\mathbf{q},\mathbf{p},q_0) + p_0\right] \tag{3.9}$$

$$= -g(\mathbf{q},\mathbf{p},t)\frac{\partial H}{\partial \mathbf{q}}.$$

The reason for dropping the second terms in the last columns is that $H + p_0 = 0$ along the path. Therefore, the equations of motion for the Hamiltonian Γ are simply the time-transformed equations of motion for the original Hamiltonian H.

The extended Hamiltonian Γ can be made separable with the choice

$$g(\mathbf{Q}, \mathbf{P}) = \frac{f(T(\mathbf{p}) + p_0) - f(-U(\mathbf{Q}))}{T(\mathbf{p}) + U(\mathbf{Q}) + p_0}, \tag{3.10}$$

so that the extended Hamiltonian reads

$$\Gamma(\mathbf{Q}, \mathbf{P}) = f(T(\mathbf{p}) + p_0) - f(-U(\mathbf{Q})), \tag{3.11}$$

which is indeed separable. The equations of motion for this Hamiltonian are:

$$\frac{\mathrm{d}q_0}{\mathrm{d}s} = f'(T(\mathbf{p}) + p_0) \tag{3.12}$$

$$\frac{\mathrm{d}\mathbf{q}}{\mathrm{d}s} = f'(T(\mathbf{p}) + p_0)\frac{\partial T}{\partial \mathbf{p}} \tag{3.13}$$

$$\frac{\mathrm{d}p_0}{\mathrm{d}s} = -f'(-U(\mathbf{Q})\frac{\partial U(\mathbf{Q})}{\partial q_0} \tag{3.14}$$

$$\frac{\mathrm{d}\mathbf{p}}{\mathrm{d}s} = -f'(-U(\mathbf{Q})\frac{\partial U(\mathbf{Q})}{\partial \mathbf{q}}. \tag{3.15}$$

Next comes the question of what choice of $f(x)$ to use. Preto & Tremaine expand Eq. (3.10) in a Taylor series to show that

$$g(\mathbf{Q}, \mathbf{P}) \approx f'(-U(\mathbf{Q})). \tag{3.16}$$

If I consider a potential of the form

$$U(\mathbf{q}, t) = -\frac{GM_\odot}{|\mathbf{q} - \mathbf{q}_\odot|} + \sum_i \Phi_i(\mathbf{q}, \mathbf{q}_i), \tag{3.17}$$

where the first term in the potential denotes the Keplerian potential of the Sun and Φ_i is the potential from planet i, one sees that for most of the particle orbit, the potential from the Sun dominates. Preto & Tremaine show that for a choice of

$$g(\mathbf{Q}, \mathbf{P}) = |\mathbf{q} - \mathbf{q}_\odot| \tag{3.18}$$

$$\approx -\frac{GM_\odot}{U(\mathbf{q}, t)} \tag{3.19}$$

the two-body problem can be solved exactly, with only a time (phase) error $\delta t/P \propto N^{-2}$, where P is the orbital period and N is the number of steps per orbit. This is a good feature because phase errors are far less important for my purposes than, for example, systematic energy drifts or numerical precession. Note that the time step is proportional to the particle's separation from the Sun, so that I have small time steps near the perihelion of the orbit and large steps near the aphelion. I use Eq. (3.18) as my choice for $g(\mathbf{Q}, \mathbf{P})$, for which the functional form of $f(x)$ is

$$f(x) = GM_\odot \log(x). \tag{3.20}$$

The adaptive time step equations of motion are implemented via a second-order leapfrog integrator (also called a Verlet integrator) with $\Delta s \simeq \Delta t/g = h$, where h is determined by the number of steps desired per orbit. For my choice of $f(x)$, and given $T = v^2/2$ and $U = U(\mathbf{r}, t)$, the change over a single fictitious time step h can be written as the mapping

$$\mathbf{r}_{1/2} = \mathbf{r}_0 + \frac{1}{2} h \frac{GM_\odot \mathbf{v}_0}{\frac{1}{2}v_0^2 + p_{0,0}} \tag{3.21}$$

$$t_{1/2} = t_0 + \frac{1}{2} h \frac{GM_\odot}{\frac{1}{2}v_0^2 + p_{0,0}} \tag{3.22}$$

$$\mathbf{v}_1 = \mathbf{v}_0 + h \frac{GM_\odot}{U(\mathbf{r}_{1/2}, t_{1/2})} \frac{\partial U(\mathbf{r}_{1/2}, t_{1/2})}{\partial \mathbf{r}} \tag{3.23}$$

$$p_{0,1} = p_{0,0} + h \frac{GM_\odot}{U(\mathbf{r}_{1/2}, t_{1/2})} \frac{\partial U(\mathbf{r}_{1/2}, t_{1/2})}{\partial t} \tag{3.24}$$

$$\mathbf{r}_1 = \mathbf{r}_{1/2} + \frac{1}{2} h \frac{GM_\odot \mathbf{v}_1}{\frac{1}{2}v_1^2 + p_{0,1}} \tag{3.25}$$

$$t_1 = t_{1/2} + \frac{1}{2} h \frac{GM_\odot}{\frac{1}{2}v_1^2 + p_{0,1}}. \tag{3.26}$$

Since my goal is to understand the behavior of a large ensemble of orbits, I am more interested in maintaining small energy errors over very long times rather than precisely integrating orbits over short times. Therefore, a second-order symplectic integrator, such as the one embodied in (3.21)–(3.26), is sufficient for my purposes. Higher-order symplectic integrators are described in Yoshida (1990) and Forest et al. (1991).

3.1.2 Errors Along the Orbital Path

In this section, I explore the behavior of the energy errors in the adaptive time step integrator as a function of energy, eccentricity, distance from the Sun, and number of steps per orbit. This study allows me, in conjunction with the results of Section 3.1.3, to determine what fictitious time step h to use, given certain accuracy requirements. For this study, I restrict myself to short integrations in order to focus on the errors of the adaptive time step integrator alone. I will discuss the long-term behavior of the integrator in subsequent sections.

To illustrate the typical behavior of WIMP orbits in planetary systems, I restrict the number of planets in the solar system to just one: Jupiter. I put Jupiter in a circular orbit about the Sun, and integrate the particle's path in the heliocentric frame. In this case (the restricted three-body problem), there is one constant of motion, the Jacobi constant

$$C_J = -2(E - n_J J_z), \tag{3.27}$$

where E is the particle energy in an inertial frame, n_J is the mean motion of Jupiter, and J_z is the z-component of the particle's angular momentum, assuming that the motions of the Sun and Jupiter are confined to the $x - y$ plane. Therefore, I can parameterize the errors in terms of the Jacobi constant. There are no analogous conserved quantities for particles orbiting in planetary systems with more than one planet or if the planetary orbit is eccentric. In those systems, one can quantify errors for integrators of the type described in Section 3.1.1 in terms of the relative energy error $\Delta E/E = (E + p_0)/E$, where E is determined by the position and velocity of the particle and p_0 is the $0-$component of the momentum in the extended phase space. If the equations of motion (3.5)–(3.9) were integrated with no error, then $p_0 = -E$ and $\Delta E/E = 0$.

In this subsection, I treat the Sun as a point mass, and consider trajectories with aphelia well inside Jupiter's orbit. I consider two different initial semi-major axes, $a = a_J/3$ and $a = a_J/6$ respectively, where a_J is the semi-major axis of Jupiter. To determine the size of the errors in C_J as a function of eccentricity, I integrate orbits with initial eccentricity

$e = 0.9, 0.99, 0.999$ and 0.9999. I perform integrations for each combination of a and e for 10 different initial, random orientations and an ensemble of step sizes. I run each integration for a total of 2×10^4 Kepler periods. The integrations are started at perihelion (to mimic the initial conditions of scattering in the Sun) with a very small $h = 10^{-8} R_{\odot}^{-1}$ year. Once the particle reaches its first aphelion, h is adjusted so that it will provide the desired number of steps per orbit. The fictitious time step is related to the number of steps per orbit via the eccentric anomaly Δu and semi-major axis a by

$$h = 2 \frac{1 - \cos \Delta u}{(G M_{\odot}/a)^{1/2} \sin \Delta u}, \tag{3.28}$$

for the symplectic mapping of Eqs. (3.21)–(3.26) in the case of the Kepler two-body problem. The number of steps per orbit is given by

$$N = \frac{2\pi}{\Delta u}. \tag{3.29}$$

I show the dependence of the error on the distance from the Sun in Figure 3.1. In this Figure, I plot the perihelion and aphelion Jacobi constant errors for a trajectory with initial $a = a_J/3$ and $e = 0.999$, integrated with 500 steps/orbit, representative of all the simulations. I plot only errors at perihelion and aphelion for clarity; a plot showing errors at each time step would be similar but with more scatter. The interior of the Sun is in the shaded region (though the integrations were done for a point-mass Sun). From Figure 3.1, it appears that

$$|\Delta C_J / C_J| \propto r^{-1} \tag{3.30}$$

This is a generic feature of the simulations, and implies that the maximum Jacobi constant or energy error occurs at perihelion. The normalization of the curve in Figure 3.1 depends on the initial conditions of the simulations, but the shape of this curve is generic. The errors are oscillatory, i.e., there is no secular growth in the error envelope with time.

In Figure 3.2, I show the maximum Jacobi constant error as a function of initial semi-major axis a_i and eccentricity e_i. To find the maximum error, I calculate the error in Jacobi constant every time e is in the range $e_i \pm 0.1(1 - e_i)$. The restriction on e isolates the effect

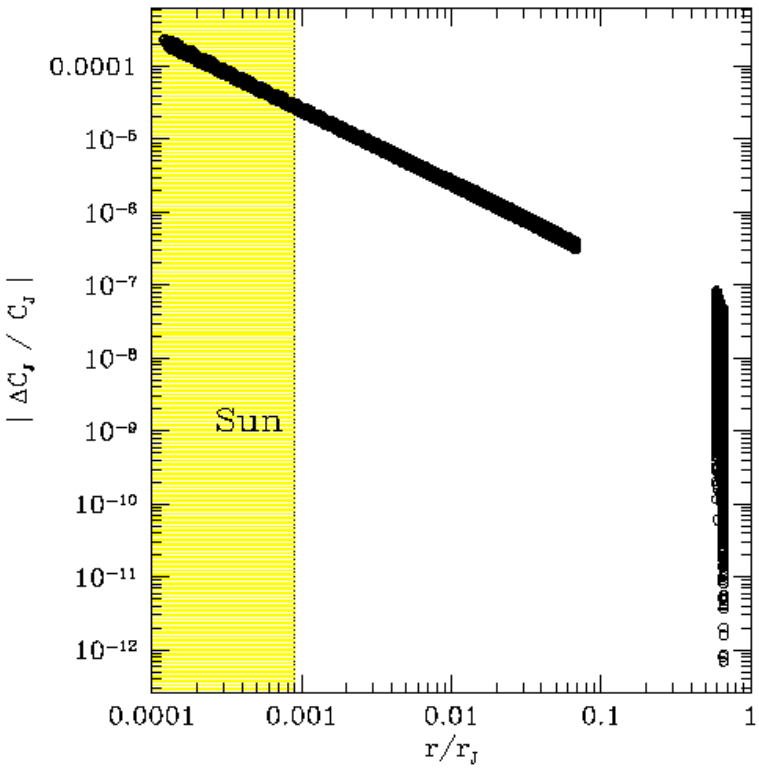

Figure 3.1: Jacobi constant errors as a function of distance from the primary for a trajectory with $a = 1.73$ AU, followed for 2×10^4 Kepler periods. This trajectory was integrated with 500 steps/orbit. Errors are calculated at perihelion and aphelion. The gap in the plot is due to the fact that the minimum eccentricity of this trajectory is $e_{min} = 0.38$. Points to the left of the vertical line lie within the volume of the Sun; however, I used a point-mass Sun for this integration.

of eccentricity on $|\Delta C_J/C_J|$, since Figure 3.1 demonstrates that the maximum error in a simulation depends on the largest eccentricity in the orbit. I then plot the maximum error found among all simulations for the same initial a_i and e_i. For each type of simulation, the maximum error occurs at perihelion. Figure 3.2 indicates that the maximum Jacobi constant error is a decreasing function of the number of steps per orbit, and an increasing function of semi-major axis and eccentricity. Furthermore, the maximum error for $e \in e_i \pm 0.1(1-e_i)$ within each simulation is a function of the initial conditions. In the simulations with fixed eccentricity and $a = a_J/6$, the spread in these central values is less than a factor of two, while the spread is about a factor of ten in the $a = a_J/3$ simulations.

All of these results can be explained in the context of this particular adaptive time step symplectic integrator, and will inform the choice of the fictitious time step h. My discussion of the error analysis for this integrator closely follows the approach of Preto & Tremaine (1999). In that paper, errors are quantified in terms of energy. I can use Eq. (3.27) to relate Jacobi constant errors to energy errors, such that

$$|\Delta C_J| = 2\,|\Delta E|\,. \tag{3.31}$$

Since J_z is often tiny in these simulations,

$$|\Delta C_J/C_J| \approx |\Delta E/E|\,. \tag{3.32}$$

Although the mapping in Eqs. (3.21)–(3.26) is symplectic, there is an error associated with the fact that the the integrator is of finite (second) order. This means that the mapping actually conserves a slightly different Hamiltonian, which Preto & Tremaine call $\widetilde{\Gamma} = \Gamma + \Gamma_{err}$, for which Γ is the Hamiltonian in Eq. (3.11) and the error Hamiltonian is

$$\Gamma_{err} \;=\; \frac{1}{12}\left[\left[f(T(\mathbf{p}+p_0), -f(-U)\right], -f(-U) + \frac{1}{2}f(T(\mathbf{p}+p_0)\right] + \mathcal{O}(h^4), \tag{3.33}$$

where in this case the square brackets are Poisson brackets. This error Hamiltonian can be found by using the Baker-Campbell-Hausdorff identity (see Section 2 in Preto & Tremaine,

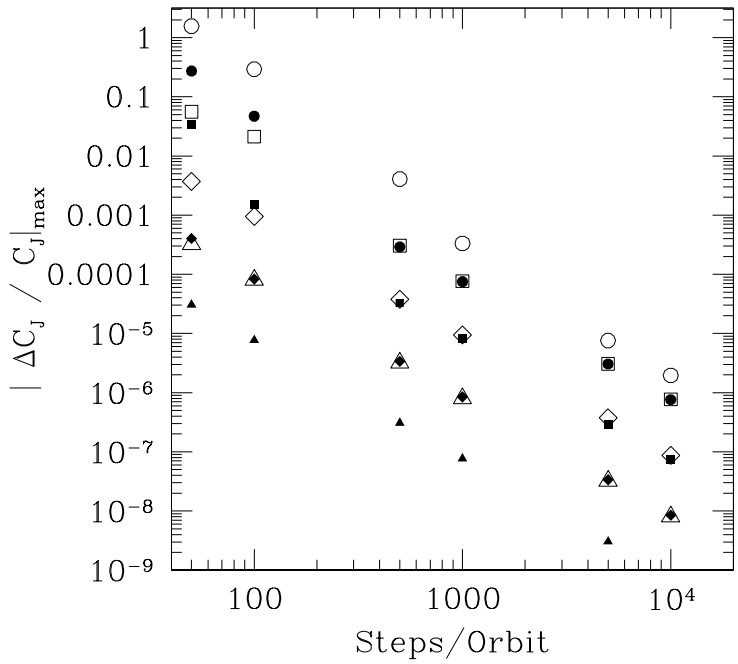

Figure 3.2: Errors in the Jacobi constant as a function of eccentricity and semi-major axis. Each point shows the maximum error for 10 trajectories initialized with the same eccentricity but with random initial orientation, and followed for 2×10^4 Kepler orbits. Since the size and frequency of the eccentricity oscillations depend on the initial orientation, I use only the maximum Jacobi errors for each orbit in the trajectory whose eccentricity matches the initial eccentricity to calculate the averaged maximum error. Open points denote those trajectories for which the semi-major axis $a = a_J/3 = 1.73$ AU; closed points refer to trajectories with $a = a_J/6 = 0.87$ AU. Circles mark trajectories with initial eccentricity $e_i = 0.9999$, squares denote those with $e_i = 0.999$, diamonds indicate those with $e_i = 0.99$, and triangles those with $e_i = 0.9$.

1999). In the regime where perturbations to the Keplerian potential of the Sun is small,

$$\frac{\Delta E}{E} = \frac{\Gamma^i_{err} - \Gamma_{err}(\mathbf{Q},\mathbf{P})}{f'(-U)E} \tag{3.34}$$

$$\approx \frac{\Gamma^i_{err} - \Gamma_{err}(\mathbf{Q},\mathbf{P})}{hrE}, \tag{3.35}$$

where Γ^i_{err} is the value of the error Hamiltonian at the start of the integration and $\Gamma_{err}(\mathbf{Q},\mathbf{P})$ is the error along the path.

From (3.35), I recover one result from the simulations, namely that the Jacobi constant or energy errors scale as r^{-1}. To recover the dependence of the energy errors on semi-major axis and eccentricity, I must examine the form of the error Hamiltonian. If U_{pert} is the perturbation in the potential energy from the Kepler potential of the Sun, then in the context of the three-body problem integrated in the heliocentric frame,

$$U_{pert}(\mathbf{r},t) = -\frac{GM_J}{|\mathbf{r}-\mathbf{r}_J|} + \frac{GM_J\mathbf{r}\cdot\mathbf{r}_J}{a_J^3}, \tag{3.36}$$

where M_J is Jupiter's mass and a_J is its semi-major axis. To first order in U_{pert}, the error Hamiltonian is

$$\begin{aligned}\Gamma_{err} \approx \frac{h^3(GM_\odot)^2}{24\left(\frac{1}{2}v^2+p_0\right)^2}\Bigg\{ & 2\frac{GM_\odot}{r^2}p_0 + 4\frac{p_0 U_{pert}}{r} + 4\left(\frac{1}{2}v^2+p_0\right)\frac{\mathbf{r}\cdot\nabla U_{pert}}{r} \\ & -rv_iv_j\frac{\partial^2 U_{pert}}{\partial x_i \partial x_j} + \frac{v^2 U_{pert}}{r} - 3\frac{(\mathbf{v}\cdot\mathbf{r})^2 U_{pert}}{r^3} - 6\frac{(\mathbf{v}\cdot\mathbf{r})\,(\mathbf{v}\cdot\nabla U_{pert})}{r} \\ & -\frac{\partial}{\partial t}\left(r\frac{\partial U_{pert}}{\partial t} + 6\frac{\mathbf{v}\cdot\mathbf{r}U_{pert}}{r} + 2r\mathbf{v}\cdot\nabla U_{pert}\right)\Bigg\}\end{aligned} \tag{3.37}$$

The first term of this expression is by far the largest, since it has no dependence on U_{pert}. It is, however, a constant, and so will not enter the expression for ΔE. Terms in (3.37) directly proportional to U_{pert} will in general be the next largest if $a \ll a_J$ since these terms will be first order in either the separation of the particle and Jupiter ($|\mathbf{r}-\mathbf{r}_J|^{-1}$) or r/a_J. Derivatives of U_{pert} result in polynomial dependence of Γ_{err} on $|\mathbf{r}-\mathbf{r}_J|^{-1}$ and r/a_J.

To find the errors at perihelion expected for the simulations given the theoretical energy error (3.35), I calculate only the non-derivative terms of Eq. (3.37) at both the initial position (for Γ^i_{err}) and at perihelion ($\Gamma_{err}(\mathbf{Q},\mathbf{P})$). This approximation should be fine for

small semi-major axes, but derivative terms should be included when the distance between the particle and Jupiter is of order the semi-major axis, since many terms in Eq. (3.37) depend on positive integer powers of $a/|\mathbf{r} - \mathbf{r}_J|$. The integrations start with a given h corresponding to a number N of steps/orbit at aphelion, so that $r = a(1+e)$ in Eq. (3.37), and $\mathbf{r} \cdot \mathbf{v} = 0$. To lowest order,

$$\Gamma^i_{err} \approx -E \left\{ \frac{h^3 GM_\odot}{12} + \frac{h^3 a(5+3e) U_{pert}}{12} \right\}, \tag{3.38}$$

where $E = -GM_\odot/2a$ is the initial energy. I can calculate the extremes in Γ^i_{err} by recognizing that the magnitude of U_{pert} is maximized when the aphelion of the particle orbit is aligned with Jupiter's position with respect to the Sun, and minimized when the position vectors are orthogonal. Therefore, the range of initial Hamiltonian errors is

$$\begin{aligned} \Gamma^i_{err} \quad \in \quad & \left\{ -E \left\{ \frac{h^3 GM_\odot}{12} + \frac{h^3 (5+3e) GM_J}{12} \left[-\frac{a}{\sqrt{a_J^2 + a^2(1+e)^2}} \right] \right\}, \right. \\ & \left. -E \left\{ \frac{h^3 GM_\odot}{12} + \frac{h^3 (5+3e) GM_J}{12} \left[-\frac{a}{|a_J - a(1+e)|} + \frac{a}{a_J} \frac{a(1+e)}{a_J} \right] \right\} \right\}. \end{aligned} \tag{3.39}$$

The range of initial errors in Γ^i_{err} increases as a function of semi-major axis. At perihelion, if the energy error is small, the range of Hamiltonian errors is

$$\begin{aligned} \Gamma_{err} \quad \in \quad & \left\{ -E \left\{ \frac{h^3 GM_\odot}{12} + \frac{h^3 (5-3e) GM_J}{12} \left[-\frac{a}{\sqrt{a_J^2 + a^2(1-e)^2}} \right] \right\}, \right. \\ & \left. -E \left\{ \frac{h^3 GM_\odot}{12} + \frac{h^3 (5-3e) GM_J}{12} \left[-\frac{a}{|a_J - a(1-e)|} + \frac{a}{a_J} \frac{a(1-e)}{a_J} \right] \right\} \right\} \end{aligned} \tag{3.40}$$

The range for Γ_{err} is small for the range of eccentricities I consider in the simulations $e \gtrsim 0.9$. For small energy errors, the fractional energy error (Eq. 3.35) does not depend on the terms in Γ^i_{err} and Γ_{err} directly proportional to $GM_\odot$. Therefore, the terms linear in

U_{pert} dominate the energy error, which leads to an energy error range at perihelion

$$\frac{\Delta E}{E} = \frac{\Gamma^i_{err} - \Gamma_{err}}{hEa(1-e)} \tag{3.41}$$

$$\in \left\{ -\frac{h^2 GM_J}{12a(1-e)} \left\{ (5+3e) \left[-\frac{a}{\sqrt{a_J^2 + a^2(1+e)^2}} \right] + \frac{(5-3e)a}{a_J} \right\} \right. \tag{3.42}$$

$$\left. -\frac{h^2 GM_J}{12a(1-e)} \left\{ (5+3e) \left[-\frac{a}{|a_J - a(1+e)|} + \frac{a}{a_J}\frac{a(1+e)}{a_J} \right] + \frac{(5-3e)a}{a_J} \right\} \right\}$$

For $(1-e) \ll 1$ and $a < a_J/2$, this expression simplifies to

$$\frac{\Delta E}{E} \in \left\{ -\frac{h^2 GM_J}{6a_J(1-e)} \left\{ 1 - \frac{4}{\sqrt{1 + 4a^2/a_J^2}} \right\}, \right. \tag{3.43}$$

$$\left. -\frac{h^2 GM_J}{6a_J(1-e)} \left\{ 1 - 4\left(\frac{1}{1-2a/a_J} + \frac{2a}{a_J} \right) \right\} \right\} \tag{3.44}$$

There are three features in Figure 3.2 that can be explained with Eq. (3.42): the dependence of the error on the number of steps per orbit, eccentricity, and semi-major axis. The first two can be extracted easily from Eq. (3.42). The energy error only depends on the number of steps per orbit through h, and $\Delta E/E \propto h^2$. From Eqs. (3.28) and (3.29), $N \propto (\Delta u)^{-1} \propto h^{-1}$ for $\Delta u \ll 1$, so that $\Delta E/E \propto N^{-2}$. The only dependence of the energy error on eccentricity comes from the denominator of (3.43), $\Delta E/E \propto (1-e)^{-1}$, which is a consequence of the fact that I the energy error is largest at perihelion $r_p = a(1-e)$. Since the simulations in this section are performed for $e = 0.9, 0.99, 0.999$, and 0.9999, for a given number of steps per orbit and semi-major axis, energy errors should be spaced by factors of 10, which is what is observed in Figure 3.2.

In Figure 3.2, it appears that the maximum energy error for $a = a_J/3$ is about an order of magnitude larger than that of $a = a_J/6$. Because of this factor, for a fixed number of steps per orbit, the energy error curve for $a = a_J/3$ overlaps the energy error curve for $a = a_J/6$ but with the next highest eccentricity simulated. The ratio of the maximum energy error (3.42) for $a = a_J/3$ to that of $a = a_J/6$ is about 4. However, the ratio of the maximum errors is around 10 using the full first order expression for Γ_{err}, Eq. (3.37). This is the factor of 10 that I see in the simulations. The range of energy error is a function

of the initial semi-major axis because the range of possible energy errors in Eq. (3.42) is strongly dependent on the initial orientation of the orbit, with the maximum possible energy error likely only for a small subset (the initial position vector $\mathbf{r}$ almost perfectly aligned with Jupiter's position vector) of possible initial orientations. For example, the maximum energy error for $a = a_J/6$ is only about 20% higher than the minimum value, but can be about a factor of 10 higher for $a = a_J/3$.

This simple analytic description does not work so well for large errors. In those cases, the error curves for fixed a and e in Figure 3.2 do not exactly follow $\Delta E/E \propto N^{-2}$ since the analytic approximation for Eq. (3.42) only holds for *small* energy errors.

To set the fictitious time step h for the simulations in this thesis, it is preferable to consider errors at a fixed, small distance from the Sun rather than exclusively at perihelion. This is because I use a mapping technique to follow perihelion passages where $r_p \leq 2R_\odot$. Therefore, I want to impose a maximum energy (or Jacobi constant) error for the simulations at $r = 2R_\odot$. In Figure 3.3, I show the maximum energy error as a function of the particle's semi-major axis at $r = 2R_\odot$ in the limit that $e = 1$. For reference, $|\Delta C_J/C_J| = |\Delta E/E|$. The error has a sharp peak at $a = 0.5a_J$, since in this case the aphelion distance coincides with Jupiter's orbit. The main point of this Figure is that while small numbers of steps per orbit, and hence, small values of h can be used to integrate fairly small orbits ($a \lesssim 1$ AU $= 0.19a_J$) with a maximum Jacobi constant error of $|\Delta C_J/C_J| = 10^{-4}$, larger orbits need to be integrated with far more steps per orbit to achieve similar accuracy.

A full discussion of how to choose the time step will be deferred to Section 3.3, after I consider the effects of close encounters with Jupiter in Section 3.1.3.

3.1.3 Special Cases: Strong Perturbations to the Keplerian Potential

While I would like to use this adaptive time step integrator as much as possible, keeping the fictitious step h fixed, there are two situations which must be handled separately.

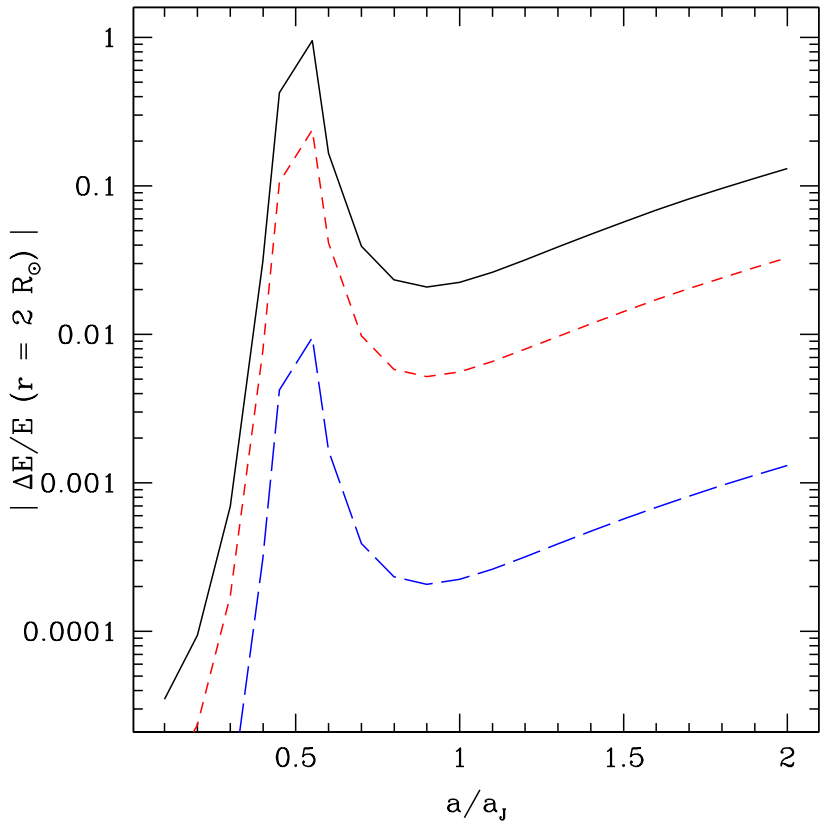

Figure 3.3: Energy errors using the maximum value of $|\Delta E/E|$ for a given a at $r = 2$ R$_\odot$ using 50 steps/orbit (*black solid line*), 100 steps/orbit (*red dashed line*), and 500 steps/orbit (*blue long dashes*). There is a sharp peak at $r = a_J/2$ where the initial position of the particle lies exactly within Jupiter. The energy error asymptotes at large values of a.

Inside the Sun

The interior of the Sun has a potential that deviates strongly from Keplerian. The integrator described in Section 3.1.1 works badly inside the Sun, both because it is designed for nearly Keplerian potentials and because the gravitational potential in the Sun is slower to calculate. Thus, I replace the integration through the Sun by a map. I exploit the fact that tidal forces from the planets are small near the Sun, so that I can ignore the planets while the particle is inside the Sun. Since the two-body problem can be solved exactly, I can define a region about the Sun (called a "bubble," with a typical radius of 0.1 AU) for which I use the exact solutions to the two-body problem. In reality, I create a map for the bubble but only use it if the orbital perihelion lies within $r = 2R_\odot$. At one point, I mapped all orbits with $r_p < 0.1$ AU, so the bubble boundary of 0.1 AU is somewhat of a relic. I can map the incoming position and velocity to the outgoing position and velocity using look-up tables for

$$\Delta t(a,e) = \frac{2}{\sqrt{GM_\odot}} \int_{r_p(a,e)}^{r_b} \frac{\mathrm{d}r}{\sqrt{2[\pm 1/2a - \tilde{\Phi}_\odot(r)] \pm a(1-e^2)/r^2}} \tag{3.45}$$

$$\Delta\phi(a,e) = 2\sqrt{\pm a(e^2-1)} \int_{r_p(a,e)}^{r_b} \frac{\mathrm{d}r}{r^2\sqrt{2[\pm 1/2a - \tilde{\Phi}_\odot(r)] \pm a(1-e^2)/r^2}} \tag{3.46}$$

which are the time Δt and phase $\Delta\phi$ through which the particle passes in the bubble region, both functions of the semi-major axis a and eccentricity e. By my convention, a is always positive, such that $E = GM_\odot/2a$ for hyperbolic orbits and $E = -GM_\odot/2a$ for eccentric orbits. The $\pm$ signs in Eqs. (3.45) and (3.46) correspond to hyperbolic orbits ($e > 1$) and elliptical orbits ($e < 1$) respectively. I have normalized the solar potential $\Phi_\odot(r)$ by $GM_\odot$, so that $\tilde{\Phi}_\odot = \Phi_\odot/GM_\odot$. I have written Δt and $\Delta\phi$ in terms of a and e instead of the energy and angular momentum for reasons that will soon become apparent. Note that r_b is the bubble radius and r_p is the true perihelion, defined by

$$\left.\frac{\mathrm{d}r}{\mathrm{d}t}\right|_{r_p} = 0 \tag{3.47}$$

$$= \sqrt{2\left(\pm 1/2a - \tilde{\Phi}_\odot(r_p)\right) \pm a(1-e^2)/r_p^2}. \tag{3.48}$$

I parameterize the look-up tables in terms of the semi-major axis and Keplerian perihelion $r_K = |a(1-e)|$.

There is one subtlety in matching the map through the bubble to the time-transformed integration outside of bubble. In the Keplerian two-body problem, one solves the equations of motion $\mathrm{d}\mathbf{p}/\mathrm{d}t$ and $\mathrm{d}\mathbf{q}/\mathrm{d}t$ instead of $\mathrm{d}\mathbf{p}/\mathrm{d}s$ and $\mathrm{d}\mathbf{q}/\mathrm{d}s$. If one divides $\mathrm{d}\mathbf{q}/\mathrm{d}s$ and $\mathrm{d}\mathbf{p}/\mathrm{d}\mathbf{s}$ by the differential equation for the time coordinate, the time-transformed equations of motion are

$$\left.\frac{\mathrm{d}\mathbf{q}}{\mathrm{d}t}\right|_\Gamma = \frac{\mathrm{d}\mathbf{q}/\mathrm{d}s}{\mathrm{d}t/\mathrm{d}s} \tag{3.49}$$

$$= \frac{f'(T+p_0)\mathrm{d}T/\mathrm{d}\mathbf{p}}{f'(T+p_0)} \tag{3.50}$$

$$= \mathbf{p} \tag{3.51}$$

$$\left.\frac{\mathrm{d}\mathbf{p}}{\mathrm{d}t}\right|_\Gamma = \frac{\mathrm{d}\mathbf{p}/\mathrm{d}s}{\mathrm{d}t/\mathrm{d}s} \tag{3.52}$$

$$= -\frac{f'(-U)\partial U/\partial \mathbf{q}}{f'(T+p_0)} \tag{3.53}$$

$$= -\frac{f'(-U)}{f'(T+p_0)}\frac{\partial U}{\partial \mathbf{q}}. \tag{3.54}$$

The second of these differs from the equations of motion of the original Hamiltonian by a multiplicative factor

$$\mu = f'(-U)/f'(T+p_0), \tag{3.55}$$

in other words, the particle follows a Kepler orbit about a Sun of mass $\mu M_\odot$. Therefore, I calculate the orbital elements using

$$a = \left|\frac{p_0}{2\mu G M_\odot}\right| \tag{3.56}$$

$$e = \sqrt{1 \pm J^2/(\mu G M_\odot a)}, \tag{3.57}$$

where the upper sign should be used for hyperbolic orbits, and lower for elliptical orbits. I use a look-up table for Δt and $\Delta\phi$ with the modification that Δt, as calculated for a and e with $\mu = 1$, must be multiplied by a factor of $\mu^{-1/2}$. The change in phase is unaffected by the choice of central mass since it is a purely geometric quantity.

Similar lookup tables are also used to determine the perihelion r_p (as a function of semi-major axis and eccentricity, and which is faster than calculating the perihelion on the fly) and optical depth (and hence, scattering probability) in the Sun. I discuss rescattering in the Sun in Section 3.2.

The procedure for using the mapping, then, is as follows. Once the particle crosses the bubble boundary, its perihelion is determined. If the perihelion lies within $r = 2R_\odot$ of the center of the Sun, I halt the adaptive time step integrator, and rotate to the orbital plane of the particle-Sun system. Since the integration does not stop exactly at the bubble boundary, I must calculate the difference in time δt and orbital phase $\delta\phi$ between the particle's position and the bubble boundary, which can be done analytically. I then determine μ, a, and e. I use those values to find Δt and $\Delta\phi$ from the map, and then rotate the position vector by an angle $\Delta\phi - \delta\phi$ in the orbital plane. The velocity vector can be found with respect to the position vector since the energy and angular momentum are known. I transform the position and velocity vectors back to the reference plane, and restart the adaptive time step integrator.

I demonstrate the robustness of the map in Figure 3.4. I will focus on the upper left-hand panel, and discuss the other panels in later sections. In the upper left-hand panel, I show errors in the Jacobi constant over a 500 Myr time span for the restricted circular three-body problem. The orbit enters the Sun $\sim 10^7$ times in this time span. I sample the orbit at the first aphelion after a 10^5 yr interval from the previous sample, and there are approximately 100 steps/orbit. This Figure shows that there are only oscillatory errors throughout this long-term integration, and these fractional errors never exceed 10^{-6} at aphelion. Long-term integrations of the two-body problem using the map demonstrate energy errors only at the level of machine precision. Therefore, I am confident that the map is not a source of error in the integrations.

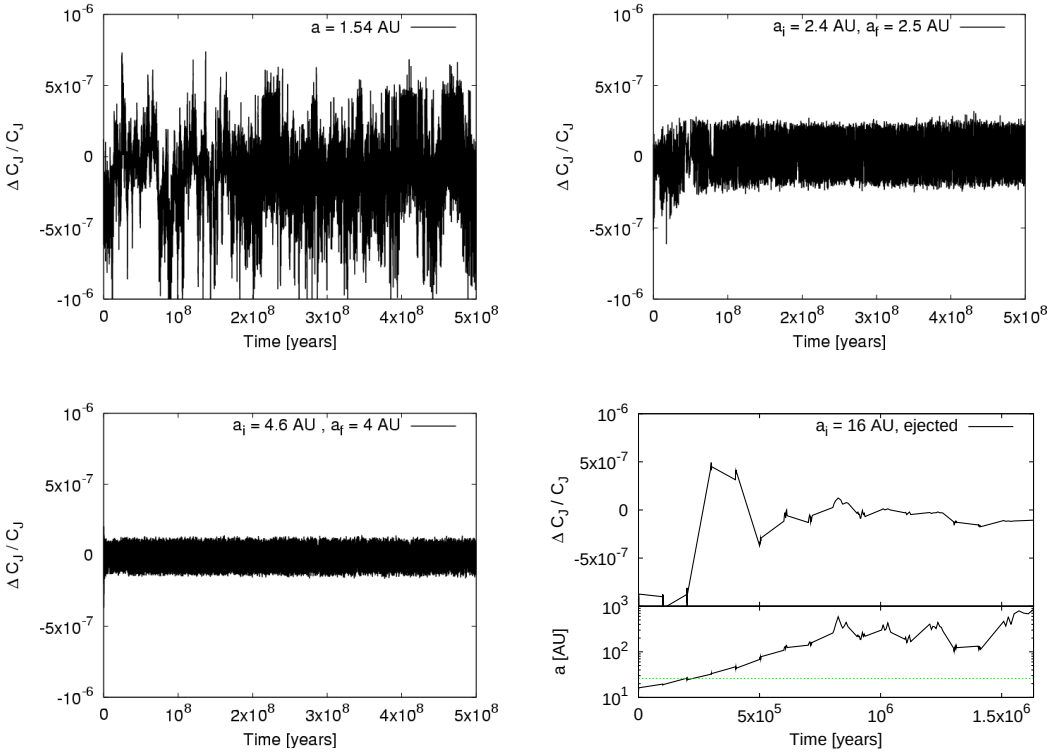

Figure 3.4: Error in the Jacobi constant as a function of time for several particles. The Jacobi constant is recorded at aphelion at 10^5 year intervals. *Top left:* A particle with $a = 1.54$ AU. This particle repeatedly goes through the Sun (about 10^7 times), but never goes through the bubble around Jupiter. It is integrated with $h = 6 \times 10^{-5} R_\odot^{-1}$ year, which corresponds to ≈ 100 steps/orbit. *Top right:* A particle that gets stuck near a Sun-skimming 2:1 resonance with Jupiter. This particle repeatedly goes through the Jupiter bubble. It is integrated with $h = 2 \times 10^{-5} R_\odot^{-1}$ year, which corresponds to ≈ 350 steps/orbit. *Bottom left:* A particle gets stuck near a 3:2 resonance with Jupiter. This orbit was integrated with $h = 1.5 \times 10^{-5} R_\odot^{-1}$ year, which corresponds to ≈ 650 steps/orbit. *Bottom right:* This particle repeatedly crosses r_c, the transition radius between barycentric and heliocentric coordinates (dashed green line marks $r_c/2$, the crossing semi-major axis for an orbit with $e \sim 1$) and has its last aphelion before ejection from the solar system at $t = 1.6 \times 10^6$ years. It is integrated with $h = 2 \times 10^{-6} R_\odot^{-1}$ year, which corresponded initially to 9×10^3 steps/orbit.

Close Encounters of the Planetary Kind

While the adaptive time step integrator works well in a near-Keplerian potential, one must treat close encounters with planets more carefully. If the time step is too large near a planet, the particle fails to "resolve" the force from the planet. This can cause growing errors in the particle's trajectory. Since I use an $f(x)$ that is optimized to the potential of the Sun, the only way to achieve a small time step near each planet is to either make the fictitious time step h small and fixed or to switch to a different integration method near each planet while using the method of Section 3.1.1 with a reasonably large h for the rest of the orbit. The advantage of the former approach is that it does not break the symplectic nature of the integrator. However, it is also prohibitively computationally expensive. Therefore, I use the latter approach.

I define a spherical region ("bubble") about each planet for which I allow a different integration scheme, while continuing to use the adaptive time step symplectic integrator (Section 3.1.1) outside the spheres. The transition between the integration schemes is not symplectic, but I reduce errors in the integration by enforcing an accuracy requirement on $|\Delta E/E| = |(p_0 + E)/E| = |(-H + E)/E|$ in the bubble of each planet.

In the bubble of each planet, I continue to use the adaptive time step integrator, but the value of h' (the prime denotes the fact that this fictitious time step is *only* used within a planet bubble) used in the bubble is selected to keep the quantity $|\Delta E/E|$ as small as possible while also keeping the total integration time short. To find the optimal value of h', I use the following algorithm. When a particle first enters a bubble, I record the particle's energy error at the first step, $|\Delta E_i/E_i|$. Then, I integrate the particle's trajectory through the bubble using the default value of h. As the particle is about to exit the bubble, I calculate the energy error $|\Delta E_f/E_f|$. If the energy error meets the accuracy criterion, or if it is less than $|\Delta E_i/E_i|$, then the integration is allowed to continue normally. If, however, $|\Delta E_f/E_f|$ does not satisfy the accuracy criterion, then I restart the integration in the bubble from the point at which the particle first entered with a smaller fictitious time step h'. This process iterates until either the energy accuracy condition is satisfied or the energy error

plateaus in value. If the energy error plateaus in value, whichever trajectory (corresponding to a particular choice of h') has the minimum $|\Delta E_f/E_f|$ is chosen.

The choice of the bubble size is related to the choice of fiducial value of h and to the mass of the planet. A larger value of h means that the bubble needs to be larger to ensure that the planet's field is properly resolved. Planets with larger masses will require larger bubbles than smaller planets because the force on the particle scales with the planet mass. In the weak scattering simulations, I choose to keep the bubble size fixed for all orbits, while for the gravitational capture simulations I use a larger bubble for higher energy orbits. In general, I tune h so that the typical energy errors for all energies are similar near each planet. The optimum sizes of the bubbles are ~ 0.05 AU for the inner planets and $\sim 1-3$ AU for the outer planets of the solar system if I require that $|\Delta E/E| \sim 10^{-7} - 10^{-6}$. In Section 3.3, I describe the exact choices for the bubble size and accuracy criterion for each simulation.

A complication arises when particles experience large changes in energy in their passage through the planetary bubble. In this case, the value of h that guaranteed a certain precision in $|\Delta E/E|$ in the pre-encounter orbit may be either too large (for adequate precision) or too small (it will slow down the orbital integration). Therefore, I change the value of h at the next aphelion. I change h at the aphelion because this is the point at which energy errors are at a minimum in the orbit. Again, this procedure breaks the symplectic nature of the integrator, but by changing h at aphelion, my experiments show that I minimize errors. In Section 3.3, I outline how h is chosen for the initial orbits, and how h is changed if the particle experiences significant changes in energy from planetary encounters.

I demonstrate the performance of the bubble for the case of the 3-body problem in Figure 3.4. In this Figure, the fractional error of the Jacobi constant is plotted against the time since the initial scatter in the Sun that produced a bound orbit, and I show the first 500 Myr of the integrations. The Jacobi constant is measured at the aphelion of the orbit at 10^5 year intervals. The trajectories of the particles in the upper right and bottom panels repeatedly pass through the bubble around Jupiter. For these integrations, the radius of the

bubble about Jupiter was ≈ 2.3 AU, and the energy criterion was $|\Delta E_f/E_f| < 2 \times 10^{-7}$. There are no secular changes of the Jacobi constant with time. Therefore, even though the planet bubble disrupts the symplecticity of the integrator, the integrator tracks the Hamiltonian well.

3.1.4 Coordinate Choice

For most of the integration, I use a heliocentric coordinate system for both the particles and the planets. There are two main reasons why I choose a heliocentric system. First, it is much simpler to use heliocentric coordinates for passages through the Sun. Secondly, consider the gravitational potential of the planets in the heliocentric frame,

$$\Phi(\mathbf{r})_{planets} = \Phi_{direct}(\mathbf{r}) + \Phi_{indirect}(\mathbf{r}) \tag{3.58}$$

$$= -\sum_P \frac{GM_P}{|\mathbf{r} - \mathbf{r}_P|} + \sum_P \frac{GM_P \mathbf{r} \cdot \mathbf{r}_P}{x_P^3}, \tag{3.59}$$

where the indirect term arises from the fact that this coordinate system is not the center-of-mass coordinate system. For orbits that are well within a planet's orbit, the direct term can be expanded into spherical harmonics

$$\Phi_{direct}(\mathbf{r}) = \sum_P \frac{GM_P}{|\mathbf{r} - \mathbf{r}_P|} \tag{3.60}$$

$$= \sum_P \left[-\frac{GM_P}{r_P} - \frac{GM_P}{r_P^3} \mathbf{r} \cdot \mathbf{r}_P - \frac{GM_P}{r_P} \sum_{l=2}^{\infty} \left(\frac{r}{r_P} \right)^l P_l \left(\frac{\mathbf{r} \cdot \mathbf{r}_P}{r r_P} \right) \right], \tag{3.61}$$

where the P_l are Legendre polynomials. The dipole term of the direct potential is canceled by the indirect potential. Therefore, the primary contributor to the force on the particle by the planet comes from the $l = 2$ tidal term of the potential; in other words, the tidal forces near the Sun are much smaller in the heliocentric frame.

While there are distinct advantages to using the heliocentric frame, it is not desirable to use the heliocentric frame in the case of large orbits. This is due to the fact that the indirect term of the potential dominates the potential at large distances from the Sun. This poses a problem for the adaptive time step integrator, since my choice of $g = -GM_\odot/U = |\mathbf{r} - \mathbf{r}_\odot|$ is only optimal if the Keplerian solar potential is dominant. Therefore, I choose to work in

the barycentric frame at large distances.

In practice, this means switching between heliocentric and barycentric coordinate systems for long-period orbits. I choose the crossover radius such that

$$\max |\Phi_{indirect,P}(r_c, \theta_P = 0)| = \epsilon \frac{GM_\odot}{r_c}, \tag{3.62}$$

where θ_P is the angle between $\mathbf{r}$ and $\mathbf{r}_P$, r_c is the crossover radius, the "max" signifies the planet for the planet P for which the indirect potential is strongest, and ϵ is a factor $\lesssim 1$. In our solar system, the planet for which the indirect potential is strongest is Jupiter. The choice of ϵ is somewhat arbitrary. Therefore, I find the crossover point to be

$$\frac{M_J r_c}{a_J^2} = \epsilon \frac{M_\odot}{r_c}, \tag{3.63}$$

or

$$r_c \approx \sqrt{\epsilon M_\odot / M_J} a_J. \tag{3.64}$$

In changing coordinates, one breaks the symplectic flow of the integrator. Therefore, one must treat the Hamiltonian, and therefore p_0, carefully at the crossover. I choose to treat the transition the same way I treat the transition into the bubble about the Sun. Namely, I calculate μ (Eq. 3.55), the factor by which the gravitational potential is modified in the integrator (see Eq. 3.54), in the initial coordinate frame i. Then I set

$$p_0 \,|_f = -\mu_i E(\mathrm{r}, t)|_f \,, \tag{3.65}$$

where quantities calculated in the final frame are denoted by f, and E is the energy derived from the position and velocity coordinates of the particle. While this transition is not symplectic, in practice it conserves the Jacobi constant to adequate precision for the circular three-body problem, for orbits that repeatedly cross the transition. This is demonstrated in the lower left panel in Figure 3.4, an orbit for which the initial semi-major axis is 50 AU. In this integration, $\epsilon = 0.1$, which translates to a crossover radius of 53 AU.

3.2 Subsequent Scattering in the Sun

Each time a particle passes through the Sun, there is a probability

$$P_{\rm scatt} = 1 - e^{-\tau} \tag{3.66}$$

that it will be scattered, given the optical depth τ along the path. Since the WIMP-nucleon cross sections relevant to this paper imply low opacity in the Sun ($\tau \lesssim 10^{-3}$ for the DAMA simulation, $\tau \lesssim 10^{-5}$ for all other simulations), the scattering probability per solar passage is well approximated by

$$\begin{aligned} P_{scatt} &= 1 - \left(1 - \tau + \mathcal{O}(\tau^2)\right) && (3.67) \\ &\approx \tau. && (3.68) \end{aligned}$$

Thus, to simulate scattering in the Sun, one simply generates a random number between 0 and 1, and if that number is less than the total optical depth τ along the path, the particle scatters.

I create a table for optical depth indexed by the semi-major axis and Kepler perihelion of the orbit, just as I did for the orbit integration in the Sun in Section 3.1.3. I interpolate in this table to determine the optical depth for a particular orbit through the Sun.

More precisely, the optical depth (in differential form) is given by

$$\begin{aligned} \frac{{\rm d}\tau}{{\rm d}l{\rm d}Q} &= \sum_A \frac{{\rm d}\tau_A}{{\rm d}l{\rm d}Q} && (3.69) \\ &= \sum_A n_A(l) \frac{{\rm d}\sigma_A}{{\rm d}Q}, && (3.70) \end{aligned}$$

where l denotes the particle trajectory, $n_A(l)$ is the number density of element A in the Sun at position l along the path, and ${\rm d}\sigma_A/{\rm d}Q$ is the differential elastic scattering cross section with respect to the energy transfer Q between element A and the WIMP. The integral over energy transfer can be computed using the form of the differential cross section in Eq. (B.1)

and the form factor in Eq. (B.2):

$$\frac{\mathrm{d}\tau}{\mathrm{d}l} = \sum_A n_A(l) \int_0^{Q_{max}} \frac{\mathrm{d}\sigma_A}{\mathrm{d}Q} \tag{3.71}$$

$$= \sum_A n_A(l) \frac{2m_A}{\pi v(l)^2} [Zf_p + (A-Z)f_n]^2 Q_A \left(1 - e^{-Q_{\max,A}/Q_A}\right), \tag{3.72}$$

where I have used the approximation of zero-temperature behavior of nuclei in the Sun to set $v_{rel} = v(l)$. The expression for the maximum energy transfer Q_{max} is extracted from Eq. (2.23):

$$Q_{\max,A} = 2\frac{\mu_A^2}{m_A} v(l)^2, \tag{3.73}$$

such that the optical depth along the path can be expressed as:

$$\frac{\mathrm{d}\tau}{\mathrm{d}l} = \frac{2}{\pi} \sum_A m_A n_A(l) Q_A [Zf_p + (A-Z)f_n]^2 \frac{1}{v(l)^2} \left(1 - e^{-2\mu_A^2 v(l)^2/m_A Q_A}\right). \tag{3.74}$$

The integral of the optical depth over the particle trajectory is greatly simplified because the Sun is modeled as spherical and the torque on the particle by Jupiter is negligible in the Sun. Therefore,

$$\mathrm{d}l = v(t)\mathrm{d}t \tag{3.75}$$

$$= v(t(r)) \left|\frac{\mathrm{d}t}{\mathrm{d}r}\right| \mathrm{d}r \tag{3.76}$$

$$= \frac{v(r(t))}{|v_r(r(t))|} \mathrm{d}r, \tag{3.77}$$

where

$$v(E, r) = \sqrt{2[E - \Phi_\odot(r)]} \tag{3.78}$$

is the particle's speed and

$$|v_r(E, J, r)| = \sqrt{2[E - \Phi_\odot(r)] - J^2/r^2} \tag{3.79}$$

is the radial velocity of the particle. I have written the speeds in terms of the energy E and angular momentum J for now. Therefore, I can write the optical depth as a function of the particle's position from the center of the Sun r and the constants of motion, so that

$$\frac{\mathrm{d}\tau(E, J)}{\mathrm{d}r} = \frac{v(r)}{|v_r(r)|} \frac{\mathrm{d}\tau}{\mathrm{d}l}. \tag{3.80}$$

Thus, the total optical depth along the path is

$$\begin{aligned}\tau(E,J) &= \frac{4}{\pi}\sum_A m_A Q_A [Z f_p + (A-Z) f_n]^2 \\ &\times \int_{r_p}^{R_\odot} \frac{n_A(r)}{v(E,r)|v_r(E,J,r)|}\left(1 - e^{-2\mu_A^2 v^2(E,r)/m_A Q_A}\right) \mathrm{d}r.\end{aligned} \tag{3.81}$$

The extra factor of two in the expression for $\tau(E,J)$ comes from the fact that the integrand is a function of the radius r instead of the total path l, and so one must account for the pre- and post-perihelion trajectories.

In order to express the optical depth τ as a function of the semi-major axis and eccentricity, I use the relations

$$E = \pm\frac{GM_c}{2a} \tag{3.82}$$

$$J^2 = \pm GM_c a(e^2-1), \tag{3.83}$$

where $M_c = \mu M_\odot$ is the central mass, as determined by Eq. (3.55), and the upper (lower) sign is used for hyperbolic (elliptical) orbits. Therefore,

$$\tilde{v}(a,r) = v(a,r)/\sqrt{GM_c} = \sqrt{2\left[\pm 1/2a - \tilde{\Phi}_\odot(r)\right]} \tag{3.84}$$

$$|\tilde{v}(a,e,r)| = |v_r(a,e,r)|/\sqrt{GM_c} = \sqrt{2\left[\pm 1/2a - \tilde{\Phi}_\odot(r)\right] \mp a(e^2-1)/r^2}. \tag{3.85}$$

If I insert these expression into Eq. (3.81),

$$\begin{aligned}\tau(a,e) &= \frac{4}{\pi}\frac{1}{GM_c}\sum_A m_A Q_A [Z f_p + (A-Z) f_n]^2 \\ &\times \int_{r_p}^{R_\odot} \frac{n_A(r)}{\tilde{v}(a,e,r)|\tilde{v}_r(a,e,r)|}\left(1 - e^{-2\mu_A^2 GM_c \tilde{v}^2(a,r)/m_A Q_A}\right) \mathrm{d}r.\end{aligned} \tag{3.86}$$

I make a look-up table for τ using for the choice $\mu = 1$, and then scale τ by a factor of μ^{-1}. There is also a factor of μ in the exponent. However, its impact on τ is negligible since $|\mu - 1| \sim 10^{-6} - 10^{-5}$.

If the particle scatters in the Sun, its new phase space coordinates can be determined

by sampling the scattering distribution

$$\frac{\mathrm{d}\tau(E,J)}{\mathrm{d}r\mathrm{d}\Omega} = \sum_A n_A(r)\frac{v(E,r)}{|v_r(E,J,r)|}\frac{\mathrm{d}\sigma_A}{\mathrm{d}\Omega} \tag{3.87}$$

$$= \sum_A \frac{\sigma_A}{4\pi} n_A(r)\frac{v(E,r)}{|v_r(E,J,r)|}e^{-Q(\cos\theta)/Q_A}. \tag{3.88}$$

Since the particle can be scattered either before or after the perihelion of its original orbit with equal probability, I randomly assign the scatter to occur before or after the perihelion of the original orbit. Therefore, these data allow one to determine the scattering position and the direction of the scattered particle. In order to determine the final energy $E' = E - Q$ of the WIMP, it is necessary to determine the nuclear species from which the dark matter particle scatters. To determine this, I weight the scattering probability by the nuclear species' contribution to $\mathrm{d}\tau/\mathrm{d}r\mathrm{d}\Omega$. Therefore, since I know the initial energy, the center-of-mass scattering angle, and the species of nucleus which scattered the dark matter particle, I can determine E', and hence, the final center-of-mass velocity $\mathbf{v}'$. I translate this vector to the orbital plane of the system, and then explicitly integrate the orbit using equations of the form Eqs. (3.45) and (3.46) (with the appropriate integration limits) to the bubble boundary. At this point, I translate the orbit to the reference plane of the system, and the adaptive time step integration resumes.

3.3 Simulation Specifics

In Figures 3.5 and 3.6, I present a schematic of the integration algorithm for the weak scattering and gravitational capture simulations respectively. I will discuss each of the flowcharts separately (Sections 3.3.1 and 3.3.2), and discuss each decision point in detail. Finally, I will describe the computers used for the simulations (Section 3.3.3).

3.3.1 Weak Scattering Simulations

I will start with the weak scattering flow chart. There are six main things that need to be set in order to run the simulations: starting conditions; the radius at which the

heliocentric-barycentric coordinate change needs to be made, r_c; methods for initializing h and potentially changing h at later times; conditions for passing through and scattering in the Sun; the size of the bubble about Jupiter, l_J, and the accuracy criterion $|\Delta E/E|$; and conditions for terminating the simulation. I will discuss each point in turn, following the flowchart (Figure 3.5).

Starting Conditions

I start all particle integrations at perihelion, even though the radius at which the halo particles first scatter onto bound orbits need not correspond to this perihelion. I do this for simplicity. I follow all particles after the initial scatter, using the map to evolve the particles to the Sun bubble boundary (0.1 AU) using map described in Section 3.1.3. I treat $\tau = 0$ for the first passage out of the Sun. In order to account for the fact that particles may experience a second scatter before leaving the Sun for the first time, I perform a rescattering Monte Carlo when I construct the distribution functions (see Chapter 4).

Once the particles have reached the bubble boundary, I initialize the adaptive time step symplectic integrator (Section 3.1.1), setting $h = 10^{-8} R_{\odot}^{-1}$ year and integrating the equations of motion in heliocentric coordinates. Even though energy errors in the the adaptive time step symplectic integrator are generally higher if the integration is started at perihelion rather than at aphelion, the magnitude of the errors will be tiny since h is so small (Preto & Tremaine, 1999). The fact that energy errors are so much larger when the integration is started at perihelion is why I do not start the integration near perihelion with the fiducial value of h (discussed below) but use the combination of the map and the integration with small h until the particle reaches aphelion before resetting h. With this choice of initial h, a particle with initial semi-major axis $a = 1$ AU will be integrated with 4.7×10^5 steps/orbit, while a particle with $a = 100$ AU will be integrated with 4.7×10^6 steps/orbit. This scaling is due to the fact that $h \propto a^{1/2}$, as per Eq. (3.28). If the semi-major axis exceeds $r_c/2$, it may be necessary to change to barycentric coordinates before the particle reaches aphelion for the first time.

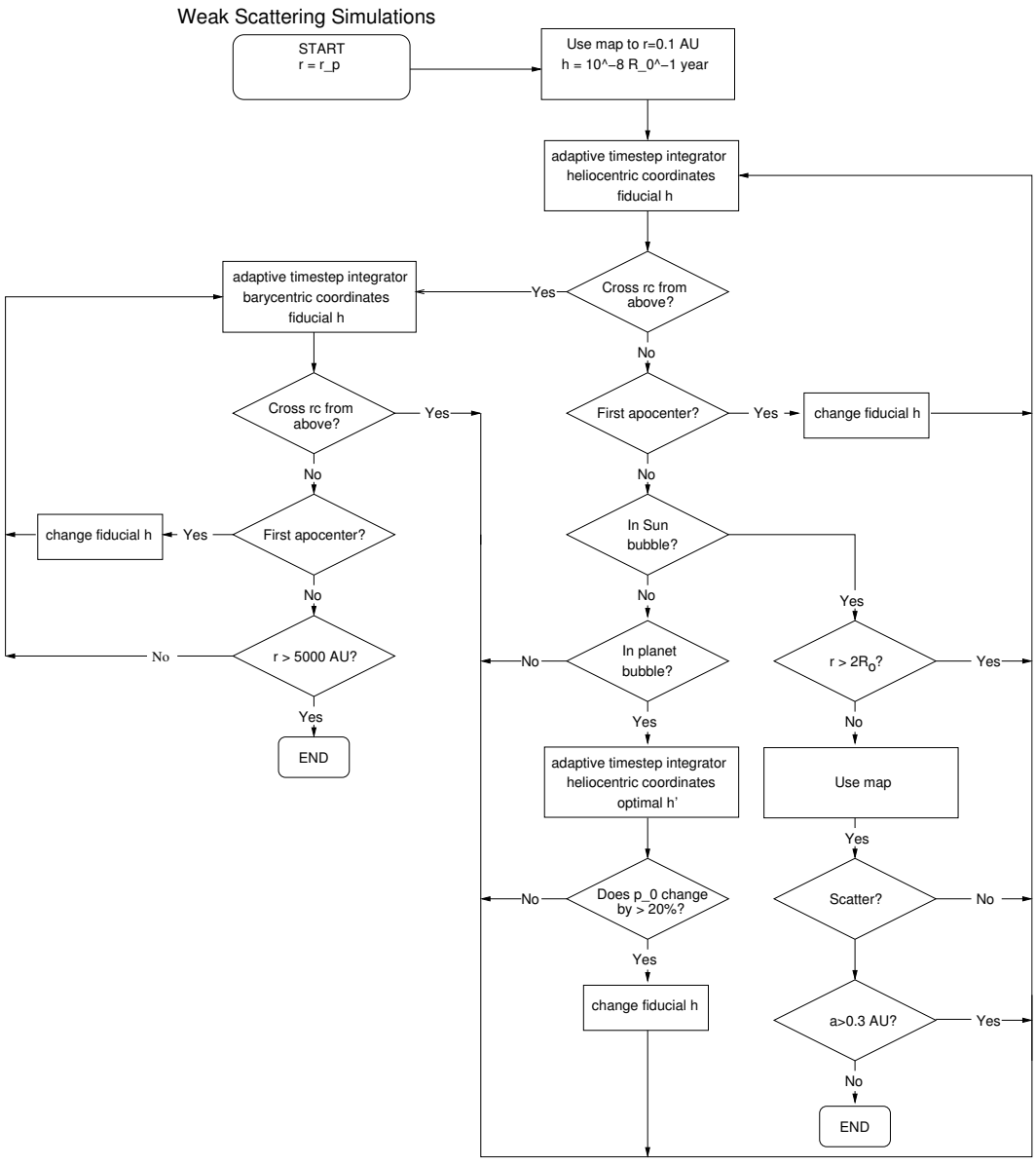

Figure 3.5: Flowchart for the simulation algorithm for the weak scattering experiments.

Table 3.1: The fictitious time step h as a function of semi-major axis for the DAMA run.

a range [AU]	$h[R_\odot^{-1}$ yr]
$a < 0.75$	1×10^{-4}
$0.75 \leq a < 1.1$	7×10^{-5}
$1.1 \leq a < 1.6$	6×10^{-5}
$1.6 \leq a < 2.2$	5×10^{-5}
$2.2 \leq a < 3.5$	4×10^{-5}
$3.5 \leq a < 6.2$	3×10^{-5}
$6.2 \leq a < 11$	2×10^{-5}
$11 \leq a < 13$	9×10^{-6}
$13 \leq a < 30$	2×10^{-6}
$30 \leq a < 45$	1×10^{-6}
$45 \leq a < 120$	6×10^{-7}
$120 \leq a < 200$	4×10^{-7}
$200 \leq a < 500$	3×10^{-7}
$a > 500$ or unbound	2×10^{-7}

Coordinate Change

For the weak scattering simulations, I set $\epsilon = 0.1$ (Eq. 3.62), thus setting the transition radius between the heliocentric and barycentric coordinated regimes to $r_c = 53$ AU. This is large enough that only a small percentage of particles routinely cross the transition radius, but small enough that the heliocentric potential does not have too large a contribution from the indirect potential.

Setting h

After the particles reach their first aphelion, h is reset according the values listed in Tables 3.1 (DAMA) and 3.2 (CDMS, Medium Mass, and Large Mass). These values of h are chosen such that both errors at perihelion ($|\Delta E/E| < 10^{-4}$) and near Jupiter ($|\Delta E/E| < 10^{-6}$) are small. The combination of the values of h and the Jupiter bubble radius l_J (see below) were determined empirically. I used slightly smaller values of h for some semi-major axes in the CDMS, Medium Mass, and Large Mass runs compared to the DAMA run in order to check that resonance sticking was not a function of properties of the Jupiter bubble.

As discussed in Section 3.1.3, a particle's energy (and hence, semi-major axis) may

Table 3.2: The fictitious time step h as a function of semi-major axis for the CDMS, Medium Mass, and Large Mass runs.

a range [AU]	$h[R_\odot^{-1}$ yr]
< 0.75	1×10^{-4}
$0.75 \leq a < 1.1$	7×10^{-5}
$1.1 \leq a < 1.6$	6×10^{-5}
$1.6 \leq a < 3.5$	2×10^{-5}
$3.5 \leq a < 6.2$	1.5×10^{-5}
$6.2 \leq a < 11$	1×10^{-5}
$11 \leq a < 30$	2×10^{-6}
$30 \leq a < 45$	1×10^{-6}
$45 \leq a < 120$	6×10^{-7}
$120 \leq a < 200$	4×10^{-7}
$200 \leq a < 500$	3×10^{-7}
$a > 500$ or unbound	2×10^{-7}

change throughout the simulation. In order to ensure appropriate values of h during the simulation, I flag particles when they go through the Jupiter bubble. If the energy changes by 20% or more from when the particle enters the bubble to when it exits, the particle is flagged to have h adjusted at the next aphelion. I do not readjust h after every aphelion, or after each time the particle passes through the bubble, because very frequent changes in h can induce secular evolution in the Jacobi constant. I impose any changes in h at aphelion instead of the bubble boundary to reduce such secular changes, since I have determined experimentally that aphelion is the optimal point at which to change h.

The Sun Bubble

When a particle first crosses into the bubble about the Sun, I calculate its perihelion. If the perihelion is larger than $2R_\odot$, I continue the adaptive time step symplectic integration. If, however, the perihelion lies within $2R_\odot$ of the center of the Sun, I proceed to map its current position and velocity to its position and velocity as it exits the bubble according to the prescription of Section 3.1.3. If the perihelion lies within the Sun, I employ a Monte Carlo simulation of scattering in the Sun, according the the method of Section 3.2. The

vast majority of the time, the particle does not scatter, and I simply use the map to move the particle back to the edge of the bubble. If the particle rescatters onto an orbit with semi-major axis $a < 0.3$ AU, I terminate the integration. If the particle rescatters onto an orbit with $a > 0.3$ AU, I use the method of Section 3.2 to evolve the new orbit to the edge of the bubble, and then resume the adaptive time step symplectic integration.

The Jupiter Bubble

For the DAMA, CDMS, and Medium Mass simulations, I set the Jupiter bubble boundary to be $l_J = 1.7$ AU, and the accuracy criterion to be $|\Delta E_f/E_f| < 10^{-6}$. I adjusted this value for some particles in order to speed up the integration. The reason for adjusting this value was that some particles had generically slightly smaller initial $|\Delta E_i/E_i|$ than $|\Delta E_f/E_f|$, and it took a longer time with $|\Delta E_f/E_f| = 10^{-6}$ to reach a sufficiently flat plateau in $|\Delta E_f/E_f|$ than with a slightly larger accuracy criterion. I also set $l_J = 3.4$ AU past 500 Myr for the Medium Mass simulation, mostly to determine if there were any effects of a larger l_J on the simulations. There were no changes the distribution function resulting from this change. For the Large Mass simulation, I experimented with a lower value of the accuracy criterion ($|\Delta E_f/E_f| < 2 \times 10^{-7}$ for the first 500 Myr, $|\Delta E_f/E_f| < 3 \times 10^{-7}$ later) and a larger bubble, $l_J = 2.1$ AU. I used the larger accuracy criterion for later times to speed up the integration. The only effect the larger accuracy criterion had was to raise slightly the maximum energy error per orbit.

Stopping Conditions

There are three reasons for terminating an integration. If the particle crosses outward through the shell $r = 5000$ AU, the integration stops. Most of the power in the distribution function comes from particles on much smaller orbits, so I do not lose much (if anything) by imposing this sort of termination condition instead of a strict condition on whether or not the particle is unbound. Particles crossing this shell will rarely cross the Earth's orbit again. Secondly, if the particle rescatters in the Sun onto an orbit with $a < 0.3$ AU, I halt

Table 3.3: The initial integration conditions for the gravitational capture simulation as a function of initial speed v and Kepler perihelion r_p. The values of h are in units of $R_\odot^{-1}$ yr.

Initial speed v [km s^{-1}]	$r_p < 5$ AU	$r_p > 5$ AU
$v < 10$	2×10^{-7}	3×10^{-7}
$10 \leq v < 20$	5×10^{-7}	10^{-6}
$v \geq 20$	10^{-6}	2×10^{-6}

the integration since the particle will soon thermalize in the Sun and is uninteresting for my purposes. Thirdly, if the particle survives for a time $t = 4.5$ Gyr, I stop the integration since this is approximately the lifetime of the solar system.

3.3.2 Gravitational Scattering Simulations

I will discuss the decision points in the gravitational capture simulation flowchart in the same order as in Section 3.3.1.

Starting Conditions

I use the method of Section 2.3 to set the initial conditions, starting all particles at a distance $R = 1000$ AU from the Sun. Using larger values of R does not change the results. I choose the initial conditions in the heliocentric frame, and then translate the coordinates to the barycentric frame to start the integration. I use the adaptive time step symplectic integrator with h set to the values listed in Table 3.3. The initial value of h is a function of the particle's initial speed (or energy) and two-body perihelion relative to the Sun. Particles with low energy and low angular momentum need to be integrated with larger numbers of steps per orbit, since they will go closer the Sun (recall that energy errors increase with decreasing distance to the Sun).

Coordinate Change

As in the case of the weak scattering simulations, I set $\epsilon = 0.1$ and $r_c = 53$ AU.

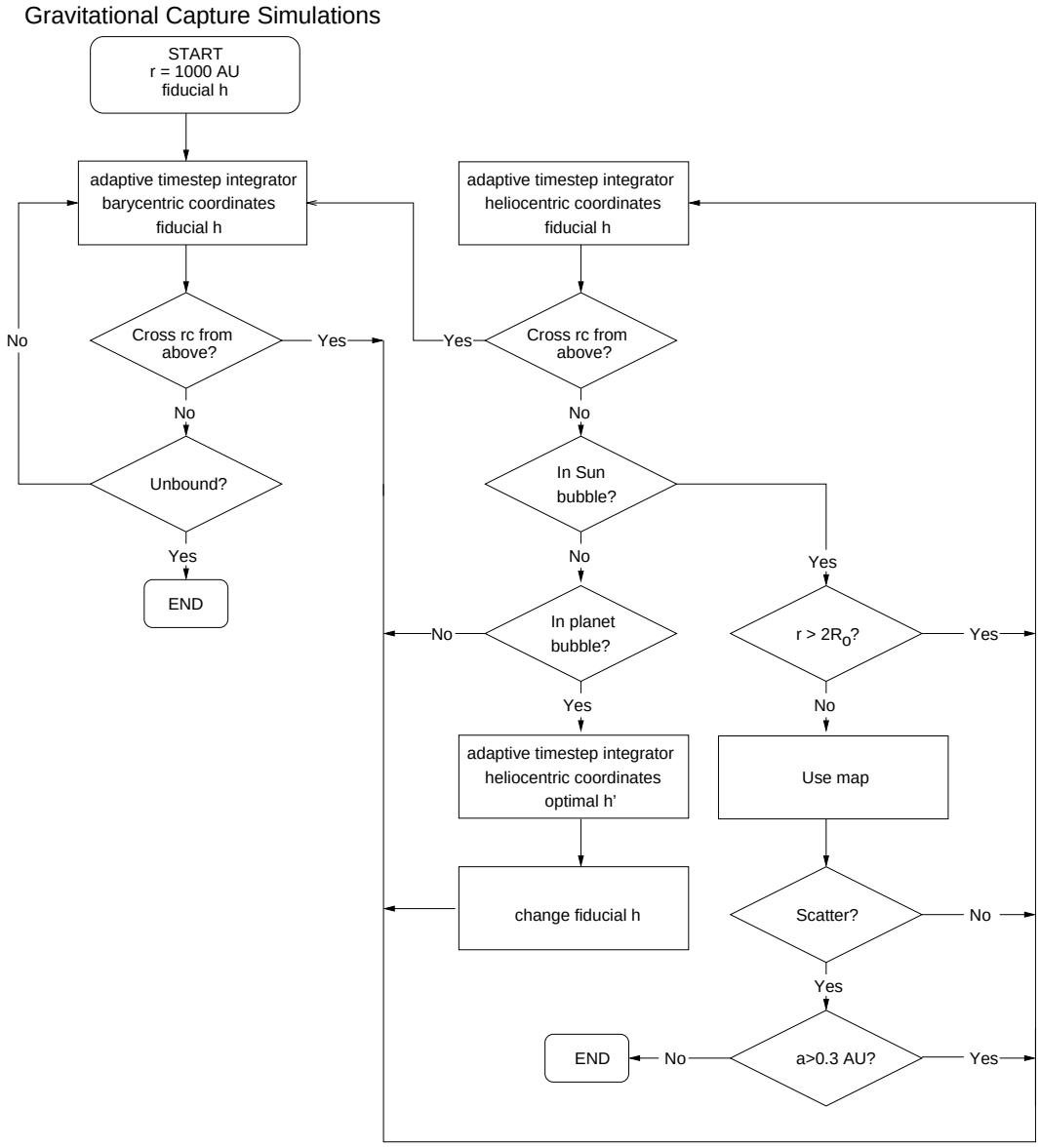

Figure 3.6: Flowchart for the simulation algorithm for the gravitational capture experiments.

Table 3.4: Choices for the fictitious time step h as a function of semi-major axis for the gravitational capture simulations. The semi-major axis refers to bound particles unless otherwise indicated.

a range [AU]	$h[R_\odot^{-1}$ yr]
< 0.75	10^{-4}
$0.75 \leq a < 1.1$	7×10^{-5}
$1.1 \leq a < 1.6$	6×10^{-5}
$1.6 \leq a < 3.5$	2×10^{-5}
$3.5 \leq a < 6.2$	1.5×10^{-5}
$6.2 \leq a < 13$	7×10^{-6}
$13 \leq a < 22$	10^{-6}
$22 \leq a < 30$	7×10^{-7}
$30 \leq a < 45$	6×10^{-7}
$45 \leq a < 120$	5×10^{-7}
$120 \leq a < 200$	4×10^{-7}
$200 \leq a < 500$	3×10^{-7}
$a > 500$ or unbound	2×10^{-7}

Setting h

I initially set h according to Table 3.3. This is sufficient for a "first pass" through the solar system. For longer term integrations, in order to both control errors near Jupiter and to speed up integration if particles settle onto tighter orbits, I reset h after the particles pass through the Jupiter bubble. I then set h according to Table 3.4. I allow h to change after each passage through the Jupiter bubble up to 10 Myr; however, to control for errors caused by breaking the symplectic nature of the integrator repeatedly, I only allow h to be reset if the energy changes by more than 20% through a Jupiter bubble passage after that time.

The Sun Bubble

I use the same prescription as in Section 3.3.1 to treat particles in the Sun bubble.

The Jupiter Bubble

For the gravitational capture simulations, I set the accuracy criterion to $|\Delta E_f/E_f| < 5 \times 10^{-7}$. The bubble size was set to $l_J = 2.1$ AU for particles with bound semi-major axes

$a < 100$ AU, and $l_J = 3.7$ AU for orbits that were either unbound or were bound but $a > 100$ AU.

Stopping Conditions

As in the weak scattering simulations, I terminate the integration if the particle rescatters in the Sun onto an uninteresting orbit or if the particle reaches $t = 4.5$ Gyr. However, instead of terminating the integration when $r > 5000$ AU, I only stop the integration if the particle becomes unbound again. I do this because some particles that are initially captured onto bound orbits are on fairly loose orbits (although typically $a < 5000$ AU).

3.3.3 Computing

Simulations were performed on three Linux beowulf computing clusters at Princeton University. The Physics Department's Feynman cluster consists of about 250 processors (the exact number changes as groups in the department add or remove processors) of various clock speeds and RAM. Most nodes are dual-core with 3.2 GHz clock speeds. The Department of Astrophysical Sciences has the Hydra cluster, consisting of 92 dual-core nodes. Most nodes have 3.06 GHz clock speeds. Princeton's TIGRESS High Performance Computing Center administers Della, a 512-node cluster. The dual-core nodes have clock speeds of 3.2 GHz. The DAMA, CDMS, and Large Mass simulations were largely run on Della and Hydra, while most of the Medium Mass simulation was run on Feynman. Each of these simulations required approximately 10^5 CPU-hours. The gravitational capture simulations were run on all three clusters, for a total of about 1.5×10^5 CPU-hours. About 70% of the CPU cycles were used for the Regular run, another 25% were devoted to the High Perihelion run. The High Energy runs used the remainder of the cycles. I used the Della cluster to run the analysis algorithms described in the following chapter.

Chapter 4

From Simulations to Distribution Functions

4.1 Distribution Function Estimators

To interpret the simulations, I construct the distribution function of dark matter particles bound to the solar system as a function of time since the birth of the solar system. As shown in the Introduction and Section 5.3, the time-dependence of the distribution function is needed to calculate the neutrino event rates from WIMP capture and annihilation in the Earth. In contrast, the direct detection rate is sensitive only to the current dark matter distribution function. In this section, I describe the outputs of the simulations, and how to estimate the bound distribution function from these data.

As I will discuss below, the most basic output of my simulations is a flux of dark matter through the Earth (more properly, through a ring of height $\pm z_c$ and radius 1 AU). Therefore, I will need some way of translating the flux to a distribution function. To convert an observed flux at position $\mathbf{x}$ and time t, $F(\mathbf{x}, t)$, into a distribution function $f(\mathbf{x}, \mathbf{v}, t)$, I make the assumption that the timescale of variation in the distribution function is much larger than the typical dynamical timescale of particles in the solar system ($\sim$ year), and that both F and f are slowly varying functions of position, so that $F(\mathbf{x}, t)$ is approximately

just a function of $\mathbf{v}$ and t. I can then adopt the usual argument (cf. Reif, 1965, p. 272) to relate the flux as a function of velocity to the distribution function. Consider particles passing *outward* through a wall of area δA with a unit vector normal to the surface $\hat{\mathbf{n}}$. For particles with velocity between $\mathbf{v}$ and $\mathbf{v} + \delta\mathbf{v}$, one can think of the particles that pass through the wall in time δt as inhabiting a prism volume of base δA, long side $v\delta t$, and height $\delta t\mathbf{v} \cdot \hat{\mathbf{n}}$. Then the total number of particles with velocity between $\mathbf{v}$ and $\mathbf{v} + \delta\mathbf{v}$ passing *out* through the surface δA per unit time δt is

$$\frac{\mathrm{d}F(\mathbf{x},t)}{\mathrm{d}\mathbf{v}}\mathrm{d}\mathbf{v}\delta A\delta t = f(\mathbf{x},\mathbf{v},t)(\mathbf{v}\delta t)\cdot(\delta A\hat{\mathbf{n}})\mathrm{d}\mathbf{v} \tag{4.1}$$

$$= f(\mathbf{x},\mathbf{v},t)v\cos\gamma\mathrm{d}\mathbf{v}\delta A\delta t, \tag{4.2}$$

where $F(\mathbf{x},t) = \int F_v(\mathbf{x},\mathbf{v},t)\mathrm{d}\mathbf{v}$ and $\cos\gamma = \mathbf{v}\cdot\hat{\mathbf{n}}/v$. In the simulations, I consider the flux of dark matter passing within a height z_c of the reference plane at the Earth's orbit. In this case, $\hat{\mathbf{x}} = \mathbf{n}$ in heliocentric coordinates, and so $\cos\gamma$ is the angle between the velocity vector and the radial direction. However, I am not interested in the direction of the flux, since I consider particles passing both ways through this surface, so I estimate the distribution function from the simulations using

$$\frac{\mathrm{d}F(\mathbf{x},t)}{\mathrm{d}\mathbf{v}}\mathrm{d}\mathbf{v}\delta A\delta t = f(\mathbf{x},\mathbf{v},t)v|\cos\gamma|\mathrm{d}\mathbf{v}\delta A\delta t, \tag{4.3}$$

or

$$f(\mathbf{x},\mathbf{v},t) = \frac{\mathrm{d}F(\mathbf{x},t)/\mathrm{d}\mathbf{v}}{v|\cos\gamma|} \tag{4.4}$$

$$= \frac{\mathrm{d}F(\mathbf{x},t)/\mathrm{d}\mathbf{v}}{|v_r|}, \tag{4.5}$$

since $v_r = v\cos\gamma$ is the velocity component in the radial direction with respect to the Sun.

I now demonstrate how fluxes are obtained from the simulations. For each simulation, I start integrating the orbits of N_p particles (see Tables 2.1 and 2.2) at time t_i since the birth of the solar system. Particles scatter into the solar system at a rate $\dot{N}(t_i)$, where t_i is the time at which the particle first scatters onto a bound orbit in the weak scattering simulations (i.e., the integral over Eq. 2.29), or when the particle first crosses inward

through a shell of radius R in the gravitational capture simulations (i.e., the integral over Eq. (2.41) with limits $E_{min} \leq E \leq E_{max}$ and $J^2_{min} \leq J^2 < J^2_{max}$). In principle, $\dot{N}$ in either type of simulation can vary with time if the halo dark matter distribution function varies on timescales shorter than the age of the solar system, but I assume that the halo distribution function is static, so that $\dot{N}(t_i) = \dot{N}$.

In order to estimate the dark matter distribution function at the Earth, I must make assumptions about the Earth's orbit. In my analysis, I treat the Earth as moving in a circular orbit of radius $a_\oplus = 1$ AU about the Sun in the Sun-Jupiter reference plane. To estimate the flux, each time a particle α crosses 1 AU within a height z_c of this reference plane, I record the time of passage $t_{\alpha\beta}$ (here, β labels the particular passage of the particle α through the Earth's orbit) since the start of the simulation at t_i, position $\mathbf{x}_{\alpha\beta}$, and velocity $\mathbf{v}_{\alpha\beta}$. The height z_c is chosen to be larger than the radius of the Earth $R_\oplus$ in order to improve statistics, but is small enough ($z_c \ll 1$ AU) so that my estimate should be unaffected by gradients in flux as a function of height. Typically, I choose $z_c \lesssim 10^{-3}$ AU.

Each particle crossing can be characterized as one point in a six-dimensional phase space: $\mathbf{n}_{\alpha\beta}$, the vector describing the orientation (ϕ, z) of the particle when it crosses the cylinder of radius $a_\oplus$; the three components of the velocity $\mathbf{v}_{\alpha\beta}$; and $t_{\alpha\beta}$. The vector $\mathbf{n}_{\alpha\beta}$ only has two independent coordinates since the radial component of $\mathbf{x}_{\alpha\beta}$ is fixed. I can estimate the flux of particles passing passing through a patch of the cylinder at position $\mathbf{n}$ in the cylinder at time t since the birth of the solar system, for which the particles had initial scattering time in the Sun (weak scattering) or initially entered the solar system (gravitational capture) at time t_i, with velocity between $\mathbf{v}$ and $\mathbf{v} + \mathrm{d}^3\mathbf{v}$, as

$$\begin{aligned} \frac{\mathrm{d}\hat{F}}{\mathrm{d}\mathbf{v}\mathrm{d}t_i} &= \sum_{\alpha=1}^{N_p}\sum_{\beta=1}^{N_\alpha} \dot{N} w(\lambda_\alpha)\delta^{(6)}(\mathbf{n}-\mathbf{n}_{\alpha\beta}, \mathbf{v}-\mathbf{v}_{\alpha\beta}, t-(t_i+t_{\alpha\beta})) \\ &\quad \Big/ \int \mathrm{d}\lambda \sum_{\alpha=1}^{N_p} w(\lambda)\delta(\lambda-\lambda_\alpha) \end{aligned} \tag{4.6}$$

for each experiment. There are many aspects of this equation which require explanation. Here, $\hat{F}$ denotes that this is an *estimator* for the true flux F, and $\hat{F}(\mathbf{n}, t)$ is the estimator for the total flux passing through the cylinder at a position $\mathbf{n}$ in the cylinder at time t. The

total flux can be estimated by integrating Eq. (4.6) over t_i and $\mathbf{v}$. N_α is the total number of times particle α crosses the Earth's orbit. The function $w(\lambda)$ weights each particle according to its initial conditions λ. The weight function describes how much I sample λ relative to the initial particle distribution at the first scatter (weak scattering simulations) or when the particles first cross a shell of radius R (gravitational capture simulations). The denominator of Eq. (4.6) exists to normalize the flux. To demonstrate how this weighting works, and why it is necessary, I will first discuss the weak simulations in detail, and then discuss the gravitational capture simulations.

For the weak scattering simulations, the initial distribution of bound particles is described by Eq. (2.29). Therefore, the initial conditions for each particle, according to Eq. (2.29), can be described by $\lambda_\alpha = (r_\alpha, v_\alpha, \Omega_\alpha)$, were α denotes that these are the initial coordinates for particle α. In these simulations, I sample the initial distribution of bound particles strictly according to Eq. (2.29). Thus, $w = 1$ for each particle α. For those simulations,

$$\sum_{\alpha=1}^{N_p} w(\lambda)\delta(\lambda - \lambda_\alpha) \quad = \quad \sum_{\alpha=1}^{N_p} \delta(\lambda - \lambda_\alpha) \tag{4.7}$$

so that

$$\int \mathrm{d}\lambda \sum_{\alpha=1}^{N_p} w(\lambda)\delta(\lambda - \lambda_\alpha) = N_p, \tag{4.8}$$

where the integral over λ spans the entire range of λ_α. For the weak scattering simulations, then, the flux at position $\mathbf{n}$ as a function of velocity, observation time, and initial time t_i is

$$\frac{\mathrm{d}\hat{F}_{weak}}{\mathrm{d}\mathbf{v}\mathrm{d}t_i} \quad = \quad \frac{\dot{N}}{N_p} \sum_{\alpha=1}^{N_p} \sum_{\beta=1}^{N_\alpha} \delta^{(6)}(\mathbf{n} - \mathbf{n}_{\alpha\beta}, \mathbf{v} - \mathbf{v}_{\alpha\beta}, t - (t_i + t_{\alpha\beta})). \tag{4.9}$$

For the gravitational capture simulations, I oversample the particle distribution in Eq. (2.41) by a factor of $(J^2(E_{max}, r_p^{max}) - J^2(E_{min}, r_p^{min}))/(J^2(E, r_p^{max}) - J^2(E, r_p^{min}))$. Thus, for these simulations,

$$w(E) = \left(J^2(E, r_p^{max}) - J^2(E, r_p^{min})\right) / \left(J^2(E_{max}, r_p^{max}) - J^2(E_{min}, r_p^{min})\right). \tag{4.10}$$

In this case, $\lambda_\alpha = (E_\alpha, J_\alpha^2)$, and so

$$\sum_{\alpha=1}^{N_p} w(\lambda)\delta(\lambda - \lambda_\alpha) = \sum_{\alpha=1}^{N_p} w(E)\delta^2(E - E_\alpha, J^2 - J_\alpha^2), \tag{4.11}$$

leading to

$$\int \mathrm{d}\lambda \sum_{\alpha=1}^{N_p} w(\lambda)\delta(\lambda - \lambda_\alpha) = \sum_{\alpha=1}^{N_p} w(E_\alpha). \tag{4.12}$$

Therefore,

$$\frac{\mathrm{d}\hat{F}_{grav}}{\mathrm{d}\mathbf{v}\mathrm{d}t_i} = \dot{N} \sum_{\alpha=1}^{N_p}\sum_{\beta=1}^{N_\alpha} w(E_\alpha)\delta^{(6)}(\mathbf{n} - \mathbf{n}_{\alpha\beta}, \mathbf{v} - \mathbf{v}_{\alpha\beta}, t - (t_i + t_{\alpha\beta}))/\sum_{\alpha=1}^{N_p} w(E_\alpha), \tag{4.13}$$

I am interested in the flux arising from particles entering the solar system at all times prior to the present, not just at a particular time t_i. Therefore, to estimate the total flux in a unit volume of velocity-space, one must integrate Eq. (4.6) over t_i, in the range between the time of the formation of the solar system and the time at which the flux is measured,

$$\frac{\mathrm{d}\hat{F}}{\mathrm{d}\mathbf{v}} = \int_0^t \mathrm{d}t_i \frac{\mathrm{d}\hat{F}}{\mathrm{d}\mathbf{v}\mathrm{d}t_i} \tag{4.14}$$

$$= \begin{cases} \dfrac{\dot{N}}{N_p}\displaystyle\sum_{\alpha=1}^{N_p}\sum_{\beta=1}^{N_\alpha} \delta^{(5)}(\mathbf{n} - \mathbf{n}_{\alpha\beta}, \mathbf{v} - \mathbf{v}_{\alpha\beta})\Theta(t - t_{\alpha\beta}), & \text{weak} \\ \dot{N}\displaystyle\sum_{\alpha=1}^{N_p}\sum_{\beta=1}^{N_\alpha} w(E_\alpha)\delta^{(5)}(\mathbf{n} - \mathbf{n}_{\alpha\beta}, \mathbf{v} - \mathbf{v}_{\alpha\beta})\Theta(t - t_{\alpha\beta}) & \\ / \displaystyle\sum_{\alpha=1}^{N_p} w(E_\alpha). & \text{gravitational} \end{cases}$$

In order to get better statistics for the flux through the Earth, I average the flux in Eq. (4.14) over all positions $\mathbf{n}$ in the cylinder. In this case,

$$\int_{cylinder} \mathrm{d}^2\mathbf{n} = \delta A = 2 \times 2\pi a_\oplus z_c, \tag{4.15}$$

the whole area through which I count particle crossings. This implies that the averaged flux is

$$\frac{\mathrm{d}\hat{\overline{F}}(\mathbf{n},t)}{\mathrm{d}\mathbf{v}} = \frac{1}{\delta A}\int_{cylinder} \mathrm{d}^2\mathbf{n}\frac{\mathrm{d}\hat{F}}{\mathrm{d}\mathbf{v}} \tag{4.16}$$

$$= \begin{cases} \dfrac{\dot{N}}{N_p}\dfrac{1}{\delta A}\displaystyle\sum_{\alpha=1}^{N_p}\sum_{\beta=1}^{N_\alpha}\delta^3(\mathbf{v}-\mathbf{v}_{\alpha\beta})\Theta(t-t_{\alpha\beta}), & \text{weak} \\ \dfrac{\dot{N}}{\delta A}\displaystyle\sum_{\alpha=1}^{N_p}\sum_{\beta=1}^{N_\alpha} w(E_\alpha)\delta^{(3)}(\mathbf{v}-\mathbf{v}_{\alpha\beta})\Theta(t-t_{\alpha\beta}) & \\ \Big/\displaystyle\sum_{\alpha=1}^{N_p} w(E_\alpha), & \text{gravitational,} \end{cases} \tag{4.17}$$

This is, in effect, averaging the flux over the Earth's orbit. I then find the local estimate of the distribution function by inserting Eq. (4.17) into Eq. (4.5).

To find the distribution function in the frame of the Earth, I make the Galilean transformation $\mathbf{u} = \mathbf{v} - \mathbf{v}_\oplus$, where $\mathbf{v}_\oplus$ is the circular velocity of the Earth about the Sun, to find

$$\hat{f}_\oplus(\mathbf{x},\mathbf{u},t) = \hat{f}(\mathbf{x},\mathbf{u}+\mathbf{v}_\oplus,t). \tag{4.18}$$

4.2 Estimating Distribution Functions in Practice

In practice, there are millions of Earth-orbit crossings for the gravitational capture simulations, and billions for the weak scatter simulations. In order to present and use the distribution functions in a manageable form, I use a small z_c and bin the distribution function in velocity-space. For the weak scattering experiments, I set $z_c = 10R_\oplus$, while for the gravitational capture simulation, I use the larger value, $z_c = 10^{-3}$ AU $\approx 23.5R_\oplus$. I use the wider range for the gravitational capture simulations since there are far fewer Earth-orbit crossings. Using different z_c up to $z_c = 10^{-3}$ AU for either type of simulation yields consistent distribution functions, demonstrating the desired result that the estimate for the distribution function does not depend on the choice of z_c.

The most straightforward way of estimating errors in the distribution function and any

calculations derived from it is to use bootstrap resampling. Bootstrap resampling yields accurate parameter and error estimation if the original data sample the underlying distribution fairly well. As is demonstrated in the next chapter, I have fairly low statistics for long-lived Jupiter-crossing particles in the weak scattering simulations, so I am not sampling the underlying distribution of this population very well. However, the simulations sample the population of long-lived particles enough for one to realize that this population is there, and may be important, even if the exact distribution of these particles is not very well known.

To estimate errors in the distribution, for each simulation I perform 500 bootstrap resamplings. In each resampling, I select N resampled initial conditions with replacement from the N original initial conditions. I also determine whether or not each particle rescatters in the Sun before leaving the Sun for the first time on a bound orbit (i.e., I estimate the fraction of particles that experience multiple scatterings in the Sun). I then calculate all the relevant quantities using the trajectories and crossings of the new sample as described in the previous section. I also use these bootstrap resamplings to estimate the direct and indirect detection rates. For the gravitational capture experiments, I sum over the Regular and High Perihelion runs, and the analytic distribution function corresponding to the High Energy run, and add the errors in quadrature since the errors ought to be independent of each other.

4.3 The Distribution Function in the Earth

In the previous section, I found distribution functions in the absence of the Earth's gravity. However, since both direct detectors and neutrino experiments are sensitive to particles well within the potential well of the Earth, it is necessary to find the mapping between the velocity coordinates at distances $\ll 1$ AU from the Earth but well outside the Earth's gravitational field and those at distances $\leq R_\oplus$ from the Earth's center. Let $\mathbf{v} = (v, \theta, \phi)$ denote the velocity outside the Earth's gravitational field in an inertial frame centered on and moving with the Earth, with the polar axis along the Earth's direction of motion,

and the velocity $\mathbf{v}_{loc} = (v_{loc}, \theta_{loc}, \phi_{loc})$ be in the Earth's gravitational field at a position $\mathbf{R} = (R, \gamma, \psi)$ from the Earth's center, where $\mathbf{v}_{loc}$ is also in an inertial frame centered on and moving with the Earth. In these coordinates, the angles θ, θ_{loc}, and γ are measured relative to the direction of motion of the Earth with respect to the Sun, and the ϕ, ϕ_{loc}, and ψ angles are azimuthal.

Since the particle energy E and angular momentum J in this frame are approximately conserved near the Earth (even though the system is embedded in the more complex gravitational field of the solar system), then the local distribution function $f_{\rm loc}$ of dark matter in the gravitational field of the Earth can be written as

$$f_{loc}(\mathbf{R}, \mathbf{v}_{loc}) = f(\mathbf{v}(\mathbf{v}_{loc}, \mathbf{R})). \tag{4.19}$$

Here, $f(\mathbf{v})$ is the dark matter distribution function in the frame of the Earth but far from the Earth's center. Eq. (4.19) is a restatement of Liouville's theorem. The number of particles in an interval between $(\mathbf{R}, \mathbf{v}_{loc})$ and $(\mathbf{R} + \mathrm{d}\mathbf{R}, \mathbf{v}_{loc} + \mathbf{dv}_{loc})$ is

$$\mathrm{d}N = f_{loc}(\mathbf{R}, \mathbf{v}_{loc})\mathrm{d}^3\mathbf{R}\mathrm{d}^3\mathbf{v}_{loc}. \tag{4.20}$$

If the distribution function $f(\mathbf{v})$ were isotropic, then the mapping between velocity coordinates would be greatly simplified. In such a situation, the speeds v and v_{loc} are related through conservation of energy,

$$E = \frac{1}{2}v^2 = \frac{1}{2}v_{\rm loc}^2(R) + \Phi_{\oplus}(R), \tag{4.21}$$

assuming that the Earth's potential $\Phi_{\oplus}$ is spherical. Therefore, the number of dark matter particles with positions between $\mathbf{R}$ and $\mathbf{R} + \mathrm{d}\mathbf{R}$ and speeds between $\mathbf{v}_{loc}$ and $\mathbf{v}_{loc} + \mathrm{d}\mathbf{v}_{loc}$ can be represented as

$$\mathrm{d}N_{iso} = 4\pi v_{loc}^2 f(v(R, v_{loc}))\mathrm{d}^3\mathbf{R}\mathrm{d}v_{loc}. \tag{4.22}$$

However, in general, the distribution functions resulting from weak and gravitational capture of particles in the solar system are not isotropic in the frame of the Earth. Thus, it is necessary to find $\mathbf{v}$ in terms of the velocity $\mathbf{v}_{loc}$ at position $\mathbf{R}$. The speeds are still

related by Eq. (4.21), so that v is a function of only two variables, v_{loc} and R. The angular coordinates (θ, ϕ), however, will now be a complicated function of all six local phase space coordinates, so that the number of particles at $(\mathbf{R}, \mathbf{v}_{loc}$ is described as

$$\mathrm{d}N = R^2 v_{loc}^2 f(v(R, v_{loc}), \cos\theta(\mathbf{R}, \mathbf{v}_{loc}), \phi(\mathbf{R}, \mathbf{v}_{loc}))\mathrm{d}R\mathrm{d}\cos\gamma\mathrm{d}\psi\mathrm{d}v_{loc}\mathrm{d}\theta_{loc}\mathrm{d}\phi_{loc}. \quad (4.23)$$

To relate the angular coordinates, I make use of angular momentum conservation as well as energy conservation, and the fact that the problem reduces to a spherically symmetric two-body problem. Since orbits are confined to a plane, one can think of $\mathbf{R}$ and $\mathbf{v}_{loc}$ as a set of basis vectors for the orbital plane, assuming that the vectors are not parallel. Then, in general, the position $\mathbf{R}_{far}$ and velocity $\mathbf{v}$ far from the Earth can be described by

$$\mathbf{R}_{far} = \alpha\mathbf{R} + \beta\mathbf{v}_{loc}, \quad (4.24)$$

$$\mathbf{v} = \gamma\mathbf{R} + \delta\mathbf{v}_{loc}, \quad (4.25)$$

where the coefficients α, β, γ, and δ only depend on the local coordinates $\mathbf{R}$ and $\mathbf{v}_{loc}$, E, and J. If the Earth's potential were purely Keplerian, α and β would be the Gauss f and g functions (see Section 2.5 in Murray & Dermott, 2000), with $\gamma = \dot{\alpha}$ and $\delta = \dot{\beta}$. The functional form of the coefficients is different in the case of non-Keplerian spherically symmetric potentials, but the general framework of Eqs. (4.24) and (4.25) holds. Therefore, Eqs. (4.24) and (4.25) describe the mapping between coordinates in the gravitational field of the Earth to those outside the Earth's sphere of influence.

Chapter 5

Results

In this Chapter, I present the results of my simulations, as well as predictions for direct detection experiments and neutrino telescopes. First, it is important to define some terms that will be used frequently throughout this chapter. "Heliocentric frame" describes an inertial frame moving with the Sun. When I discuss "heliocentric speeds," I will generally mean particle speeds relative to the Sun, measured at the Earth assuming the Earth has zero mass. "Geocentric frame" refers to an inertial frame moving with the Earth. If I refer to a distribution function as being defined in the geocentric frame, it is to be understood that the velocities are those that I would obtain if the Earth had zero mass. The "free space" distribution function, Eq. (2.6), is the angle-averaged halo distribution function in an inertial frame moving with the Sun, outside of the gravitational sphere of influence of the Sun. The "unbound" distribution function refers to the Liouville transformation of the free space distribution function to the position of the Earth (Eq. 2.9), including the effects of the gravitational field of the Sun but not the Earth. In the text, I will make it clear whether I use this distribution function in the heliocentric or geocentric frame.

In Section 5.1, I present the bound distribution functions from the simulations, and I describe how the distribution functions depend on the WIMP mass and elastic scattering cross sections, both spin-independent and spin-dependent. In Section 5.2, I find the contribution of the bound particles to direct detection event rates, and in Section 5.3, I present

neutrino-induced muon event rates from bound WIMPs that annihilate in the Earth.

5.1 Distribution Functions

In this section, I present the bound dark matter distribution functions resulting from my simulations. First, I will discuss the results of the weak scattering simulations. The interpretation of these results will allow me to generalize the distribution functions to broad ranges of WIMP mass and both spin-independent and spin-dependent cross sections. Next, I will examine the results of the gravitational capture simulations, and will discuss the results in the context of WIMP parameter space, as well as unmodeled effects such as the stripping of high energy bound orbits due to the Galactic tidal field.

5.1.1 Weak Scatter Simulations

Raw Results

I present the results of my simulations in Figures 5.1 and 5.2. In Figure 5.1, I show the two-dimensional distribution function $f(v, \cos\theta) = \int \mathrm{d}\phi f(v, \cos\theta, \phi)$ for the CDMS simulation (Table 2.1) in both (a) heliocentric and (b) geocentric coordinates. The angle between the velocity vector and the direction of the Earth's motion is θ, while ϕ is an azimuthal angle, with $\phi = 0$ corresponding to the direction of the north ecliptic pole if $\theta = \pi/2$. The distribution functions are plotted on a logarithmic scale to highlight structure. I only show the CDMS simulation results in this Figure because the phase space structure of the distribution function is virtually the same in all simulations, while the magnitude of the distribution functions is most easily displayed using the one-dimensional representation in Figure 5.2.

In Figure 5.2, I present the one-dimensional geocentric distribution functions divided by the halo WIMP number density n_χ (see Section 2.1.2 for the definition) resulting from all simulations. These distribution functions have already been integrated over angles, and are normalized such that the bound dark matter density $n_{\chi,bound} = \int \mathrm{d}v v^2 f(v)$, where

(a)

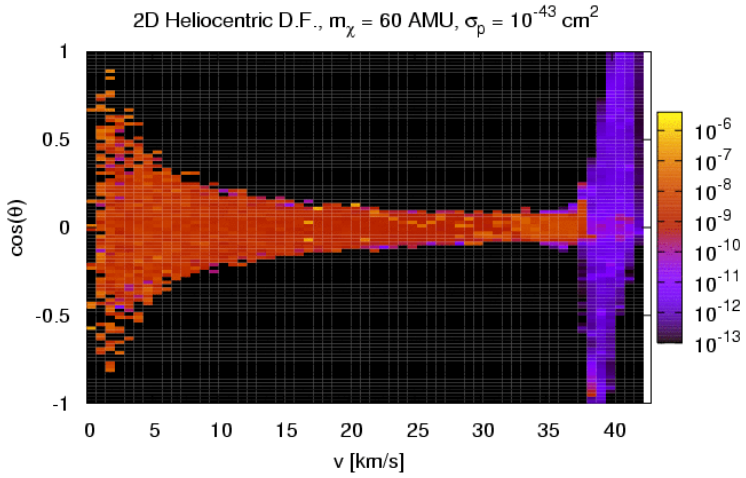

(b)

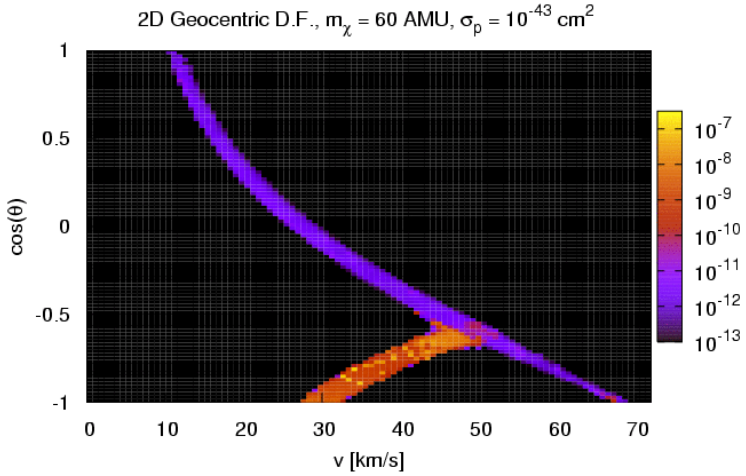

Figure 5.1: Distribution functions divided by n_χ in the $v - \cos\theta$ plane (integrated over ϕ) for both (a) heliocentric and (b) geocentric frames. These distribution functions come from the CDMS simulation, and the units are $(\text{km s}^{-1})^{-3}$

(a)

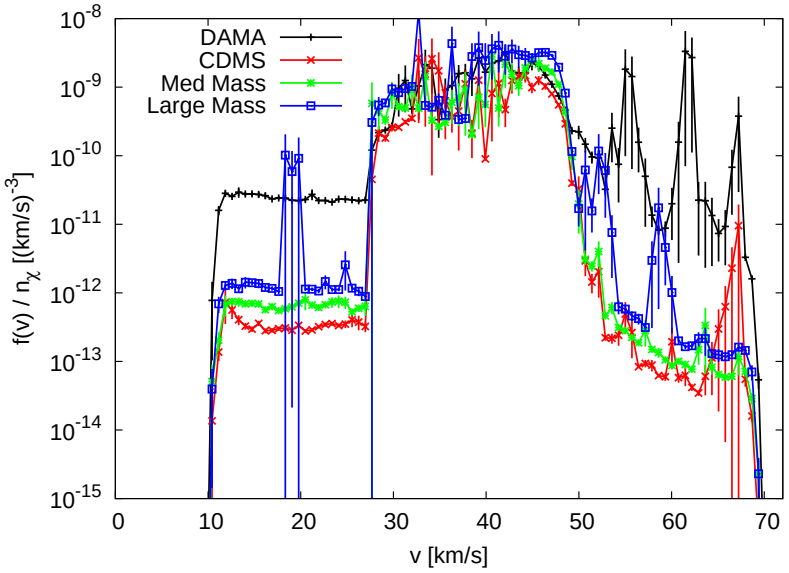

(b)

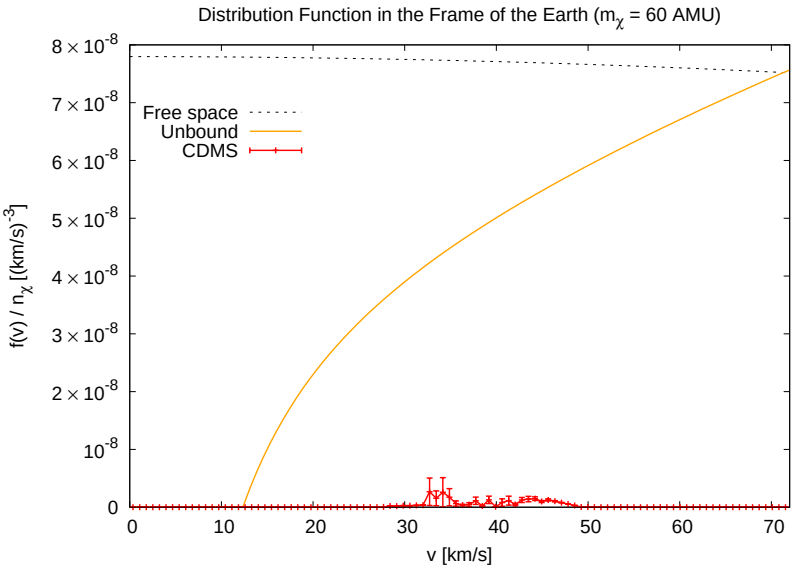

Figure 5.2: Geocentric distribution functions from the simulations. (a) Results from all simulations. (b) The CDMS distribution function relative to theoretical distribution functions for unbound WIMPs.

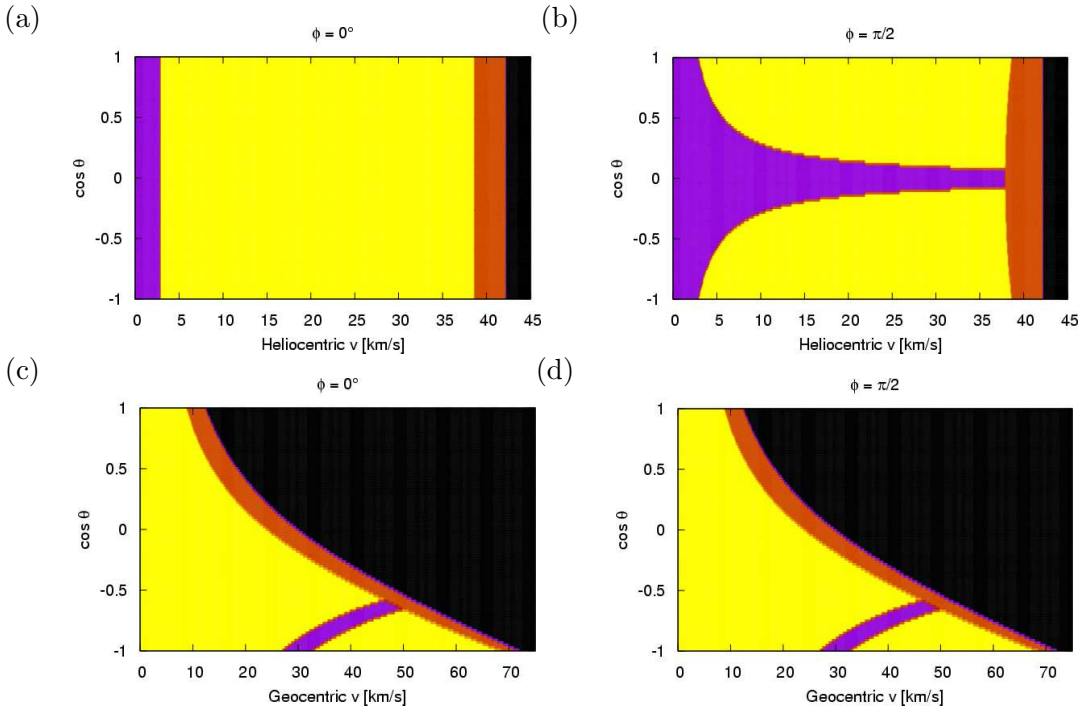

Figure 5.3: Locations of various types of orbits in the (a) $\phi = 0$ and (b) $\phi = \pi/2$ slices of heliocentric velocity space, and (c) $\phi = 0$ and (d) $\phi = \pi/2$ slices of geocentric velocity space.

$f(v) = \int \mathrm{d}\Omega f(\mathbf{v})$. I plot the distribution functions in Figure 5.2(a) on a logarithmic scale in order to highlight the structure of the distribution functions, while I plot the CDMS (Table 2.1) result on a linear scale in Figure 5.2(b) to compare the simulation results with theoretical distribution functions. The distribution functions are based on $(1-4) \times 10^8$ passages of particles within a height $|z| < 10R_\oplus = z_c$ of the Earth's orbit. The distribution functions are insensitive to z_c, at least in the range $1 \lesssim z_c \lesssim 25R_\oplus$. Error bars are based on 500 bootstrap resamplings of the initial scattered particle distributions for each simulation.

Before I delve into the details of how the distribution functions depend on WIMP parameters, I will explain the morphology of the phase space density of the bound particles. First, I will focus on the two-dimensional distribution functions shown in Figure 5.1. The features in these distribution functions can be explained by the graphs in Figure 5.3. In this Figure, I show what types of orbits inhabit $(v, \cos\theta)$ space for fixed ϕ in both heliocentric

and geocentric coordinates. For each point in velocity space, I calculate the energy and angular momentum of the orbit. The black region of velocity space represents unbound orbits. All points in velocity space for which orbits are bound and have perihelia inside the Sun are marked in purple, while all orbits that are bound and cross Jupiter's orbit are marked in orange. The yellow regions correspond to bound orbits that neither enter the Sun nor cross Jupiter's path. The $\phi = \pi/2$ slices corresponds to motions lying in the reference plane of the solar system, while the $\phi = 0$ slice corresponds to motion lying in a plane defined by the direction of motion of the Earth and the north ecliptic pole. In the heliocentric plots, there is a much broader swath of Sun-penetrating orbits in the $\phi = \pi/2$ slice than the $\phi = 0$ slice because the angular momenta in the $\phi = 0$ slice are higher ($J = a_{\oplus} v \sqrt{\cos^2\theta + \sin^2\theta \cos^2\phi}$) than in the $\phi = \pi/2$ slice for a given θ. However, the two slices look similar in the geocentric frame because the velocities in this frame have to be translated to the heliocentric frame to find E and J.

Figure 5.3 was computed for a system without planets. Once Jupiter is added, another type of orbit that may exist is a bound orbit for which J_z is fixed but J can have a range of values for fixed v. This is a Kozai-type orbit. In this case, $J_z = a_{\oplus} v \cos\theta$ in the heliocentric frame. In the special case that $\phi = \pi/2$, $J = J_z$. Therefore, the parts of $(v, \cos\theta)$ phase space in the $\phi = \pi/2$ plane corresponding to Sun-penetrating orbits also cover orbits with J_z fixed by the initial scatter in the Sun for other values of ϕ.

The main result from Figure 5.3 is that the $\phi = \pi/2$ plots are almost identical to those in Figure 5.1, with an extra bit in the heliocentric velocity phase space covered by the distribution function (near $v = 37$ km s^{-1} for all $\cos\theta$) corresponding to lower-ϕ slices. However, there are some small discrepancies between the two sets of plots, for example, in the heliocentric distribution function at $v > 40$ km s^{-1} and $\cos\theta < 0$. I will describe those discrepancies when I describe the related features in Figure 5.2. In general, Figure 5.3 is a guide to understanding which orbits correspond to which parts of the distribution functions in Figure 5.1.

Now let me focus on Figure 5.2(a). The four simulation distribution functions generally

have the same form, and in particular, share three distinct features. The first is a "high plateau" spanning the speed range $27 < v < 50$ km s^{-1}. From Figure 5.3(d), one sees that there are three types of orbits that correspond to these velocities: Sun-penetrating particles, particles with fixed J_z, and a subset of Jupiter-crossing particles. However, from Figure 5.1(b), it is clear that the non-Jupiter-crossing orbits have far higher phase space density. Therefore, this high plateau represents the contribution from particles that are *not* on Jupiter-crossing orbits.

The second feature of the distribution functions in Figure 5.2 is what I will call the "low plateau." This is the relatively flat part of the distribution function that extends from ≈ 10 km s^{-1} to ≈ 70 km s^{-1}. This low plateau corresponds to the part of the two-dimensional distribution function in Figure 5.1(b) which has been identified by Figure 5.3(d) as representing Jupiter-crossing orbits. However, one can ask the question, why doesn't the range extend down to $v = 8.8$ km s^{-1}, which is the minimum speed a Jupiter-crossing particle can reach in the geocentric frame (Figure 5.3(d)), or up to $v = 71.9$ km s^{-1}, which is the speed a parabolic particle with its speed upon Earth-crossing exactly anti-aligned with the Earth's motion? These velocities are allowed in Figure 5.3(d), but the distribution function in the range $8.8 < v < 10$ km s^{-1} and $70 < v < 71.9$ km s^{-1} is zero in Figures 5.1(b) and Figure 5.2.

The reason for truncation in v is a direct result of the narrow range of Jacobi constant C_J resulting from scatter in the Sun. Here, I describe how to find the minimum v_{min} and maximum v_{max} geocentric speeds allowed by the initial distribution of particles in phase space. Small geocentric speeds are achieved by exactly aligning a small heliocentric speed vector with the direction of motion of the Earth. Quantitatively, the heliocentric speed of a particle at the Earth with semi-major axis a is given by Eq. (1.62), and increasing function such that $v(0.5a_\oplus) = 0$ and $v(\infty) = v_{esc}^\odot = \sqrt{2}v_\oplus$. For Jupiter-crossing orbits, the minimum heliocentric speed is $v(a_J/2)$, and so the minimum geocentric speed for Jupiter-crossing orbits is $v(a_J/2) - v_\odot = 8.8$ km s^{-1}, such that the speed vectors are parallel. Maximum geocentric speeds are reached by antialigning nearly parabolic orbits with respect to $\mathbf{v}_\oplus$.

These points are highlighted in the endpoints of the Jupiter-crossing two-dimensional geocentric distribution function for the CDMS run in Figure 5.1(b). Recalling Chapter 3, the Jacobi constant is defined as

$$C_J = -2(E - n_J J_z), \tag{5.1}$$

where E is the particle energy and n_J is the mean motion of Jupiter. The Jacobi constant for Jupiter-crossing particles can be approximately described by

$$C_J^i \approx -2E_i = \frac{GM_\odot}{a_i}, \tag{5.2}$$

where a_i is the initial semi-major axis of the particle, where I have neglected the (small) contributions to C_J from Jupiter and the small initial value of $|J_z|$.

First, let me describe how to find the minimum allowable geocentric particle speed. There are two important points in finding the minimum allowable geocentric speed given Jacobi constant conservation. First, the statement that a particle must have its heliocentric velocity vector colinear with the direction of the Earth's motion is equivalent to the statement that the particle must have a large, positive J_z, and that $J \approx J_z$. In addition, the particle should either be at perihelion or aphelion when it intersects the Earth's orbit, such that $J_z = a_\oplus v(a_{min})$, where a_{min} is the semi-major axis corresponding to v_{min} (Eq. 1.62). Therefore, from Eq. (5.1), one sees that in order to find the J_z corresponding to v_{min}, a_i should be as small as possible while still allowing Jupiter to significantly change the Jacobi constant. This means that $a_i = a_J/2$ for $C_J^{max} = GM_\odot/a_i$, since Jupiter cannot perturb J_z enough for smaller orbits. This fact is evident in Figure 5.1(a); if Jupiter could significantly perturb J_z, than the distribution function would spread out into the regions of Figure 5.3(b) that correspond to orbits that do not penetrate the Sun or have J_z fixed by the initial scatter.

Secondly, as J_z increases (as it must in order for the velocity vector to align with the direction of the Earth's motion), E must increase in order to conserve C_J. Therefore, the smallest orbit for which a Jupiter-crossing particle can be exactly aligned with the Earth's motion is greater than $a = a_J/2$. Since $v(a)$ increases with a (Eq. 1.62), the minimum geo-

centric speed for which the bound distribution function at the Earth is non-zero is greater than $v = 8.8$ km s^{-1}. Using $J_z = a_\oplus v(a_{min})$, One can then solve

$$C_J^i = C_J(v_{min}) \tag{5.3}$$

$$\frac{2GM_\odot}{a_J} = -2\left(-\frac{GM_\odot}{2a_{min}} - n_J a_\oplus v(a_{min})\right) \tag{5.4}$$

for a_{min}, and hence find the smallest $v_s(a_{min})$ and geocentric v_{min}. The semi-major axis corresponding to v_{min} is

$$a_{min} = \frac{1}{2}\frac{a_J}{a_\oplus}\frac{1}{1-(a_\oplus/a_J)^{1/2}} \times a_\oplus \tag{5.5}$$

$$\approx 4.6 \text{ AU}, \tag{5.6}$$

which leads to a minimum speed of $v_{min} \approx 10$ km s^{-1}, consistent with what I find in Figure 5.2.

This set of arguments also explains why the heliocentric distribution function in Figure 5.1(a) is not symmetric about $\cos\theta = 0$ for Jupiter-crossing orbits, which it should be if all Jupiter-crossing orbits in Figure 5.3(b) were represented in the distribution function. Above $v > v(a_J/2) = 38$ km s^{-1}, orbits with $\cos\theta > 0$ are suppressed due to the initial distribution of C_J. To find the minimum speed for a given $\cos\theta$ in the heliocentric frame, one finds an expression for $J_z(\cos\theta)$, and then plugs that into Eq. (5.1), and solves for a assuming $a_i = a_J/2$.

To find the maximum allowed geocentric speed, one must find the maximum heliocentric speed (alternatively, the largest semi-major axis a) that may be anti-aligned with respect to the Earth's motion given the C_J distribution of Jupiter-crossing particles. This is equivalent to finding a very negative J_z. If the particle speed exactly anti-aligned with respect to the Earth's motion when crossing the Earth's orbit, then $J_z = -a_\oplus v(a)$, and so

$$C_J = -2\left(-GM_\odot/2a + n_J a_\oplus v(a)\right). \tag{5.7}$$

As in the case of the minimum geocentric speed, the maximum geocentric speed is achieved by a particle with initial semi-major axis $a = a_J/2$. Setting $C_J = GM_\odot/(a_J/2)$ and

solving Eq. (5.7), one finds that the maximum semi-major axis for which the orbit can be instantaneously anti-aligned with the direction of the Earth's motion is

$$a(v_{max}) = a_{\oplus}\frac{1}{2}\frac{1}{[y-y^3]-[2y^3-2y^4+y^6]^{1/2}} \quad (5.8)$$

$$\approx 6.4 \text{ AU}, \quad (5.9)$$

where I have set $y = a_{\oplus}/a_J$, corresponding to a maximum geocentric speed of

$$v_{max} \approx 70 \text{ km s}^{-1}, \quad (5.10)$$

which is consistent with the simulation results.

As with the arguments leading up to an analytic expression for v_{min}, one can extend the arguments in this section to explain the structure of the heliocentric two-dimensional distribution function in Figure 5.1(b). There is a speed-dependent dearth of phase space at large heliocentric speeds for $\cos\theta < 0$. The maximum speed allowed for a given $\cos\theta$ can be determined by finding an expression for J_z as a function of $\cos\theta$, and then solve Eq. (5.1) for a, and hence v_{max}, given $a_i = a_J/2$.

The third common set of features in the one-dimensional geocentric distribution function in Figure 5.2 are spikes in the low plateau. These spikes result from Jupiter-crossing or nearly Jupiter-crossing particles that spend long times near mean motion resonances. While some particles spend a long time near external resonances, most of the power in the spikes comes from particles that either spend the majority of their lifetimes near the $3:1$ ($a = 2.5$ AU) or $2:1$ ($a = 3.27$ AU) resonances, or are at or migrating between minor resonances between the $3:1$ and $2:1$ resonances. The minimum semi-major axis for these spikes corresponds to the 3:1 resonance, $a \approx 2.5$ AU. It has been observed, in the context of comet orbits, that chaotic orbits exterior to the orbit of Jupiter can hover near mean motion resonances for long periods of time, causing the existence of a long lifetime tail for comet orbits (Malyshkin & Tremaine, 1999). This phenomenon has been dubbed "resonance sticking." The particles are not captured into a resonance (in the original Malyshkin & Tremaine (1999) paper, there is no mechanism for capture), but are on chaotic orbits that stay near the resonance. While resonance sticking has only been explored in the context

of nearly parabolic orbits coplanar with Jupiter's orbital plane, it seems likely that this mechanism is at work for bound dark matter particles. The error bars on the spikes are large due to the very low numbers of particles in the resonances. Not all major resonances have such a long-lived particles stick to them in each simulation, which is why the different simulations do not have the same spike distributions.

Another aspect of Figure 5.2 is that some of the error bars on the non-resonant distribution function are fairly large. As I will discuss below, these error bars are large because a sizable fraction of the distribution function comes from a small number (a few hundred) long-lived particles in each simulation. It is likely that I am not sampling the population of long-lived particles very densely since I did not *a priori* know which WIMPs would dominate the distribution function (and hence, could not design the numerical experiment to oversample those particles), so some of the error bars are likely to be underestimated. However, the true height of the high plateau in each simulation is likely to not be too far off from those shown in Figure 5.2.

It is, in fact, highly unlikely that simulating more particle orbits will make the low plateau rise above its very low height. The last important fact about the distribution functions from the simulations is that the bound distribution function is much, much lower than the unbound distribution function for low speeds. Later in this section, I will explore how the distribution function depends on the WIMP mass and spin-independent cross section, as well as estimate the dependence on the spin-dependent cross section. The goal of those explanations will be to find the maximum distribution function consistent with current constraints on the WIMP parameter space.

I now examine what types of particle orbits contribute most to the bound distribution functions in each simulation. First, I will classify particle orbits using information on particle lifetimes. Then, I will describe the time evolution of the distribution functions and the local bound dark matter number density. It will then be possible to determine which types of particle orbits dominate the distribution function. Later, I will describe how the distribution function depends on the WIMP mass and the WIMP-baryon cross section.

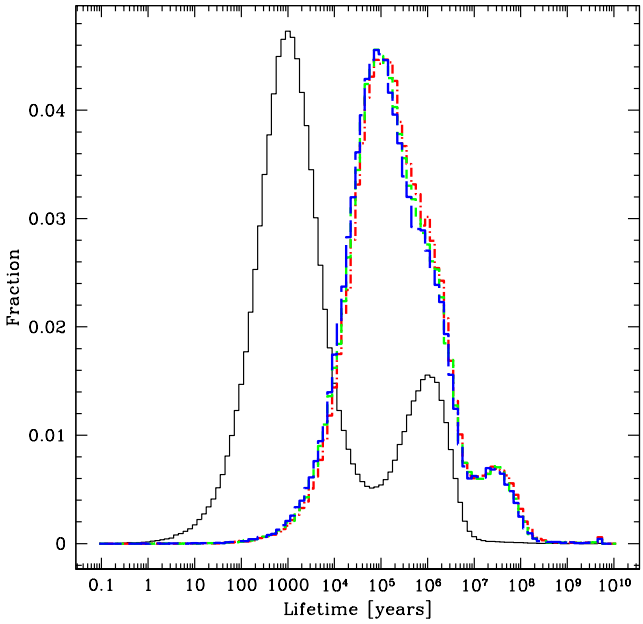

Figure 5.4: Particle lifetime distributions for the DAMA (*solid black*), CDMS (*red dot-dashes*), Medium Mass (*short green dashes*), and Large Mass (*long blue dashes*) simulations.

In Figure 5.4, I present the lifetime distributions for the DAMA (*black line*), CDMS (*red dot-dashes*), Medium Mass (*short green dashes*) and Large Mass (*long blue dashes*) simulations. There are several notable features in this plot. First, and most striking, many of the bound particles survive for very long times—up to $10^6 - 10^8$ yr. Secondly, the lifetime distribution functions of the CDMS, Medium Mass, and Large Mass runs are very similar, with only slight shifts in the distributions due to the fact that the scattering probabilities in the Sun are somewhat dependent on m_χ. However, these lifetime distributions are quite different from that of the DAMA simulation. The main peak in the DAMA simulation is shifted by a factor of 100 (10^3 yr instead of 10^5 yr) and the DAMA simulation is missing the bump in long-lived ($t_{life} \sim 10^7 - 10^8$ yr) particles. The differences in the lifetime distributions are due almost entirely to the elastic scattering cross section, at least for the range of WIMP masses I consider. In none of the simulations is there a large population of particles that survive for times of order the age of the solar system, although there is a

small population that does (the notch at $t_{SS} = 4.5$ Gyr in Figure 5.4).

In order to explain these features, it is useful to examine the lifetime distributions as a function of the initial semi-major axis a_i after the first scatter in the Sun, as shown in Figure 5.5. I plot the histograms in Figure 5.5 on a logarithmic scale to bring out some of the long-lifetime features. The particles are binned by semi-major axis (0.5 AU $\leq a_i <$ 1 AU; 1 AU $\leq a_i <$ 1.5 AU; 1.5 AU $\leq a_i <$ 2 AU; 2 AU $\leq a_i < a_J/2$; $a_i \geq a_J/2$).

The first obvious feature is the strong peak at $t_{life} \sim 10^3$ yr for the DAMA simulation and $t_{life} \sim 10^5$ yr for the simulations with $\sigma_p^{SI} = 10^{-43}$ cm^2, which I will call the "rescattering hump." It encompasses the majority of particles in each simulation. This feature results from WIMPs that rescatter in the Sun before they are ejected from the solar system by Jupiter or precess onto orbits that do not intersect the Sun (Kozai cycles). This rescattering hump is offset between DAMA and the other simulations because the lifetime is inversely proportional to the scattering probability in the Sun, and so $t_{life} \propto \sigma_p^{-1}$. There is one important difference in the morphologies of the rescattering hump between the DAMA and other simulations. Note in Figure 5.5 that particles on Jupiter-crossing orbits exhibit a rescattering feature in the DAMA simulation but not in the other simulations. Indeed, about 23% of Jupiter-crossing particles in the DAMA simulation are rescattered in the Sun, while $< 2\%$ are rescattered in the other simulations. The expanation is that the timescales on which Jupiter can perturb the perihelia of Jupiter-crossing orbits out of the Sun are significantly shorter than rescattering timescales for the $\sigma_p^{SI} = 10^{-43}$ cm^2 simulations, but the two timescales become closer at higher cross sections ($\sigma_p^{SI} = 10^{-41}$ cm^2 for the DAMA simulation).

A second feature occurs at $t_{life} \sim 10^6$ yr, which I call the "ejection hump." This feature occurs at the same time for each simulation, and arises from Jupiter-crossing orbits. It is blended with the rescattering hump for the CDMS, Medium Mass and Large Mass simulations, while it is blended with a different feature in the DAMA simulation. As suggested by the name, the ejection hump results from Jupiter-crossing particles ejected from the solar system, and its characteristic lifetime is therefore independent of cross section.

A third feature, called the "quasi-Kozai hump," is centered at $t_{life} \sim 10^6$ yr in the DAMA simulation, and $t_{life} \sim 10^8$ yr in the other simulations. The feature is seen in the 1.5 AU $\leq a_i <$ 2 AU and 2 AU $\leq a_i < a_J/2$ bins. The particles in the quasi-Kozai hump are not on true Kozai cycles. Recall that Kozai cycles are described in a picture where the Hamiltonian to quadrupole order is time-averaged in such a way as to eliminate short-period and resonant terms (Section 1.4.1). The averaging means that the Hamiltonian is independent of two of the angles, and so two action variables are fixed. This translates to a and $J_z = \sqrt{GM_\odot a(1-e^2)}\cos I$ being fixed. However, there are many major and minor resonances with Jupiter between $a = 1.5 - 2.6$ AU, and therefore, short-term and resonant parts of the Hamiltonian have a significant effect on particle orbits. Thus, Kozai cycles provide a poor description of particle orbits in this range of semi-major axis. In the simulations, particles in the quasi-Kozai hump are observed to alternate between rescattering hump-type orbits with perihelion well inside the Sun, and orbits that look like Kozai cycles with the minimum perihelion located in the outskirts (low optical depth) of the Sun (although the perihelia also are outside the Sun a significant part of the time), even though the particles originate deep within the Sun. Both the semi-major axis and J_z vary with time; neither is conserved although the combination giving the Jacobi constant C_J is fixed (Eq. 5.1). There are some orbits at the low end of the semi-major axis range 1.5 AU $< a \leq a_J/2$ for which a and J_z are conserved and the Kozai description is accurate.

The typical lifetime in the quasi-Kozai hump is inversely proportional to the cross section, since particles are eventually removed from the orbits by rescattering in the Sun. The height of the quasi-Kozai hump relative to the rescattering hump in each relevant semi-major axis bin is also dependent on the elastic scattering cross section. The rescattering hump is higher in the DAMA simulation relative to the other simulations because the optical depth in the Sun is high enough that particles originating deep within the Sun rescatter before the torque from Jupiter can pull the perihelion towards the surface of the Sun. Perhaps more interestingly, the median lifetimes of the particles with 1.5 AU $\leq a_i < a_J/2$ are quite a bit higher than they would be if particles were either on strictly Kozai orbits or

rescattering hump orbits. This is due to the fact that there is much larger participation in these long lifetime orbits relative to particles with significantly lower semi-major axes. Low semi-major axis orbits ($a \sim 1$ AU) can only have long lifetimes if the particle was originally scattered onto a bound orbit in the outskirts of the Sun, which accounts for only a tiny fraction of all particle orbits. However, even particles originating deep in the Sun can have quasi-Kozai orbits unless they rescatter first.

The fourth feature is not obvious in Figure 5.4, but is once the lifetime distribution is displayed on logarithmic scales in Figure 5.5. This feature is the "Kozai hump." This hump is located at about $t_{life} \sim 10^8$ yr for the DAMA simulation, and near $t_{life} \sim t_{SS} = 4.5$ Gyr for the other simulations. This feature results from particles whose orbital evolution can be described by Kozai cycles (a, J_z conserved). For the CDMS, Medium Mass, and Large Mass simulations, the peak is at t_{SS} because that is the point in time at which I terminate the simulations. Particles on these orbits have $a_i < 1.5$ AU, and originate in the outer $r \gtrsim 0.5 R_\odot$ in the Sun. They constitute only a very small fraction of all orbits with $a_i < 1.5$ AU, but dominate the lifetime distribution of particles with lifetimes $\gtrsim 10^8$ yr. The typical lifetime of particles on Kozai cycles depends on the WIMP-nucleon cross section, so it obvious that Damour & Krauss's assumption of lifetimes $t \gg t_{SS}$ is wrong unless the WIMP-nucleon cross section is very small.

Note also that there is very little variation in the morphology of the lifetime distributions for the three simulations with $\sigma_p^{SI} = 10^{-43}$ cm^2. Therefore, the shape of the lifetime distribution is determined almost solely by the elastic scattering cross section, not the particle mass, at least in the range of masses considered in these simulations. It is possible that the lifetime distribution for a very high or very low mass WIMP would perhaps look different from those in Figure 5.5, since particles will preferentially scatter onto high energy orbits (large semi-major axis) if the WIMP mass were high enough. The behavior of bound orbits as a function of WIMP mass and cross section is discussed further in the "Interpretation" and "Implications for High Spin-Dependent Cross Sections" sections.

I will next focus on the time evolution of the dark matter distribution function. The

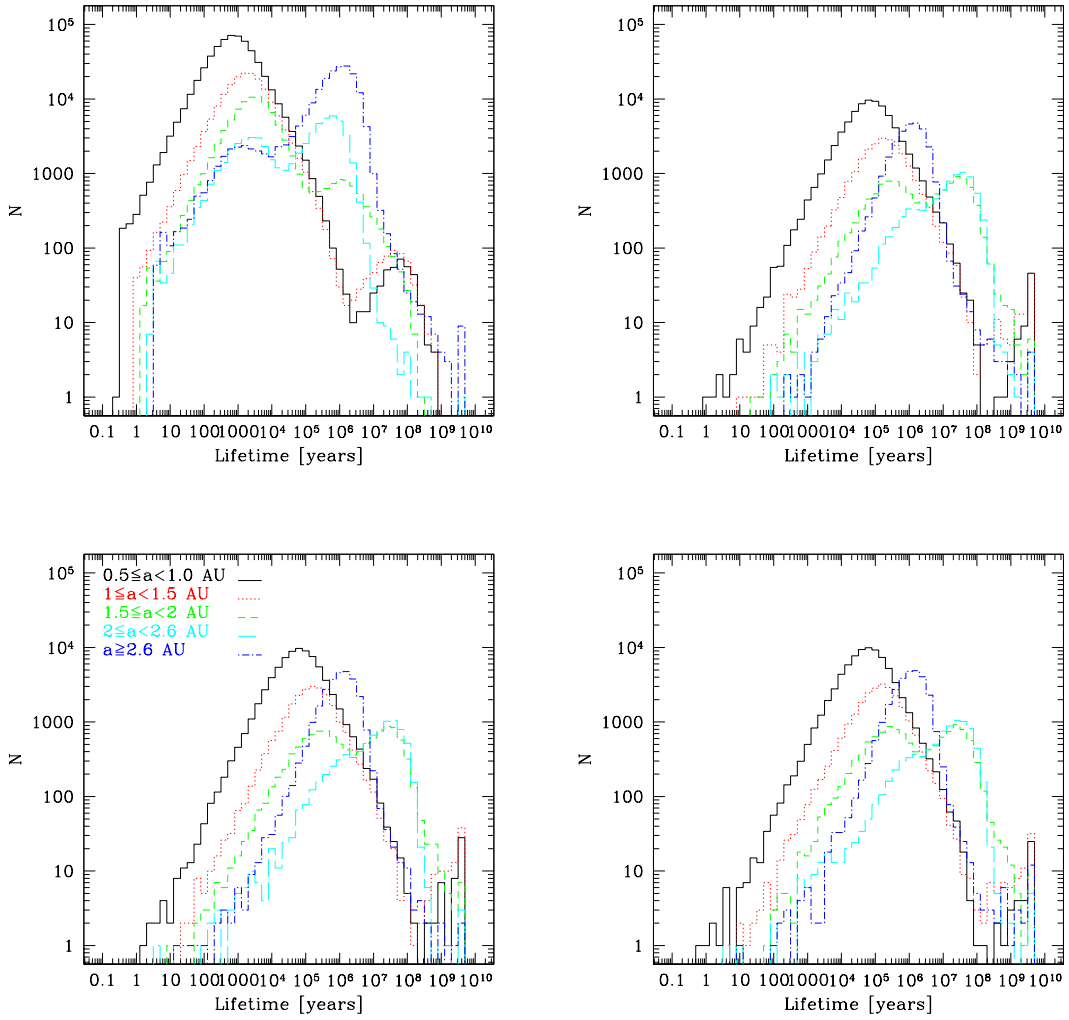

Figure 5.5: Lifetime distributions as a function of initial semi-major axis for the DAMA (*upper left*), CDMS (*upper right*), Medium Mass (*lower left*) and Large Mass (*lower right*) simulations. The solid black line represents particles with 0.5 AU $\leq a_i <$ 1.0 AU, red dots those with 1.0 AU $\leq a_i <$ 1.5 AU, short green dashes those with 1.5 AU $\leq a_i <$ 2 AU, long cyan dashes those with 2 AU $\leq a_i <$ 2.6 AU, and the blue dash-dotted line indicates those with $a_i \geq$ 2.6 AU $= a_J/2$.

evolution of the distribution function as a function of time is closely related to what types of orbits dominate the distribution function. For example, if the rescattering hump particles dominated the distribution function, I would expect that the distribution function would look somewhat like the high plateau in Figure 5.2. This plateau would include Jupiter-crossing particles on near-radial orbits that rescatter before Jupiter can pull the perihelia outside of the Sun. The height of the plateau would reach equilibrium on a timescale of $t_{life} \propto (\sigma_p^{SI})^{-1}$. In contrast, recall that Damour & Krauss (1999) postulate that the distribution function is dominated by particles on Kozai cycles for which the rescattering timescale is longer than the age of the solar system; if this were true in the simulations, then the height of the high plateau ought to increase linearly as a function of time. Moreover, the final height of the plateau would be proportional to σ_P^{SI}, since this determines the initial scattering rate onto bound orbits $\dot{N}_\oplus$.

In Figure 5.6, I show the time evolution of the geocentric speed distributions (using the same normalizations as in Figure 5.2) for the (a) DAMA and (b) CDMS simulations. I focus on these two simulations since the results for the Medium Mass and Large Mass simulations closely resemble those of the CDMS run. In each plot, I show distribution functions constructed with crossing times $t_{cross} < 10^6$ yr (equivalent to the distribution function 10^6 yr after the formation of the solar system), $t_{cross} < 10^7$ yr, $t_{cross} < 10^8$ yr, $t_{cross} < 10^9$ yr, and all crossing times less than the age of the solar system, which I take to be $t_{SS} = 4.5$ Gyr. The crossing time t_{cross} is the time since the start of the simulation at which a particle crosses the Earth's orbit (see also Section 4.1).

Let me first discuss the similarities, and then the differences between the distribution function buildups. First, it is clear that the low plateau, due to Jupiter-crossing particles, is in place by 10^7 yr; in other words, 10 Myr after the birth of the solar system, the low plateau has reached equilibrium. The only growth in the low plateau after 10 Myr comes from particles on resonance-sticking orbits that pump up the spikes. The time evolution of the low plateau (but not its final equilibrium height) is largely independent of cross section over two orders of magnitude in WIMP-baryon cross section. The height of the low plateau

is proportional to the rate at which particles are initially scattered onto Jupiter-crossing orbits, $\dot{N}_J$. Since the scattering rate is proportional to the cross section, the height of the low plateau is proportional to the spin-independent cross section, at least in these simulations. This is illustrated in Figure 5.7, which shows the part of the distribution function due to particles with initial semi-major axis $a_i \geq a_J/2$, for which the distribution functions with $\sigma_p^{SI} = 10^{-43}$ cm^2 are normalized such that the $\dot{N}$ used in Eq. (4.17) to construct the distribution functions is set to the value of $\dot{N}$ for $m_\chi = 60$ AMU. I use this particular normalization so that I can ignore the mass dependence of $\dot{N}$ and isolate the dependence of the low plateau on the cross section. All the features in the DAMA distribution function are about two orders of magnitude higher than those for the other simulations.

The buildup of the high plateau does depend on the cross section, but not in the way predicted by Damour & Krauss (1999). The height of the plateau does not grow linearly with time, nor is the height of the plateau at a given time proportional to the elastic scattering cross section. The high plateau is mostly fixed by $t = 10^8$ yr in the DAMA simulation. Although the plateau grows as a function of time in the CDMS simulation, it is not growing linearly with time. These results are not surprising, given that I have argued that the classical Kozai behavior assumed by Damour & Krauss is seen only in a small fraction of the bound particles, and that those particles have a lifetime that is small with respect to the age of the solar system.

In the DAMA simulation, intersections with the Earth's orbit occurring within 1 Myr of the first scattering in the Sun contribute a total of $\approx 10\%$ to the total number density ($n_\chi^{bound} = \int v^2 f(v) \mathrm{d}v$), those with crossing times $t_{cross} < 10$ Myr contribute $\approx 20\%$ of the total, $\approx 50\%$ have $t_{cross} < 10^8$ yr, and 70% of the number density at the Earth is built up within 1 Gyr (Figure 5.6(a)). The small humps in the $t_{cross} < 10^6$ year and $t_{cross} < 10^7$ year distribution functions near the high speed edge of the high plateau come from quasi-Kozai particles. Almost all of the growth in the distribution function (and number density) from crossing times $t_{cross} > 10^9$ yr is due to resonance-sticking particles. Only one non-Jupiter crossing particle (out of an initial 8×10^5) survives longer than 1 Gyr. These conclusions

(a)

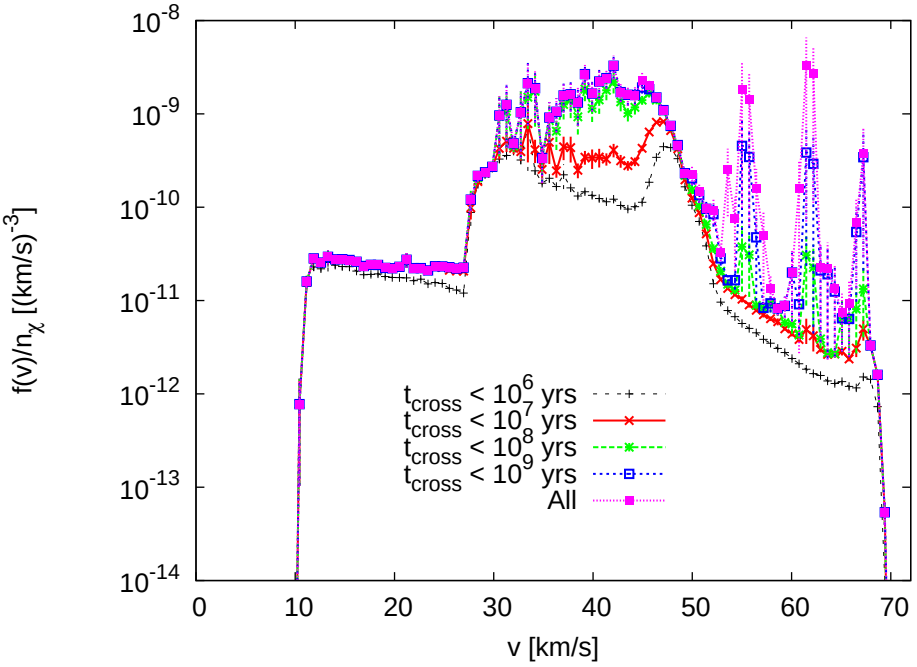

(b)

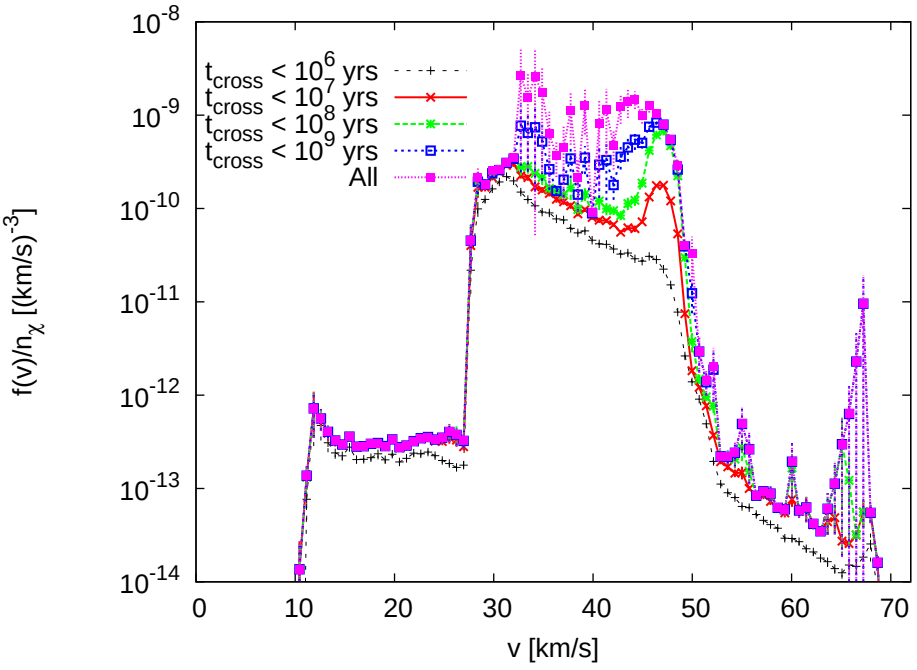

Figure 5.6: Growth of the distribution functions as a function of time for the (a) DAMA and (b) CDMS simulations.

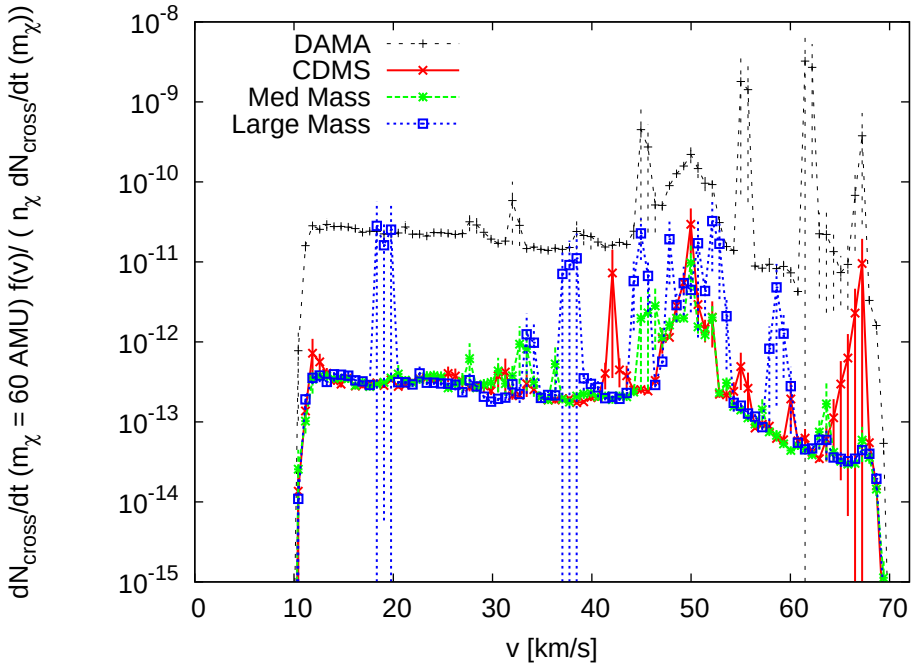

Figure 5.7: Geocentric distribution functions for $a_i > a_J/2$.

are consistent with the lifetime distribution in Figure 5.5, which showed that the median of the Kozai and quasi-Kozai cycle lifetimes was significantly less than 1 Gyr, and that a few Jupiter-crossing particles survive to long times. Therefore, the high plateau in the DAMA simulation has reached equilibrium on timescales shorter than the age of the solar system.

There are several consequences of this finding. First, as I include particles with ever greater crossing times, the error bars on the distribution function increase, since a relatively small number of longer-lived particles dominate the total distribution function. For example, crossings in the time span 10 Myr $< t_{cross} <$ 100 Myr contribute 30% of the current bound dark matter density at the Earth, even though only about 2,500 particles have lifetimes $t_{life} > 10$ Myr, out of a total of $> 10^6$ particle orbits simulated. As demonstrated in Figure 5.5, most of those particles are on Kozai or quasi-Kozai orbits, although there are some long-lived Jupiter-crossing particles, too. Secondly, even at the cross section used in the DAMA simulation ($\sigma_p^{SI} = 10^{-41}$ cm^2), which is smaller than some cross sections considered in Damour & Krauss (1999), the approximation that particles on Kozai cycles have lifetimes

longer than the solar system is inaccurate. Thus, since the particle lifetimes in the high plateau are proportional to the cross section, the high plateau for $\sigma_p^{SI} > 10^{-41}$ cm^2 should be the same as the DAMA high plateau (the shorter lifetime due to the increased cross section is cancelled by the increased initial scattering rate $\dot{N}_\oplus$, which is proportional to the cross section). This approximation should be valid until the elastic scattering cross section is high enough that the Sun is optically thick to WIMPs.

The time evolution of the distribution function is a bit different in the simulations for which $\sigma_p^{SI} = 10^{-43}$ cm^2. As in the case of the DAMA simulation, Earth orbit intersections with $t_{cross} < 1$ Myr contribute about 10% to the total current number density at the Earth. The number density from crossings with $t_{cross} < 10^7$ yr is $15 - 20\%$ of the total depending on the simulation, compared with $30 - 40\%$ for $t_{cross} < 10^8$ yr, and approximately half for $t_{cross} < 1$ Gyr. Just as for the DAMA simulations, this means that the majority of particles (i.e., the ones in the rescattering hump) contribute very little to the distribution function. The error bars on the total distribution function are larger than in the DAMA simulation because fewer ($\sim 100 - 200$) long-lived particles are responsible for half the current number density of particles (versus ~ 300 for DAMA). Unlike in the DAMA simulation, a number of particles have lifetimes longer than the age of the solar system (~ 100 out of $\sim 10^5$). One consequence of this is that the distribution functions should be somewhat smaller than the DAMA distribution function, since the high plateau of the DAMA simulation has reached its maximum height by the present but the $\sigma_p^{SI} = 10^{-43}$ cm^2 distribution functions are still growing. The maximum should be reached once all Kozai particles have been rescattered and then absorbed by the Sun and the distribution function reaches equilibrium.

In the DAMA simulation, about half of the bound dark matter density at the Earth is built up by $t = 10^8$ yr; the other half is due to particles with longer lifetimes. Those long-lived particles are on Kozai cycles, quasi-Kozai cycles, or stick to resonances. Another interesting way to examine what types of orbits dominate the distribution function is to find the number density of particles as a function of initial energy and angular momentum. In Figure 5.8(a), I plot the number density as a function of initial semi-major axis and

(a)

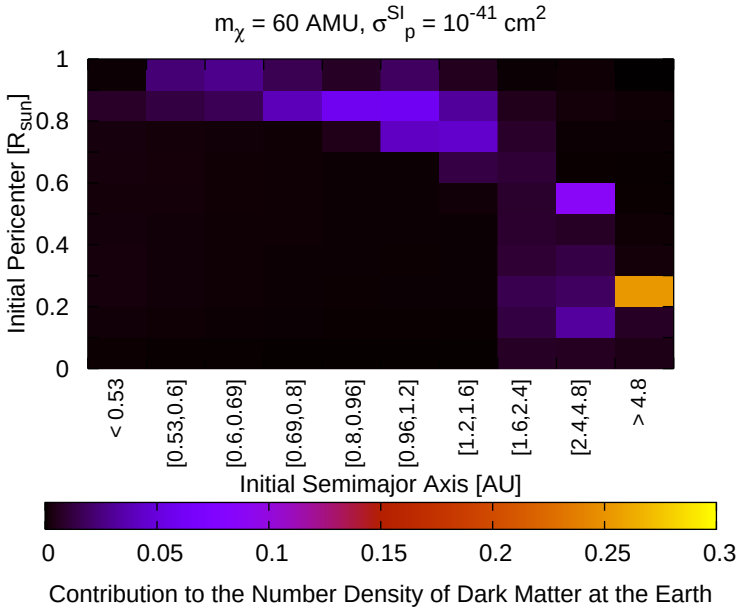

(b)

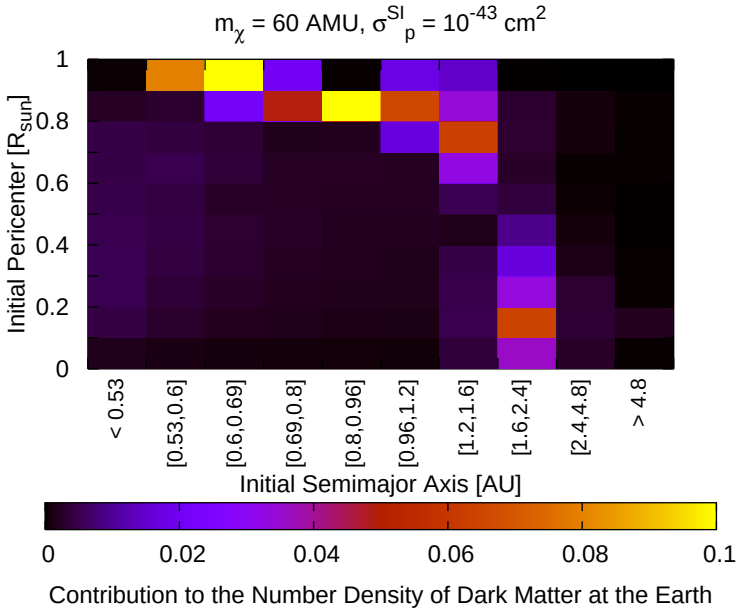

Figure 5.8: Contributions to the number density of bound particles at the Earth as a function of both the initial semi-major axis and initial perihelion in the Sun for the (a) DAMA and (b) CDMS simulations.

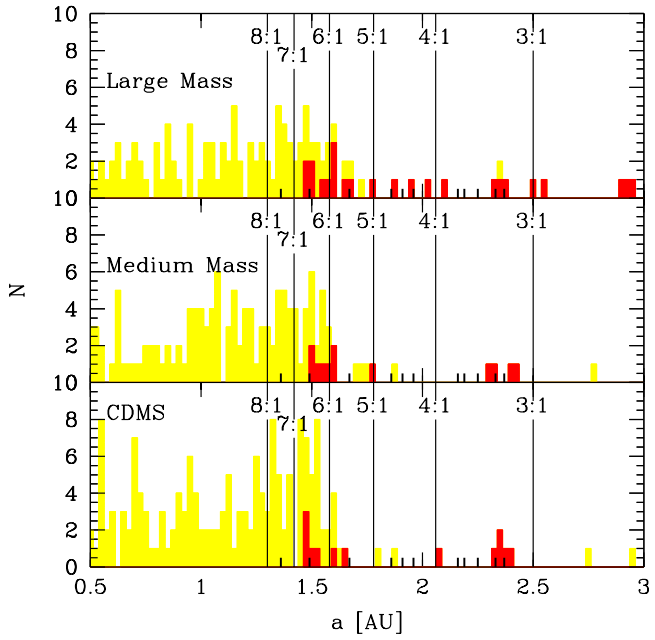

Figure 5.9: Initial semi-major axis distribution of particles with lifetimes $t_{\rm surv} > 1$ Gyr. The top panel is for the Large Mass run, middle for the Medium Mass run, and the bottom panel shows the results from the CDMS run. The light yellow histogram shows the distribution of semi-major axes for $a < 3$ AU. The red line indicates the subset of particles which had initial perihelia ($r < 0.5 R_\odot$), i.e., the particles that initially scattered deep within the Sun. The solid vertical lines indicate the major resonances, and the small thick lines indicate all minor resonances between the 8:1 and 3:1 resonances up to $m : n$ with $m = 15$.

initial perihelion. The semi-major axes are binned in such a way that if the distribution of semi-major axes is described by Eq. (2.34), then there should be equal numbers of particles in each bin. The perihelia are binned in intervals of $0.1R_\odot$. The distribution of perihelia is sharply peaked near $r \sim 0.15R_\odot$. In the plot, one can clearly see the Kozai cycle contributions (small a_i and large r_p), as well as a small quasi-Kozai contribution (1.6 AU $< a_i <$ 2.4AU, $r_p < 0.9$). Particles on Jupiter-crossing orbits ($a_i \gtrsim 2.6$ AU) make up a non-trivial component of the number density, although many of those bins are dominated by only a few particles.

Since particles with $t_{life} > 1$ Gyr dominate the distribution function for the $\sigma_p^{SI} = 10^{-43}$ cm^2 runs, it is interesting to see which particles constitute this class. Figure 5.9 shows the initial semi-major axis distribution of these particles up to $a_i = 3$ AU. In each simulation, there are about ten particles that survive $t_{life} > 1$ Gyr that have $a_i > 3$ AU. The long-lived particles are divided by whether the initial perihelion was within $r_p < 0.5R_\odot$ of the center of the Sun (*red histogram*) or in the outskirts $r_p > 0.5R_\odot$ (*yellow histogram*). The major mean motion resonances are marked by long black lines, and minor resonances down to 15 : 1 are denoted by short black lines. There are several important conclusions stemming from the plot. First, the vast majority of particles that survive $t_{life} > 1$ Gyr had very high initial perihelia. These particles are on Kozai cycles. In each of the simulations represented in Figure 5.9, only about 3% of all particles have initial perihelia $r_p > 0.5R_\odot$ (only a fraction of these particles can be on Kozai cycles), and only about 3% of the particles with initial perihelia in the outskirts of the Sun are on Kozai cycles with lifetimes greater than 1 Gyr. The percentage of particles on long-lived Kozai cycles decreases as a function of WIMP mass. Secondly, those few particles that originate deep in the Sun but manage to survive are in the long lifetime tail of the quasi-Kozai distribution. There are more of these particles in the Large Mass simulation than the others, but this is probably due to Poisson noise. There is no physical reason why there should be more long-lived quasi-Kozai particles in that particular simulation.

These long-lived particles ($t_{life} > 10^9$ yr) only contribute about half of the total number

density of particles at the Earth in the $\sigma_p^{SI} = 10^{-43}$ cm^2 simulations. To find which types of particle orbits fill in the other half, I plot the local number density of particles at the present as a function of initial semi-major axis and perihelion for each simulation, in Figures 5.8(b) and 5.10. All simulations show a rotated L-shaped structure. This structure, along with the time evolution of the distribution functions shown in Figure 5.6, demonstrates that the bound WIMP number density is composed mostly of particles on Kozai cycles (low a_i and high r_p) or quasi-Kozai cycles ($a_i \approx 2$ AU, all perihelia). Therefore, the orbits representing the two highest lifetime humps in Figures 5.4 and 5.5 dominate the distribution function, even though the total number of particles in those humps is relatively low. The pure Kozai cycles are more prominent in the bound WIMP number density even though there are proportionally fewer Kozai cycling particles than there are particles on quasi-Kozai cycles. There is a hint of contribution from the low a_i, small r_p segment of the initial particle distribution.

Next, I describe how the distribution functions depend on the WIMP mass and spin-independent WIMP-nucleon cross section. First, I will discuss the mass dependence of the distribution functions for a fixed spin-independent cross section. There are three effects that might induce a mass dependence on the cross section. First, the mass can affect the initial energy and angular momentum distribution of bound WIMPs. As discussed in Section 2.2, it is increasingly difficult to scatter halo WIMPs onto bound orbits as the WIMP mass increases. This is because the maximum energy transfer Q_{max} approaches an asymptote for large WIMP masses, but the unbound WIMP energy increases since energy $E \propto m_\chi$. Thus, the minimum scattered particle energy $E' = E - Q_{min}$ increases for fixed initial speed but increasing WIMP mass. Therefore, while the initial distribution of semi-major axes $\mathrm{d}\log\dot{N}/\mathrm{d}\log a = -1$ (this is Eq. 2.34 in Section 2.2) for WIMP masses not too different from the masses of the nucleons in the Sun, the distribution gets skewed to higher semi-major axes for high WIMP mass. This is illustrated in Figure 5.11(a), in which I plot percentage of the total simulated particles in each semi-major axis bin for the CDMS (*solid black*, $m_\chi = 60$ AMU), Medium Mass (*green dots*, $m_\chi = 150$ AMU), and Large Mass (*blue*

(a)

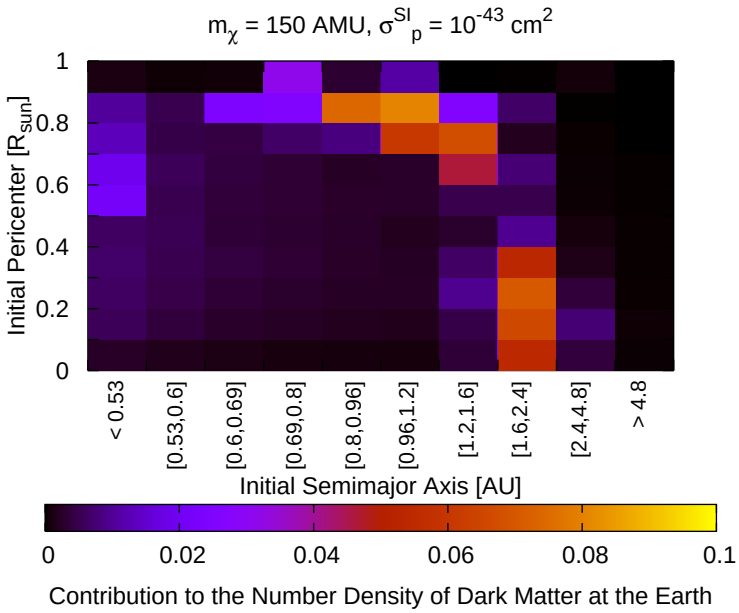

(b)

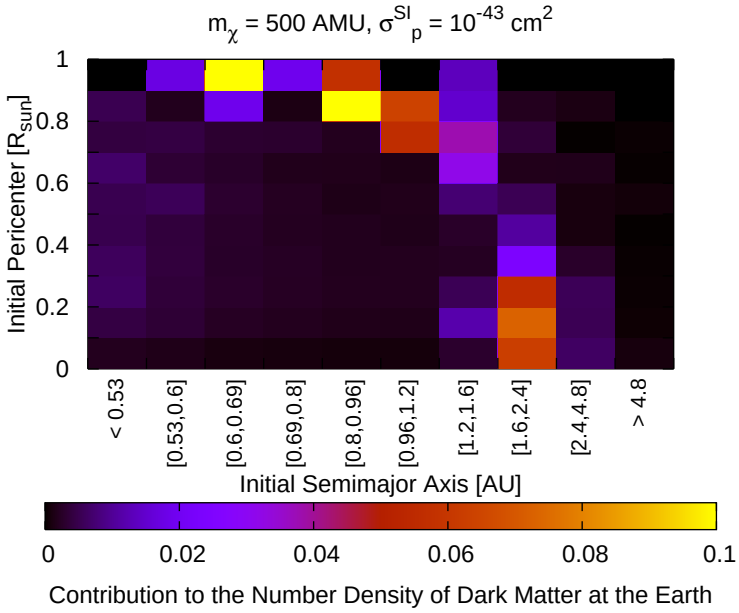

Figure 5.10: Contributions to the number density of bound particles at the Earth as a function of both the initial semi-major axis and initial perihelion in the Sun for the (a) Medium Mass and (b) Large Mass simulations.

dashes, $m_\chi = 500$ AMU) simulations. The DAMA particles are not plotted because their distribution has the same form as the CDMS simulation, since those two simulations have the same WIMP mass. If the particle distribution were exactly that of Eq. (2.34), then each bin should have the same number of particles (apart from Poisson noise). It is clear that the Large Mass distribution is skewed to large semi-major axes relative to the other simulations, although not radically so.

The angular momentum distribution is also affected by the WIMP mass, as parametrized by the initial particle perihelion in Figure 5.11(b). As discussed in Section 2.2, the maximum angular momentum decreases with increasing m_χ since high mass particles scattering onto bound orbits must do so at smaller distances from the center of the Sun. Thus, the Medium Mass and Large Mass simulations have a deficit of large perihelion particles relative to the CDMS simulation. The direction of skewing in both energy and angular momentum suggest that high energy particles will become increasingly common for higher mass WIMPs, and that there will be fewer particles on Kozai cycles as the WIMP mass increases.

Secondly, the particle mass affects the rescattering probability in the Sun, for two reasons. First, in Eq. (3.72), the scattering probability along a path is proportional to $\mathrm{d}\tau/\mathrm{d}l \propto \left(1 - e^{-Q_{max}/Q_A}\right)$, which is a mildly increasing function of WIMP mass m_χ (since Q_{max} is mass-dependent). The optical depth for the Large Mass simulation ($m_\chi = 500$ AMU) for a given path is about 15% higher than for $m_\chi = 60$ AMU. However, while high mass WIMPs have a higher scattering probability than low mass WIMPs, they also rescatter far more often onto Earth-crossing orbits. Therefore, it is not clear from the outset whether high mass WIMPs will have longer or shorter lifetimes relative to low mass WIMPs.

The WIMP mass also affects the overall amplitude of the final bound dark matter distribution function due to the fact that the WIMP mass determines the scattering rate of halo particles onto bound, Earth-crossing orbits. For high mass WIMPs, the *total* capture rate of halo WIMPs in the Sun is (e.g., Gould, 1992)

$$\dot{N}_{tot}/n_\chi \propto m_\chi^{-1}, \quad m_\chi \gg m_A \tag{5.11}$$

which can be derived from Eq. (2.29) in the limit $m_\chi \gg m_A$ using $f(r, v) \approx f(v_s = 0)$ (I give

(a)

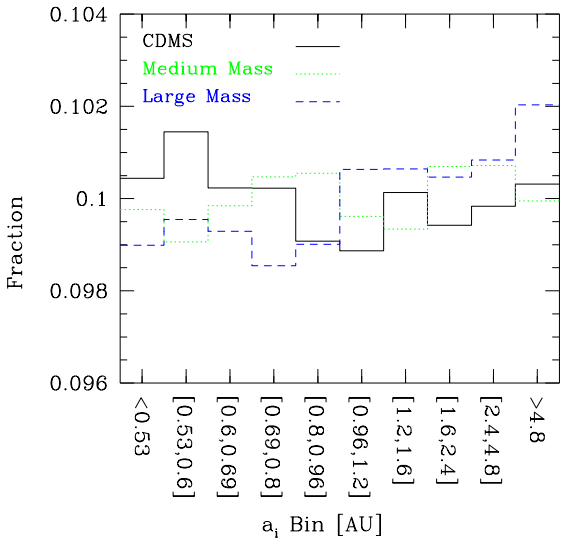

(b)

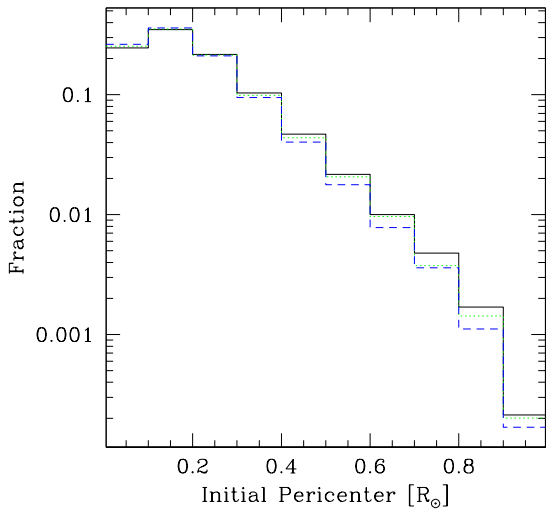

Figure 5.11: Percentages of particles in each (a) initial semi-major axis bin or (b) initial perihelion bin. The semi-major axis bins were designed such that, if $d\dot{N}_{\oplus}/da \propto a^{-1}$, each bin would have the same percentage of particles (apart from Poisson errors).

the relation for $\dot{N}_{tot}/n_\chi$, not $\dot{N}_{tot}$ in order to cancel out the decrease in the scattering rate simply due to the fact that the number density of particles falls for fixed mass density as the WIMP mass increases). The function $\dot{N}_{tot}/n_\chi$ is plotted in Figure 5.12(a) for the capture rate due to all species in the Sun (*solid red*) and for scattering only on hydrogen (*blue dots*; calculated in the limit of a cold Sun). The capture rate of particles onto *Earth-crossing* orbits is shown in Figure 5.12(b). Note that the capture rate $\dot{N}_\oplus/n_\chi$ onto Earth-crossing orbits is an increasing function of WIMP mass until about $m_\chi = 3$ TeV (≈ 100 GeV in the case of only hydrogen scattering). This is due to the fact that low mass WIMPs may be scattered onto very tight orbits (whose aphelia may be within the Sun), which are kinematically suppressed for higher mass WIMPs. Even though the total WIMP capture rate decreases for higher WIMP mass, those WIMPs that are captured are preferentially scattered onto Earth-crossing orbits. The function $\dot{N}_\oplus/n_\chi$ turns over when most captured particles are on Earth-crossing orbits, and then the function follows the familiar $\dot{N}_\oplus/n_\chi \propto m_\chi^{-1}$. In Figure 5.12(c), I show the ratio of the Earth-crossing scattering rate to the total scattering rate. This is a clearly increasing function of m_χ, and reaches unity for $m_\chi \gtrsim 1$ TeV in the case of scattering on hydrogen alone.

The consequence of these scattering rates of halo WIMPs in the Sun is that, if the distribution functions were otherwise independent of WIMP mass, the high mass distribution functions would be greater than the low mass distribution functions simply due to the prefactor in Eq. (4.17). In order to isolate the effects of WIMP mass on the initial distribution of energy and angular momentum as well as subsequent rescattering, I divide the three distribution functions from the simulations with $\sigma_p^{SI} = 10^{-43}$ cm^2 in Figure 5.2(a) by $\dot{N}_\oplus$ and show these functions in Figure 5.13. The low plateaus do not appear to be significantly different. There are some discrepancies in the spikes, which are due to the very low numbers of particles in each simulation that contribute to the spikes. The high plateaus look relatively consistent with each other, given the large error bars and low sampling of Kozai cycles. These large error bars are due to the fact that the high plateaus are largely built up of a very few particles that survive longer than $t_{life} > 1$ Gyr and are on Kozai cycles.

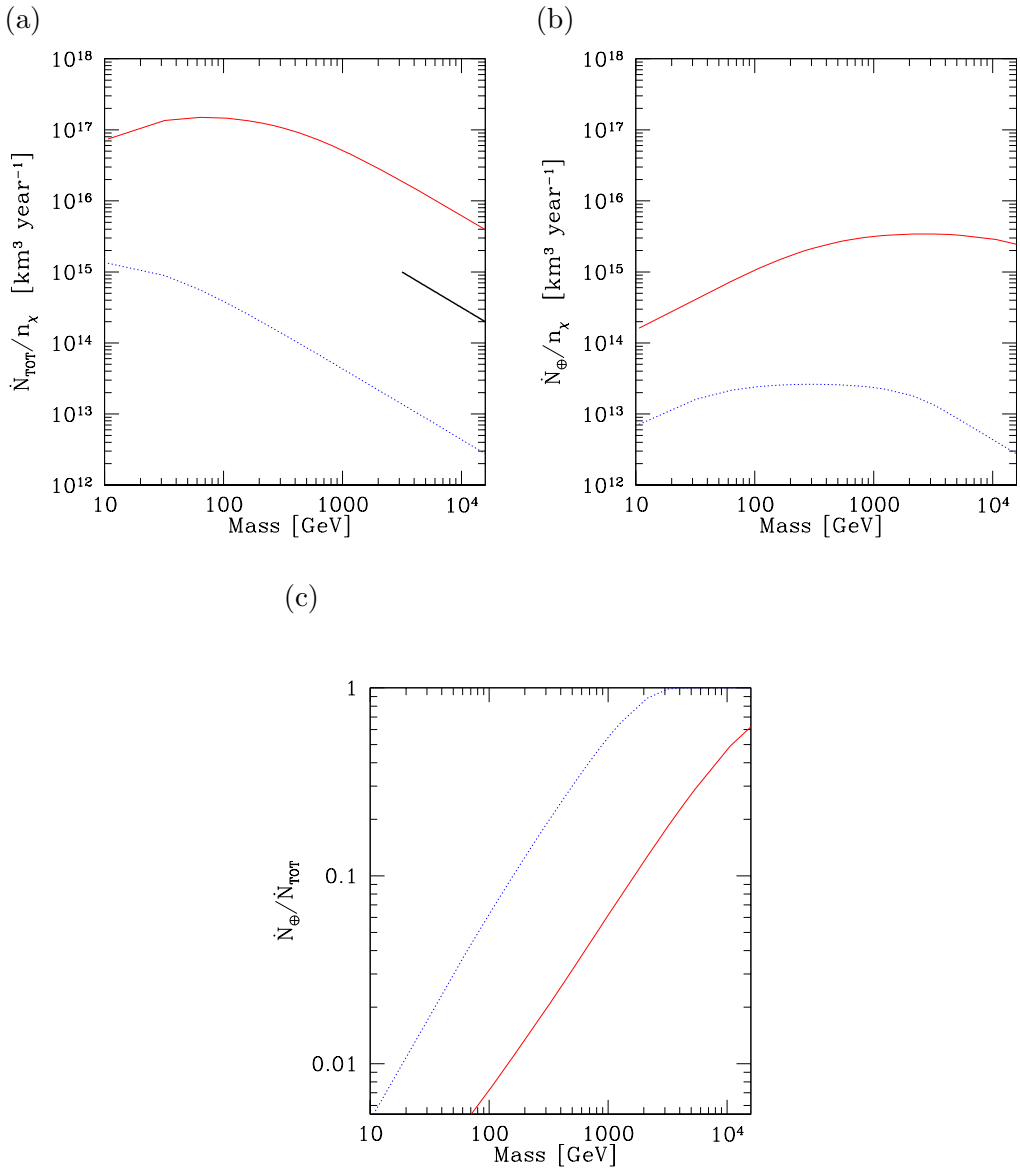

Figure 5.12: In each plot, the red solid line denotes all species in the Sun, and the dotted blue line represents hydrogen. (a): The capture rate $\dot{N}$ of WIMPs by the Sun for $\sigma_p^{SI} = 10^{-43}$ cm^2, divided by the halo number density of WIMPs. The short solid black line gives the slope $\dot{N}/n_\chi \propto m_\chi^{-1}$, the limiting slope for $m_\chi \gg m_A$ for a nuclear species A. (b): The capture rate $\dot{N}_\oplus$ to Earth-crossing orbits divided by the halo WIMP number density. (c): $\dot{N}/\dot{N}_\oplus$.

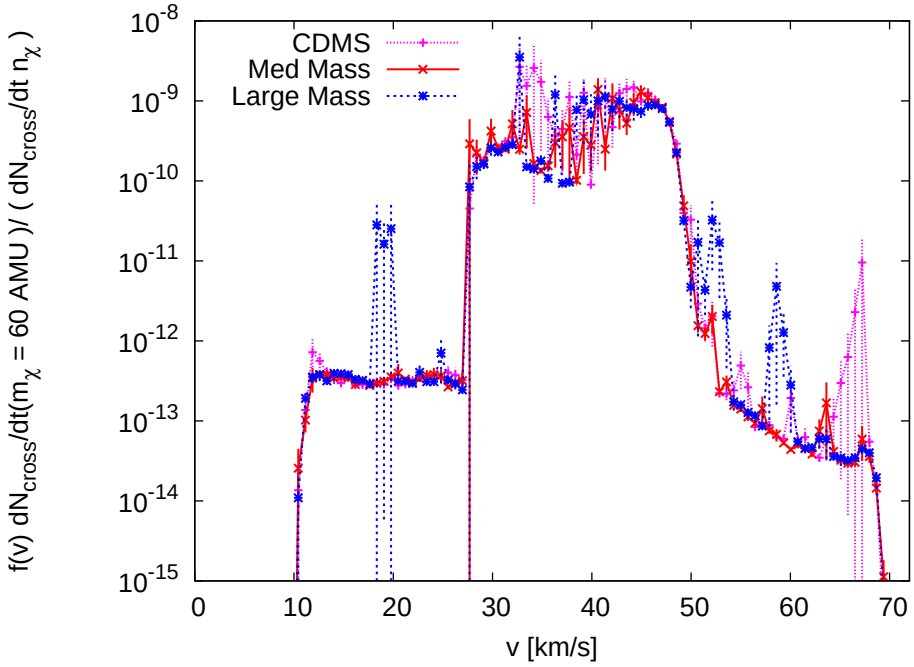

Figure 5.13: Distribution functions for the three simulations with $\sigma_p^{SI} = 10^{-43}$ cm^2 scaled by $\dot{N}_\oplus$.

Given the fairly low statistics of particles that dominate the distribution function, I conclude only that the distribution function for a fixed WIMP-baryon scattering cross section has only a modest, if any, dependence on particle mass for the range of masses I consider in the simulations. In the "Interpretation" subsection following this current section, I will comment on any mass dependence I would expect to see if I had a larger sample of particles that contribute to the distribution function.

Next, I will summarize the effects of changes in the cross section on the low and high plateaus, as well as the spikes in the distribution function. This discussion will be fairly brief since I have alluded to most of the main results previously in this section. As noted in the discussion surrounding Figure 5.7, the height of the low plateau reaches equilibrium on short (< 10 Myr) timescales, and is approximately proportional to the WIMP cross section, at least in the range $\sigma_p^{SI} = 10^{-43} - 10^{-41}$ cm^2. The height is almost certainly proportional to the cross section for lower cross sections, since in those cases almost no particles will

be rescattered in the Sun. For higher cross sections, it seems likely that the height of the low plateau will grow more slowly with cross section since more and more particles will be rescattered rather than ejected. The height of the low plateau is only a weak function of cross section for the range of cross sections represented in these simulations. The height of the DAMA high plateau is about a factor of three higher than that of the other simulations (if the distribution functions have $\dot{N}_{\oplus}$ divided out), since the non-DAMA distribution functions are still growing with time during at present.

The one feature of the distribution functions I have not discussed in the context of the elastic scattering cross section is the spiked contribution. Spikes are prominent in all the distribution functions. However, proportionally more particles end up on long-lived resonance-sticking orbits for the $\sigma_p^{SI} = 10^{-43}$ cm^2 simulations than in the DAMA simulation (see Figure 5.5). The resonance-sticking particles do pass through the Sun, so that the particle lifetimes depend on the optical depth of the Sun. Many spend quite a bit of time in the Sun before sticking to a resonance and have perihelia just barely grazing the Sun. Therefore, I would expect the height of the spikes relative to the low plateau to decrease with increasing WIMP-nucleon cross section. However, the spike contribution to the total distribution function may increase because the overall height of the low plateau increases with increasing cross section.

The last topic I will discuss in this section is what types of orbits dominate the distribution function as a function of the cross section. This is illustrated in Figures 5.8 and 5.10. The main differences between the contributions to the DAMA number density and the number density resulting from the simulations with smaller cross section are that: (i) Jupiter-crossing particles are more important at higher cross sections, and (ii) the quasi-Kozai contribution increases with decreasing cross section.

Interpretation

There are two more issues I would like to discuss before I present the results of the gravitational capture simulations. First, I would like to explain why the assumptions of Damour

& Krauss (1999) with respect to Kozai cycles were wrong. In particular, their estimates for the flux of WIMPs on Earth-crossing orbits were too high by a factor $\sim 10^2 - 10^3$. Then, I will discuss predictions for the maximum possible bound dark matter distribution function given current constraints on the WIMP mass and elastic scattering cross section.

The main reasons that the density of bound WIMPs is much smaller than estimated by Damour & Krauss is that particles on Kozai cycles have lifetimes before rescattering that are much less than the age of the solar system. These lifetimes are short for two reasons. First, the periods of the Kozai cycles are quite small. In the point mass three-body problem, the period of Kozai oscillations in eccentricity or inclination would be of order (cf. Kiseleva et al., 1998)

$$T \propto \frac{P_J^2}{P}\frac{M_\odot}{M_J}. \tag{5.12}$$

Here, P denotes the orbital period of a particle and P_J represents the orbital period of Jupiter. For typical particle orbits, $T \lesssim 10^5$ yr.

The other important timescale is the timescale on which the orbital perihelion is moved out of the Sun. Since the optical depth in the outskirts of the Sun is extremely low ($\tau \sim 10^{-5}$ for an orbit with $r_p \approx 0.7R_\odot$ in the DAMA simulation, dropping rapidly as the perihelion approaches the surface), then particles could survive many Kozai cycles before being rescattered if it only took a few orbital periods for the perihelion to cross the Sun. However, I will show that it takes many orbital periods for the Jupiter to pull the perihelia out of the Sun, hence making the optical depth per Kozai cycle much larger than the optical depth for a single passage through the Sun.

The change in the angular momentum is

$$\frac{\mathrm{d}J}{\mathrm{d}t} = K_J, \tag{5.13}$$

where K_J is the torque on the particle orbit by Jupiter. The torque is far higher at the particle aphelion r_a for particles with $a < a_J/2$ than at any other point in the orbit, and

can be approximately described as a kick

$$K_J \sim r\nabla\Phi_J\big|_{r=r_a} \tag{5.14}$$

$$\sim \frac{GM_J a^2}{a_J^3}. \tag{5.15}$$

This form for the torque comes from using the $l = 2$ term in the spherical harmonic expansion of potential from Jupiter Φ_J (Eq. 3.61). The angular momentum must change by of order

$$\Delta J \sim \sqrt{GM_\odot R_\odot} \tag{5.16}$$

for the perihelion to exit the Sun. Therefore, the total time it takes a particle with a particle with initial perihelion in the Sun to have its first perihelion outside the Sun is

$$\Delta t \sim \frac{\Delta J}{K}. \tag{5.17}$$

Using the expressions for K_J and ΔJ in Eqs. (5.15) and (5.16), I find

$$\frac{\Delta t}{P} \sim \frac{M_\odot}{M_J}\left(\frac{a}{R_\odot}\right)^{-1/2}\left(\frac{a}{a_J}\right)^{-3} \tag{5.18}$$

$$\sim 10^4, \text{ for } a = 1 \text{ AU}, \tag{5.19}$$

where P is the period of the particle. Therefore, a particle passes through the Sun many times during each Kozai cycle. In the simulations, I usually find that the total optical depth per Kozai cycle is $\sim 10^3$ times the optical depth at maximum eccentricity. Even if the optical depth at maximum eccentricity is only 10^{-5} per orbital period (typical of the DAMA simulation), the total optical depth per Kozai cycle is $\sim 10^{-2}$. It only takes about 100 Kozai cycles for such a particle to rescatter in the Sun. Thus, the result is that the lifetimes of particles are less than the age of the solar system, and that the estimates of Damour & Krauss (1999) are wildly optimistic.

One can, however, see how Damour & Krauss (1999) found such high bound particle number densities given their assumptions. Harking back to Figure 5.6(a), the high plateau is mostly composed of long lived particles on Kozai cycles in the DAMA simulation. However,

as per Figure 5.5, the median lifetime for the particles on Kozai cycles in the DAMA simulation is of order $t_{life}^{med} \sim 10^8$ yr. The number of times a Kozai-cycling WIMP intersects the Earth's orbit is proportional to its lifetime. If the WIMPs on Kozai cycles survived longer than the age of the solar system in the DAMA simulation (i.e., the assumption of Damour & Krauss, 1999), then the height of the high plateau ought to be $t_{SS}/t_{life}^{med} \sim 50$ times higher than it was in the simulation. Damour & Krauss (1999) found the biggest number densities for massive WIMPs (m_χ of order several hundred GeV), so that by virtue of the fact that $\dot{N}_\oplus/n_\chi$ increases as a function of mass, the bound WIMP density for $m_\chi \approx 500$ GeV and $\sigma_p^{SI} = 10^{-41}$ cm^2 could be several hundred times the WIMP density found in the DAMA simulation. The DAMA WIMP bound number density was $n_\chi^{bound} \sim 10^{-4} n_\chi^{halo}$. Therefore, if the Kozai cycle lifetimes were $t_{life} \gtrsim 10^{10}$ yr, the bound WIMP number density could be several percent of the halo number density. Since Damour & Krauss (1999) explored cross sections higher than the DAMA simulation value (constraints on the spin-independent cross section were orders of magnitude weaker when they wrote their paper than they are today), one can see how they found bound WIMP number densities comparable to the halo number density.

So far, I have discussed the results of the simulations and argued how the bound dark matter distribution function depends on both WIMP mass and spin-independent cross section. However, I have not concisely described in which part of the allowed WIMP parameter space I expect the maximal bound WIMP number density, or what the distribution function looks like in the allowed region. First, let me return to Figure 1.7 to describe which parts of WIMP parameter space have not been excluded. The strongest current limits come from the XENON experiment, with the lowest point in the exclusion curve at $m_\chi \approx 30$ GeV, $\sigma_p^{SI} \approx 4 \times 10^{-44}$ cm^2. The limits on the spin-independent cross section become substantially weaker for smaller or larger mass WIMPs. The maximum distribution functions for a given WIMP mass in the allowed parameter space will occur at the boundary of the allowed and excluded regions. So, one can ask, what do the distribution functions look like along the exclusion curve? How do those distribution functions compare to those I found in my

simulations, and where along the curve would one expect to find the maximum signal from a bound dark matter distribution function?

Let me focus on the minimum point on the exclusion curve first. It is at this point that I also expect the smallest n_χ/n_χ^{halo} along the curve. The reasons for this are twofold. First, I showed that even for WIMP-proton cross sections of order $\sigma_p^{SI} = 10^{-43}$ cm^2, the high plateau is still growing at the present, since many particles on Kozai cycles survive longer than the age of the solar system. This means that the distribution function has not yet reached equilibrium. Since the low point in the exclusion curve has a smaller cross section than in the CDMS-type simulations, the distribution function at that point will be even further from its maximum. Another way to think about this is that any particles with lifetimes exceeding the age of the solar system in the CDMS simulation will also have lifetimes greater than the age of the solar system if the cross section is smaller. Therefore, those particles will have exactly the same number of crossings of the Earth's orbit for both cross sections, even though the rate of scattering onto bound orbits is smaller for the low point in the XENON exclusion curve than it is for $\sigma_p^{SI} = 10^{-43}$ cm^2. This implies that the contribution of those particles to the distribution function gets smaller with decreasing cross section. Those particles that have lifetimes less than the age of the solar system in the CDMS-type simulations would have about the same contribution to the distribution function for lower cross sections since, in those cases, the lifetimes (and hence, crossings with the Earth's orbit) will increase as $(\sigma_p^{SI})^{-1}$, while the capture rate increases as $\propto \sigma_p^{SI}$. The combined effect is that the height of both high and low plateaus should go down with decreased elastic scattering cross section, although the spikes may become more prominent with respect to the low plateau as particles are less likely to rescatter before sticking to resonances. The second reason why the distribution function should be lowest at the minimum of the XENON exclusion curve is that $\dot{N}_\oplus/n_\chi$ decreases with decreasing m_χ in this mass range (Figure 5.12(b)). Overall, the distribution function at the minimum of the exclusion curve should be a factor of several smaller than the CDMS distribution function, with the low plateau being even smaller relative to the low plateau of the CDMS simulation.

Since MSSM models strongly disfavor neutralino masses smaller than 30 GeV, I will focus on the large mass branch of the exclusion curve to find a maximal value for the distribution function. As the WIMP mass increases along the exclusion curve, I expect the bound distribution function to get bigger—to a point, and then it will start decreasing again. There are two effects that drive the distribution function higher along the exclusion curve. First, the constraint on σ_p^{SI} weakens with increasing WIMP mass. Since the high plateau modestly rises with cross section in the regime where the distribution function grows with time, and the low plateau height is proportional to the cross section for the cross sections under consideration, the total distribution function should grow. In addition, the distribution function should increase for increasing WIMP mass, up to about $m_\chi \approx 2$ TeV by virtue of the growth in $\dot{N}_\oplus/n_\chi$ (see Figure 5.11(b)). However, as the WIMP mass grows, it becomes harder to capture halo WIMPs on bound orbits in the outskirts of the Sun, so fewer particles land on Kozai cycle orbits. Recall that I previously found that there was little difference in the height of the high plateaus in the CDMS, Medium Mass, and Large Mass simulations after I divided out $\dot{N}_\oplus$. If I had a better statistical sample of the particles that dominate the distribution function, I would expect to see some modest differences between the CDMS, Medium Mass, and Large Mass simulations. Namely, I would have expected a decrease in plateau height with increasing WIMP mass. I already see that the number of long-lived Kozai cycle particles decreases as a function of mass, but there is quite a bit of particle-to-particle variation in how much a Kozai cycle particle contributes to the distribution function. The height of high mass high plateaus should be suppressed relative to low mass high plateaus if $\dot{N}_\oplus/n_\chi$ were fixed. For masses approaching $m_\chi \approx 3$ TeV, there is a fierce competition between the suppression of scattering onto Kozai cycles and increase in $\dot{N}_\oplus$. The maximum distribution function almost certainly occurs for a mass < 3 TeV since, all else being equal, $\dot{N}_\oplus$ flattens and the decreases, regardless of any Kozai cycle suppression. Given the ratio between the peak of $\dot{N}_\oplus$ relative to the value at $m_\chi = 500$ GeV, and the only modest rise in the high plateau as a function of cross section near $\sigma_p^{SI} \sim 10^{-42}$ cm^2, I expect the maximum distribution function (and bound number

density) to be at most about 1.5 times the Large Mass simulation quantities. This would imply a maximum bound number density of $n_\chi^{bound} \sim 10^{-4} n_\chi^{halo}$, occurring for $m_\chi \sim 1$ TeV and $\sigma_p^{SI} \sim 10^{-42}$ cm^2.

In conclusion, even the most optimistic distribution function for bound dark matter particles yields bound dark matter number densities from elastic, spin-independent scattering in the Sun that are at least three orders of magnitude smaller than the halo dark matter number density at the Earth.

Implications for High Spin-Dependent Cross Sections

So far, I have only explored the dark matter distribution function in the case where WIMP-nucleon scatters in the Sun are dominated by spin-independent, scalar interactions. There are several reasons to extend this discussion to spin-dependent scattering. First, the limits on spin-dependent WIMP-proton scattering are much weaker than those on spin-independent scattering, as illustrated in Figures 5.14(a) and 1.7. As mentioned in Chapter 2, hydrogen is the most abundant nuclear species in the Sun, and it is the only non-trace isotope in the Sun (other than ^{14}N) to have non-zero spin-dependent interactions with WIMPs. The combination of the weak exclusion limits on the spin-dependent cross section and the high abundance of hydrogen in the Sun means that it possible that the Sun may have a much higher optical depth for spin-dependent WIMP interactions than for spin-independent interactions. Secondly, in large parts of MSSM parameter space, the spin-dependent cross section is far greater than the spin-independent cross section. In Figure 5.14(b), I show a scatter plot of σ_p^{SI} vs. σ_p^{SD} for a scan I performed of a small slice of the MSSM parameter space. The details of the scan through parameter space are given in Section 5.3. In the Figure, I only show points for which the cosmological WIMP density is $0.05 < \Omega_\chi h^2 < 0.135$. The upper limit is several standard deviations above the best fit *WMAP*-3 value (Spergel et al., 2007). The lower limit is set such that it is marginally possible for the local dark matter density to consist mainly of neutralinos.

I only show models with $\sigma_p^{SI} > 8 \times 10^{-44}$ cm^2, only slightly smaller than the cross

(a) (b)

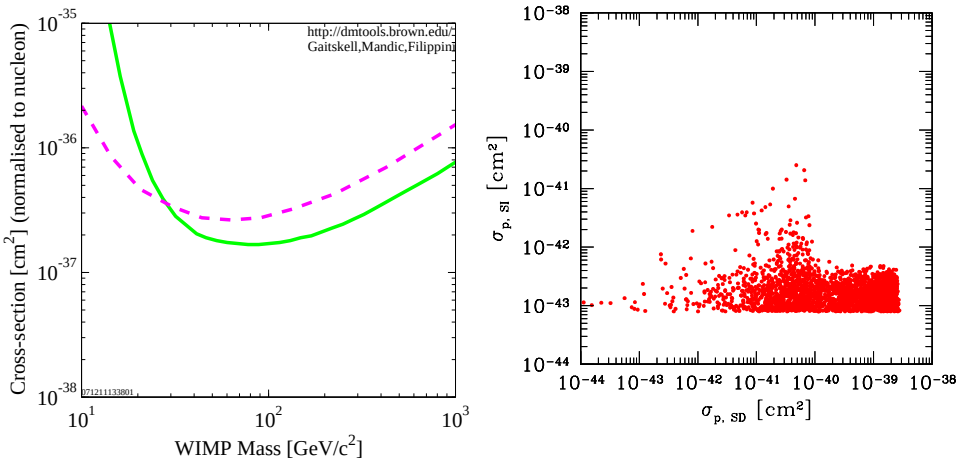

Figure 5.14: *(a):* Limits on the spin-dependent WIMP-proton cross section from the NAIAD (*dashed*) and KIMS (*solid*) experiments. These are the most stringent current limits. *(b):* Spin-dependent vs. spin-independent neutralino-proton cross sections for a selection of supersymmetric models with $0.05 < \Omega_\chi h^2 < 0.135$. Only models with $\sigma_p^{SI} > 8 \times 10^{-44}$ cm^2 are shown.

section used for the CDMS, Medium Mass, and Large Mass simulations. Even though there are a few models in the plot for which the spin-independent cross section $\sigma_p^{SD} \gtrsim 100\sigma_p^{SI}$ and as such is likely to dominate scattering in the Sun (see Section 2.1.1), there are many more models for which the spin-dependent cross section dominates. Note that there are many models for which spin-dependent interactions will dominate in the Sun, but spin-independent cross sections will dominate and be relatively high in the Earth, which is relevant for capture and annihilation of WIMPs in the Earth (see Section 5.3).

In the description of the spin-independent simulation results, I showed that, for the range of spin-independent cross sections explored in the simulations, the height of the low plateau is proportional to the WIMP-nucleon cross section (Figure 5.7), whereas the high plateau slowly grows as a function of cross section until the plateau reaches equilibrium. More precisely, the height of the low plateau is proportional to the scattering rate of halo WIMPs onto bound, Jupiter-crossing orbits. Given how weak the current constraints are on the spin-dependent cross section, then the low plateau may be able to dominate the

bound dark matter distribution function, and may even exceed the unbound geocentric distribution function at low speeds. In Figure 5.15, I show a prediction for the low plateau for $m_\chi = 500$ AMU and $\sigma_p^{SD} = 10^{-36}$ cm^2, neglecting any differences in the initial energy and angular momentum distribution of particles resulting from hydrogen, not the heavy elements, being the primary target in the Sun. The cross section is slightly above the $m_\chi - \sigma_p^{SD}$ exclusion curve in Figure 5.14(a), and it is chosen to demonstrate an approximate maximum possible bound distribution function assuming that the plateau height is strictly proportional to $\dot{N}_\oplus^H$, where the H denotes scattering by hydrogen alone. To estimate the distribution function for this set of WIMP parameters, I have used the DAMA distribution function with the spikes removed. I removed the spikes because particles on resonance-sticking orbits in the DAMA simulation would have rescattered in the Sun before sticking to a resonance for the high cross section assumed in Figure 5.15. I then rescale the DAMA low plateau by a factor of $\dot{N}_\oplus(60 \text{ AMU})/\dot{N}_\oplus^H(500 \text{ AMU})$. The large central peak in the predicted distribution function arises from the nearly radial orbits. This feature is also noticeable in Figure 5.7 for all simulations. It is clear from Figure 5.15 that in this case, the Jupiter-crossing particles dominate the bound distribution function, and can swamp the unbound distribution function at low speeds.

However, such a high distribution function is only possible if the height of the low plateau scales as the scattering rate of particles onto bound, Jupiter-crossing orbits. There are some indications within my simulations that the low plateau will grow less rapidly with cross section than in this simple model. Recall that $\approx 98\%$ of Jupiter-crossing WIMPs are ejected in the CDMS, Medium Mass, and Large Mass simulations. However, a smaller fraction ($\approx 73\%$) of WIMPs are ejected in the DAMA simulation because a significant number of particles rescatter in the Sun before they are ejected. If more and more particles rescatter in the Sun before they can be ejected from the solar system with increasing elastic scattering cross section, the height of the low plateau should approach an asymptote. At even higher cross sections, I would expect the low plateau to drop again, as particles have a significant probability of multiple scatters in the Sun. The question is, how high can the

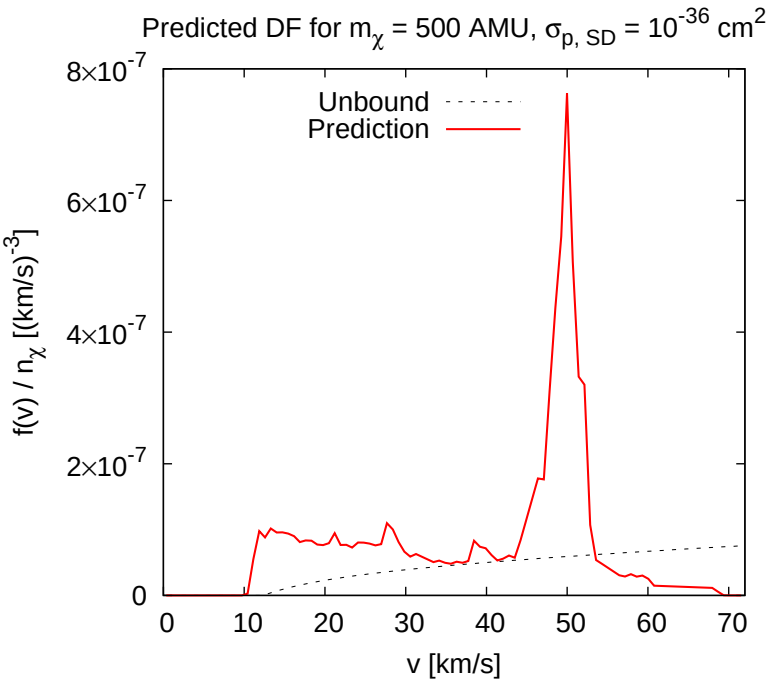

Figure 5.15: Predicted geocentric distribution function if $\sigma_p^{SD} = 10^{-36}$ cm^2, assuming $f(v) \propto \sigma_p^{SI,SD}$ for Jupiter-crossing orbits. This prediction is based on the output of the DAMA simulation, without contributions from long-lived near-resonant particles.

low plateau get?

I attempt to estimate the bound dark matter distribution function for various spin-dependent cross sections using the DAMA simulation as a starting point. I want to explore all parts of the distribution function, not just the part originating from Jupiter-crossing orbits. The basic premise of my approach is that I scale the total optical depth of each particle in the DAMA simulation by an estimate of the optical depth for a particular spin-dependent cross section. For particles that are not on Jupiter-crossing orbits, I scale the particle lifetimes for particles on Earth-crossing orbits by the ratio of the optical depth for the particular spin-dependent cross section and the DAMA optical depth. For the particles on Jupiter-crossing orbits, I use the optical depth data from the DAMA simulation to find the approximate time at which each particle hits a total optical depth $\tau = 1$ for the new cross section, and declare that point to be the particle lifetime. I then calculate the distribution functions just as I did for the raw simulation results. Before I include any particle in the distribution function, I do a Monte Carlo simulation of which particles scatter at least once more after the initial scatter that puts the particles on bound orbits before the particle exits the Sun the first time. If a particle rescatters before emerging from the Sun, it is not included in the distribution function.

There are several assumptions in this approach. First, I use the initial distribution of semi-major axis and eccentricity derived from the DAMA simulation without any kinematic corrections due to the extreme mass difference between hydrogen atoms and WIMPs. This has two consequences: I will tend to overestimate the Kozai contribution to the distribution function since scattering in the outer part of the Sun is suppressed for high m_χ, and underestimate the contribution of Jupiter-crossing particles since the semi-major axis distribution skews to higher a for large imbalances between the WIMP and target mass. This last point is illustrated in Figure 5.12(c), in which I plot the ratio of the scattering rate of halo particles onto Earth-crossing orbits to the total scattering rate onto bound orbits. As m_χ/m_H increases, the particle energies are pushed towards $E \to 0$. For hydrogen, the ratio of scattering rates approaches unity for $m_\chi \sim 1$ TeV. The ratio is smaller by about a

factor of 5 for Jupiter-crossing particles. Between $m_\chi = 60$ AMU and $m_\chi = 500$ AMU, the fraction of Earth-crossing particles that are also Jupiter-crossing increases from 18.9% to 21.5% if the particles scatter only on hydrogen. When I show my estimates of the distribution functions, it is important to remember that the non-Jupiter-crossing part is an *upper limit*. The Jupiter-crossing part may be slightly underestimated, but the errors due to the other approximations are likely to be greater than the size of the underestimate.

Secondly, I use the cold Sun approximation of Section 2.2 to find scattering rates onto bound orbits and rescattering probabilities. This is not technically correct, since the thermal speed of hydrogen in the Sun is nontrivial relative to the WIMP speeds. However, the approximation will be good to a few percent, good enough for my purposes.

Thirdly, I do not recalculate optical depths along each path every particle takes through the Sun. This would be too time-consuming. Instead, I scale the optical depths of each particle by the ratio of the scattering rate of $E = 0$ halo particles with the new cross section to the scattering rate of $E = 0$ halo particles in the DAMA simulation. Since bound Earth-crossing particles do not have energies with respect to the Sun that vary significantly from $E = 0$ relative to typical energies of unbound halo particles, using the ratio of the scattering rates to scale the DAMA optical depths should be a reasonable proxy for finding optical depths for specific paths through the Sun. However, this approximation does neglect any differences in the radial distributions of hydrogen and heavier elements in the Sun, as well as any kinematic effects due to scattering off hydrogen rather than heavier atoms. This approximation is good enough if the goal of this exercise is to determine, at a somewhat crude level, the behavior of the low plateau at high cross sections.

I estimate distribution functions for $m_\chi = 60$ AMU at $\sigma_p^{SD} = 1.3 \times 10^{-39}, 10^{-38}, 10^{-37}$, and 10^{-36} cm^2, and then extrapolate the results to other WIMP masses by rescaling the distribution functions by $\dot{N}_\oplus^H(m_\chi)$. By using this kind of rescaling to other masses, I ignore any effects that cause the distribution function $f(\mathbf{v})/\dot{N}$ to vary with WIMP mass. The cross section $\sigma_p^{SD} = 1.3 \times 10^{-39}$ cm^2 yields similar same optical depths in the Sun as $\sigma_p^{SI} = 10^{-41}$ cm^2 for $m_\chi = 60$ AMU. I used about 50 bootstrap resamplings for each spin-dependent

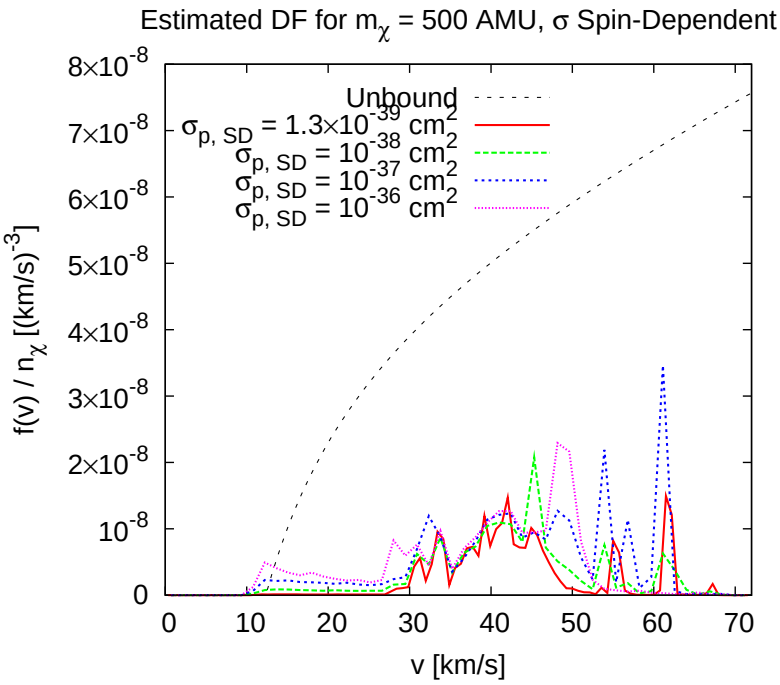

Figure 5.16: Estimated geocentric distribution functions for $\sigma_p^{SD} = 1.3 \times 10^{-39}$, 10^{-38}, 10^{-37}, and 10^{-36} cm^2. The estimated distribution function for $\sigma_p^{SD} = 1.3 \times 10^{-39}$ cm^2 is based on the DAMA simulation result, since the optical depth of the Sun for $\sigma_p^{SI} = 10^{-41}$ cm^2 is approximately the same as $\sigma_p^{SD} = 1.3 \times 10^{-39}$ cm^2.

cross section to estimate the distribution functions. I extrapolate the distribution function to $m_\chi = 500$ AMU using my simple prescription. The results, without error bars, are shown in Figure 5.16, displaying $f(v)/n_\chi$ for each cross section against the geocentric unbound distribution function.

There are several conclusions to be drawn from this plot. The central part of the distribution function for each cross section ($v = 30 - 45$ km s^{-1}) is approximately independent of cross section, which is what one would expect if Kozai cycles dominate this region and particles have lifetimes of at least one Kozai cycle. This region is relatively unaffected by multiple scatters because the particles on Kozai cycles originate in a part of the Sun that still has very low optical depth, even for the highest cross section considered. The spikes grow for a while and then disappear, a consequence of rescattering in the Sun before the relevant particles stick to resonances.

The most striking result of Figure 5.16 is that the low plateau is quite a bit lower than the naive prediction in Figure 5.15. In fact, the phase space density of bound WIMPs is quite a bit less than that of unbound particles at the same geocentric speeds, except in the small region that is inaccessible to unbound particles. It appears that, while the low plateau does rise for large WIMP-proton cross sections, rescattering in the Sun plays an integral role in severely reducing Jupiter-crossing particle lifetimes. To examine the low plateau in more detail, I plot just the $a \geq a_J/2$ contribution to the distribution function in Figure 5.17, both on (a) linear and (b) logarithmic scales. From these plots, it is clear that while the low plateau is still increasing rapidly with cross section below $\sigma_p^{SD} = 10^{-38}$ cm^2, the growth is severely retarded at higher cross sections. In fact, the distribution function for $v > 50$ km s^{-1} starts decreasing as a function of cross section for large σ_p^{SD}. As the cross section increases, it becomes harder and harder for WIMPs originating in even the outskirts of the Sun to have their perihelia perturbed out of the Sun before the particles rescatter.

The bottom line on particles captured to the solar system by weak scattering in the Sun is that they are a very small population relative to the halo population, even if the spin-dependent WIMP-proton elastic scattering cross section is quite large. Improving on the approximations I used in this section is unlikely to change this conclusion. The largest bound populations occur in the following circumstances: First, if the WIMP-proton cross section (either spin-dependent or spin-independent) were small, it would be nice if the WIMP mass were fairly large to gain the $\dot{N}_\oplus$ advantage, but not so large as to suppress the Kozai cycles. If the WIMP-proton cross section were high, which is allowed both experimentally and theoretically, then it would be advantageous to have a WIMP mass that is high enough to pump large numbers of particles onto Jupiter-crossing orbits, but not so large as to hit the drop-off in $\dot{N}_\oplus^H$ (see Figure 5.12(b)). However, in none of these cases will the bound WIMP phase space density be comparable to the unbound phase space density.

(a)

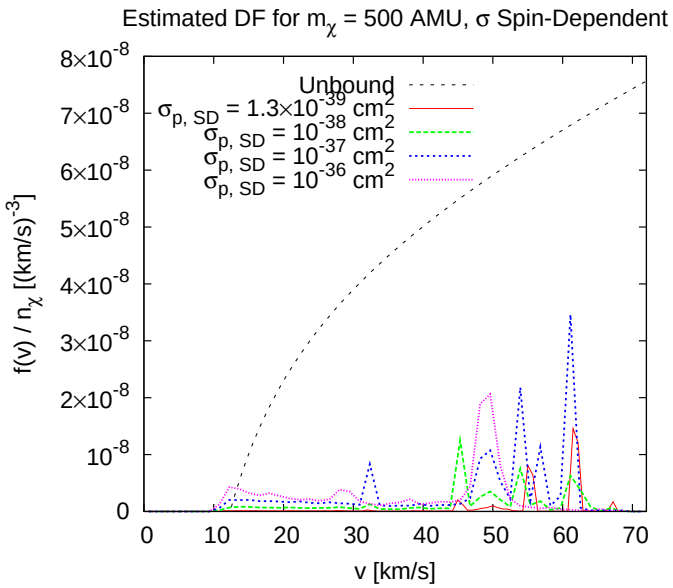

(b)

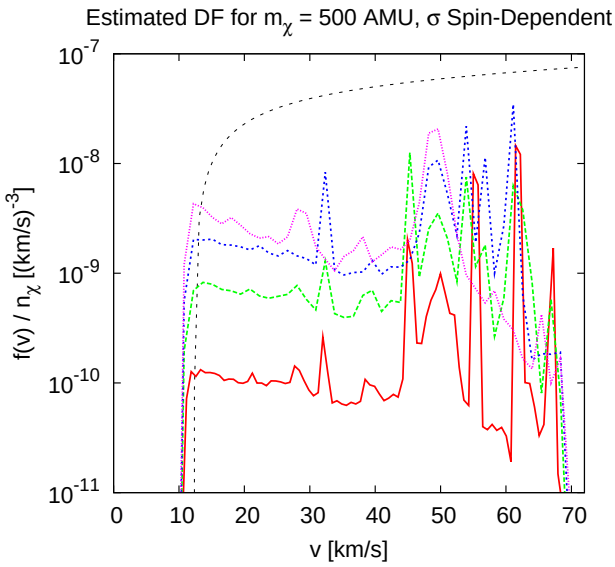

Figure 5.17: The Jupiter-crossing part of the estimated geocentric distribution functions with various WIMP-proton spin-dependent cross sections. *(a)*: Distribution functions on a linear scale. *(b)*: Distribution functions plotted on a logarithmic scale to highlight dependence on the cross section.

.

5.1.2 Gravitational Capture Simulations

Now that I have established that weak scattering in the Sun can only produce a small bound WIMP population at the Earth, I next determine the size of the bound WIMP distribution due to gravitational capture. In this section, I present the results of the gravitational capture simulations. First, I discuss the raw results from the simulation, and then I will address two potential loss mechanisms for bound particles: scattering in the Sun, and Galactic tides.

Raw Results

The main result of this set of simulations is presented in Figure 5.18. The function in this Figure is $f(v)/n_{\chi}^{halo}$, which is the integral of the distribution function over both angular directions, as a function of the geocentric speed v. Each distribution function in the Figure contains contributions from both unbound and bound particles. Distribution functions for each simulation run were estimated according to the procedures outlined in Chapter 4.

For the Regular run simulation, the distribution was derived from a total of 369084 crossings within $z_c = 0.001$ AU of the Earth's orbit, a result of integrating $\approx 4.8 \times 10^9$ particles with initial conditions distributed as in Eq. (2.60). Of those particles, 322441 particles become bound to the solar system for at least a short time, and 1224 of those bound orbits go through the Sun at least once. However, not a single particle is weakly scattered in the Sun. Of the 322441 particles that become bound to the solar system, only 5856 ever cross the Earth's path ($R = 1$ AU, $|z| \leq z_c$), of which 772 also go through the Sun. Therefore, while only a small fraction of the bound orbits in this simulation contribute to the distribution function at the Earth, a large fraction of Sun-penetrating particles do. I will explore this further in the discussion of loss mechanisms below.

In the High Perihelion run (10 AU $< r_p <$ 20 AU), there were only 9473 intersections of bound and unbound particles with the Earth's orbit. Of the nearly 4×10^9 particle orbits simulated for the High Perihelion Run, 64559 become temporarily captured in the solar system, and 54 go through the Sun. As in the Regular run, none of the particles going through the Sun are weakly scattered onto smaller orbits. The only particles that

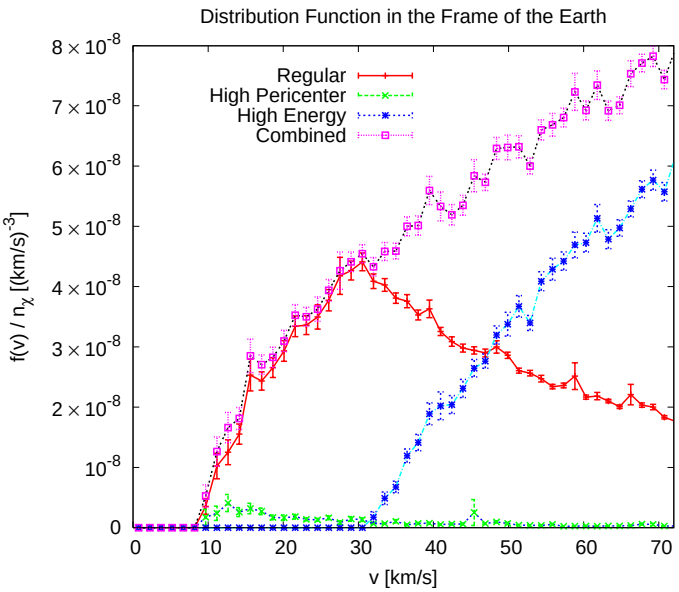

Figure 5.18: Distribution function from the gravitational capture experiments. The distribution function is normalized such that $\int_0^{v_{\max}} f(v)v^2 \mathrm{d}v = n_\chi^{sim}(v < v_{\max})$, where n_χ^{sim} is the number density of particles in the simulation with $v < v_{\max}$. The error bars are estimated using bootstrap resampling of the original particle distribution.

contribute to the distribution function at the Earth are those that do intersect the Sun; the intersection of 51 of 54 bound, Sun-going orbits with the Earth's orbit account for all 9473 data points for the distribution function.

The distribution function for the High Energy run is based on 211413 intersections with the Earth's orbit. Since the energies of particles in this run are so large that Jupiter cannot capture them, this distribution function can also be determined analytically using Liouville's theorem by assuming that Jupiter does not significantly alter the distribution function. Therefore, comparing the High Energy distribution function with the analytically derived distribution function provides a good check on my analysis methods. In Figure 5.19, I present both distribution functions. The simulation-derived distribution function is well-fit by the analytic distribution function, which is a sign that the analysis pipeline is functioning properly.

There are several questions to ask about the distribution function. First, have I sampled enough orbits for the distribution function derived from the simulations to obtain a good

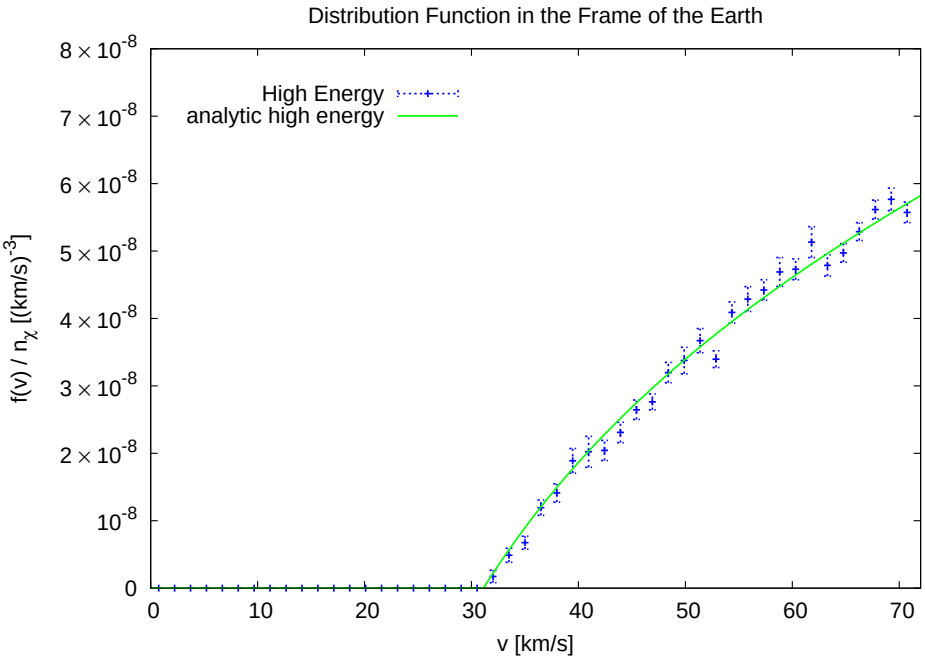

Figure 5.19: The distribution function from the High Energy run compared with that which is analytically derived using Liouville's theorem.

estimate of the true distribution function? In other words, can the error bars generated by bootstrap resampling be trusted? The answer for this is a qualified yes. I think the general shape of the distribution functions from each simulation is correct. However, the Regular Run distribution function is based on only about 5900 particle orbits, and the High Perihelion Run is derived using only 51 orbits. It is possible that parts of the distribution function are either undersampled or oversampled. In particular, the low number of orbits means that I could have zero contribution from very rare orbits that nevertheless contribute significantly to the distribution function. The Regular Run simulation appears to be fairly well sampled, but the High Perihelion distribution function could use more orbits that sample $v > 30$ km s^{-1}. Even if I were to simulate more orbits, I do not think that the shape of the distribution functions would change qualitatively. To make believable comparisons with theoretical models, it would be best to simulate more orbits.

In Figure 5.20, I show the geocentric distribution function from the simulations along with some theoretical curves. In this case, I determine the full distribution function at the

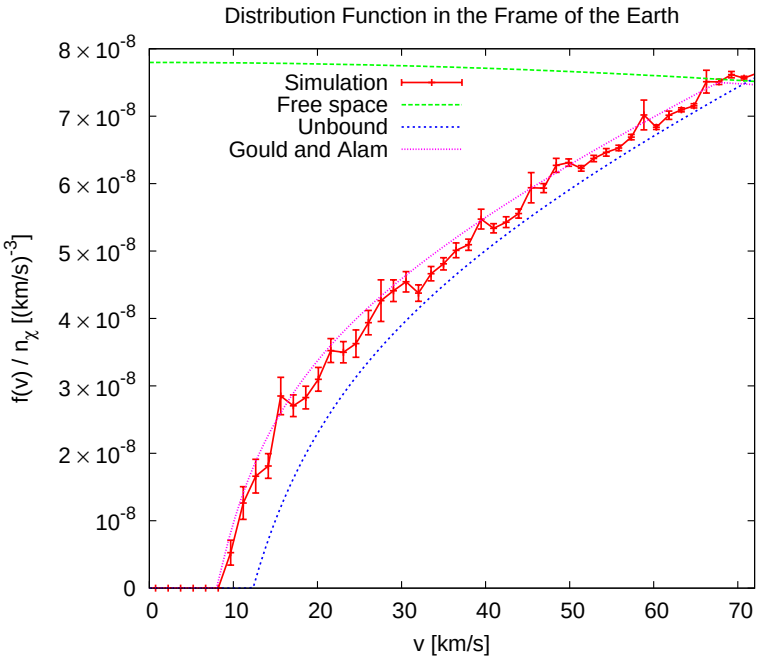

Figure 5.20: The total distribution function from the gravitational capture simulations (using the theoretical High Energy curve) compared against several theoretical distribution functions.

Earth with $v \leq (\sqrt{2}+1)v_\oplus$ using the simulated Regular and High Perihelion distribution functions but with the analytic High Energy distribution function. The distribution functions from each run can be summed because, as discussed in Section 2.3, the simulation runs sample separate pieces of the halo distribution function. This total distribution function describes the entire geocentric distribution function, including both bound and unbound orbits, for $v < (\sqrt{2}+1)v_\oplus$. As shown in Figure 5.20, the simulation distribution function is clearly distinguishable from the analytic unbound halo distribution function (blue dots; this is Eq. 2.3 transformed to the geocentric frame).

One can compare the distribution function from these simulations with previous predictions for the distribution function in the case that particles are captured in a solar system in which Jupiter is the only planet. Lundberg & Edsjö (2004) claim that their solution to the differential equations for gravitational capture indicates that the distribution function of particles in a solar system containing only Jupiter is that described in Gould (1991), which

is approximated as the "conservative scenario" in Gould & Alam (2001). The "conservative scenario" is defined by a distribution function at the position of the Earth given by the free space distribution function (Eq. 2.6) for all unbound and Jupiter-crossing orbits (i.e., all orbits with $a \geq a_J/2$), and is set to zero for all other velocities. In other words, the "conservative" distribution function at the Earth but in heliocentric coordinates is,

$$f(a_\oplus, v_s) = \frac{1}{2(2\pi)^{3/2}} \frac{n_\chi}{\sigma v_\odot v_s} \left[e^{-(v_s - v_\odot)^2/2\sigma^2} - e^{-(v_s + v_\odot)^2/2\sigma^2} \right], \quad (5.20)$$
$$v_s \leq \left[2(1 - (a_J/a_\oplus)^{-1}) \right]^{1/2} v_\oplus.$$

The distribution function in the geocentric frame is attained by making a Galilean transformation. This is the distribution function labeled "Gould and Alam" in Figure 5.20.

The theory behind this distribution function is as follows. Gould (1991) noted that, when a particle passes near or in a planet, its speed does not change with respect to the planet as a result of the encounter, but its direction does. As discussed in Section 2.3, such changes in direction in the frame of the planet translate to changes in energy of the particle with respect to the Sun. In the absence of other forces or loss mechanisms, when the particle encounters the planet again, it should do so in the same direction (up to a change in azimuth) as the direction from the last gravitational encounter. Gould found a time-averaged rate of change in the square of direction change in the limit of small deflections (see Eq. 2.1 and 2.2 in Gould, 1991). He describes the changes in direction as "diffusion," and states that such diffusion should fill accessible bound orbits to the same density as unbound orbits once equilibrium between bound and unbound states is achieved (i.e., on timescales of the time-angled rate of change in direction). The timescale for Jupiter to fill Jupiter-crossing bound orbits is $\sim$ Myr, so on times longer than that, Gould (1991) predicted that Eq. (5.20) ought to describe the distribution function of particles at the Earth in a solar system containing only Jupiter, and neglecting any sort of loss mechanism such as scattering in the Sun or gravitational scattering by Galactic tides.

From Figure 5.20, one can see that the distribution function from the simulations is fairly well fit by the conservative distribution function at low speeds, and is between the unbound and conservative distribution functions at higher speeds. In the low speed section

(a) (b)

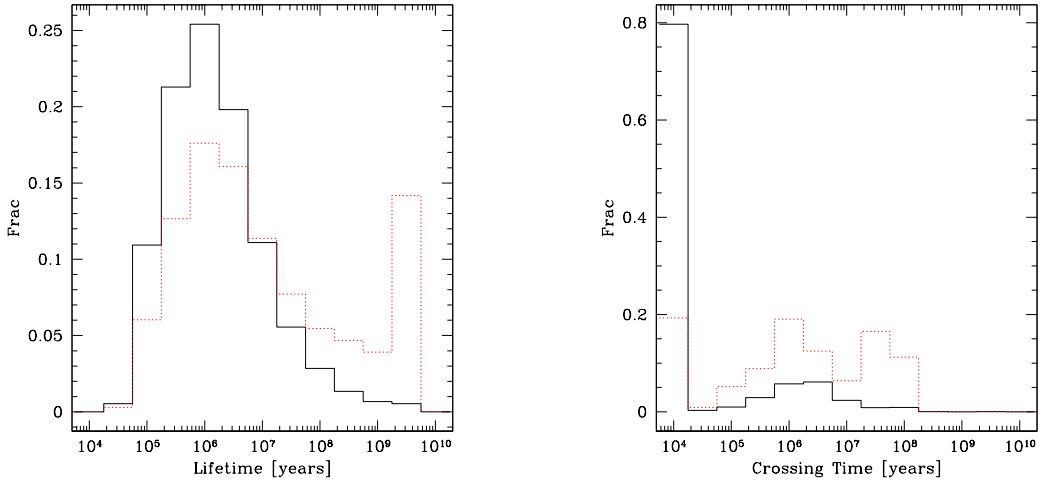

Figure 5.21: (a) Particle lifetime distribution for the Regular run (*solid black*) and the High Perihelion run (*red dots*). (b) Distribution of times at which particles cross the Earth's orbit.

of the distribution function, neighboring error bars are of similar size, suggesting (perhaps) that the true distribution function is fairly well sampled by the simulations. For the larger speeds, it is unclear how well the conservative distribution function fits to either the true distribution function or the simulation distribution function, given that the distribution function may be undersampled in the simulation. However, it seems likely that the conservative distribution function is at least an approximate fit to the true distribution function at the Earth for my model solar system and assumed halo distribution function. This ought to be true unless there are rare (but not too rare) orbits that are bound for a very long time and have a high frequency of intersecting the Earth's orbit. I will discuss this point in more detail in the conclusion of this thesis.

One of the assumptions I made prior to running the simulations was that it would be acceptable to use an angle-averaged distribution function for both this and the last set of simulations. Recalling Section 2.1.2, it was argued that the angle-average was similar to a time average over the normal of the plane of the solar system with respect to the Galactic pole. The period of the Sun's orbit about the Galactic Center is $t_\odot \approx 200$ Myr. If the life-

time of particles in the solar system is long with respect to $t_\odot$, then using a time-averaged distribution function for the initial conditions would be an appropriate approximation.

For the gravitationally captured particles, the time averaging turns out not to be justified. In Figure 5.21(a), I present the lifetimes of the bound particles in both the Regular and High Perihelion runs, as well as the distribution of times at which the (bound and unbound) particles cross the Earth's orbit. The solid black lines represent Regular run distributions, while the dotted red lines denote those of the High Perihelion run. For the Regular run, the median lifetime of a gravitationally bound particle in the solar system is a little more than 1 Myr. The corresponding time is about 5 Myr in the High Perihelion Run. The high lifetime tail of the distributions is due to very large orbits and "resonance-sticking" outside Jupiter's orbit, orbits which may last a long time in the solar system but do not contribute to the distribution function of dark matter particles at the Earth. This fact becomes clear when one examines the distribution of crossing times in Figure 5.21(b). The short-time peak in the crossing time distribution represents unbound particles on their only pass through the solar system and crossings of short-lived bound particles. Although the bin size is 10^4 yr, the crossing times of the particles in the short-time peak is actually quite a bit smaller than 10^4 yr. In the crossing time distribution plot, it is clear that the distribution function is completely set on timescales shorter than the Sun's orbital period about the Galactic Center.

The consequence of this fact is that, while the results and interpretation here are qualitatively correct, to make a precise prediction of the distribution function of gravitationally bound particles in the solar system, one should use the original, anisotropic halo distribution function (Eq. 2.3) to generate initial conditions for particle orbits as a function of time.

The main results of these simulations are twofold. First, the phase space density of unbound orbits is still quite a bit higher than that of the bound orbits above geocentric speeds $v \gtrsim 15$ km s^{-1}. I expect that this will be true even if anisotropic initial conditions are used, and once better statistics of bound orbits are obtained. Secondly, the phase space

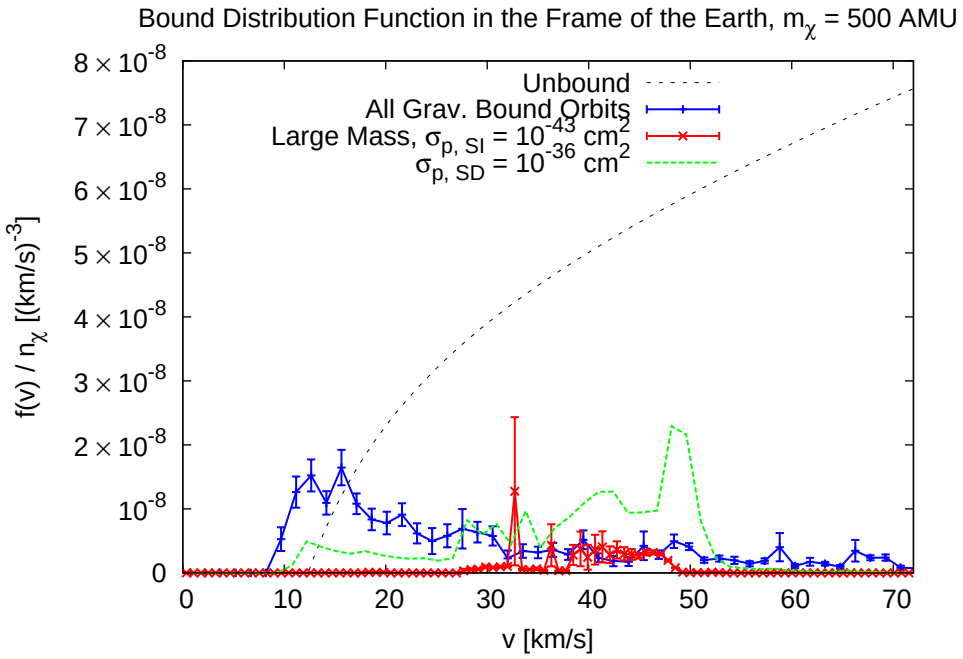

Figure 5.22: Comparison of the geocentric bound distribution functions for $m_\chi = 500$ AMU. The dashed black line indicates the phase space density of unbound orbits. The blue line shows the results from the gravitational capture simulations, the red line is the Large Mass distribution function ($\sigma_p^{SI} = 10^{-43}$ cm^2 and $\sigma_p^{SD} = 0$, and the green dashed line indicates the estimated distribution function for the maximal value of $\sigma_p^{SD} = 10^{-36}$ cm^2.

density of particles bound to the solar system by gravitationally scattering on Jupiter is generally quite a bit higher than that of particles bound by elastic scattering in the Sun for geocentric speeds $v < 30$ km s^{-1} and $v > 50$ km s^{-1}. This is demonstrated in Figure 5.22, in which I show the results of the gravitational capture simulation as well as distribution functions from the weak scattering simulations. If the spin-dependent cross section is high, then the bound distribution function for the elastically scattered particles may be higher than the gravitationally captured particles for 30 km s^{-1} $< v <$ 50 km s^{-1}, but will be smaller or of approximately the same size as the gravitational capture distribution function in the case that spin-independent scattering dominates in the Sun.

Loss Mechanisms

There are two means by which particles may be lost to the solar system other than gravitational scatter by planets:

1. Weak scatter in the Sun (or, very rarely, the planets). Even though no bound orbits were scattered in the Sun in any of the gravitational capture simulations, it is important to determine how the distribution function changes as a function of the strength of the dark matter-baryon interaction.

2. Interactions with external gravitational fields. Galactic tides and encounters with distant stars become important for bound orbits with $a \gtrsim 1000$ AU. Such Galactic gravitational fields are thought to be important in scattering Oort cloud comets into the solar system (Heisler & Tremaine, 1986; Duncan et al., 1987). In addition, if comets originate in the outer solar system (near the outer planets), then Galactic tidal fields can help move the orbital perihelia *outside* the orbits of the planets. It is important to understand how external fields will affect the distribution and lifetimes of WIMPs.

In order to estimate the effect of the WIMP-nucleon cross section on the bound distribution function, I recorded the integrated optical depth of each particle's orbit through the solar system. Very few of the bound orbits (1224/322441) ever go through the Sun, but the optical depths τ of those that do are represented in Figure 5.23. The median optical depth of Sun-crossing particles in the Regular run is $\tau_{med} \approx 10^{-5}$, and $\tau_{med} \approx 2 \times 10^{-4}$ in the High Perihelion run. I have not weighted the distribution according to Eq. (4.10), although, to good approximation, the initial energies of most of the orbits are small enough that the weights are the same. Figure 5.23 illustrates that very few particles have even a moderately high total optical depth if $m_\chi = 500$ AMU, $\sigma_p^{SI} = 10^{-43}$ cm^2, and $\sigma_p^{SD} = 0$. The WIMP-nucleon cross section (and hence, Solar opacity) would need to be much, much higher in order for scattering in the Sun to rescatter any of the particles that pass through the Sun.

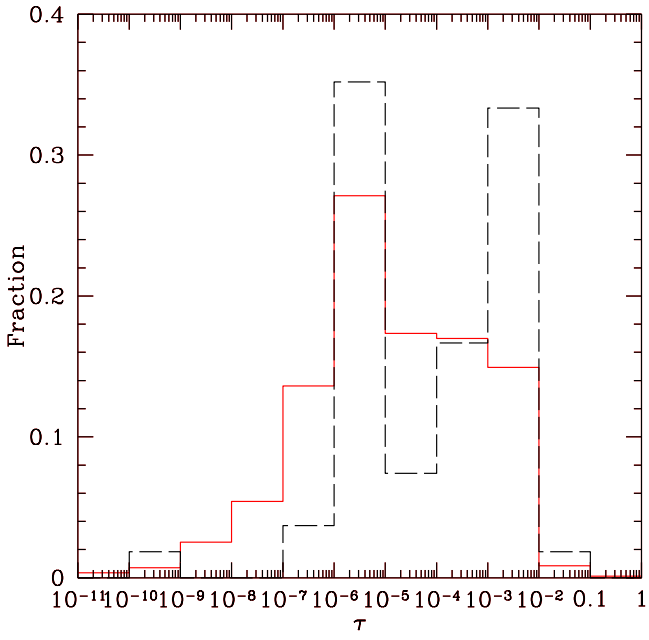

Figure 5.23: The distribution of total optical depth per particle of those particles that enter the Sun. The solid red line indicates the distribution for the Regular simulation, while the dashed black line indicates that of the High Perihelion run.

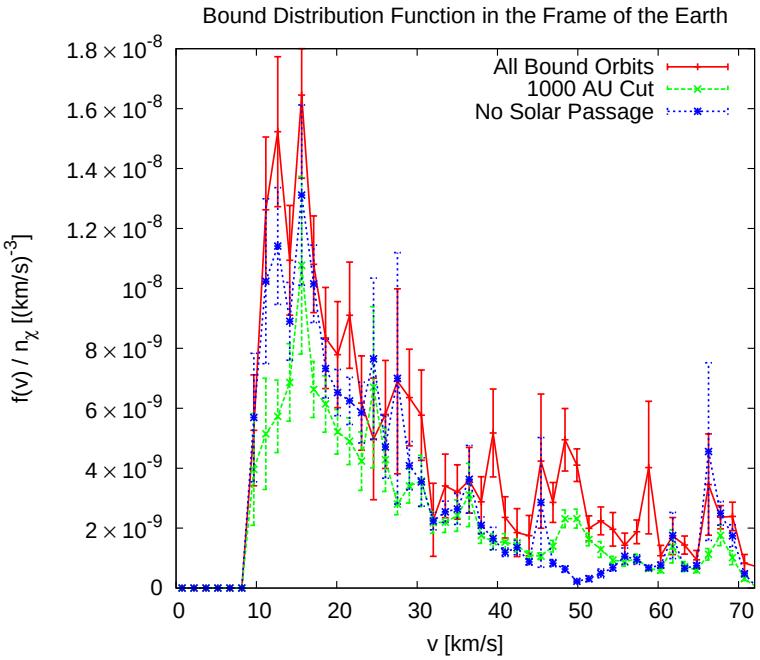

Figure 5.24: The distribution function of bound particles from the gravitational capture simulations. The solid red line indicates the raw distribution function from the simulations minus the unbound halo distribution function. The long-dashed green line with data points indicates the distribution function of particles before they are lost to the solar system by Galactic tides. The short-dashed blue line and data points indicate the distribution function of particles that never enter the Sun.

To find the maximum effect of scattering in the Sun, I find the bound distribution function of only those particles that never enter the Sun. This is represented by the crosses with the dotted blue error bars in Figure 5.24. This comparison plot shows the bound part of the conservative distribution function, and the bound distribution function from the simulations. Even though the Sun-crossing particles contribute significantly to the distribution function, the majority of the bound particle distribution function is built up by particles that never enter the Sun. Therefore, at least at the Earth's orbit, the distribution function of particles gravitationally bound to the solar system depends only weakly on the strength or type of the WIMP-baryon interaction.

The effects of the external gravitational fields are independent of the WIMP mass and the WIMP-nucleon cross section. In order to estimate the consequences of these these forces, I assume that Galactic tides pull the perihelia of all orbits crossing outward through 1000 AU out of the solar system. In Figure 5.24, I show the bound dark matter distribution function, arising from particle-Earth orbit intersections that occur before the particle passes outward through 1000 AU. The density of particles is noticeably lower but by less than a factor of two. I conclude that for trajectories relevant to the WIMP distribution function along the Earth's orbit, the initial gravitational interaction with Jupiter puts many particles on orbits small enough to be relatively unaffected by Galactic tides, or other gravitational forces originating outside of the solar system.

Tides may remove more particles from the solar system than weak scattering in the Sun, especially for at low-speed end of the geocentric dark matter distribution function. Current limits on either the spin-dependent and spin-independent cross sections are strong enough to rule out significant loss in the Sun for gravitationally bound particles. However, the error bars on the bound distribution functions are quite large, and I have not actually included tides in the simulation but have only crudely estimated their effects. Therefore, it is not clear how much tides will affect the distribution functions, nor is certain which loss mechanism would have the greater effect. Future more sophisticated studies of bound WIMPs should include a proper treatment of Galactic tides and tidal fields from passing

stars.

5.1.3 Summary of the Gravitationally Captured WIMPs

Let me summarize the gravitational capture results by placing the results in the context of the original goals of these simulations. In the Introduction, I claimed that previous attempts to find the WIMP distribution function at the Earth resulting from gravitational capture had serious flaws. They did not account for any possible resonant or short duration effects, and treatment (or lack thereof) of weak scattering in the Sun was crude at best. In my simulations, I have a realistic treatment of scattering in the Sun and all gravitational scattering due to the dominant planet, Jupiter.

I find that the distribution function of particles bound by gravitational scatter is approximately described by the conservative distribution function of Gould & Alam (2001). However, there are several caveats to this statement. First, of the nearly 10^{10} orbits I simulate that could be captured in the solar system (i.e., the particles in the Regular and High Perihelion runs), only $\sim 3 \times 10^5$ spend any time bound to the solar system, and only about 6×10^3 of those bound particles contribute to the distribution function at the Earth. For such a relatively small number of contributing particles, it is possible that I miss rare particles that spend a long time bouncing around the solar system. While I have found no shortage of resonance sticking particles, most of those resonances are exterior to Jupiter and never go near the Earth. There could be a few spikes in the distribution function, but one would need a larger sample of particles to resolve them. It is therefore plausible, but not certain, that Gould & Alam's conservative distribution function will continue to be a reasonable approximation for the bound WIMP population, at least for geocentric speeds $v < 30$ km s^{-1}. The question is, just how important is the long-lifetime tail to the distribution functions?

I have also investigated the effects of two loss mechanisms: scattering in the Sun and removal by external gravitational interactions. I have demonstrated that the Sun will remove very few particles from the distribution function, even for high WIMP-nucleon cross

sections. However, it is possible that Galactic tides and other external gravitational forces may significantly reduce the bound distribution function, by up to a factor of two. This case needs a more careful treatment than my crude removal scheme described in the previous section.

It is also important to consider which mechanism for binding particles to the solar system, elastic scattering in the Sun or gravitational scattering by Jupiter, will dominate the bound distribution function. The bound distribution functions are compared with the unbound distribution function in Figure 5.22. Even if the gravitational bound distribution function were smaller by a factor of two due to scattering in the Sun and removal by Galactic tides, the bound distribution function due to gravitational capture will still be larger at small ($v \lesssim 30$ km s^{-1}) and large ($v \gtrsim 50$ km s^{-1}) geocentric speeds. At intermediate speeds, the relative contribution will depend on the optical depth in the Sun.

5.2 Impact on Direct Detection Experiments

Direct detection experiments currently place the tightest constraints on the spin-independent WIMP-nucleon elastic scattering cross section, and are starting to make inroads into spin-dependent WIMP parameter space. The next generation of experiments, with fiducial masses approaching one ton, should be sensitive to event rates of $< 10^{-4}$ kg^{-1} day^{-1}, and to spin-independent WIMP-proton cross sections down to $\sim 10^{-46}$ cm^2. If these experiments do not find a statistically significant signal for WIMP-nucleon scattering, they will have excluded a large set of SUSY parameter space, and will start hacking through the space of the simplest Kaluza-Klein models. More optimistically, if WIMP-nucleon scattering is observed, not only can the WIMP-nucleon spin-independent scattering cross section be determined (rather, $\rho_\chi \sigma_p^{SI}$, the cross section times the local halo WIMP density), but the shape of the differential energy spectrum of events can yield constraints on the WIMP mass, assuming that the various astronomical parameters are well-understood and that the halo dark matter distribution function is not wildly different from smooth and approximately Maxwellian (see the discussion in Section 1.3.2 and Figure 1.15). Particles bound to the

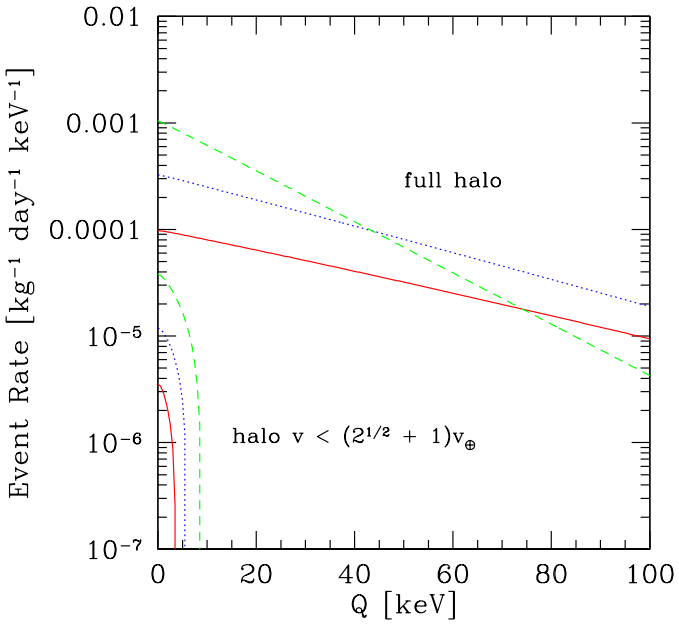

Figure 5.25: Direct detection event rates as a function of the energy transfer Q for a WIMP of mass 500 AMUs and interaction cross section $\sigma_p^{SI} = 10^{-43}$ cm^2 with argon (*solid red line*), germanium (*blue dots*), and xenon (*green dashed*) as targets. The upper curves indicate the event rate for the full halo distribution function under the gravitational influence of the Sun. The lower curves indicate the contribution to the total event rate from only the unbound orbits in the halo distribution function with $v < (\sqrt{2}+1)v_{\oplus}$ in the frame of the Earth, the range of speeds accessible to bound particles.

solar system will contribute to the direct detection rate if the experimental energy threshold is small enough. In this section, I will determine the contribution of the bound distribution function to the direct detection rate.

I focus on direct detection rates for spin-independent interactions, since most of the progress in constraining WIMP parameter space with upcoming experiments will be in the spin-independent sector. However, the results of this section can be applied qualitatively to spin-dependent interactions as well. Any arguments concerning kinematics are completely transferable. Any arguments concerning form factor suppression should apply to spin-dependent interactions as well, although one should use the spin-dependent form factor (Appendix B.2) instead of the spin-independent one for quantitative results.

First, it is instructive to examine the differential event rate $\mathrm{d}R/\mathrm{d}Q$ due to unbound halo particles interacting with various target nuclei. In the class of experiments with one ton target mass, the three most common choices for targets are argon (^{40}Ar), germanium (both ^{73}Ge, which can also experience spin-dependent WIMP-neutron interactions, and ^{76}Ge), and xenon (^{131}Xe). Argon is used by several groups because it is cheap (see the unit prices in Gaitskell, 2007), and liquid noble gas experiments are easily scalable. However, the threshold for these experiments is usually quite large, $Q_{th} \approx 40$ keV, in order to distinguish WIMP from background events. Liquid xenon is used due to its relatively high spin-independent cross section with WIMPs. Xenon-based technology is also quite scalable. The analysis threshold for the initial XENON10 analysis was $Q_{th} = 4.5$ keV (Angle et al., 2007). Germanium is being used for the SuperCDMS experiment, since the cryogenic detection techniques relevant to such experiments are quite advanced. In order to reduce the backgrounds in the analysis window, the low energy limit for the analysis window is taken to be $Q_{th} \approx 10$ keV in current germanium-based experiments.

In Figure 5.25, the event rates $\mathrm{d}R/\mathrm{d}Q$ are indicated for a WIMP mass of $m_\chi = 500$ AMU for both the angle-averaged full halo distribution function (Eq. 2.9) in an inertial frame moving with the Earth (upper lines) and for only those particles with a geocentric speed of $v < (\sqrt{2}+1)v_\oplus$, the geocentric speed range for which orbits bound to the Sun are possible (lower lines). I show the event rates for the low speed particles for the following reason. Most direct detection experiments are not sensitive to the direction of the incoming WIMP. Even though bound WIMPs inhabit a different part of velocity space than unbound WIMPs (see Figure 5.3), they overlap in speed in the geocentric frame. Therefore, the signal from WIMPs on low geocentric speeds will overlap. The rate $\mathrm{d}R/\mathrm{d}Q$ calculated with unbound WIMPs with low geocentric speeds shows the range of transfer energies that are also accessible to bound WIMPs. To calculate actual event rates, one should use the anisotropic halo distribution function, Eq. (2.3), translated to the gravitational influence of the Sun and an inertial frame moving with the Earth, but I use the angle-averaged distribution function for illustrative purposes.

Even though I calculate these event rates using the isotropized halo distribution function, the geocentric halo distribution function is anisotropic due to the motion of the Earth. Therefore, to translate the distribution function outside the sphere of influence of the Earth to the corresponding distribution function at the detector, one should use the mapping technique in Section 4.3, averaged over the detector's daily motion about the Earth's rotation axis. However, using the mapping $\theta_{loc} = \theta$, $\phi_{loc} = \phi$ produces errors in $\mathrm{d}R/\mathrm{d}Q$ of at most a few percent for the low speed event rate, and $< 0.1\%$ for the event rates calculated using the full halo distribution function. Therefore, I use this simplification in calculating $\mathrm{d}R/\mathrm{d}Q$.

There are two main features to the event rate curves for the full distribution function. First, the event rate is higher for more massive target nuclei and lower energies. This is simply a result of the $\sigma_A^{SI} \propto A^2\mu_A^2$ dependence of the spin-independent cross section with nuclear mass m_A. Secondly, the event rates for higher mass nuclei drop off rapidly as a function of energy transfer Q due to form-factor suppression. In the case of spin-dependent event rates, the height of the curve will depend on the spin properties of the target nucleus, as will the slope of $\mathrm{d}R/\mathrm{d}Q$.

The direct detection rate for particles with $v < (\sqrt{2}+1)v_\oplus$ in the frame of the Earth is much lower than that for all particles. In fact, for a given energy transfer, the contribution of low speed halo WIMPs to the direct detection rate never exceeds 4% for the distribution function described in Eq. (2.9), with the maximum occuring at zero energy transfer. This is because a particle must have a minimum speed of

$$v_{min} = (m_A Q/2\mu_A^2)^{1/2} \tag{5.21}$$

to transfer energy Q from the WIMP to the nucleus. In the expression for the differential event rate $\mathrm{d}R/\mathrm{d}Q$ in Eq. (1.19), the integrand peaks at a much higher speed than $v = (\sqrt{2}+1)v_\oplus$, so most of the direct detection signal comes from higher speed particles. One can also use Eq. (5.21) to find the maximum allowable Q_{max} for a given particle speed v with respect to the detector, in the frame and in the gravitational influence of the Earth. In Figure 5.25, it is clear that for a high WIMP mass, the differential event rate with a xenon

target extends to much higher energy transfer than either of the other targets. Given current experimental designs and understanding of backgrounds, only the xenon-based experiments have thresholds low enough to include bound WIMPs in their analysis window if WIMP mass is $m_\chi \gtrsim 200$ AMU. The argon-based experiments are really sensitive only to high speed WIMPs, while germanium-based experiments may only see bound WIMPs if the analysis threshold is dropped below $E_{th} \approx 8$ keV.

For the spin-dependent case, the maximum Q for a given target mass and WIMP mass will not change. However, the shapes of the differential event rate curves may differ from the spin-independent curves. The ratio of the $v < (\sqrt{2}+1)v_\oplus$ differential event rate to the full differential event rate should be the same as in the case of spin-independent interactions since the ratio depends on the form (or cutoff) of the distribution function, not the form factor.

Still, it is important to understand the event rates of low energy transfer scatters in case the analysis windows of future experiments can be expanded to low energy transfer. In Figure 5.26, I present the direct detection event rates from the weak scattering simulations. The top set of three lines, as before, represent the event rates for three different target isotopes for the all the unbound halo particles. The middle set of three lines (with the label "halo $v < (2^{1/2}+1)v_\oplus$") represent unbound halo particles that have geocentric speeds in the same range as those of bound particles. The lowest set of three lines, with the data points and error bars and marked "simulation", represent the event rates derived from the simulations, with the error bars determined by bootstrap resampling. The bound particles contribute, at maximum, a few parts in 10^4 to $\mathrm{d}R/\mathrm{d}Q$, with the maximum contribution occurring for $Q = 0$. The bound particles contribute a maximum of about 1% to the event rate of particles with geocentric speeds of $v < (\sqrt{2}+1)v_\oplus$. As indicated by Eq. (5.21), the event rate $\mathrm{d}R/\mathrm{d}Q$ extends farther in Q for high mass WIMPs and high mass targets than for low mass WIMPs and target atoms, but the contributions to the total differential event rate are negligible at high Q.

To find an upper bound on the direct detection rate from particles captured to the solar

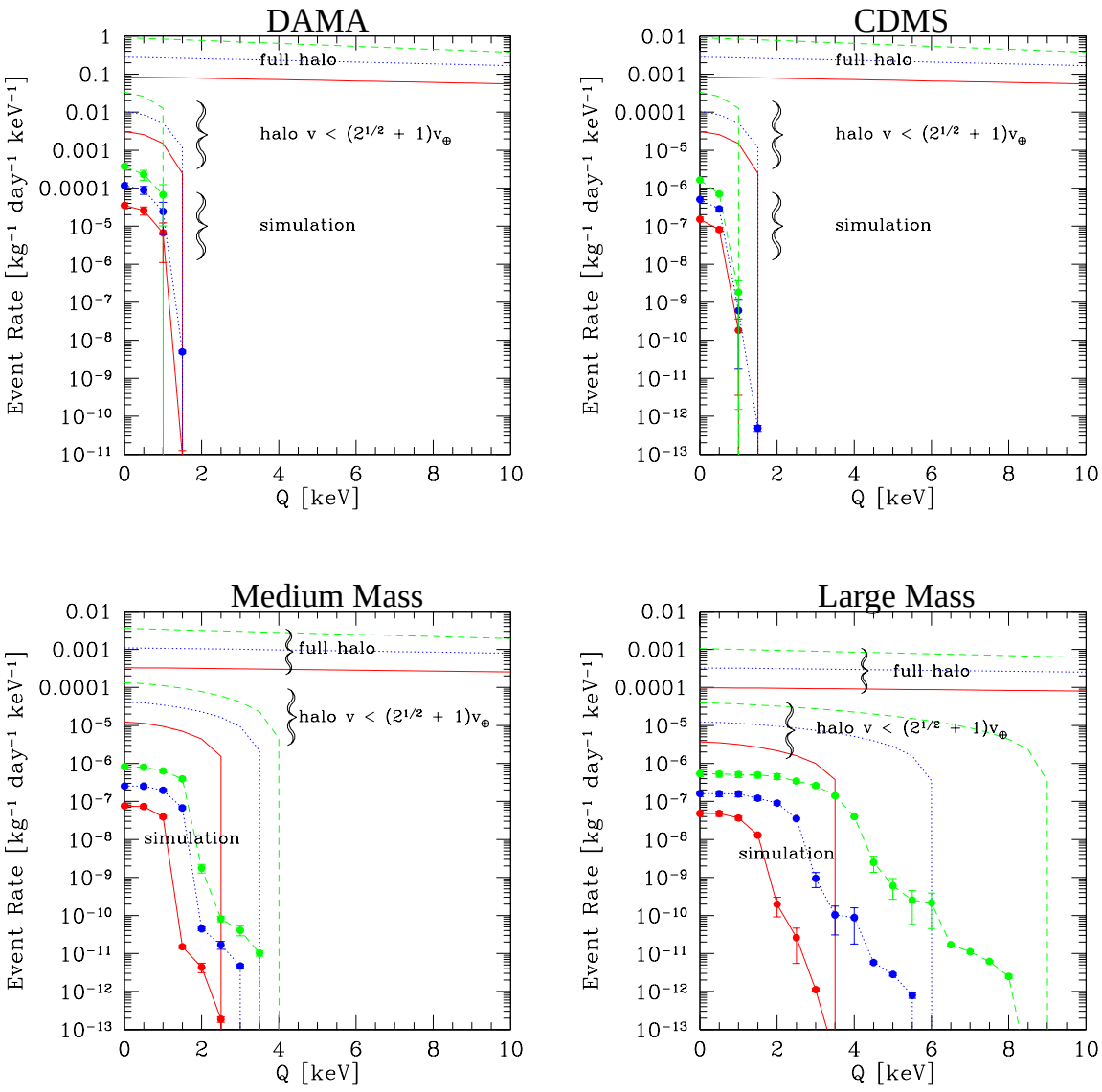

Figure 5.26: Differential direct detection rates for each weak scattering simulation. As in Figure 5.25, solid red lines indicate detection rates for a target of argon, dotted blue lines assume germanium as a target, and dashed green lines indicate rates for xenon.

system by weak scattering in the Sun, I find $\mathrm{d}R/\mathrm{d}Q$ with $\sigma_p^{SI} = 10^{-43}$ cm^2 in the case that the spin-dependent cross section dominates the capture rate in the Sun. In Figure 5.27(a), I show $\mathrm{d}R/\mathrm{d}Q$ for a $m_\chi = 500$ AMU WIMP and a ^{131}Xe target. The uppermost line represents the event rate for all unbound particles, the red dotted line represents the event rate from unbound particles with $v < (\sqrt{2}+1)v_\oplus$, the magenta long-dashed line represents the estimate for bound particles if σ_p^{SD} cm$^2 = 10^{-36}$ cm^2, the black dot-dashed line represents $\sigma_p^{SD} = 1.3 \times 10^{-39}$ cm^2 (i.e., when the Sun has the same opacity as for the DAMA simulation, but with the opacity due to spin-dependent scattering), and the cyan short-dashed line shows the event rate from the Large Mass simulation ($\sigma_p^{SI} = 10^{-43}$ cm^2, $\sigma_p^{SD} = 0$). I choose the two spin-dependent cases because they bracket the rates for spin-dependent cross sections in the range $10^{-36} < \sigma_p^{SD} < 1.3 \times 10^{-39}$ cm^2. For the spin-dependent cases, the direct detection event rate is substantially higher than for the purely spin-independent cases, thanks to loose constraints on σ_p^{SD}. The bound particles can now make up a maximum of $\approx 8\%$ of $\mathrm{d}R/\mathrm{d}Q$ for particles with $v < (\sqrt{2}+1)v_\oplus$, which is still quite small. In Figure 5.26(b), the various $\mathrm{d}R/\mathrm{d}Q$ rates for particles with $v < (\sqrt{2}+1)v_\oplus$ are shown on a linear scale. It is clear that particles captured in the solar system by weak scattering in the Sun still make only a tiny contribution to the total direct detection event rate.

One would expect the event rate from particles bound to the solar system by gravitational capture to be larger than that of particles bound by weak scattering, since the gravitationally bound distribution function (Figure 5.24) is bigger than the maximum distribution function for weakly scattered particles for most of the bound geocentric speed range (Figure 5.22). This is indeed the case, as shown in Figure 5.28. Here, I show the event rates for unbound particles with $v < (\sqrt{2}+1)v_\oplus$ alone for WIMPs with mass $m_\chi = 500$ AMU scattering against ^{131}Xe (green solid line), ^{73}Ge (blue dashed), and ^{40}Ar (red dot-dashed), as well as the sum for gravitationally bound and unbound particles with $v < (\sqrt{2}+1)v_\oplus$ (lines with data points). The bound particles now add a maximum of 25% to the low speed event rate, with this maximum occuring at $Q = 0$.

(a) (b)

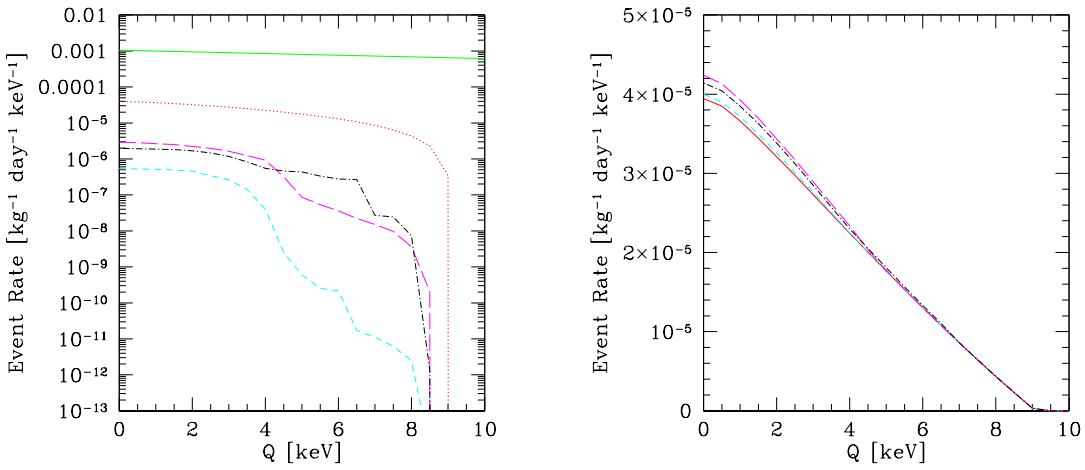

Figure 5.27: Contribution of the estimated distribution functions for significant spin-dependent cross sections to the event rate for a target composed of xenon and for a WIMP of mass $m_\chi = 500$ AMUs. The spin-independent cross section, used to estimate the scattering rate on xenon, is $\sigma_p^{SI} = 10^{-43}$ cm^2. Shown are the contribution from all unbound orbits (*green solid line*), unbound orbits with $v < (\sqrt{2}+1)v_\oplus$ (*red dots*), bound orbits for a distribution function estimated for $\sigma_p^{SD} = 1.3\times10^{-39}$ cm^2 (*black dot-dashes*) and for $\sigma_p^{SD} = 10^{-36}$ cm^2 (*magenta long dashes*), and for direct result from the Large Mass simulation (*cyan short dashes*). *(a)*: Log scale. *(b)*: Linear scale. In this case, the contribution from unbound orbits alone with $v < (\sqrt{2}+1)v_\oplus$ is shown with a red solid line, and the results from the weak simulation have the contribution from the unbound orbits with $v < (\sqrt{2}+1)v_\oplus$ added in.

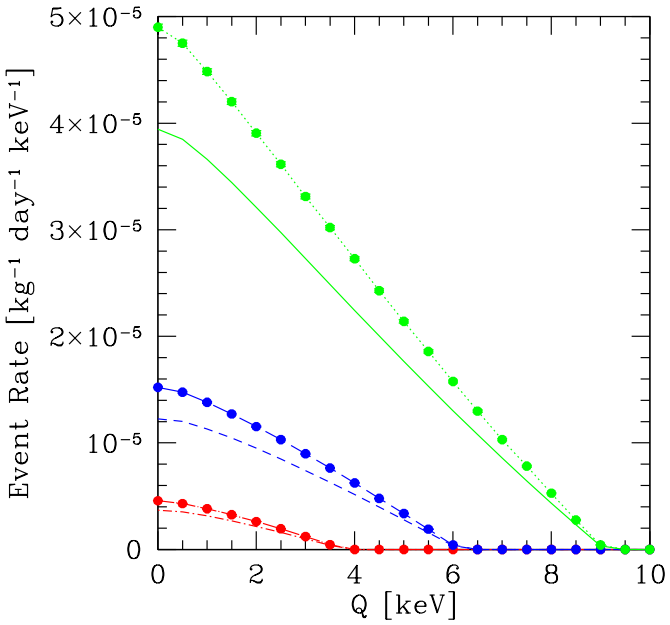

Figure 5.28: Direct detection rates from the gravitational capture simulations with $m_\chi = 500$ AMU. The two red lines represent differential event rates for a target of argon for the purely unbound orbits with $v < (\sqrt{2}+1)v_\oplus$ (*dot-dashed*) and the sum of the simulations (*with data points*), the middle two blue lines represent scattering on germanium (*dashes, unbound; solid with data points, simulation*), and the top green lines denote scattering on xenon (*solid, unbound; dotted with data points, simulation*). Error bars are of the same size as the points marking the data.

In Figure 5.29, I show the maximum direct detection signal due to particles with geocentric speed $v < (\sqrt{2}+1)v_{\oplus}$ (top line), as well as the event rate due to low speed unbound particles alone. Again, I set the WIMP mass to $m_{\chi} = 500$ AMU, and show only the case of a xenon target. The bound particles increase the event rate by a maximum of about a third above the low speed event rate. At $Q = 4.5$ keV, the current analysis threshold for the XENON10 experiment, the increase is about 25%. For lower WIMP masses, one would expect the bound event rate to drop due to the kinematic effect noted in Eq. (5.21). Also, one would expect this percentage to drop for targets made of less massive nuclei. While the bound particles can noticeably increase the low speed event rate, they contribute only about a maximum of 1% of the total differential event rate, with the maximum occuring below current analysis thresholds. The increase in the differential event rate is a function of the energy transfer Q, with the differential event rate excess dropping dramatically for higher Q.

The small, energy-dependent increase in the differential event rate has several consequences. First, the bound particles only negligibly increase the total event rate (integrating $\mathrm{d}R/\mathrm{d}Q$ over the range of Q's allowed in the analysis window), if at all, so estimates of the spin-independent cross section from direct detection experiments will not be affected by bound particles. Secondly, the WIMP mass is extracted from the shape of the differential event rate. However, the bound particles will tilt the spectrum of events only very slightly. The errors on the WIMP mass will likely be dominated by, for example, the uncertainty in the Sun's speed with respect to the Galactic center.

The main conclusion of this section is that bound particles contribute negligibly to both the differential and total event rate, in the case that particles are bound to a solar system containing only Jupiter and the Sun. Since bound particles can only transfer a small amount of energy to target nuclei, they may not be observable at all by high threshold experiments, such as those with argon or germanium as a target. Furthermore, even for experiments with sufficiently low thresholds, errors in the estimate of the WIMP mass and cross section based on the differential event rate will likely be dominated by astrophysical uncertainty

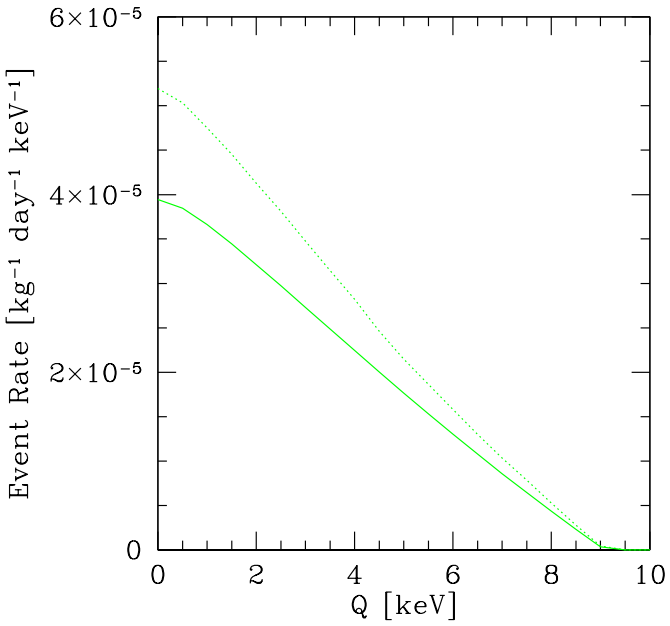

Figure 5.29: The maximum contribution to the differential direct detection rate for $m_\chi = 500$ AMU and $\sigma_p^{SI} = 10^{-43}$ cm^2. The solid green line shows the contribution to the total differential event rate for unbound orbits with $v < (\sqrt{2}+1)v_\oplus$, while the dotted line shows the sum of the gravitational capture experiment and the estimated rate for the bound orbits from weak scattering in the Sun with $\sigma_p^{SD} = 10^{-36}$ cm^2.

rather than by the excess events from bound particles.

5.3 Impact on Neutrino Telescope Event Rates

While the contribution of bound particles to the direct detection rate is expected to be minuscule, there is some hope that the bound particles can significantly boost the neutrino-induced muon event rate from WIMP annihilation in the Earth. As discussed in Section 1.2.2, the capture rate of WIMPs in the Earth is extremely sensitive to the low-velocity part of the WIMP distribution function unless $m_\chi \approx m_A$ for an isotope A in the Earth. Since unbound WIMPs are only capturable in the Earth if $m_\chi \lesssim 400$ GeV (see Figure 1.14), only bound WIMPs are capturable if the WIMP mass is large.

In this section, I focus on neutrino-induced muon event rates from neutralino annihilation in the Earth. As I discussed in Section 2.1.1, it was not necessary for me to specify a dark matter candidate for the simulations. However, the neutrino spectrum from WIMP annihilation is very sensitive to the annihilation modes. Therefore, in order to predict neutrino fluxes for neutrino telescopes, I should do a scan of parameter space for each WIMP candidate. Of the two dark matter candidates I have discussed in this thesis, the neutralino from supersymmetry and the $B^{(1)}$ in Kaluza-Klein models, only the neutralino can produce a neutrino flux observable by km^3 telescopes. This is due to the fact that only spin-independent interactions may produce non-trivial capture rates in the Earth $C \propto \sigma_p^{SI}$ (see Section 1.2.2), and that if the capture and annihilation rates have not reached equilibrium, the neutrino flux $\Phi_\nu \propto C^2 \propto (\sigma_p^{SI})^2$. The Kaluza-Klein models predict low $\sigma_p^{SI} \lesssim 10^{-45}$ cm^2, which i far too low (as will be obvious by the end of this Section) to produce an observable neutrino flux. However, parts of MSSM parameter space allow large spin-independent cross sections. Therefore, I will only explore the neutrino spectrum from neutralino annihilation.

To estimate the neutrino-induced muon event rate for neutrino telescopes from neutralino annihilation in the Earth, I use routines from the publicly available DarkSUSY code (Gondolo et al., 2004). This is a program that calculates, for a user-specified set of

MSSM parameters, a number of interesting quantities, including the WIMP relic density, the spectrum of masses for a given energy scale, cross sections, estimated event rates from annihilation in the Galaxy, the Earth, and the Sun, etc. One can also check whether a model described by a set of SUSY parameters is consistent with current collider constraints. In this program, one can specify all SUSY parameters (of which there are dozens) in the general soft-supersymmetry breaking MSSM Lagrangian (see, for example, Jungman et al., 1996; Chung et al., 2005) or use a simplified set of eight inputs specified at the weak-breaking scale: μ, the Higgsino (Higgs boson superpartner) mass parameter; $\tan\beta$, the ratio of the Higgs vacuum expectation values, since the MSSM requires two Higgs; M_2, one of the gaugino (superparter of a Standard Model gauge field), through which the other two gaugino masses are specified; m_{CP}, the mass of the CP-odd Higgs; m_0, which sets the masses of the lepton and quark superpartners; and A_t and A_b, which parametrize the strengths of the trilinear couplings in the most general MSSM Lagrangian. All other MSSM parameters are derived from just these eight inputs. In effect, one samples an eight-dimensional hypersurface of the MSSM parameter space. No model-specific SUSY-breaking scheme (e.g., supergravity) is assumed.

The first step to finding neutrino-induced muon event rates is to calculate the capture rates of WIMPs in the Earth. Here, I use the potential and isotope distributions found in the DarkSUSY code, which in turn come from Encyclopædia Britannica (1994-1999) and McDonough (2003). In order to reduce computational time, I use an approximation to calculate the capture rate. The full capture rate in Eq. (1.21) is an integral over seven dimensions. However, since the Earth is approximately spherical, and I integrate the capture rate in the whole Earth, to good approximation I can separate the volume and velocity integrals such that the number of particles in a small patch of phase space centered on $(\mathbf{R}, \mathbf{v}_{loc})$ is

$$\mathrm{d}N = f(v(v_{loc}(R)), \theta, \phi)\mathrm{d}^3\mathbf{R}v_{loc}^2\mathrm{d}v_{loc}\mathrm{d}\cos\theta\mathrm{d}\phi. \tag{5.22}$$

I have checked calculations of the capture rate using several distribution functions and WIMP masses, and the simplified capture rate agrees with the full seven-dimensional cap-

ture rate to several percent. This approximation greatly simplifies the capture rate calculations.

In Figure 5.30, I show the rates (in captures/year) as a function of neutralino mass, for $\sigma_p^{SI} = 10^{-43}$ cm^2 and various distribution functions. The peaks in the capture rate correspond to points at which the neutralino mass is nearly exactly the same as a one of the common elements in the Earth. The peak at the iron mass (≈ 56 AMU $= 53$ GeV) is especially prominent. The solid black line is the free space capture rate. Lundberg & Edsjö (2004) claim, using their gravitational capture simulations, that this is a good approximation to the distribution function at the Earth if scattering in the Sun is neglected. The capture rate at high mass remains high because the distribution function is large at small speeds (see, e.g., Figure 5.20). The capture rate of just the unbound particles in the solar system result is represented by the thick red line in Figure 5.30. This capture rate is many orders of magnitude smaller than that of the angle-averaged halo capture rate, and goes to zero for neutralinos with masses higher than $m_\chi \approx 400$ GeV. The green long-dashed line represents the capture rate estimated for both unbound particles and particles bound to the solar system by spin-independent weak scattering in the Sun. To find the distribution function of mass, the distribution functions (rather, $f(\mathbf{v})/\dot{N}_\oplus(m_\chi)$) from the three simulations with $\sigma_p^{SI} = 10^{-43}$ cm^2 are averaged, and then multiplied by the appropriate initial scattering rate in the Sun. The cyan short dash-dotted and magenta long dash-dotted lines represent the distribution functions estimated for $\sigma_p^{SD} = 1.3 \times 10^{-39}$ cm^2 and $\sigma_p^{SD} = 10^{-36}$ cm^2 respectively, which have been added to capture rate of unbound orbits. The capture rates estimated here are larger than those from the raw spin-independent weak scatter simulations because the contribution of the Jupiter-crossing particles goes up as a function of cross section, filling in the distribution function below $v = v_\oplus$. The blue dashed line represents the results from the gravitational capture experiments in the geocentric speed range $v < (\sqrt{2}+1)v_\oplus$ in addition to the unbound orbits with $v > (\sqrt{2}+1)v_\oplus$. This demonstrates that gravitationally captured WIMPs contribute far more heavily to the capture rate in the Earth than even the maximal contribution from WIMPs bound to the solar system by weak

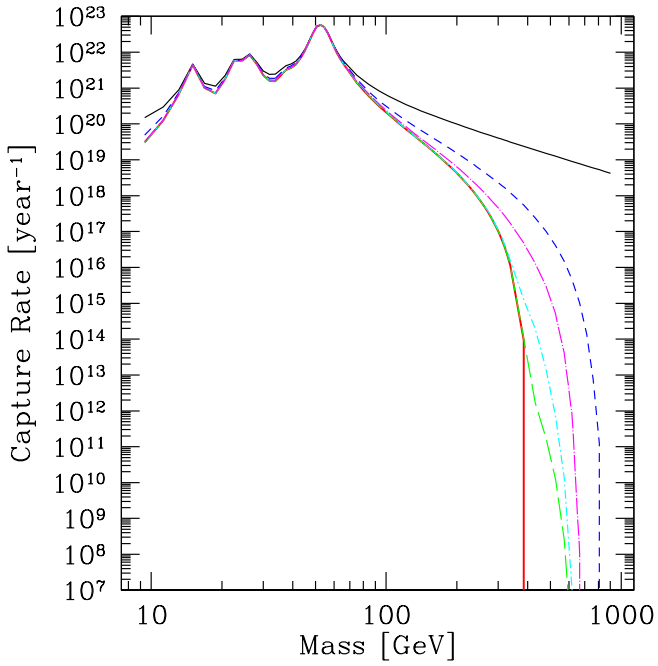

Figure 5.30: Capture rate of WIMPs in the Earth as a function of WIMP mass for $\sigma_p^{SI} = 10^{-43}$ cm^2. The lines correspond to distribution functions for: the halo in the absence of the gravitational field of the Sun (*black solid line*), the result from the gravitational simulation along with the Liouville traced distribution function of unbound orbits above $v = (\sqrt{2}+1)v_\oplus$ (*blue medium dashes*), the estimate for $\sigma_p^{SD} = 10^{-36}$ cm^2 with $\sigma_P^{SI} = 10^{-43}$ cm^2 (*magenta long dash dotted line*), the estimate for $\sigma_p^{SD} = 1.3 \times 10^{-39}$ cm^2 and $\sigma_p^{SI} = 10^{-43}$ cm^2 (*cyan short dash dotted line*), the result of the simulations for $\sigma_p^{SI} = 10^{-43}$ cm^2 (*green long dashed*), and for only unbound orbits (*thick red line*).

scattering in the Sun, as expected.

In order to translate these capture rates into event rates in a neutrino detector, one must explore MSSM parameter space. To generate a set of MSSM models for the neutralino, I make a scan of the MSSM parameter space using the restricted set of inputs. The range used for each parameter, given in Table 5.1, are the default ranges in DarkSUSY. For μ, M_2, m_{CP}, $\tan\beta$, and m_0, I randomly sample the logarithmic range, while I sample the other parameters linearly in their ranges. I keep a model if it makes it through the collider constraints, $0.05 < \Omega_\chi h^2 < 0.135$, and $\sigma_p^{SI} \geq 8 \times 10^{-44}$ cm^2. I choose this lower limit on σ_p^{SI} to include models that are not too much below my choice of σ_p^{SI} in the WIMP simulations.

Table 5.1: Ranges of Parameters for the Restricted DarkSUSY MSSM Inputs at the Weak Scale

SUSY parameters:	μ [GeV]	M_2 [GeV]	m_{CP} [GeV]	$\tan\beta$	m_0 [GeV]	A_t	A_b
min	10	10	10	1	50	-3	-3
max	10000	10000	100	60	1000	3	3

The allowed region of $\Omega_\chi h^2$ is approximately the 4σ range of $\Omega_{dm} h^2$ from the *WMAP*-3 analysis (Spergel et al., 2007).

There are several important points about how DarkSUSY calculates neutrino-induced muon fluxes. For the muon flux calculations in DarkSUSY, neutrino oscillations are ignored, and only the flux of muons from outside the detector volume is calculated. While Bergström et al. (1998a) find that muons created inside the detector volume dominate the signal for smaller WIMP masses ($m_\chi \lesssim 300$ GeV) in large (km^3) telescopes, the expected event rate from muons created within the detector volume depends quite sensitively on the configuration of detectors inside that volume. Therefore, the event rates here ought to be considered a lower limit to the actual event rate in a large detector for neutralino masses $m_\chi \lesssim 300$ GeV. The cases for which the true event rate in the telescope is probably similar to the DarkSUSY calculation are those for which the neutralino mass is large, $m_\chi \gtrsim 300$ GeV.

To estimate the muon event rate in a neutrino telescope, I set the muon energy threshold to $E_\mu^{th} = 1$ GeV. This is somewhat optimistic for the IceCube experiment (The IceCube Collaboration, 2001; Lundberg & Edsjö, 2004) unless muon trajectories lie near and exactly parallel to the PMT strings, but it is reasonable for the more densely packed water experiments (e.g., Super-Kamiokande, ANTARES). However, the signal will drop precipitously with increasing threshold, as shown in Figure 1.11. I assume that the material surrounding the detector volume, the target material for neutrino interactions, is either water or ice. For the muon event rate, I include all muons oriented within a 30° cone relative to the direction of the center of the Earth. The reason for this large cone is that, while one can treat the WIMP annihilation region in the Earth as approximately a point source for heavy

WIMPs, neutrino-induced muons resulting from WIMP annihilation can have quite an angular spread. There are two contributing factors for this spread. First, if one treats the neutralinos as having thermalized in the Earth before annihilating, the WIMP annihilation region is bigger for smaller mass WIMPs. This is a consequence of the fact that if WIMPs are in thermal equilibrium with baryonic species in the Earth, the WIMP number density is

$$n(r) \propto e^{-E/kT(r)} \tag{5.23}$$

$$\propto e^{-m_\chi \Phi_\oplus(r)/kT(r)}, \tag{5.24}$$

where $T(r)$ is the temperature in the Earth at a position r from its center and $\Phi_\oplus$ is the gravitational potential of the Earth. Therefore, the more massive WIMPs are concentrated into a small volume near the center of the Earth. Secondly, when neutrinos undergo charged-current interactions in the medium surrounding the telescope, the muons are more likely to be aligned with the neutrino direction if the neutrinos have higher energy, which is more likely if the neutralino mass is higher (Edsjö & Gondolo, 1995).

In the following figures, I present muon event rates in neutrino telescopes for various distribution functions. In Figure 5.31, I show the event rates assuming a free space distribution function at the Earth, for reference. The solid black line on Figure 5.31 represents the most optimistic flux threshold for IceCube (Lundberg & Edsjö, 2004, and references therein). To show how the event rates depend on the SUSY models for a given spin-independent cross section, I mark the models on the Figure according to which direct detection experiments bracket the cross section for a given neutralino mass. The red open circles correspond to SUSY models with cross sections that lie above the final Edelweiss (Sanglard et al., 2005) spin-independent cross section limit (Figure 1.7). Green open triangles mark models with σ_p^{SI} lying between the Edelweiss and Zeplin-II (Alner et al., 2007) exclusion curves, while filled cyan triangles denote those models with σ_p^{SI} between the Zeplin-II and CDMS (Akerib et al., 2006b) limits. Blue dots show models with limits between the CDMS and the recent XENON10 (Angle et al., 2007) limits, and magenta open boxes show models below the XENON10 exclusion curve. Since I kept models with only $\sigma_p^{SI} > 8 \times 10^{-44}$ cm^2, no models

below the XENON10 exclusion curve with masses less than 70 GeV are shown. From Figure 5.31, it is apparent that with the fiducial local halo mass density ($\rho_\chi = 0.3$ GeV cm^{-3}), the muon event rate of muons created outside the detector volume will be well below threshold for most models consistent with bounds on σ_p^{SI}, even for this distribution function which is unrealistically large at small speeds because it neglects the acceleration of unbound WIMPs due to solar gravity. The only models which have event rates above threshold are those for which the neutralino mass is near the iron mass. If the event rate due to muons created within the detector volume were included, or if the true local dark matter density were a factor of several higher (since the event rate is proportional to ρ_χ^2), it might be possible to push some of those magenta boxes above the IceCube threshold.

I compare these results with event rates from neutralinos that were unbound to the solar system prior to capture in the Earth, including gravitational focusing by the Sun. These event rates are presented in Figure 5.32. The event rates are sharply reduced relative to those in Figure 5.31, making it unlikely that muons from unbound halo particles will be identified unless the WIMP mass lies near the iron mass. In Figure 5.33, I add the capture rate from weak scatter in the Sun (assuming that spin-independent interactions dominate scatter in the Sun) to the capture rate of unbound particles, and estimate the muon event rate. In order to determine the capture rate due to weak scattering in the Sun, I make some assumptions on the cross section and time dependence of the distribution function. The basis for the distribution function is the average of $f(\mathbf{v})/\dot{N}_\oplus$ over the three $\sigma_p^{SI} = 10^{-43}$ cm^2 simulations. Since a large part of the distribution function is in place by 1 Gyr, and the low speed ($v < v_\oplus$) reaches equilibrium by 10 Myr, I treat the distribution function as constant with time so that I can use the solution Eq. (1.23) for the differential equation in Eq. (1.20). The full time-dependent solution to Eq. (1.20) is non-trivial. The approximation should be okay for WIMP cross sections $\sigma_p^{SI} \gtrsim 10^{-43}$ since half or more of the buildup in the distribution function should occur on timescales $t < 10^9$ yr, and should in any case be more than valid for speeds $v < v_\oplus$. I assume that the portion of the distribution function $f(v)$ due to non-Jupiter-crossing particles is fixed as a function of cross section, and that

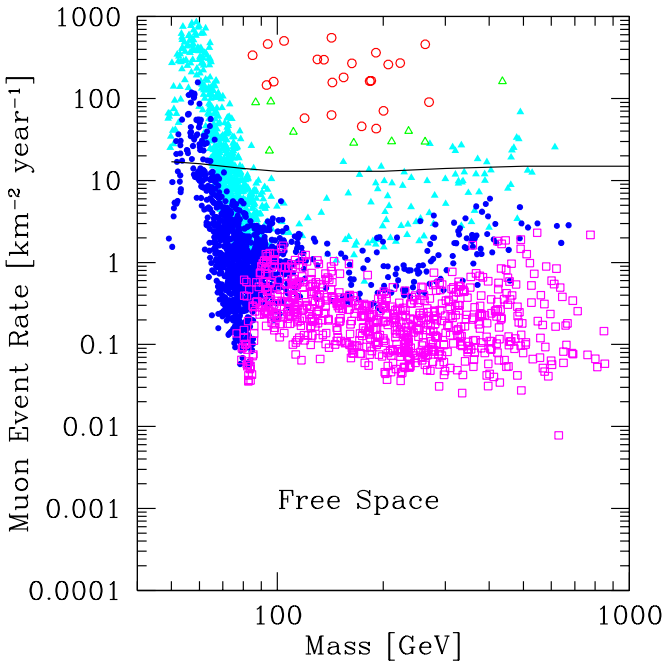

Figure 5.31: Muon event rates with an optimistic energy threshold of 1 GeV for a sample of SUSY models. The dark matter distribution function is the halo distribution function in the absence of the solar system. The SUSY models marked with red open circles have spin-independent cross sections above the Edelweiss limit (see Figure 1.7 and Sanglard et al., 2005), those marked with open green triangles have σ_p^{SI} lying between the Edelweiss and Zeplin-II limits (Alner et al., 2007), cyan triangles denote those with the cross section between the Zeplin-II and CDMS limits (Akerib et al., 2006b), blue dots mark models with spin-independent cross sections between the CDMS (Akerib et al., 2006b) and XENON10 limits, and magenta-outlined boxes denote models with σ_P^{SI} lower than the XENON10 limit (Angle et al., 2007).

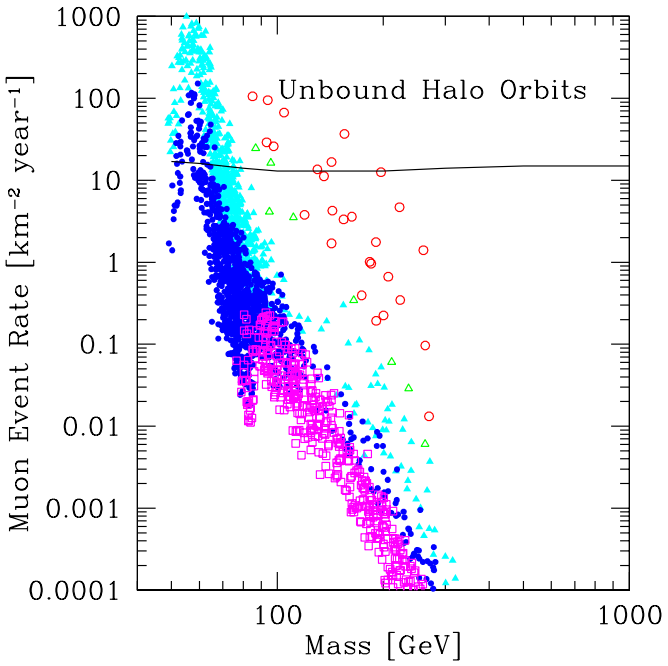

Figure 5.32: Muon event rates from halo WIMPs unbound to the solar system. The symbols have the same meanings as those in Figure 5.31.

$f(v)/\dot{N}_{\oplus}$ is fixed for Jupiter-crossing orbits. The latter assumption should be valid for all spin-independent cross sections represented in my MSSM parameter scan, while I would expect the former assumption to be violated for high cross section. This is because there is a factor of three rise between the high plateau of the $\sigma_p^{SI} = 10^{-43}$ simulations and the DAMA simulation. Therefore, the points in Figure 5.33 above the Edelweiss limit and with $m_\chi < 150$ GeV should be somewhat higher than shown on the plot. However, as one would expect from the capture rates in Figure 5.30, the event rate from neutralinos bound to the solar system via spin-independent elastic scattering in the Sun is extraordinarily low, given constraints on the spin-independent cross section. Figure 5.33 is indistinguishable from Figure 5.32.

The event rate can be boosted if the spin-dependent cross section is large, since constraints on the spin-dependent cross sections are far weaker than those on the spin-independent cross section. To find a maximum event rate due to weak scattering in the Sun,

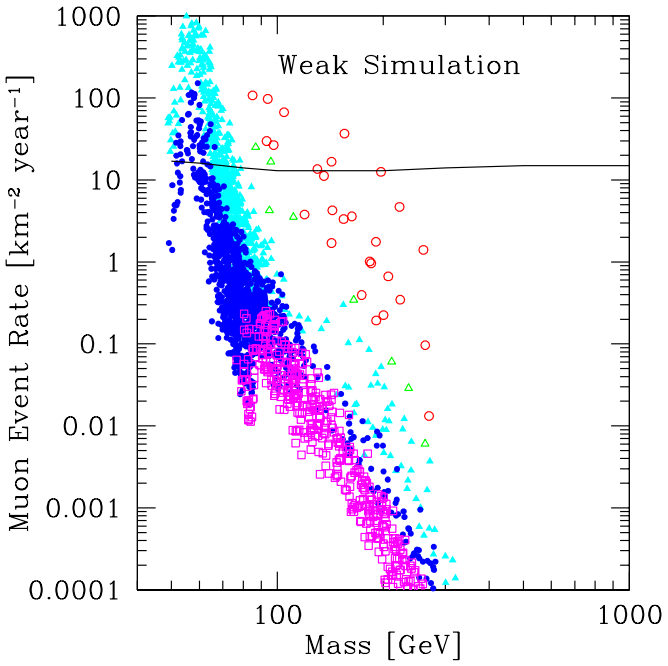

Figure 5.33: Muon event rates using the results of the weak scattering simulation and including the contribution particles unbound to the solar system. The distribution function is based on the average of the three simulations with $\sigma_P^{SI} = 10^{-43}$ cm^2. The symbols have the same meaning as those in Figure 5.31.

I use the estimated distribution function for $\sigma_p^{SD} = 10^{-36}$ cm^2. I assume that the distribution function is independent of the spin-independent cross section, and that $f(\mathbf{v})/\dot{N}_\oplus^H$ is independent of WIMP mass. The spin-dependent cross section is slightly above the NAIAD exclusion limit (Alner et al., 2005), and definitely above the KIMS limit (Lee et al., 2007), and marks the point at which the Sun can no longer be thought of as being optically thin for WIMPs. For the SUSY models I generated, all σ_p^{SD} lie below 10^{-36} cm^2, so technically I should not be using the estimated distribution function for $\sigma_p^{SD} = 10^{-36}$ cm^2 for these models. However, it is possible that in some part of SUSY parameter space that I have not explored, such high cross sections are possible and have a similar annihilation spectrum as the SUSY models I have generated. Therefore, the event rates estimated with this distribution function ought to be considered an *upper limit* on the muon event rate. The estimated muon event rates are presented in Figure 5.34. While the event rates are certainly higher than those for purely spin-independent scattering in the Sun, they are still, with the usual exception of the iron resonance, well below the IceCube detection threshold for those models with spin-independent cross sections consistent with recent experiments.

In Figure 5.35, I show the event rates estimated from the gravitational capture experiments. In this case, using the Eq. (1.23) time-independent solution to Eq. (1.20) is valid, since the distribution function is fixed by 100 Myr. The distribution function is independent of both elastic scattering cross section and WIMP mass. The capture rate used to determine the muon event rate is determined by the gravitational simulation for geocentric speeds $v < (\sqrt{2}+1)v_\oplus$ and the unbound halo distribution function above those speeds. The event rates from gravitational capture to the solar system are significantly higher, especially at high masses, than the maximum event rate from the bound population from weak scattering in the Sun. However, the event rates for most models still lie below the IceCube threshold.

The final event rate estimate I include (Figure 5.36) is the combination of the maximum weak scattering and the gravitational scattering result. This should be considered to be an upper limit to the event rate from particles scattered onto bound orbits in a solar system

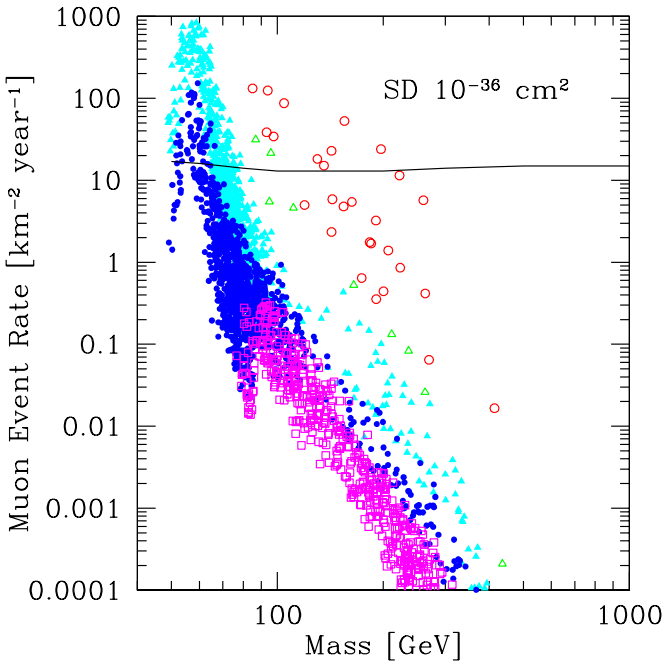

Figure 5.34: Muon event rates using the estimated distribution function for $\sigma_p^{SD} = 10^{-36}$ cm^2. Symbols mark the same models as in Figure 5.31.

consisting only of the Sun and Jupiter, in the absence of neutrino oscillations and muons created within the detector volume. The event rates for models consistent with either CDMS or XENON10 are still well below the IceCube threshold especially for high masses, with the exception of models with neutralino masses near the iron mass. This is consistent with what was expected even from Figure 5.31. The combined bound distribution function is still far less at low geocentric speeds than the free space distribution function.

Even though the prospect for seeing a neutrino-induced muon signal from WIMP annihilation in the Earth is dim, there are several reasons to hope that the signal might be boosted above these estimates. First, the event rates have been calculated assuming that neutrinos do not oscillate. While this might have been a conservative assumption when the relevant section of the DarkSUSY code was written in circa 1996, it is clearly a poor assumption to make now. Blennow et al. (2007) have demonstrated that neutrino oscillation in the Earth will increase the muon-neutrino flux at the surface by a factor of several at low

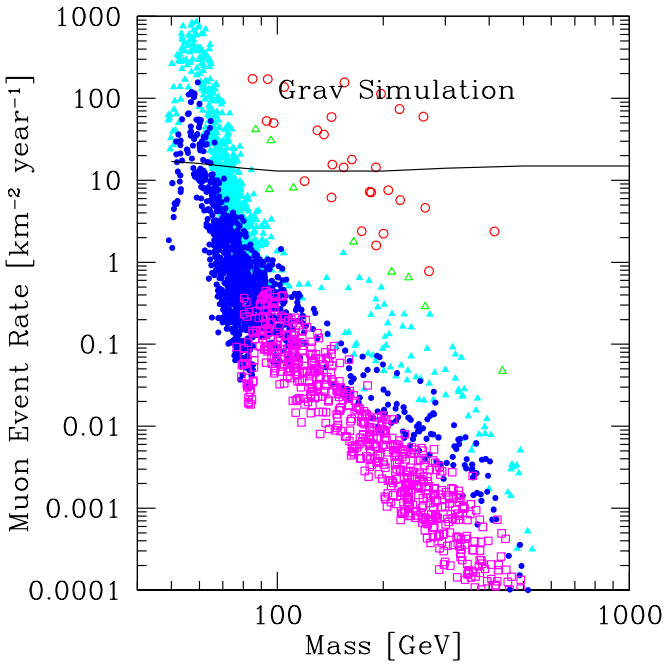

Figure 5.35: Muon event rates using the result from the gravitational capture simulations. Symbols mark the same models as in Figure 5.31.

energies, although oscillation makes less of an impact on the expected rates of the higher, more easily observed neutrinos (see their Figure 8). Secondly, the muon event rates ought to be considered a lower bound on the event rate in an actual detector since DarkSUSY only considers the flux of muons that are created outside the detector volume. Since, in particular, the IceCube experiment has a fairly large volume, one might expect events originating inside the detector to be quite important, especially at the low end of the neutrino energy spectrum. Bergström et al. (1998a) find that the muon event rate is increased by up to an order of magnitude for WIMP masses of $m_\chi \lesssim 300$ GeV in the class of km^3 telescopes, although the expected enhancement depends on the detector design. The enhancement is negligible for smaller detector volumes. Thirdly, I have assumed a local neutralino density of $\rho_\chi = 0.3$ GeV cm^{-3}. This is rather at the low end of the allowed range of ρ_χ given current constraints (see Section 1.3). If the true dark matter density were $2-3$ times higher than my fiducial density, then the expected signal would go up a factor of $4-9$. Finally, if the

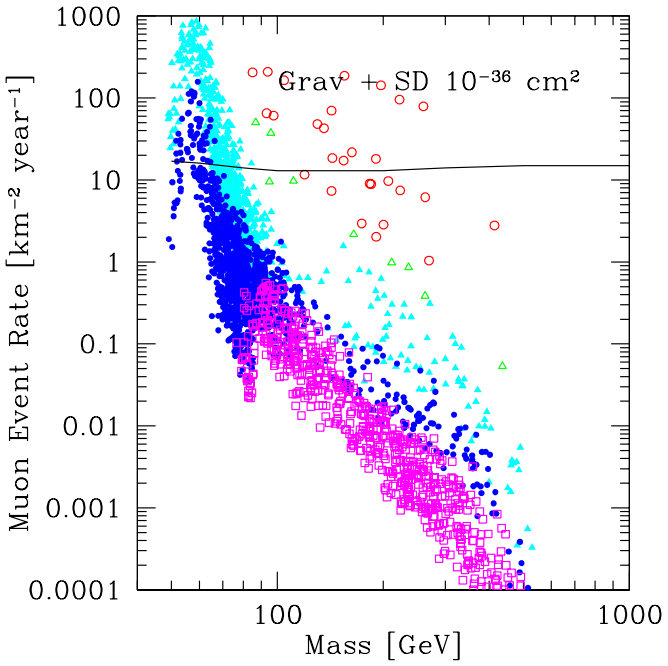

Figure 5.36: Muon event rates using the estimated distribution function for $\sigma_p^{SD} = 10^{-36}$ cm^2 and the results from the gravitational capture simulation. This is the maximum total event rate in Jupiter is the only planet in the solar system. Symbols mark the same models as in Figure 5.31.

other planets were included in the model solar system, the effect would likely be to increase the lifetimes of bound particles. They would also smear out the the particles' z-component of the angular momentum, thereby opening up the dark matter distribution function below the 8.8 km s^{-1} geocentric speed threshold. Therefore, the true bound distribution function is likely to be larger at lower speeds than that estimated in this work.

However, in spite of all of these effects that may boost the muon rate in neutrino telescopes, it may never be possible to observe products of WIMP annihilation in the Earth if the spin-independent cross section is much lower than the current XENON10 exclusion limits unless a truly monstrous neutrino observatory is built. In addition, the flux limit for IceCube will likely be higher than that indicated in the plots in this section (Lundberg & Edsjö, 2004). As demonstrated in Figure 1.11, the muon event rate drops dramatically as a function of increasing experimental threshold. Even though there is a big signal at $E_{\mu}^{th} = 1$ GeV for WIMPs with $m_{\chi} \approx m_{Fe}$, the signal drops by more than four orders of magnitude if the threshold is raised to $E_{th} = 50$ GeV. Therefore, even if the muon event estimates in this section are low, it still may not be possible to definitively detect neutrino-induced muons from WIMP annihilation in the Earth.

5.3.1 An Aside on Neutrinos from the Sun

Another possible source of neutrinos is WIMP annihilation is the Sun. Even though the center of the Sun is a factor of 2×10^7 further away from neutrino observatories than is the center of the Earth, the Sun has the potential to capture far more WIMPs than the Earth (see Section 1.2.2), and may be able to provide a higher flux for neutrino observatories than the Earth, especially if the spin-independent cross section is quite low. Recently, the prospect of indirect detection of WIMPs from the Sun has become more attractive because it has been suggested that it could do better than direct detection experiments in constraining the proton-WIMP interaction (Halzen & Hooper, 2006). Currently, upcoming ton-scale direct detection experiments are not expected to constrain the spin-dependent WIMP-proton cross section very well. The targets of proposed ton-scale experiments will

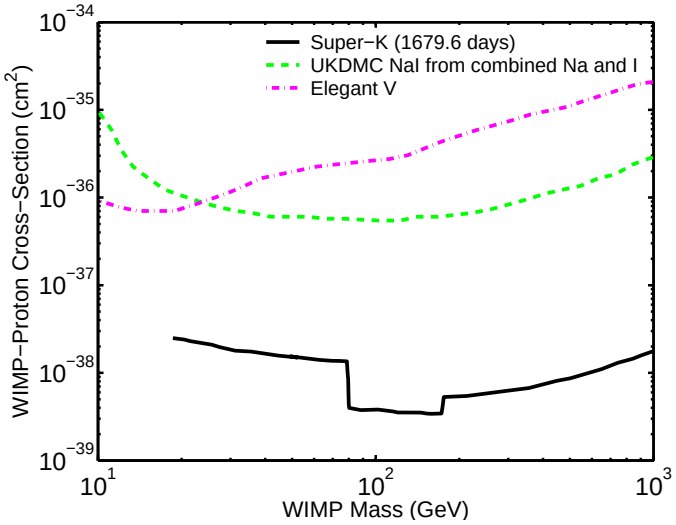

Figure 5.37: Limits on the proton-WIMP cross section from the Super-Kamiokande (Desai et al., 2004), ELEGANT V (Yoshida et al., 2000b) and UKDMC (NAIAD) (Alner et al., 2005) experiments. This figure is from Desai et al. (2004).

largely consist of isotopes that will have unpaired neutrons but not unpaired protons, or will have even numbers of both protons and neutrons. Hence, upcoming experiments will be far more sensitive to the WIMP-neutron cross section than the WIMP-proton cross section (Girard & Giuliani, 2007). This disparity results from the main science goal of the experiments, which is to probe the spin-independent cross section. The best limits for this cross section have come from (and will continue to be from) experiments with target nuclei containing even numbers of protons. Therefore, the tightest future constraints on the WIMP-proton cross section will likely come from indirect detection experiments.

While many experiments have placed upper limits on the event rates of neutrino-induced muons from the Sun (AMANDA, Ackermann et al. (2006); MACRO, Ambrosio et al. (1999); Baksan, Boliev et al. (1996)), the Super-Kamiokande group is the first to attempt to translate the upper limit on muon flux to an upper limit on the WIMP-proton cross section (Figure 5.37). The Super-K procedure illustrates the promise of using indirect detection to constrain the WIMP-proton cross section as well as some already known complications and uncertainties. A major concern in interpreting a neutrino-induced muon signal from

WIMP annihilation is that the event rate depends not only on the capture rate but also on the annihilation branching ratios. In order to determine the resulting spread in event rates for a fixed WIMP mass, Kamionkowski et al. (1995) computed neutrino energy spectra for a variety of WIMP annihilation modes. They then compute the ratio of the direct to the indirect detection rate for specific channels for a fixed WIMP mass. The maximum ratio $\gamma(m_{\rm WIMP})$ is determined by the annihilation mode that produces the lowest indirect detection event rate. Desai et al. (2004) then use $\gamma(m_{\rm WIMP})$ to place a conservative upper limit on σ_p^{SD} by first translating the neutrino-induced muon event rate to a direct detection rate, which in turn has a one-to-one relation with the spin-dependent cross section in the absence of scalar interactions. Here, I use $m_{\rm WIMP}$ instead of m_χ since it is possible that Kaluza-Klein WIMPs could produce an observable signal.

As demonstrated in Figure 5.37, this method appears to be more than competitive with current direct detection experiments in constraining the WIMP-proton cross section. However, aside from the known astrophysical uncertainties in the dark matter distribution function, which complicate the interpretation of signals, there are several other effects that can seriously affect the ability to properly translate signals to constraints on dark matter models. It is extremely important to take neutrino oscillations and the interactions of neutrinos in the Sun into account. Neither of these effects were included in the Desai et al. (2004) analysis. Various authors have demonstrated that these effects can either greatly increase or decrease the expected indirect detection signal depending on the WIMP annihilation branching ratios (Cirelli et al., 2005; Barger et al., 2007a; Blennow et al., 2007; Lehnert & Weiler, 2007).

I would like to focus attention on an effect that may decrease the expected indirect detection signal from the Sun for very massive WIMPs. In particular, I would like to address the calculation of the capture rate of WIMPs in the Sun. It is usually assumed that once a particle is captured by the Sun, it quickly thermalizes (with the thermalization time many orders of magnitude below the age of the solar system), becomes concentrated in the inner $r < 0.01 R_\odot$, and annihilates with another WIMP. However, if the spin-dependent mode

dominates capture within the Sun, almost 100% of WIMPs are captured onto Earth-crossing orbits for $m_{\rm WIMP} \gtrsim 1$ TeV, as demonstrated by Figure 5.12(c). In this chapter, I have found that WIMPs that are initially scattered onto Jupiter-crossing or near-Jupiter-crossing orbits generally escape before rescattering in the Sun for modest cross sections. These particles will never thermalize. In addition, particles with $a > 1.5$ AU have a fairly high probability of experiencing quasi-Kozai behavior, thus drastically extending their lifetimes in the solar system and hence, delaying thermalization times. Moreover, for such high WIMP masses, particles are likely to rescatter onto fairly high energy orbits, thus prolonging lifetimes even more. Therefore, for modest cross section ($\sigma_p^{SD} \lesssim 10^{-39}$ cm^2), most particles with initial semi-major axes $a_i > 1.5$ AU either never thermalize or thermalize millions to billions of yr after their initial capture in the solar system. Thus, to properly predict the capture rate of particles that can thermalize in the Sun, it is necessary to determine what fraction of particles captured in the Sun are captured onto orbits of $a > 1.5$ AU.

I use a cold Sun approximation to estimate what percentage of particles cannot thermalize, at least very quickly. For a WIMP mass $m_{\rm WIMP} = 100$ GeV, about 2% of captured particles are on orbits with $a > 1.5$ AU. This percentage increases to $\approx 10\%$ for $m_{\rm WIMP} = 500$ GeV, 20% for $m_{\rm WIMP} = 1$ TeV, and 40% if $m_{\rm WIMP} = 2$ TeV. The upper end of this mass range is preferred by Kaluza-Klein models. If the WIMP were a truly massive 10 TeV, then nearly all captured particles would have $a > 1.5$ AU. Therefore, if the WIMP mass is very large, and if the spin-dependent WIMP-proton cross section is $\sigma_p^{SD} \lesssim 10^{-39}$ cm^2, a significant fraction of WIMPs initially captured by the Sun never thermalize. While prospects for constraining the spin-dependent WIMP-proton cross section from WIMP annihilation in the Sun are good if the WIMP is only moderately massive ($m_{\rm WIMP} < 1$ TeV), they become quite poor if the WIMP is quite massive. Estimating the neutrino event rate will depend on the detailed properties of how the WIMPs thermalize in the Sun; these could be determined by simulations similar to the ones in this thesis.

Chapter 6

Conclusion

6.1 Summary

In this thesis, I have developed numerical techniques and codes that allow me to follow the evolution of the WIMP population bound to the solar system. These techniques include an orbit integrator that can follow even highly eccentric orbits penetrating the Sun for billions of years with only small, oscillatory energy errors. I have applied these codes to the problem of determining the distribution function and event rates at the Earth of WIMPs bound to a simplified solar system with only one planet, Jupiter. In Chapter 5, I presented the results of my simulations for a selected set of WIMP masses and cross sections (Tables 2.1 and 2.2), and determined approximately how the results change as a function of WIMP mass and elastic scattering cross section. The main result of that chapter was that the bound distribution function is never very big. In Section 5.1, I showed that the bound distribution function arising from particles scattering in the Sun will probably be largest relative to the unbound distribution if the WIMP-proton cross section is large and the WIMP mass is fairly modest (no more than several hundred GeV). Even in this case, the phase space density would still be quite a bit smaller than that of unbound particles streaming through the solar system, such that the number density of particles is $< 10^{-3} n_\chi^{halo}$.

The smallness of the bound distribution function is in sharp contrast to the analytic

predictions of Damour & Krauss (1999), and results from a combination of the three main effects: (i) The lifetimes of particles on Kozai cycles are small relative to the age of the solar system. (ii) The phase space density of bound, Jupiter-crossing orbits grows slowly as a function of WIMP-nucleon cross section for high cross sections (the WIMPs are more likely to be captured on bound orbits but also more likely to be rescattered in the Sun). (iii) Current experimental limits on the scattering cross section are substantially smaller than those assumed by Damour & Krauss. The bound distribution function due to gravitational capture in the solar system is approximately described (within 20% for $v < 30$ km s^{-1} and to within a factor of two for higher speeds) by the "conservative scenario" of Gould & Alam (2001). This distribution function is relatively insensitive to the WIMP mass and the WIMP-nucleon elastic scattering cross section.

The smallness of the bound WIMP population has several implications for Earth-based WIMP detection experiments. For more massive target nuclei, it will be possible for events to lie above the analysis threshold. For example, in the case of a target of ^{131}Xe, bound WIMPs of $m_\chi \gtrsim 200$ GeV can produce events that lie above the XENON10 analysis threshold of $Q_{th} = 4.5$ keV. However, the maximum possible differential direct detection event rate due to bound particles is about $\lesssim 1\%$ of the unbound halo event rate. Moreover, the maximum energy transfer Q for bound particles will always be small, $Q_{max} \lesssim 10$ keV, so the *total* increase to the integrated event rate will also be very small. A pessimist's view of this result is that bound WIMPs will not raise the expected event rate for any plausible WIMP parameters, in contrast to the very optimistic prediction of Damour & Krauss (1999). An optimist's viewof this result is that parameter estimation based on the spectrum of recoil events (or lack of events, which is currently the case), which is currently based on unbound orbits alone, is unlikely to be affected by the presence of bound WIMPs.

The smallness of the bound distribution function also makes it unlikely that WIMP capture and annihilation in the Earth will be detected in upcoming large neutrino experiments. In Figure 5.31, I showed through-going muon event rates for a neutrino telescope with a threshold of $E_\mu^{th} = 1$ GeV using the free space distribution function at the Earth. Even with

this distribution function, which is large relative to the true unbound distribution function in the potential well of the Sun and Earth at low speeds, the flux of neutrino-induced muons falls well below the IceCube threshold for MSSM models with σ_p^{SI} consistent with the recent XENON10 results. The maximum event rate from my simulations is at least two orders of magnitude below the IceCube threshold unless the WIMP mass is approximately the iron nucleus mass (this is due to a resonance, such that the WIMP can transfer all its energy to the nucleus for arbitrary initial energy), and is in general orders of magnitude smaller than the free space event rate for the same WIMP model (by a factor of about ~ 10 near $m_\chi = 100$ GeV, by a factor of $\sim 10^4$ for $m_\chi = 300$ GeV; see Figure 5.36). Moreover, the energy threshold for an IceCube-type experiment is likely to be much higher than $E_\mu^{th} = 1$ GeV (although not for current water-based neutrino telescope configurations), and the expected event rate drops rapidly as a function of telescope energy threshold. Therefore, it is quite unlikely that products of WIMP annihilation in the Earth can be distinguished in planned neutrino telescopes.

6.2 Future Directions

In this section, I will discuss some possible extensions to the work in this thesis. First, I will suggest some possible speed-ups to the simulations, and potential methods to get better statistics on the dark matter distribution functions. Secondly, I make the argument for studying both weak scatter and gravitational capture experiments using all the planets in the solar system, not just Jupiter.

6.2.1 Possible Speed-Ups

Three types of orbits dominate the computational time: Kozai-cycles, quasi-Kozai cycles, and relatively long-lived Jupiter-crossing orbits. It would be of great interest to reduce the computation time of such trajectories to improve the error bars on the distribution functions. Such a speed-up would also allow for a more thorough investigation of dependence of the distribution function on the $m_\chi - \sigma_p^{SI}$ parameter space.

After an integration time of $\sim 10^6$ years, it should be easy to distinguish particles on Kozai cycles from all other types of orbits. As long as the initial semi-major axis is not near a resonance, the contribution of a particle on a Kozai resonance to the distribution function is governed by three factors: (i) the lifetime of the Kozai cycle; (ii) the optical depth per Kozai cycle; and (iii) the intersections the particle orbit with the Earth's orbit, which determines the contribution to the distribution function of a particle in one Kozai cycle. Therefore, one can use the initial 10^6 year integration to determine all three of these properties. Then, instead of doing probabilistic scattering in the Sun for each passage in the Sun, one can compute probabilistic scattering on a per Kozai cycle basis, as long as $\tau_{Kozai} \ll 1$. The part of the distribution function due to each particle is then the distribution function from one cycle multiplied by the number of cycles the particle survives. One can then do a Monte Carlo treatment of the rescattering and continue to follow the particle.

The efficiency would also be greatly enhanced by a mapping method for the quasi-Kozai and Jupiter-crossing particles. Several groups (Malyshkin & Tremaine, 1999; Pan & Sari, 2004) have found symplectic maps for highly eccentric comets with low inclinations in the restricted circular three-body problem. Malyshkin & Tremaine (1999) are interested in long-period, planet-crossing orbits, whereas Pan & Sari (2004) are concerned with describing resonances for eccentric orbits entirely exterior to a planet, in a very narrow range of Jacobi constant. In both of these maps, the torque from the planet is applied as a "kick" at perihelion (Malyshkin & Tremaine, 1999). In order to make the maps symplectic, these authors require several big approximations regarding the treatment of the kicks. In general, the kick in energy and angular momentum due to tidal torques depends on the energy and angular momentum of the orbit. However, in the limit of high eccentricity, the angular momentum is almost zero, and both the perihelion of the orbit as well as the energy can be approximated to depend only on the Jacobi constant. Therefore, for the case of high eccentricity and large semi-major axis, which are the limits examined by the two different maps, the kicks depend only on the orientation between the perihelion and the planet, and the change in angle between the perihelion and the planet only depends on a via the period

of the particle's orbit.

I have attempted to generalize these sorts of eccentric maps to a fully three-dimensional three-body problem, in the case where the particle is fully interior to the planet's orbit. In this case, I "kick" the energy and angular momentum at aphelion $r_a \approx 2a$. This approach has not yet been successful for several reasons: (i) Real orbits can have small eccentricities, which are very difficult for these eccentric maps to describe well. (ii) To construct my distribution functions, it is vital to understand how the osculating orbital plane intersects the reference frame. Particles with low eccentricity can boost the distribution function since their orbits are not very radial and $f(v) \propto v_r^{-1}$. Therefore, eccentric maps fail where they are most needed. (iii) Kicks are not described very well as being applied only at aphelion, because the perihelia may not be far away from the planet, either. Also, $r_a \neq 2a$, which is a problem if torques are applied at an aphelion of $r_a = 2a$.

I have not experimented with maps for Jupiter-crossing orbits, but I suspect there will be similar problems, although Malyshkin & Tremaine (1999) say that their map "provide[s] a fair representation of the behavior of orbits with short periods." Aside from symplectic maps, another approach to speeding understanding the statistical properties of small bodies (comets, asteroids, WIMPs) in the solar system is the Öpik approach (Öpik, 1951). In this model, encounters of small bodies with planets are modeled as two-body encounters within the Hill sphere (of radius r_H, defined as the point where the gravitational potential of the Sun $\Phi_\odot(r_H) = \Phi_P(r_H)$ is equal to the potential of planet P, Φ_P). Typically, codes that apply this type of encounter assume that encounters with planets are uncorrelated (see the introduction of Dones et al., 1999). However, Dones et al. (1999) show that these methods do not describe the orbits of long-period comets or meteorite orbits well at all because they cannot, by design, describe secular, Kozai, or mean motion resonances. These resonances are largely responsible for the behavior of the bodies of interest to Dones et al.. I have shown in Chapter 5 that much of the WIMP distribution function is governed by Kozai and mean motion resonances. Therefore, unless I can find a symplectic map that applies for arbitrary eccentricity, it will continue to be necessary to do numerical integration of

quasi-Kozai and Jupiter-crossing orbits.

6.2.2 The Full Solar System Simulation

The simulations of WIMPs in my model solar system consisting only of the Sun and Jupiter have some limitations compared with simulations with a full complement of planets. First, WIMPs have access to a much smaller region of phase space in the restricted solar system. For example, recall from the discussion in Chapter 5 that the minimum accessible geocentric speed is $v \approx 8.8$ km s^{-1} in a solar system containing only Jupiter. Particles that are initially scattered in the Sun onto orbits of $a < a_J/2$ may only have a very small z-component of angular momentum since there is no mechanism through which the angular momentum may be significantly altered to reach smaller geocentric speeds. From Figures 5.1 and 5.3, one sees that the particles in either the weak scattering or gravitational capture simulation only inhabit a small portion of the full velocity space at the Earth. Secondly, all timescales in the model solar system are either related to Jupiter or the optical depth of the Sun. There are many more planets in our solar system that may affect the low-speed end of the velocity distribution function and change the timescales for rescattering or ejection.

In the discussion below, I specify which results from my simulations I expect to hold even with a more realistic solar system, and which results I think may change. I will split the discussion into four parts, corresponding to each type of orbit that contributes to the weak scattering bound distribution function (see Figure 5.5): rescattering hump, quasi-Kozai cycle, Kozai cycle, and Jupiter-crossing orbits. The discussion of Jupiter-crossing orbits will also be relevant for the gravitational capture simulation. In each part of the discussion, I will address the following questions: (i) Does the presence of the other planets extend lifetimes in the solar system? (ii) Do the orbits differ significantly from those in the toy model solar system?

The Rescattering Hump

The distribution function of particles captured to the solar sytem by weak scattering in the Sun could be greatly increased if the planets were to either (i) pull a larger percentage of particles out of the rescattering hump and onto orbits that only occasionally enter the Sun or (ii) extend the lifetimes of particles that already did exit the Sun in the toy model solar system simulations. The particles in the rescattering hump in Figure 5.5 largely cannot exit the Sun under the influence of Jupiter alone, although a small minority of the particles would have exited the Sun had they not been prematurely rescattered. The vast majority of the rescattering hump particles never cross Jupiter's orbit. These types of orbits suggest two ways that the full solar system might alter the rescattering hump particles: (i) The presence of the other planets can alter the structure of Kozai cycles, thus perhaps changing the number of particles that are on Kozai cycles for which the minimum value of the eccentricity places perihelia outside the Sun for some time. (ii) Through chaotic interactions with the inner planets, the angular momenta can increase to the point that the perihelia emerge from the Sun.

Both the inner and outer planets can affect the structure of Kozai cycles. Let me discuss the outer planets first. I argue that torques from the outer planets are unlikely to change the number of particles whose perihelia exit the Sun. As demonstrated in Eq. (5.15), the torque on a particle by a faraway planet goes as $K \propto M_P a^2 a_P^{-3}$, where M_P and a_P are the mass and semi-major axis of the planet, and a is the semi-major axis of the particle. A planet will provide a torque

$$K_P = \frac{M_P}{M_J} \left(\frac{a_J}{a_P} \right)^3 K_J \tag{6.1}$$

relative to the torque from Jupiter. Even Saturn, the next largest planet in the solar system, and the second nearest gas giant to the Earth, will only produce a torque about 5% that from Jupiter. Jupiter dominates the tidal field for particles that do not cross the orbits of the outer planets, and so it dominates the structure of the Kozai cycles.

Among the inner planets, Michel & Thomas (1996) find that the Earth and Venus can

dominate the structure of the Kozai cycles if the semi-major axis of the particle is near the semi-major axis of either planet, the initial eccentricity of the particle orbits is small, and the maximum inclination of the orbit is low. However, given that Michel & Thomas's interest was in near-Earth asteroids, they did not investigate the structure of highly eccentric orbits, the type relevant to this thesis. One can gain some insight as to how important the inner planets will be for highly eccentric particle orbits from work on the structure of Kozai cycles in the outer solar system. Thomas & Morbidelli (1996) find that the presence of all gas giants greatly changes the structure of Kozai cycles of outer planet-crossing comets, but *only* for comets that initially had large J_z. For comets will small J_z, the Kozai structure in the 4-planet model was virtually identical to that of a 1-planet model consisting only of Jupiter. Therefore, I do not expect the structure of Kozai cycles in the full system for non-Jupiter-crossing particles to be much different from the toy model solar system. The extra planets will not increase the number of particles on Kozai cycles in the inner solar system.

Therefore, I will focus on examining the diffusion effects of the inner planets. If particle-planet interactions can be modeled as two-body encounters, each time a particle of heliocentric speed v crosses a planet's orbit, the particle's planet-centric speed u changes by

$$\delta u \sim \frac{GM_P}{bu}, \tag{6.2}$$

where b is the impact parameter. Particles in the rescattering hump are generally on extremely eccentric orbits, so that to good approximation, $u = \sqrt{v^2 + v_P^2}$, where $v_P^2 = GM_\odot/a_P$. For the moment, I assume that changes to the particle's energy over many such encounters is far slower than the time it takes a particle's perihelion to diffuse out of the Sun. I will come back to problem of changes to the particle's energy in the discussion of quasi-Kozai cycle orbits. With these assumptions, the change in planet-centric speed can be related to the change in heliocentric speed by

$$\delta v \sim \frac{u\delta u}{v} \tag{6.3}$$

$$= \frac{GM_P}{bv}. \tag{6.4}$$

The change in angular momentum per encounter is thus

$$\delta J \sim a_P \delta v. \tag{6.5}$$

I use the approximation that the angular momentum undergoes a random walk to estimate the timescale on which a particle's angular momentum changes of order $\Delta J_{out} \sim \sqrt{GM_\odot R_\odot}$ in order for the orbital perihelion to lie outside the Sun. The rms change in angular momentum will go as

$$\langle (\Delta J)^2 \rangle \sim N (\delta J)^2, \tag{6.6}$$

where the particle encounters planet P with an impact parameter b or less a total of N times in a time span t. In general,

$$N \sim \frac{t}{(a_P/b)^2 P_\chi}, \tag{6.7}$$

where P_χ is the orbital period of the WIMP. The factor $(b/a_P)^2$ can be thought of as the probability per WIMP period that the WIMP comes within a distance b of the planet. Thus, with some rearranging, I find

$$\frac{\langle (\Delta J)^2 \rangle}{(\Delta J_{out})^2} \sim \left(\frac{M_P}{M_\odot}\right)^2 \left(\frac{a_P}{R_\odot}\right) \left(\frac{a}{a_\oplus}\right)^{-3/2} \left(2 - \frac{a_P}{a}\right)^{-1} \left(\frac{t}{\mathrm{yr}}\right). \tag{6.8}$$

There is a coefficient of order unity involved in this equation to represent the integral over all impact parameters. Using this formula, one can see that the timescale for

$$\langle (\Delta J)^2 \rangle / (\Delta J_{out})^2 \sim 1 \tag{6.9}$$

is of order $t \sim 10^9$ yr *unless* $a \approx 0.5 a_\oplus$. In the latter case, the approximation that $u = \sqrt{v^2 + v_P^2}$ is no longer so good, since even eccentric particles have $\mathbf{r} \cdot \mathbf{v} = 0$ at aphelion. More careful treatments show that orbits with $a \approx 0.5 a_\oplus$ will have larger rms variation in angular momentum than orbits with larger a.

It is useful to compare the timescale for $\langle (\Delta J)^2 \rangle = (\Delta J_{out})^2$ to the timescale on which WIMPs rescatter in the Sun. For particles in the simulations with $\sigma_p^{SI} = 10^{-43}$ cm^2, the rescattering timescale was $t \sim 10^5$ yr. The timescale for angular momentum diffusion is far

greater than this, so it is unlikely that angular momentum diffusion due to the inner planets will increase the number of long-lifetime WIMPs unless the WIMP-nucleon cross section is several orders of magnitude smaller. Therefore, neither changes to the Kozai structure nor the diffusion of angular momentum are likely to increase the number of particles which will at some point have their orbital perihelia outside the Sun. Given that the simplest way to boost the distribution function of bound particles is to increase the number of particles for which the perihelion may leave the Sun, it is unlikely that the total bound distribution function due to particles scattering weakly in the Sun will be much larger than predicted by the toy model solar system simulations.

Quasi-Kozai Cycles

There are several ways that the presence of more planets can affect particles on quasi-Kozai orbits. First, with the additional planets there will be more mean motion and secular resonances which can interact with the Kozai cycles. However, these extra resonances are unlikely to change the rescattering timescales since the lifetime distribution of these particles is already governed by a mix of Kozai and mean motion resonances. In addition, particles on quasi-Kozai cycles may have close interactions with the inner planets. Such interactions have the potential to change the lifetime, energy, and angular momentum distribution of this population of particles. To estimate how much the presence of the inner planets affects the quasi-Kozai orbits, I examine the rms change to the semi-major axes as a function of time in the random walk approximation. Particles on quasi-Kozai cycles cannot be perfectly described by the random walk approximation due to the presence of resonances in the problem. However, the orbits do show chaos, so the random walk approximation is probably not completely invalid.

The rms change in a WIMP's semi-major axis $\langle(\Delta a)^2\rangle$ can be described by

$$\langle(\Delta a)^2\rangle \sim N(\delta a)^2, \tag{6.10}$$

where as in Eq. (6.6), δa is the change in semi-major axis per encounter and N is the total number of interactions a particle has with a planet P with impact parameter b. Since

$$\delta a = \frac{a^2}{GM_\odot} v \delta v, \tag{6.11}$$

I can use the expression for δv in Eq. (6.4) to find

$$\delta a = \left(\frac{M_P}{M_\odot}\right) \frac{a^2}{b}. \tag{6.12}$$

Using the expression for N in Eq. (6.7), I find that

$$\frac{\langle (\Delta a)^2 \rangle}{a^2} \sim \left(\frac{M_P}{M_\odot}\right)^2 \left(\frac{a}{a_P}\right)^2 \left(\frac{a}{a_\oplus}\right)^{-3/2} \left(\frac{t}{\mathrm{yr}}\right). \tag{6.13}$$

The inner planets which will perturb the orbits the most are Venus and the Earth. However, even for these planets, the timescale for $\langle (\Delta a)^2 \rangle^{1/2}/a \sim 1$ is $10^{10} - 10^{11}$ yr, far longer than the age of the solar system. This suggests that the inner planets will not be very effective in smearing out the semi-major axis distribution.

One can use the argument starting with Eq. (6.2) to argue that the inner planets will also not be very effective in smearing out the distribution of J_z. Unless $a \approx a_\oplus/2$, the total change in J_z will only be a few times $\sqrt{GM_\odot R_\odot}$ before the particles are rescattered in the Sun. This fact, combined with the analysis of the rms changes in the semi-major axis, suggests that the lifetime and distribution function of quasi-Kozai particles in the full solar system will be similar to that in the toy model solar system.

Kozai Cycles

The big question to ask in the context of the full solar system is, how robust are the Kozai cycles to collisions with the inner planets? The analysis in the previous section on quasi-Kozai cycles suggests that, in general, the effects of the inner planets are small. However, there are two issues that are very different for pure Kozai cycles than quasi-Kozai cycles. First, changes in the orbital elements cannot be modeled in the random walk approximation, since the particle orbits will always intersect the orbits of the inner planets in the same way if there are no close encounters. Secondly, even small changes to the Kozai cycles can have a

major impact on the distribution function, since the distribution function of particles bound to the solar system by weak interactions in the Sun is dominated by these pure Kozai cycles, which typically have the longest lifetimes of any population of particles in the toy model solar system. Therefore, it will be important to simulate, in the full solar system, orbits that would have been pure Kozai cycles in the toy solar system.

Jupiter-Crossing Particles

Before discussing the effects of other planets on Jupiter-crossing particles, I will summarize the main points of the Jupiter-crossing distribution function. In both the weak scattering and gravitational capture simulations, the distribution functions were for the most part set by $t \sim 10^7$ yr, with some additional growth from long-lived particles in both simulations. For the weak scattering simulation, most of the growth at later times resulted from a small percentage of Jupiter-crossing particles having interactions with mean motion resonances. The distribution of particles captured by gravitational interactions with Jupiter is similar to the conservative scenario of Gould & Alam (2001) for small ($v < 30$ km s^{-1}) geocentric speeds, and between the unbound distribution function and the conservative scenario for higher speeds, even though some of the Jupiter-crossing particles experience periods of Kozai behavior.

If the other planets can boost the number of particles captured gravitationally in the solar system or if even a small percentage ($\lesssim 1\%$) of the Jupiter-crossing particles could have their lifetimes extended, $t_{life} \gg 10^7$ yr, the distribution function of Jupiter-crossing particles could rise dramatically. To determine how many WIMPs each planet will capture from the halo, consider the following argument. In order for a halo particle of energy E to be captured, the energy change resulting from the encounter must be of order

$$\delta E \sim E. \tag{6.14}$$

From Eq. (6.4), one has an approximate expression for the change in heliocentric speed δv, such that

$$\delta E = v\delta v \sim \frac{GM_P}{b}. \tag{6.15}$$

Since the particle energy $E \sim v^2$, one finds that the maximum possible impact parameter for which a particle may be captured in the solar system by a planet P is

$$b \sim \frac{GM_P}{v}. \tag{6.16}$$

Since the gravitational cross section goes as $\propto b^2$, we find that the cross section for a particle to be bound to the solar system by an encounter with planet P is

$$\sigma_{bound} \propto M_P^2. \tag{6.17}$$

Since Jupiter is the largest planet in the solar system by a factor of ~ 3, it will capture at least ~ 10 times more that any other planet. Therefore, I expect that capture directly from the halo by the other planets will produce only a small increase in the bound distribution function.

To estimate the impact of the other planets on the lifetimes and distribution of Jupiter-crossing, I will sketch Gould (1992)'s random walk approximation to the problem. In the absence of resonances, the effects of the other planets in the solar system can be approximated in the random walk regime. Later, I will address the fact that there are numerous mean motion, secular, and Kozai resonances in the full solar system. Recall from the discussion either in Sections 1.4.2 and 2.3 that during two-body encounters of a particle with a planet, the center-of-mass speed u of the particle does not change but its direction θ relative to the planet's direction of motion will change. Gould (1988, 1992) finds that the random walk rms change in the direction of motion is

$$\langle(\Delta\theta)^2\rangle \sim 6 \ln\Lambda \left(\frac{M_P}{M_\odot}\right)^2 \left(\frac{v_P}{u}\right)^5 \gamma^{-1} \left(\frac{t}{\mathrm{yr}}\right), \tag{6.18}$$

where $\ln\Lambda \sim 10$ is the Coulomb logarithm, v_P is the circular speed of a planet about the Sun, and $\gamma \sim 1$ except for orbits near the escape velocity, for which γ diverges (see Gould,

1988, for a more precise definition). There are several things to note in this equation. First, the timescales for $\langle(\Delta\theta)^2\rangle \sim 1$ depend sensitively on the mass of the planet doing the perturbing. Secondly, if the planet-centric speed of a particle is small, it diffuses very rapidly in θ. This means that the particles will diffuse rapidly in both energy and angular momentum,

$$E = \frac{1}{2}|\mathbf{u}+\mathbf{v}_P|^2 - \frac{GM_\odot}{a_P} \tag{6.19}$$

$$J = a_P u\left[\left(\cos\theta + \frac{v_P}{u}\right)^2 + \sin^2\theta\cos^2\phi\right]. \tag{6.20}$$

In a toy model solar system containing just Jupiter, in the absence of resonances, particles diffuse in the solar system on timescales of

$$t \sim 10^{-2}\gamma\left(\frac{M_\odot}{M_J}\right)^2\left(\frac{u}{v_J}\right)^5 \text{ yr}, \tag{6.21}$$

which is of order $\sim$ kyr$-$Myr unless an orbit is near the escape velocity. In both the weak scattering and gravitational capture simulation, I did see such fast spreading of the WIMPs in phase space, in spite of resonances. However, in a solar system with just Jupiter, the geocentric speeds of Jupiter-crossing particles are restricted 8.8 km s$^{-1} < u$. In order to diffuse particles onto smaller geocentric velocity, another mechanism is required. Gould (1992) found that diffusion timescales for the Earth and Venus are shorter than or of order the age of the solar system for small planet-centric speeds. The Earth cannot, of course, change the geocentric speeds of the particles. However, it can change their directions provided that $u \lesssim 27$ km s^{-1} (the speed at which the diffusion timescale is $\sim t_{SS}$. Venus *can* change the geocentric speeds of particles that have small Venus-centric speeds, and in particular can populate orbits with geocentric speed $u < 8.8$ km s^{-1}, which the Earth can then diffuse in the $\theta-$direction. Gould (1992) estimated that the density of bound particles with geocentric speeds $u < 27$ km s^{-1} should be approximately the same as the free space density, but that the density would be lower at higher speeds since the Earth cannot diffuse particles efficiently for $u > 27$ km s^{-1}. Therefore, the gravitational interactions between the inner planets and the WIMPs might increase the lifetimes of some of the originally Jupiter-crossing particles.

There are two major caveats to this sort of argument. First, particles may be rescattered in the Sun, which would decrease the lifetimes of the diffused particles. This point was crudely addressed by Lundberg & Edsjö (2004), who excluded particles from the distribution function after the first passage through the Sun (see Section 1.4.2), finding that the distribution function is barely larger than the bound distribution function I found in Section 5.1.2. If they neglected scattering in the Sun, they found that the distribution function was a factor several greater that what I found in Section 5.1.2, and that it was approximately described by the free space distribution function. The Sun has an optical depth $\tau \ll 1$ for any spin-dependent or spin-independent cross section consistent with current exclusion limits, so the distribution function may still be a factor of a few larger than that in Section 5.1.2, although the exact size of the distribution function will depend on the optical depth in the Sun and the type of elastic scattering that dominates in the Sun.

The second major caveat is that there will be numerous possible mean motion, secular, and Kozai resonances in the full solar system. The size of the distribution function depends crucially on whether the presence of the extra resonances decreases particle lifetimes (for example, by driving particles into the Sun via Kozai or quasi-Kozai cycles), or if WIMPs can be captured for long times in any one of the resonances. For example, in the examination of six near-Earth asteroid orbits, Michel & Thomas (1996) found that asteroids simultaneously in mean motion resonances with either the Earth or Venus, and a Jupiter-dominated Kozai cycle, were protected from close encounters with the Earth on timescales $\sim 10^5 - 10^6$ years. It is conceivable that there exists a long lifetime tail to this protection mechanism. The distribution function will be very sensitive to the fraction of particles originally captured onto Jupiter-crossing orbits (either by weak interactions or gravitational capture) that survive $t_{life} \gtrsim 10^9$ yr. It is hard from the outset to tell how much the various resonances will affect the distribution function.

Discussion

There are several key points to the discussion above:

- It is unlikely that the presence of the other planets in the solar system will either cause more particles to be pulled out of the Sun by weak scattering or out of the Galactic halo by gravitational interactions than in the toy solar system. This means that the only way to increase the bound distribution function is to extend the lifetimes of those particles that are already captured onto relatively long-lived orbits, or to smear those orbits into parts of velocity space not allowed in the toy model solar system.

- For capture by weak scattering in the Sun, it is most important to focus on the Kozai cycling and Jupiter-crossing populations. If the inner planets can move particles off of pure Kozai orbits on timescales shorter than the age of the solar system, the bound distribution function may be significantly altered, although it is not clear how the lifetime distribution would be affected. The lifetime distribution could be skewed high if the planets act to pull the orbits out of the Sun even more than Kozai cycles do, but it could be skewed low if the planets push the perihelia deep into the Sun. For the Jupiter-crossing particles, it will be crucial to determine how fast the inner planets can diffuse orbits, and how much the diffusion will be disrupted or altered by the presence of the many resonances that exist in a realistic solar system. This latter point is also crucial for the case in which particles are captured directly from the halo by gravitational interactions with the planets.

- Given the points above, it is unlikely that the bound distribution function in the full solar system will be more than a factor of a few above the bound distribution function in the toy solar system. Therefore, the main result from my thesis that I expect will hold in the true solar system is that the bound distribution function will not completely overwhelm the halo distribution function, as predicted by Damour & Krauss. It would be interesting to know how much the inner planets can pump particles into portions of velocity space forbidden in the toy model solar system, especially for low geocentric speeds. It would also be interesting to explore how this would depend on the optical depth in the Sun.

What are the implications for either direct or indirect detection? The prospects are grim in the case of WIMP annihilation in the Earth. Even if the low speed distribution function is similar to the free space distribution function (which has a factor of several more bound particles than in the toy model solar system), it is unlikely that IceCube will be able to resolve a signal for $m_\chi \gtrsim 100$ GeV (see Figure 5.31), even if the spin-independent cross section is just below the XENON10 limit, the halo number density of WIMPs is a factor of two or three greater than the fiducial value, or if a significant number of events are generated in the detector volume. As indicated by Figure 2.1, limits on the spin-independent cross section are expected to get dramatically better in the next decade. If these experiments do not find a signal, it is unlikely that *any* reasonable neutrino telescope will ever see annihilation products from the Earth, even if the distribution function is boosted by large long lifetime tails resulting from resonances in the solar system.

The prospects for direct detection are brighter. If the number density of bound particles increases by a factor of several over what is found in this thesis, then bound particles may become an interesting signal (or an important systematic!) in direct detection experiments. Because of this prospect, it is worthwhile to examine the orbits in a full solar system, although it will require careful selection of initial conditions of particle orbits and a large amount of CPU time in order to have a good statistical sample of the various effects in the solar system. The integration methods of Chapter 3 should be extendable to a full solar system. In fact, given that the IAU has decided that there are eight planets about our Sun, the integration in a full solar system should only take about twice as long as the case of a one-planet system since the code is completely vectorized, all else being equal. Integration of particles in the full solar system is doable and should be done (by me).

6.2.3 Other Applications of the Integration Code

There are other types of problems that may be addressed using the numerical methods developed in this thesis. These methods are applicable in problems for which the gravitational field is dominated by a few objects on regular orbits or an external gravitational field, and

for which the "test particles" have negligible self-interaction.

Oort Cloud

The existence of the Oort cloud (Oort, 1950), a cloud of $\sim$ km-sized objects with distances $r \sim 10^3 - 10^5$ AU from the Sun, is inferred from the distribution of long-period comets (with periods greater than 200 yr). The Oort cloud is thought to have originated from debris left over from planet formation ($r \sim 4 - 40$ AU), and to have reached its current configuration by the combined effects of the outer planets (interactions with which pump up the semi-major axes) and passing stars, molecular clouds, and the Galactic tide (which primarily alter the distribution of perihelion distances; see, e.g., Heisler & Tremaine, 1986; Duncan et al., 1987; Dones et al., 2004). Long-period comets are thought to originate in the "outer" Oort cloud ($a \gtrsim 20,000$ AU), a spherical shell of comets, while a posited "inner" Oort cloud is significantly flattened in the plane of the solar system. Comets from the inner Oort cloud are not observed to pass near the Earth because the Earth sits in the empty loss cone of the inner Oort cloud (Dones et al., 2004; Tremaine, 2005).

There are a number of interesting and unsolved problems concerning the formation and evolution of the Oort cloud that may be addressed using the codes in this thesis. Here, I will highlight two particular problem. Recently, two comets have been observed with estimated perihelia outside of Neptune's orbit, and with semi-major axes that place these objects in the innermost part of the Oort cloud (Gladman et al., 2001; Brown et al., 2004). However, the origin of these objects is not well understood (Morbidelli & Levison, 2004). Using my code, I can integrate the orbits of these objects backwards in time, including the effects of the planets, other stars, Galactic tides, and molecular clouds, to constrain theories for the origin of such objects. Secondly, it has been shown that the passage of molecular clouds near the solar system reduces the lifetimes of comets in the outer Oort cloud. It is not clear if mass loss in the outer Oort cloud is consistent with the current observed rate of long-period comet passages through the inner solar system, or if some mechanism is required to continuously refill the outer Oort cloud. With my code, I can simulate billions of

comet orbits under the influence of various types of perturbers and constrain theories on the outer Oort cloud. Both problems are well-suited to my code: the Oort cloud comets have negligible self-interaction, and it is straight-forward to include the perturbing potentials in the code.

Nuclear Star Clusters

Some of the methods developed in this thesis may, with some modification, be used to study secular instability in nuclear star clusters about supermassive black holes (SMBH). Nuclear star clusters are ubiquitous (estimated to be in $\approx 50-75\%$ of local galaxies), small (with masses $M_{nuc} \approx 0.003 M_{bulge}$, where M_{bulge} is the mass of the galaxy bulge; and sizes of order $\sim$ pc -10 pc) clouds of stars surrounding galactic centers (see Merritt, 2008, and references therein). In the Milky Way, the nuclear star cluster is estimated to have a mass $M_{nuc} \approx 1.5 \times 10^6 M_\odot$. Most galaxies have central SMBH (Magorrian et al., 1998), large enough such that they dominate the gravitational potential of much of the surrounding nuclear star cluster. Therefore, the evolution of the nuclear star clusters will be dominated by the SMBH. In particular, the presence of the supermassive black hole greatly increases the relaxation time t_r of cluster, and prevents core collapse on timescales greater than the age of the universe.

Most work on nuclear star clusters has focused on two regimes: collisionless, where $t_r > 10^{10}$ yr; and collisional, where $t_r < 10^{10}$ yr. In the collisionless regime, two-body relaxation in the cluster has not had time to significantly modify the density of stars near the SMBH. Therefore, the distribution of stars near the SMBH may retain some hints evolution of the central regions of galaxies (Merritt, 2006). For example, binary black hole mergers tend to force the density of stars near the final SMBH to be core-like instead of cusp-like. However, these collisionless systems, while they appear to be dominant in the local universe (Merritt, 2006), are difficult to resolve due to the very small ($\sim 1-10$ pc) radii of the nuclear star clusters. In the Local Group, nuclear star clusters (including in the Milky Way) appear to be in the collisional regime. In this case, two-body relaxation should

be effective in forcing the nuclear star cluster to a steady state. The distribution function of stars within the sphere of influence of the black hole goes as $f(E) \propto |E|^{1/4}$ (resulting in a stellar number density $n(r) \propto r^{-7/4}$) except for small angular momenta (Bahcall & Wolf, 1976; Lightman & Shapiro, 1977; Cohn & Kulsrud, 1978). Recent N-body simulations have confirmed this result, which was originally based on solutions to the Fokker-Planck equation (Baumgardt et al., 2004; Preto et al., 2004). If the perihelion of a star's orbit lies within the radius r_t at which stars become tidally disrupted by a SMBH of mass M_{SMBH}, the star is lost. Therefore, a particle with angular momentum $J^2 < 2Er_t^2 + GM_{SMBH}r_t$, is lost within one orbital period. However, two-body relaxation can only refill orbits of such angular momenta on timescales of order the relaxation time unless the energy of the stellar orbit is high enough that a star can be perturbed onto a low angular momentum orbit in one crossing of the nuclear star cluster. Therefore, at low energies and low angular momenta, there exists a "loss cone" where the distribution function vanishes.

This last point is important for the following reason. Tremaine (2005) has demonstrated that the self-gravitation of nuclear star clusters can induce secular precession of orbits on timescales $t_{sec} \sim t_{dyn}M_{SMBH}/(Nm^2)$, where t_{dyn} is the dynamical time of the system, N is the total number of stars in the cluster, and m is the mass per star. In general, $t_{sec} \ll t_r$. Moreover, Tremaine showed that flattened systems with empty loss cones are unstable to secular modes, while secular modes are only neutrally stable in spherical systems. Therefore, secular perturbations may be more important in shaping the evolution of nuclear star clusters than two-body relaxation. It would be good to gauge the effect of secular perturbations using N-body simulations. However, current direct N-body technology cannot resolve the loss cone. Moreover, current direct N-body codes must treat close encounters of stars with the SMBH separately from the rest of the integration. In addition, current schemes to handle close encounters are not expected to work if the ratio $M_{SMBH}/m \gtrsim 10^6$.

My code may speed up N-body codes in the following ways. First, close encounters of stars with the SMBH can be treated with a map, as in Section 3.1.3, assuming that tidal forces from the other stars in the cluster are unimportant for small separations between

a star and the SMBH. General relativistic effects can easily be incorporated in the map. Finally, it may be useful to use the adaptive time step sympectic integrator (although perhaps to higher order than the Verlet scheme discussed in Section 3.1.1) instead of current symplectic mappings. This may be especially useful for resolving the loss cone, since particles in or near the loss cone may be on highly eccentric orbits. The main difference between integrations in this system and integrations of WIMPs in the solar system is that it will be necessary to include the two-body interactions of stars in order to model the stellar cluster self-consistently.

Appendix A

The 1-d Velocity Dispersion of Galactic WIMPs in the Solar Neighborhood

Let us consider the form of the distribution function of the Milky Way's dark matter halo. If one assumes that the phase-space distribution of the dark matter halo is isotropic in velocity space, it can be shown by the Jeans theorem that the distribution function should only depend on energy E (Binney & Tremaine, 1987), and that *any* non-negative function of E is a valid distribution function for the system. If it is assumed in addition that the dark matter distribution is spherically symmetric, then by either specifying both the number density and the gravitational potential as a function of radius, or by specifying the number density as a function of the potential, one can find a unique distribution function $f(E)$ to describe the halo. One can use either the potential and density information (via the Jeans equation) or the distribution function (by taking velocity moments of the distribution) to specify the dark matter velocity dispersion σ, the RMS velocity component along a given direction.

In our Galaxy, the circular velocity curve is constant from a radius much smaller than the orbital radius of the Sun to at least $r \sim 60$ kpc (Xue et al., 2008). Zaritsky et al. (1993)

show that the velocity curves of spiral galaxies similar to the Milky Way are flat out to $r \sim 200$ kpc. Since

$$v_c^2(r) = r\frac{\mathrm{d}\Phi}{\mathrm{d}r} \tag{A.1}$$

for a spherically symmetric system, the potential of the Galaxy has the form

$$\Phi(r) = v_c^2 \log(r) + \Phi_0, \tag{A.2}$$

where Φ_0 is a constant. I have ignored the fact that the Galactic disk is, as the name would imply, not spherically symmetric. However, the spherical approximation is good enough for this argument. If the dark matter is distributed as a power law,

$$n(r) = \frac{\rho_{\mathrm{WIMP}}}{m_{\mathrm{WIMP}}} \propto r^{-\beta}, \tag{A.3}$$

where ρ_{WIMP} is the WIMP mass density, then one can show (e.g., by solving Eq. 4-140 in Binney & Tremaine, 1987) that for the potential (A.2), the distribution function of the halo is Maxwellian,

$$f(E) = \frac{n_0}{(2\pi\sigma^2)^{3/2}} e^{-E/\sigma^2} \tag{A.4}$$

$$= \frac{n_0}{(2\pi\sigma^2)^{3/2}} e^{-\left[\frac{1}{2}v^2+\Phi(r)\right]/\sigma^2}, \tag{A.5}$$

which is of the same form as the dark matter distribution function given in Eq. (2.1). Here, n_0 is a constant and v is the Galactocentric particle speed. The velocity dispersion σ is constant for this gravitational potential–density pair. The local dark matter density can be recovered by integrating Eq. (A.4) over velocity,

$$n(r) = n_0 e^{-\Phi(r)/\sigma^2}. \tag{A.6}$$

One can then relate the velocity dispersion to the power law index of the density by setting Eqs. (A.3) and (A.6) equal to each other, finding

$$r^{-\beta} \propto e^{-\Phi(r)/\sigma^2} \tag{A.7}$$

$$\propto e^{-(v_c^2/\sigma^2)\log(r)} \tag{A.8}$$

$$= r^{-v_c^2/\sigma^2}. \tag{A.9}$$

Therefore,

$$\sigma = \frac{v_c}{\sqrt{\beta}}. \tag{A.10}$$

This relation holds specifically for logarithmic gravitational potentials (which appears reasonable for our Galaxy) and power law densities. Cosmological dark matter simulations (Navarro et al., 1997, usually abbreviated as NFW; Moore et al., 1998) suggest that the dark matter halo ought to have a double-power law number density,

$$n(r) = \frac{n_s}{(r/r_s)^\alpha \left[1 + (r/r_s)^\gamma\right]^{(3-\alpha)/\gamma}}, \tag{A.11}$$

with α in the range $\alpha = 1$ (NFW; $\gamma = 1$) to $\alpha = 1.5$ (Moore; $\gamma = 1.5$). The quantities n_s and r_s are the scale number density and scale radius, respectively. Adiabatic contraction of the halo during baryonic infall, an effect that is not included in the NFW or Moore simulations, may increase the inner slope to $\alpha \approx 2$ (Gnedin et al., 2004). All simulations demonstrate that $n(r) \propto r^{-3}$ at large r.

Technically, to find the velocity distribution as a function of radius in these models, one should solve Binney & Tremaine's Eq. (4-140) for $f(E)$ using the density profile (A.11). However, simulations show that the phase space density of v is approximately described by a Maxwell-Boltzmann distribution at the solar circle, so over a limited range of radii, a single power law approximation is reasonable, $n(r) \propto r^{-\beta}$ (Moore et al., 2001; Helmi et al., 2002). In this case, Eq. (A.4) is a local approximation to the distribution function. Therefore, it is acceptable to model the local dark matter distribution as a Gaussian with the velocity dispersion described by Eq. (A.10).

Using this approximation, $\beta = \alpha$ for $r/r_s \ll 1$, $\beta = 3$ for $r/r_s \gg 1$, with intermediate values in between those two extrema. If the Sun is located well within the scale radius in the NFW case, then $\beta = \alpha = 1$, and $\sigma = v_c$. If the distance to the Sun from the center of the halo is much greater than the scale radius, then $\beta = 3$, so $\sigma = v_c/\sqrt{3}$. I compromise by using the intermediate case, $r \sim r_s$, so $\beta \approx 2$ and

$$\sigma = v_c/\sqrt{2}. \tag{A.12}$$

Appendix B

WIMP Elastic Scattering

B.1 Spin-Independent Scattering

For particle physics models of dark matter, the general spin-independent ("SI"; scalar) scattering cross section has the form (Jungman et al., 1996; Hooper & Profumo, 2007):

$$\frac{d\sigma^{SI}}{dQ} = \frac{2m_A}{\pi g_A^2} \left[Z f_p + (A - Z) f_n\right]^2 F_{SI}^2(Q), \tag{B.1}$$

where Q is the energy transferred from the WIMP to a nucleus of mass m_A (with atomic mass A and charge Z) during the scatter, g_A is the relative velocity between the particles, f_p and f_n are the proton and neutron effective couplings to the WIMP, and $F_{SI}(Q)$ is a nuclear form factor. The nuclear form factor used in this set of calculations is of the standard exponential form,

$$F_{SI}(Q) = e^{-Q/2Q_A}, \tag{B.2}$$

where the coherence energy is

$$Q_A = \frac{1.5\hbar^2}{m_A R_A^2}, \tag{B.3}$$

and the coherence length (the radius of the nucleus A) is set to

$$R_A = 1 \text{ fm}[0.3 + 0.91(m_A/(\text{GeV}/c^2))^{1/3}]. \tag{B.4}$$

The nuclear form factor quantifies the extent to which the WIMP interacts coherently with the nucleus as a whole (if the de Broglie wavelength of the nucleus is small), or incoherently with the nucleons individually. A consequence of the incoherence of the nuclear interaction is that the $\propto A^3$ enhancement of the differential cross section is mitigated for large energy transfers.

It is often more convenient to use the center-of-mass differential cross section. Using the functional form of the energy transfer

$$Q = 2\frac{\mu_A^2}{m_A} g_A^2 \left(\frac{1-\cos\theta}{2}\right), \tag{B.5}$$

where

$$\mu_A = \frac{m_A m_{WIMP}}{m_A + m_{WIMP}}, \tag{B.6}$$

the differential cross section is

$$\begin{aligned}
\frac{d\sigma^{SI}}{d\Omega} &= \frac{1}{2\pi}\frac{dQ}{d(\cos\theta)}\frac{d\sigma}{dQ} && \text{(B.7)}\\
&= \frac{1}{2\pi}\frac{\mu_A^2}{m_A} g_A^2 \left(\frac{d\sigma}{dQ}\right) && \text{(B.8)}\\
&= \frac{1}{4\pi}\frac{4}{\pi}\mu_A^2 \left[Z f_p + (A-Z) f_n\right]^2 F^2(Q) && \text{(B.9)}\\
&= \frac{\sigma_A^{SI} F^2(Q(\cos\theta))}{4\pi}. && \text{(B.10)}
\end{aligned}$$

I have parameterized the strength of the interaction by σ_A. If $f_p = f_n$, which is often a good approximation for both supersymmetric and UED models,

$$\sigma_A^{SI} = \frac{4}{\pi}\mu_A^2 A^2 f_n^2, \tag{B.11}$$

so that the strength of the coupling between a nucleus and the WIMP depends only on the atomic number of the nucleus. This coupling can also be parameterized in terms of the strength of the WIMP-proton (or -neutron) cross section:

$$\sigma_A^{SI} = \frac{\mu_A^2}{\mu_p^2} A^2 \sigma_p^{SI}, \tag{B.12}$$

which is useful since experimental constraints on the spin-independent cross section are reported in terms of the WIMP-nucleon cross section. In the limit of high WIMP mass,

$$\mu_A \rightarrow m_A \tag{B.13}$$

$$\mu_p \rightarrow m_p \tag{B.14}$$

$$\sigma_A^{SI} \rightarrow \frac{m_A^2}{m_p^2} A^2 \sigma_p^{SI} \tag{B.15}$$

$$\approx A^4 \sigma_p^{SI}, \tag{B.16}$$

where the last approximation can be made since $m_A \approx A m_p$.

B.2 Spin-Dependent Scattering

The likely WIMP candidates for both the MSSM (χ particle) and UED ($B^{(1)}$) theories can have elastic axial-vector interactions with quarks, via squarks in the MSSM or the lightest Kaluza-Klein excitation of quarks $q^{(1)}$ in UED models. In both cases, the spin-dependent (SD) WIMP interaction with a nucleus of atomic number A can be parameterized as (Jungman et al., 1996; Servant & Tait, 2002)

$$\frac{\mathrm{d}\sigma^{SD}}{\mathrm{d}Q} = \alpha \times \frac{2m_A}{\pi g_A^2} \Lambda^2 J(J+1) F_{SD}^2(|\mathbf{q}|), \tag{B.17}$$

where

$$\alpha = \begin{cases} 8G_F^2 & \text{MSSM} \\ \frac{1}{6} \frac{g'^4}{(m_{B^{(1)}}^2 - m_{q^{(1)}}^2)^2} & \text{UED} \end{cases} \tag{B.18}$$

parameterizes the coupling in each theory. Here, g' is the coupling constant for the B boson in electroweak theory, and $m_{B^{(1)}}$ and $m_{q^{(1)}}$ are the masses of the $B^{(1)}$ and $q^{(1)}$ particles respectively. The other quantities in Eq. (B.17) depend on nuclear properties. Here J is the total angular momentum of the nucleus, and

$$\Lambda = \frac{1}{J} \left[a_p \langle S_p \rangle + a_n \langle S_n \rangle \right], \tag{B.19}$$

where a_n and a_p describe the WIMP couplings to the neutron and proton, and $\langle S_n \rangle$ and $\langle S_p \rangle$ are the spin expectation values for the neutrons and protons within the nucleus. The couplings a_n and a_p are derived from specific WIMP models, while the spin expectation values must be calculated using detailed nuclear physics models (e.g., Dimitrov et al., 1995; Jungman et al., 1996; Ressell et al., 1993; Ressell & Dean, 1997), and calculations using different techniques often yield different results. The function $F_{SD}(|\mathbf{q}|)$ is the spin-dependent nuclear form factor as a function of the momentum transfer $|\mathbf{q}|$. Its form must be carefully calculated for each nucleus of interest (Gondolo, 1996, and references therein).

There are several important differences between the form of the spin-dependent and spin-independent cross sections that have major implications for detection experiment design. The first point is that nuclei with even numbers of protons and neutrons will have *zero* spin-dependent interactions with WIMPs. Secondly, the spin-dependent cross section has a much weaker dependence on the atomic mass than the spin-independent cross section. This is apparent if Eq. (B.17) is written in the same form as Eq. (B.10),

$$\frac{\mathrm{d}\sigma^{SD}}{\mathrm{d}\Omega} = \frac{1}{2\pi}\frac{\mathrm{d}Q}{\mathrm{d}\cos\theta}\frac{\mathrm{d}\sigma^{SD}}{\mathrm{d}Q} \tag{B.20}$$

$$= \frac{1}{2\pi}\frac{\mu_A^2 g_A^2}{m_A}\frac{2m_A}{\pi g_A^2}J(J+1)\alpha\Lambda^2 F_{SD}^2(|\mathbf{q}|) \tag{B.21}$$

$$= \frac{1}{4\pi}\sigma_A^{SD}F^2(|\mathbf{q}|), \tag{B.22}$$

where

$$\sigma_A^{SD} = \frac{4}{\pi}\mu_A^2 J(J+1)\alpha\Lambda^2. \tag{B.23}$$

In the limit that $m_{WIMP} \gg m_A$,

$$\sigma_A^{SD} \propto A^2, \tag{B.24}$$

unlike

$$\sigma_A^{SI} \propto A^4 \tag{B.25}$$

for the spin-independent case. Therefore, even if $\sigma_p^{SD} > \sigma_p^{SI}$ or $\sigma_n^{SD} > \sigma_n^{SI}$, the spin-independent cross section may dominate for heavy nuclei. The spin-dependent cross section

could be large if J scaled with A (since $\sigma_A \propto J^2$), but this is not the case for heavy nuclei. Note that, in contrast to predictions for spin-independent scattering, the spin-dependent WIMP-proton and WIMP-neutron cross sections are generally *not* the same to within a few percent.

References

Achterberg, A. et al. 2006, Astropart. Phys., 26, 129

Ackermann, M. et al. 2006, Astropart. Phys., 24, 459

Aharonian, F. & Neronov, A. 2005, Astrophys. Space Sci., 300, 255

Aharonian, F. et al. 2006, Phys. Rev. Lett., 97, 221102

Ahrens, J. et al. 2002, Phys. Rev. D, 66, 032006

Akerib, D. S. et al. 2006a, Phys. Rev. D, 73, 011102

—. 2006b, Phys. Rev. Lett., 96, 011302

—. 2006c, Nucl. Instr. Meth. A, 559, 411

Albrecht, A. et al. 1982, Phys. Rev. Lett., 48, 1437

Alner, G. J. et al. 2005, Phys. Lett. B, 616, 17

—. 2007, astro-ph/0701858

Ambrosio, M. et al. 1999, Phys. Rev. D, 60, 082002

Amram, P. et al. 1999, Nucl. Phys. B Proc. Suppl., 75, 415

Anderson, D. L. 2005, New Theory of the Earth (Cambridge, UK, Cambridge University Press)

Angle, J. et al. 2007, astro-ph/0706.0039

Angus, G. W. & Zhao, H. 2007, Mon. Not. Roy. Astron. Soc., 375, 1146

Angus, G. W. et al. 2007, Astrophys. J., 654, L13

Appelquist, T. et al. 2001, Phys. Rev. D, 64, 035002

Aprile, E. et al. 2002, astro-ph/0207670

—. 2005, New Astron. Rev., 49, 289

Araújo, H. M. et al. 2006, Astropart. Phys., 26, 140

Arkani-Hamed, N. et al. 1998, Phys. Lett. B, 429, 263

—. 1999, Phys. Rev. D, 59, 086004

—. 2006a, JHEP, 8, 70

—. 2006b, Nucl. Phys. B, 741, 108

Atac, M. et al. 2005, New Astron. Rev., 49, 283

Aynutdinov, V. et al. 2006, Nucl. Instr. Meth. A, 567, 423

Bahcall, J. N. 1984a, Astrophys. J., 287, 926

—. 1984b, Astrophys. J., 276, 156

Bahcall, J. N. & Wolf, R. A. 1976, Astrophys. J., 209, 214

Bahcall, J. N. et al. 2005, Astrophys. J., 621, L85

Baltz, E. A. & Wai, L. 2004, Phys. Rev. D, 70, 023512

Barger, V. et al. 2007a, hep-ph/0708.1325

—. 2007b, astro-ph/0709.3301

Baumgardt, H., Makino, J., & Ebisuzaki, T. 2004, Astrophys. J., 613, 1133

Begeman, K. G. et al. 1991, Mon. Not. Roy. Astron. Soc., 249, 523

Bekenstein, J. D. 2004, astro-ph/0412652

Bekenstein, J. D. & Sanders, R. H. 2006, in EAS Publications Series, ed. G. A. Mamon, F. Combes, C. Deffayet, & B. Fort, Vol. 20, 225–230

Bélanger, G. et al. 2006, Comput. Phys. Commun., 174, 577

Belanger, G. et al. 2006, hep-ph/0607059

Belli, P. et al. 2000, Phys. Rev. D, 61, 023512

Benetti, P. et al. 2007, astro-ph/0701286

Bennett, C. L. et al. 2003, Astrophys. J. Suppl., 148, 97

Berezinsky, V. et al. 2003, Phys. Rev. D, 68, 103003

—. 2006, Phys. Rev. D, 73, 063504

Bergström, L. & Hooper, D. 2006, Phys. Rev. D, 73, 063510

Bergström, L. et al. 1998a, Phys. Rev. D, 58, 103519

—. 1998b, Astropart. Phys., 9, 137

—. 1999, JHEP, 8, 10

Bergström, L. et al. 2001, in Identification of Dark Matter, ed. N. J. C. Spooner & V. Kudryavtsev, 305–+

Bernabei, R. et al. 1996, Phys. Lett. B, 389, 757

—. 2000a, New J. Phys., 2, 15

—. 2000b, Phys. Lett. B, 480, 23

Bertone, G. 2007, New Astron. Rev., 51, 321

Bertone, G. & Merritt, D. 2005, Mod. Phys. Lett. A, 20, 1021

Bertone, G. et al. 2005a, Phys. Rev. D, 72, 103517

—. 2005b, Phys. Rep., 405, 279

—. 2006, astro-ph/0612387

Bett, P. et al. 2007, Mon. Not. Roy. Astron. Soc., 376, 215

Binney, J. & Merrifield, M. 1998, Galactic Astronomy (Princeton, NJ, Princeton University Press)

Binney, J. & Tremaine, S. 1987, Galactic Dynamics (Princeton, NJ, Princeton University Press)

Blennow, M. et al. 2007, hep-ph/0709.3898

Boliev, M. M. et al. 1996, Nucl. Phys. B Proc. Suppl., 48, 83

Bosma, A. 1981, Astron. J., 86, 1825

Bouwens, R. J. et al. 2006, Astrophys. J., 653, 53

Bradač, M. et al. 2007, astro-ph/0711.4850

Brink, P. L. et al. 2005, astro-ph/0503583

Brodwin, M. et al. 2006, Astrophys. J., 651, 791

Bromm, V. & Loeb, A. 2003, Astrophys. J., 596, 34

Brown, M. E., Trujillo, C. A., & Rabinowitz, D. L. 2004, IAU Circ., 8304, 1

Brownstein, J. R. & Moffat, J. W. 2007, astro-ph/0702146

Brunetti, R. et al. 2005, New Astron. Rev., 49, 265

Canepa, A. 2006, hep-ex/0603032

Carena, M. et al. 2007, Phys. Rev. D, 75, 055010

Carr, B. 1994, Ann. Rev. Astron. Astrophys., 32, 531

Chambers, J. E. 1999, Mon. Not. Roy. Astron. Soc., 304, 793

Chiang, E. I. & Jordan, A. B. 2002, Astron. J., 124, 3430

Chung, D. J. H. et al. 2005, Phys. Rep., 407, 1

Cirelli, M. et al. 2005, Nucl. Phys. B, 727, 99

Clowe, D. et al. 2006a, Astrophys. J., 648, L109

—. 2006b, astro-ph/0611496

Cohn, H. & Kulsrud, R. M. 1978, Astrophys. J., 226, 1087

Cole, S. et al. 2001, Mon. Not. Roy. Astron. Soc., 326, 255

Comerford, J. M., Meneghetti, M., Bartelmann, M., & Schirmer, M. 2006, Astrophys. J., 642, 39

Corless, V. L. & King, L. J. 2007, Mon. Not. Roy. Astron. Soc., 380, 149

Damour, T. & Krauss, L. M. 1999, Phys. Rev. D, 59, 063509

Davé, R. et al. 2001, Astrophys. J., 547, 574

de Blok, W. J. G. & Bosma, A. 2002, Astron. Astrophys., 385, 816

de Blok, W. J. G. et al. 2001, Astron. J., 122, 2396

Dehnen, W. & Binney, J. J. 1998, Mon. Not. Roy. Astron. Soc., 298, 387

Desai, S. et al. 2004, Phys. Rev. D, 70, 083523

Desiati, P. et al. 2006, astro-ph/0611603

Diemand, J. et al. 2005, Nature, 433, 389

—. 2006, Astrophys. J., 649, 1

—. 2007, Astrophys. J., 657, 262

Dimitrov, V. I. et al. 1995, Phys. Rev. D, 51, 291

Djouadi, A. et al. 2002, hep-ph/0211331

Dodelson, S. 2003, Modern Cosmology (Amsterdam, Academic Press)

Dones, L. et al. 1999, Icarus, 142, 509

Dones, L. et al. 2004, in Astronomical Society of the Pacific Conference Series, Vol. 323, Star Formation in the Interstellar Medium: In Honor of David Hollenbach, ed. D. Johnstone, F. C. Adams, D. N. C. Lin, D. A. Neufeeld, & E. C. Ostriker, 371–+

Dumm, J., Landsman, H., & the Ice Cube Collaboration. 2007, J. Phys. Conf. Ser., 60, 334

Duncan, M. et al. 1987, Astron. J., 94, 1330

Edsjö, J. & Gondolo, P. 1995, Phys. Lett. B, 357, 595

Ellis, J. et al. 1988, Phys. Lett. B, 212, 375

Encyclopædia Britannica. 1994-1999, The Earth: Its Properties, Composition, and Structure (Britannica CD, Version 99. Encyclopædia Britannica, Inc.)

Engel, J. & Vogel, P. 2000, Phys. Rev. D, 61, 063503

Esposito, J. A. et al. 1999, Astrophys. J. Suppl., 123, 203

Evrard, A. E. et al. 2002, Astrophys. J., 573, 7

Fabrycky, D. & Tremaine, S. 2007, Astrophys. J., 669, 1298

Feix, M. et al. 2007, astro-ph/0707.0790

Finkbeiner, D. P. 2004a, Astrophys. J., 614, 186

—. 2004b, astro-ph/0409027

Forest, É. et al. 1991, Phys. Lett. A, 158, 99

Freese, K., Fields, B., & Graff, D. 2000, Nucl. Phys. B Proc. Suppl., 80, C305+

Freese, K. et al. 1988, Phys. Rev. D, 37, 3388

Frei, Z., Guhathakurta, P., Gunn, J. E., & Tyson, J. A. 1996, Astron. J., 111, 174

Fukugita, M. & Peebles, P. J. E. 2004, Astrophys. J., 616, 643

Fushimi, K. et al. 2006, astro-ph/0611700

Gaitskell, R. 2007, APS Meeting Abstracts, H3002+, slides available at http://xenon.astro.columbia.edu/talks/APS2007/070415_DM_Noble_Gaitskell_v08.pdf

Girard, T. & Giuliani, F. 2007, Phys. Rev. D, 75, 043512

Gladman, B. et al. 2001, Minor Planet Electronic Circulars, 42

Gnedin, O. Y. & Ostriker, J. P. 2001, Astrophys. J., 561, 61

Gnedin, O. Y. et al. 2004, Astrophys. J., 616, 16

Goerdt, T. et al. 2007, Mon. Not. Roy. Astron. Soc., 375, 191

Gondolo, P. 1996, in Dark Matter in Cosmology Quantam Measurements Experimental Gravitation, ed. R. Ansari, Y. Giraud-Heraud, & J. Tran Thanh van, 41–+

Gondolo, P. & Gelmini, G. 2005, Phys. Rev. D, 71, 123520

Gondolo, P. & Silk, J. 1999, Phys. Rev. Lett., 83, 1719

Gondolo, P. et al. 2004, JCAP, 7, 8

Gott, J. R. I. et al. 2005, Astrophys. J., 624, 463

Gould, A. 1987, Astrophys. J., 321, 571

—. 1988, Astrophys. J., 328, 919

—. 1990, Mon. Not. Roy. Astron. Soc., 244, 25

—. 1991, Astrophys. J., 368, 610

—. 1992, Astrophys. J., 388, 338

Gould, A. & Alam, S. M. K. 2001, Astrophys. J., 549, 72

Green, A. M. 2002, Phys. Rev. D, 66, 083003

—. 2003, Phys. Rev. D, 68, 023004

—. 2007, JCAP, 8, 22

Green, A. M. & Goodwin, S. P. 2007, Mon. Not. Roy. Astron. Soc., 1518

Green, A. M. & Morgan, B. 2008, Phys. Rev. D, 77, 027303

Green, A. M. et al. 2004, Mon. Not. Roy. Astron. Soc., 353, L23

—. 2005, JCAP, 8, 3

Gunn, J. E. et al. 1979, Astron. J., 84, 1181

Guth, A. H. 1981, Phys. Rev. D, 23, 347

Habig, A. et al. 2001, in International Cosmic Ray Conference, Vol. 4, 1558–+

Halzen, F. & Hooper, D. 2002, Rep. Prog. Phys., 65, 1025

—. 2006, Phys. Rev. D, 73, 123507

Hartman, R. C. et al. 1999, Astrophys. J. Suppl., 123, 79

Hayashi, E. & Navarro, J. F. 2006, Mon. Not. Roy. Astron. Soc., 373, 1117

Hayashi, E. et al. 2004, Mon. Not. Roy. Astron. Soc., 355, 794

—. 2007, Mon. Not. Roy. Astron. Soc., 377, 50

Heisler, J. & Tremaine, S. 1986, Icarus, 65, 13

Helmi, A. et al. 2002, Phys. Rev. D, 66, 063502

Hill, G. C. et al. 2006, astro-ph/0611773

Hime, A. 2007, APS Meeting Abstracts, 14002

Hinshaw, G. et al. 2007, Astrophys. J. Suppl., 170, 288

Hofmann, S. et al. 2001, Phys. Rev. D, 64, 083507

Holder, J. et al. 2006, astro-ph/0611598

Holmberg, J. & Flynn, C. 2000, Mon. Not. Roy. Astron. Soc., 313, 209

—. 2004, Mon. Not. Roy. Astron. Soc., 352, 440

Hooper, D. & Dingus, B. 2002, astro-ph/0212509

Hooper, D., Finkbeiner, D. P., & Dobler, G. 2007a, astro-ph/0705.3655

Hooper, D. & Kribs, G. D. 2003, Phys. Rev. D, 67, 055003

Hooper, D. & Profumo, S. 2007, hep-ph/0701197

Hooper, D. & Taylor, A. M. 2007, JCAP, 3, 17

Hooper, D. & Wang, L.-T. 2004, Phys. Rev. D, 69, 035001

Hooper, D. & Zaharijas, G. 2007, Phys. Rev. D, 75, 035010

Hooper, D. et al. 2007b, astro-ph/0709.4113

Huchra, J. et al. 1983, Astrophys. J. Suppl., 52, 89

Hut, P. & Tremaine, S. 1985, Astron. J., 90, 1548

Islam, R. R. et al. 2004, Mon. Not. Roy. Astron. Soc., 354, 427

Ito, T. & Tanikawa, K. 2002, Mon. Not. Roy. Astron. Soc., 336, 483

Jing, Y. P. & Suto, Y. 2002, Astrophys. J., 574, 538

Jungman, G. et al. 1996, Phys. Rep., 267, 195

Kamionkowski, M. 2007, astro-ph/0706.2986

Kamionkowski, M. & Koushiappas, S. M. 2008, astro-ph/0801.3269

Kamionkowski, M. et al. 1995, Phys. Rev. Lett., 74, 5174

Karle, A. et al. 2003, Nucl. Phys. B Proc. Suppl., 118, 388

Katz, U. F. 2006, Prog. Part. Nucl. Phys., 57, 273

Keeton, C. R. 2001, Astrophys. J., 561, 46

Kent, S. M. & Gunn, J. E. 1982, Astron. J., 87, 945

Kerr, F. J. & Lynden-Bell, D. 1986, Mon. Not. Roy. Astron. Soc., 221, 1023

Khoury, J. et al. 2001, Phys. Rev. D, 64, 123522

—. 2002a, Phys. Rev. D, 66, 046005

—. 2002b, Phys. Rev. D, 65, 086007

Kiseleva, L. G., Eggleton, P. P., & Mikkola, S. 1998, Mon. Not. Roy. Astron. Soc., 300, 292

Knapp, G. R. et al. 1978, Astron. J., 83, 1585

Kochanek, C. S. et al. 2003, Astrophys. J., 585, 161

Kolb, E. W. & Turner, M. S. 1990, The Early Universe (Reading, MA, Addison-Wesley)

Komatsu, E. et al. 2008, astro-ph/0803.0547

Kozai, Y. 1962, Astron. J., 67, 591

Kraus, C. et al. 2005, Euro. Phys. J. C, 40, 447

Kubo, H. et al. 2004, New Astron. Rev., 48, 323

Kubo, J. M. et al. 2007, Astrophys. J., 671, 1466

Kuhlen, M. et al. 2007, in American Institute of Physics Conference Series, Vol. 921, 135–138

Kuijken, K. 1991, Astrophys. J., 372, 125

Kuijken, K. & Gilmore, G. 1989a, Mon. Not. Roy. Astron. Soc., 239, 605

—. 1989b, Mon. Not. Roy. Astron. Soc., 239, 651

—. 1989c, Mon. Not. Roy. Astron. Soc., 239, 571

—. 1991, Astrophys. J., 367, L9

Kuzio de Naray, R. et al. 2006, Astrophys. J. Suppl., 165, 461

Lee, H. S. et al. 2007, Phys. Rev. Lett., 99, 091301

Lehnert, R. & Weiler, T. J. 2007, hep-ph/0708.1035

Liboff, R. L. 2003, Kinetic Theory : Classical, Quantum, and Relativistic Descriptions (New York, Springer)

Lightman, A. P. & Shapiro, S. L. 1977, Astrophys. J., 211, 244

Limousin, M. et al. 2008, astro.ph/0802.4292

Linde, A. 2007, hep-th/0705.0164

Linde, A. D. 1982, Phys. Lett. B, 116, 335

Loeb, A. & Zaldarriaga, M. 2005, Phys. Rev. D, 71, 103520

Lundberg, J. & Edsjö, J. 2004, Phys. Rev. D, 69, 123505

Mack, K. J. et al. 2006, astro-ph/0608642

Magorrian, J. et al. 1998, Astron. J., 115, 2285

Mahdavi, A. et al. 2007, Astrophys. J., 664, 162

Malyshkin, L. & Tremaine, S. 1999, Icarus, 141, 341

Mandelbaum, R. et al. 2006a, Mon. Not. Roy. Astron. Soc., 372, 758

—. 2006b, Mon. Not. Roy. Astron. Soc., 372, 758

—. 2006c, Mon. Not. Roy. Astron. Soc., 370, 1008

Markevitch, M. et al. 2002, Astrophys. J., 567, L27

Mayer-Hasselwander, H. A. et al. 1998, Astron. Astrophys., 335, 161

McDonough, W. F. 2003, Treatise on Geochemistry, Vol. 2 (Amsterdam, Elsevier)

McGaugh, S. S. & de Blok, W. J. G. 1998, Astrophys. J., 499, 41

Meneghetti, M., Bartelmann, M., Jenkins, A., & Frenk, C. 2007, Mon. Not. Roy. Astron. Soc., 381, 171

Merritt, D. 1987, Astrophys. J., 313, 121

—. 2006, Rep. Prog. Phys., 69, 2513

—. 2008, astro-ph/0802.3186

Merritt, D. et al. 2002, Phys. Rev. Lett., 88, 191301

—. 2007, Phys. Rev. D, 75, 043517

Michel, P. & Thomas, F. 1996, Astron. Astrophys., 307, 310

Mikkola, S. & Tanikawa, K. 1999, Cel. Mech. Dyn. Astron., 74, 287

Milgrom, M. 1983a, Astrophys. J., 270, 371

—. 1983b, Astrophys. J., 270, 365

Miller, C. J. et al. 2006, in Bulletin of the American Astronomical Society, Vol. 38, 998–+

Miralda-Escudé, J. 2002, Astrophys. J., 564, 60

Moore, B. et al. 1996, Astrophys. J., 457, 455

—. 1998, Astrophys. J., 499, L5+

—. 1999, Mon. Not. Roy. Astron. Soc., 310, 1147

—. 2001, Phys. Rev. D, 64, 063508

Morbidelli, A. & Levison, H. F. 2004, Astron. J., 128, 2564

Moskalenko, I. V. 2007, astro-ph/0707.3797

Murray, C. D. & Dermott, S. F. 2000, Solar System Dynamics (Cambridge, UK, Cambridge University Press)

Narayan, R. & Bartelmann, M. 1996, astro-ph/9606001

Navarro, J. F. et al. 1997, Astrophys. J., 490, 493

—. 2004, Mon. Not. Roy. Astron. Soc., 349, 1039

Ni, K. & Baudis, L. 2006, astro-ph/0611124

Nolan, P. L. et al. 2003, Astrophys. J., 597, 615

Oort, J. H. 1950, Bull. Astron. Inst. Neth., 11, 91

Öpik, E. J. 1951, Proc. R. Irish Acad. Sect. A, 54, 165

Ostriker, E. C. et al. 1988, Astron. J., 96, 1775

Ostriker, J. P. & Steinhardt, P. J. 1995, Nature, 377, 600

Pan, M. & Sari, R. 2004, Astron. J., 128, 1418

Percival, W. J. et al. 2007, Astrophys. J., 657, 645

Persic, M. & Salucci, P. 1992, Mon. Not. Roy. Astron. Soc., 258, 14P

Press, W. H. & Spergel, D. N. 1985, Astrophys. J., 296, 679

Press, W. H. et al. 1992, Numerical Recipes in C: The Art of Scientific Computing (Cambridge, UK, University Press, 2nd ed.)

Preto, M., Merritt, D., & Spurzem, R. 2004, Astrophys. J., 613, L109

Preto, M. & Tremaine, S. 1999, Astron. J., 118, 2532

Randall, L. & Sundrum, R. 1999a, Phys. Rev. Lett., 83, 4690

—. 1999b, Phys. Rev. Lett., 83, 3370

Randall, S. W. et al. 2007, astro-ph/0704.0261

Reif, F. 1965, Fundamentals of Statistical and Thermal Physics (New York, McGraw-Hill)

Ressell, M. T. & Dean, D. J. 1997, Phys. Rev. C, 56, 535

Ressell, M. T. et al. 1993, Phys. Rev. D, 48, 5519

Roszkowski, L. et al. 2007, astro-ph/0707.0622

Rubin, V. C. et al. 1978, Astrophys. J., 225, L107

—. 1980, Astrophys. J., 238, 471

Saha, P. & Tremaine, S. 1994, Astron. J., 108, 1962

Sanglard, V. et al. 2005, Phys. Rev. D, 71, 122002

Savage, C. et al. 2004, Phys. Rev. D, 70, 123513

Sehgal, N. et al. 2005, Astrophys. J., 635, 22

Servant, G. & Tait, T. M. P. 2002, New J. Phys., 4, 99

Shutt, T. et al. 2007, Nucl. Instr. Meth. A, 579, 451

Spergel, D. N. & Press, W. H. 1985, Astrophys. J., 294, 663

Spergel, D. N. & Steinhardt, P. J. 2000, Phys. Rev. Lett., 84, 3760

Spergel, D. N. et al. 2007, Astrophys. J. Suppl., 170, 377

SuperCDMS Collaboration. 2005, astro-ph/0502435

Tasitsiomi, A. & Olinto, A. V. 2002, Phys. Rev. D, 66, 083006

Tasitsiomi, A. et al. 2004, Astropart. Phys., 21, 637

Taylor, J. E. & Babul, A. 2005, Mon. Not. Roy. Astron. Soc., 364, 535

The ANTARES Collaboration. 2007, Nucl. Phys. B Proc. Suppl., 165, 188

The H. E. S. S. Collaboration. 2006, Nucl. Phys. B Proc. Suppl., 151, 373

The IceCube Collaboration. 2001, http://www.icecube.wisc.edu/science/publications/pdd/

The Xmass Collaboration. 2005, Nucl. Phys. B Proc. Suppl., 143, 506

Thomas, F. & Morbidelli, A. 1996, Cel. Mech. Dyn. Astron., 64, 209

Thomas, P. A. et al. 1998, Mon. Not. Roy. Astron. Soc., 296, 1061

Tremaine, S. 2005, Astrophys. J., 625, 143

Treu, T. & Koopmans, L. V. E. 2004, Astrophys. J., 611, 739

Tsuchiya, K. et al. 2004, Astrophys. J., 606, L115

Ullio, P. & Kamionkowski, M. 2001, JHEP, 3, 49

Ullio, P. et al. 2001a, Phys. Rev. D, 64, 043504

—. 2001b, JHEP, 7, 44

van der Marel, R. P. 2004, in Coevolution of Black Holes and Galaxies, ed. L. C. Ho, 37–+

van der Marel, R. P. et al. 2000, Astron. J., 119, 2038

Volonteri, M. & Perna, R. 2005, Mon. Not. Roy. Astron. Soc., 358, 913

Wai, L. et al. 2007, astro-ph/0701884

Wess, J. & Bagger, J. 1992, Supersymmetry and Supergravity (Princeton, NJ, Princeton University Press)

Wisdom, J. & Holman, M. 1991, Astron. J., 102, 1528

Wood, M. et al. 2008, ArXiv e-prints, 801, astro-ph/0801.1708

Wyithe, J. S. B. et al. 2001, Astrophys. J., 555, 504

Xue, X. . et al. 2008, astro-ph/0801.1232

York, D. G. et al. 2000, Astron. J., 120, 1579

Yoshida, H. 1990, Phys. Lett. A, 150, 262

Yoshida, N. et al. 2000a, Astrophys. J., 535, L103

Yoshida, S. et al. 2000b, Nucl. Phys. B Proc. Suppl., 87, 58

Zaharijas, G. & Hooper, D. 2006, Phys. Rev. D, 73, 103501

Zaritsky, D. et al. 1993, Astrophys. J., 405, 464

Zhao, H. 2007, astro-ph/0704.0094

Zhao, H. & Silk, J. 2005, Phys. Rev. Lett., 95, 011301

Zhao, H. et al. 2007, Astrophys. J., 654, 697

Zwicky, F. 1933, Helvetica Physica Acta, 6, 110